Stochastic Dynamics in Periodic Potentials

Sarah Naylor, BSc

Thesis submitted to the University of Nottingham
for the degree of Doctor of Philosophy
March 2006

Abstract

This thesis describes the dynamics of both electrons and atoms in periodic potentials. In particular, it explores how such potentials can be used to realise a new type of quantum chaos in which the effective classical Hamiltonian originates from the intrinsically quantum nature of energy bands.

Firstly, this study examines electron dynamics in a superlattice with an applied voltage and a tilted magnetic field. This system displays a rare type of chaos known as non-KAM (Kolmogorov-Arnold-Moser) chaos, which switches on abruptly when an applied perturbation reaches certain critical values. The onset of chaos in the system leads to the formation of complex patterns in phase space known as *stochastic webs*. The electron behaviour under these conditions is analysed both semiclassically and quantum mechanically, and the results compared to experimental studies. We show that the presence of stochastic webs strongly enhances electron transport. We calculate Wigner functions of the electron wavefunction at various times and show that, when compared to the Poincaré sections, evidence of stochastic web formation is observed in the quantum mechanical phase space. Two designs of superlattice are studied and we show, in a full quantum mechanical analysis, that the design of the superlattice has a pronounced effect on the probability of inter-miniband tunnelling and hence the calculated and measured transport characteristics.

Secondly, we explore the dynamics of an ultra-cold sodium atom falling through an optical lattice whilst confined in a harmonic gutter potential that is tilted at an angle to the lattice axis. We show this system is analogous to the case of an electron in a superlattice, and that the atomic dynamics show similar enhanced transport properties for certain trapping frequencies. We also find that in a full quantum mechanical calculation, the atomic wavepacket tends to fragment as the angle at which the gutter potential is tilted is increased.

Finally, we examine the dynamics of a Bose-Einstein condensate falling through an optical lattice whilst confined in a harmonic gutter potential. We vary the strength of the interatomic interaction parameter to investigate the role of interactions in the system and find that, even for small tilt angles, the condensate wavefunction fragments. For large interaction parameters combined with large tilt angles, the wavefunction explodes catastrophically.

Acknowledgements

I would like to thank:
My supervisor Mark Fromhold, for all his help, advice and occasionally legible feedback over the past four years.
Robin Scott for his advice on Bose-Einstein condensation problems and numerical methods.
Sylwia Bujkiewcz for her helpful discussions on the formation of stochastic webs in semiconductor superlattices.
David Hardwick for his indispensable help and tolerance with all matters computer-related.
My office mate, Samantha Hooley, for putting up with my daily grumbling.
All my family and friends for their support, but especially Emma Simpson for always being there for me.
My husband Andrew for, well... everything.
And also the EPSRC for funding my research.

List of Symbols

Symbol	Meaning
A_B	Amplitude of Bloch oscillations:
	Δ_{SL}/eF for electrons in a superlattice
	$\Delta_{OL}/m_a g$ for an atom in an optical lattice
B	The strength of the applied magnetic field:
B_0	Magnetic field at which Feshbach resonance occurs
E_{crit}	Critical energy for LO-phonon scattering
F	The strength of the applied electric field
G	Differential conductance, dI/dV
G^i_{SL}	Energy of ith minigap within superlattice
I	The electronic current along the x axis
I_i,θ_i	The action-angle variables associated with the Hamiltonian
J_l	A Bessel function of the first kind
K	Wavevector associated with the plane waves driving the simple harmonic oscillator derived in section 3.2.5, $d\tan\theta/\hbar$
$L_{x,y,z}$	Characteristic length or spread of a wavepacket in a given direction
N_A	Number of atoms in a Bose-Einstein condensate
P	Scattering probability
P_z	A direction in phase space considered in in section 3.2.5, $\dot{p}_z/\omega_{\|\|}$
T	Temperature
T_c	Transition temperature
U_0	Effective interaction between two atoms in a condensate, $4\pi\hbar^2 a/m_a$
V	Voltage
V_{ext}	Potential due to externally applied fields
V_0	Amplitude of optical lattice potential
V_{OL}	Optical lattice potential
V_{SL}	Superlattice potential
a	Binary s-wave scattering length
d_X	Period of a periodic potential
	$X = SL$ for superlattice, $X = OL$ for optical lattice
$-e$	The charge on an electron
g	Acceleration due to gravity
m	Mass
m^*	Effective mass of a particle moving in a periodic potential

Symbol	Meaning
m_a	Mass of ^{23}Na atom
m_e	Mass of an electron
m_p	Mass of a proton
n	Atom density
$\mathbf{p}$	Momentum
q_y	Linearised momentum along the y-axis
r_c	Cyclotron radius, $r_c = \sqrt{\hbar/Be}$
r	Order of resonance, $\omega_B/\omega_{\|\|}$
v_d	Drift velocity
x_t, z_t	Tilted co-ordinate system
Δ_X^i	Width of ith band arising from periodic potential
	$X = SL$ for superlattice, $X = OL$ for optical lattice
$\Delta_{t,n}$	Time steps employed in numerical methods
$\Delta_{x,z,xz}$	Spatial steps employed in numerical methods
Δ_{FB}	Width of Feshbach resonance
ϵ	Dimensionless parameter representing strength of perturbation
ϕ	Phase
λ	Laser wavelength
λ_{dB}	Thermal de Broglie wavelength
ω_B	The Bloch frequency:
	$eFd_{SL}/\hbar$ for electrons in a superlattice
	$mgd_{OL}/\hbar$ for an atom in an optical lattice
ω_c	Cyclotron frequency, eB/m^*
ω_G	Frequency characterising curvature of gutter potential
	Equal to ω_c for superlattice system, ω_z for optical lattice system
$\omega_{x,z}$	Trapping frequencies in the x_t, z_t directions
$\omega_{\|\|}$	Component of ω_G in the direction of the lattice, $\omega_G \cos\theta$
θ	Angle by which gutter potential is tilted with respect to lattice axis
ρ, φ	Polar coordinates in 2D (see equation (3.57))
τ_B	Time period of Bloch oscillations:
	h/eFd_{SL} for electrons in a superlattice
	h/mgd_{OL} for an atom in an optical lattice
τ	The scattering time of an electron in a superlattice
ξ	Healing length, or coherence length

Contents

1 Periodic potentials **4**

1.1 Introduction 4

1.2 Band Theory 4

1.2.1 Semiclassical model of band transport 7

1.2.2 Bragg reflection and Bloch oscillations 7

1.3 Semiconductor superlattices 10

1.3.1 Effective mass approximation 13

1.3.2 Electronic drift velocity 17

1.4 Optical lattices 19

2 Cold atoms **22**

2.1 Introduction 22

2.2 Atomic trapping and cooling 22

2.2.1 The Zeeman effect 22

2.2.2 Magnetic trapping 24

2.2.3 Cooling techniques 26

2.3 Bose-Einstein condensation 30

2.4 Theoretical Discussion 32

2.4.1 Statistical Mechanics 32

2.4.2 Gross-Pitaevskii Equation 35

2.4.3 Solitons and Vortices 37

3 Stochastic dynamics **41**

3.1 Introduction 41

3.2 Classical chaos 42

3.2.1 Hamiltonian systems 42

3.2.2 Integrability of a system 43

3.2.3 Poincaré sections 46

3.2.4 The KAM theorem and non-KAM chaos 48
3.2.5 Prediction of the stochastic web 51
3.3 Quantum chaos 62
3.3.1 The Wigner function 63

4 Semiclassical and quantum electron transport in a superlattice with an applied bias voltage and a tilted magnetic field 66
4.1 Introduction 66
4.2 The semiclassical mechanics of the system 69
4.2.1 Stroboscopic Poincaré sections 75
4.2.2 Semiclassical electron trajectories 77
4.2.3 Semiclassical drift velocity field curves 86
4.3 The quantum mechanics of the system 93
4.3.1 Determination of the initial wavefunction 93
4.3.2 Quantum mechanical electron trajectories 99
4.3.3 Wigner functions of the system 123
4.3.4 Quantum calculations of the drift velocity 132
4.4 Comparison of theory with experiment 156

5 Dynamics of an ultracold sodium atom in an optical lattice and a tilted magnetic gutter 160
5.1 Introduction 160
5.2 The semiclassical mechanics of the system 163
5.2.1 Semiclassical atom trajectories 166
5.2.2 Stroboscopic Poincaré sections 170
5.3 The quantum mechanics of the system 171
5.3.1 Determining the ground state 174
5.3.2 Quantum mechanical atom trajectories 176
5.3.3 Time evolution of the atom wavefunction 177

6 Bose-Einstein condensates in an optical lattice and a tilted magnetic gutter 191
6.1 Introduction 191
6.2 The quantum mechanics of the system 193
6.3 Quantum mechanical trajectories 197
6.3.1 Results for $a = 0.45$ nm 197
6.3.2 Results for $a = 4.5$ nm 197

6.4 Consideration of the condensate wavefunction 199
6.4.1 Results for $a = 0.45$ nm 200
6.4.2 Results for $a = 4.5$ nm 208

7 Conclusion **217**
7.1 Summary and overview 217
7.2 Suggestions for further study 218

A Derivation of the Fourier coefficients for the dispersion relation of the lowest energy band of a 1D periodic potential **220**

B The $4^{\text{th}}/5^{\text{th}}$ order adaptive Runge-Kutta method **222**

C The Crank-Nicolson Method **225**

D Choice of colourscale for two-dimensional surface plots **230**

Chapter 1

Periodic potentials

1.1 Introduction

Periodic potentials arise in countless areas of physics, giving rise to unique dynamical effects that have interested scientists for many years. In particular, periodic potentials facilitate realisation of a rare type of chaos known as non-KAM chaos (which will be discussed in detail in chapter 3). This subject forms the bulk of this thesis, and its effects will be studied within two categories of periodic potential: namely superlattices and optical lattices. Superlattices are semiconductor heterostructures originally proposed by Esaki and Tsu [1] in 1970 and shall form the basis of the system considered in chapter 4. Optical lattices are standing light waves generated by counter-propagating lasers and have become invaluable tools for investigating the dynamics of cold atoms during the last decade. They form the basis of the system studied in chapters 5 and 6. Whilst later chapters will try to understand the correspondence between the classical and quantum dynamics of particles in such systems, we shall begin here by considering the general system properties arising from periodic potentials, before going on to consider in greater detail the characteristics of each lattice type.

1.2 Band Theory

Periodic potentials have a profound effect upon quantum transport. Band theory predicts that particles propagating through such a potential are restricted to certain permitted energy ranges, known as *bands*. Allowed bands are separated by *band gaps* of forbidden energy states.

To illustrate the existence of such regions, we begin by considering the periodic potential which occurs due to an atomic crystal lattice structure. Such a three-dimensional crystal lattice is specified as follows [2]. The directions of the crystal co-ordinate axes are defined by three *primitive lattice vectors* $\mathbf{a}_1$, $\mathbf{a}_2$ and $\mathbf{a}_3$. These vectors join any lattice point to three near neighbours, and thus a *lattice vector* $\mathbf{R}$ between any two lattice points may be constructed:

$$\mathbf{R} = n_1\mathbf{a}_1 + n_2\mathbf{a}_2 + n_3\mathbf{a}_3 \tag{1.1}$$

where n_i is an integer.

A particle of energy E moving within the periodic potential $V(\mathbf{r})$ set up by such a crystal lattice must be in an eigenstate $\psi(\mathbf{r})$ that satisfies

$$H\psi = \left(-\frac{\hbar^2}{2m}\nabla^2 + V(\mathbf{r})\right)\psi(\mathbf{r}) = E\psi(\mathbf{r}). \tag{1.2}$$

Bloch's theorem is a direct result of the fact that the lattice potential $V(\mathbf{r})$ is periodic [3], and states that:

$$\psi(\mathbf{r}+\mathbf{R}) = e^{i\mathbf{k}\cdot\mathbf{R}}\psi(\mathbf{r}). \tag{1.3}$$

In this expression $\mathbf{k}$ represents a vector in *reciprocal space*, or *wavevector*:

$$\mathbf{k} = l_1\mathbf{b}_1 + l_2\mathbf{b}_2 + l_3\mathbf{b}_3 \tag{1.4}$$

where l_n are integers. The vectors $\mathbf{b}_1$, $\mathbf{b}_2$ and $\mathbf{b}_3$ generate the reciprocal lattice in the same way as $\mathbf{a}_1$, $\mathbf{a}_2$ and $\mathbf{a}_3$ generate the real space lattice. They are known as the *primitive reciprocal lattice vectors* and must satisfy the conditions:

$$\mathbf{b}_i \cdot \mathbf{a}_j = 2\pi\delta_{ij}. \tag{1.5}$$

Note that the primitive cell in reciprocal space is known as the *first Brillouin zone.*

A wavefunction which satisfies Bloch's theorem is known as a *Bloch function* and may be written:

$$\psi_{\mathbf{k}}(\mathbf{r}) = u_{\mathbf{k}}(\mathbf{r})e^{i\mathbf{k}\cdot\mathbf{r}}. \tag{1.6}$$

It is clear from equations (1.3) - (1.6) that $u_{\mathbf{k}}(\mathbf{r})$ must have the periodicity of the lattice. A second important property to note is the fact that any value of

$\mathbf{k}$ is equivalent to some wavevector that lies within the first Brillouin zone. For example, consider a Bloch function

$$\psi_{\mathbf{k}}(\mathbf{r}+\mathbf{R}) = e^{i\mathbf{k}\cdot\mathbf{R}}\psi_{\mathbf{k}}(\mathbf{r}) \tag{1.7}$$

for which $\mathbf{k} = \mathbf{k}' + \mathbf{K}$, where $\mathbf{k}$ lies outside the first Brillouin zone and $\mathbf{k}'$ is the equivalent wavevector within it. The vector $\mathbf{K}$ is defined by

$$\mathbf{K} = n_1\mathbf{b}_1 + n_2\mathbf{b}_2 + n_3\mathbf{b}_3 \tag{1.8}$$

where n_i is an integer. A simple substitution for $\mathbf{k}$ in equation (1.7), and knowledge of the fact that $\mathbf{K}\cdot\mathbf{R} = 2n_I\pi$, where n_I is an integer, demonstrates that:

$$\psi_{\mathbf{k}}(\mathbf{r}+\mathbf{R}) = e^{i(\mathbf{k}'+\mathbf{K})\cdot\mathbf{R}}\psi_{\mathbf{k}}(\mathbf{r}) = e^{i\mathbf{k}'\cdot\mathbf{R}}e^{i\mathbf{K}\cdot\mathbf{R}}\psi_{\mathbf{k}}(\mathbf{r}) = e^{i\mathbf{k}'\cdot\mathbf{R}}\psi_{\mathbf{k}}(\mathbf{r}). \tag{1.9}$$

Hence comparing equations (1.3) and (1.9), we see that $\mathbf{k}'$ is indeed equivalent to $\mathbf{k}$, and so we need only consider wavevectors within the first Brillouin zone from here on.

In general, the first Brillouin zone does not have simple geometry, however we will consider the case where it is centred at the origin in reciprocal space. Hence the limits of the first Brillouin zone in this case lie at $\pm\frac{\mathbf{b}_i}{2}$. Applying the condition specified in (1.5) it is clear that the Brillouin zone boundary in the direction $\mathbf{b}_i$ given by $\pm\frac{\pi}{d_i}$, where d_i is the spatial period of the lattice in the direction $\mathbf{a}_i$.

The possible values which $\mathbf{k}$ can take are determined by applying the *Born-Von Karman boundary condition* to Bloch's theorem:

$$\psi(\mathbf{r}+N_i\mathbf{a}_i) = \psi(\mathbf{r}). \tag{1.10}$$

N_i are integers whose product is the total number of lattice points, N [3]. We find that

$$k = 0, \pm\frac{|\mathbf{b}_i|}{N_i}, \pm\frac{2\,|\mathbf{b}_i|}{N_i}, \ldots, \pm\frac{|\mathbf{b}_i|}{2} \tag{1.11}$$

where k is the component of $\mathbf{k}$ in the direction of $\mathbf{b}_i$.

In addition, we find that for each allowed crystal momentum, there are an infinite number of energy eigenvalues E_n, where n is a quantum number known as the *band index*. A typical plot of energy E as a function of n and k is shown in figure 1.1 for $\mathbf{k}$ along the direction of a reciprocal lattice vector. Note that since all values of $\mathbf{k}$ have an equivalent within the first Brillouin zone, all possible

solutions to the Schrödinger equation for a periodic potential are represented in the diagram (for the direction $\mathbf{b}_i$) - this is known as the *reduced zone scheme.*

1.2.1 Semiclassical model of band transport

The semiclassical model of transport in a periodic potential is used to describe the motion of particles when exposed to externally applied electric and magnetic fields which vary slowly over the dimensions of the particle wavepacket [3]. It is known as the semiclassical model for the following reason. The external fields are treated classically - the evolution of the position and wavevector of the particle when subjected to slowly spatially-varying forces are determined by considering classical equations of motion. On the other hand, the periodic potential which gives rise to the band structure varies on a scale that is small compared to the particle wavepacket and therefore must be treated quantum mechanically. Thus the semiclassical model takes the dispersion relation $E(\mathbf{k})$ for the band in which the particle moves (which arises from the quantisation of allowed $\mathbf{k}$-states) as a given function to enable the calculation of the transport properties.

It is important to note that although in the case of free particles, the momentum is given by $\hbar\mathbf{k}$, this is *not* the case in the semiclassical model. In the case of Bloch electrons, the quantity $\hbar\mathbf{k}$ is known as the *crystal momentum.* The rate of change of the crystal momentum is determined by the forces exerted by externally applied fields - whereas the rate of change of the *actual* momentum must consider the *total* force acting on the particle, including the force experienced due to the periodic potential.

1.2.2 Bragg reflection and Bloch oscillations

We now consider briefly the effect of some externally applied scalar potential energy field G upon a particle in a periodic potential, according to the semiclassical model. As discussed previously, the rate of change of crystal momentum is determined by the force due to G:

$$\hbar\dot{\mathbf{k}} = -\nabla G. \tag{1.12}$$

In addition, the semiclassical model states that a particle moving in band n with wavevector $\mathbf{k}$ has velocity

$$\mathbf{v}_n(\mathbf{k}) = \frac{1}{\hbar}\nabla_{\mathbf{k}} E_n(\mathbf{k}) \tag{1.13}$$

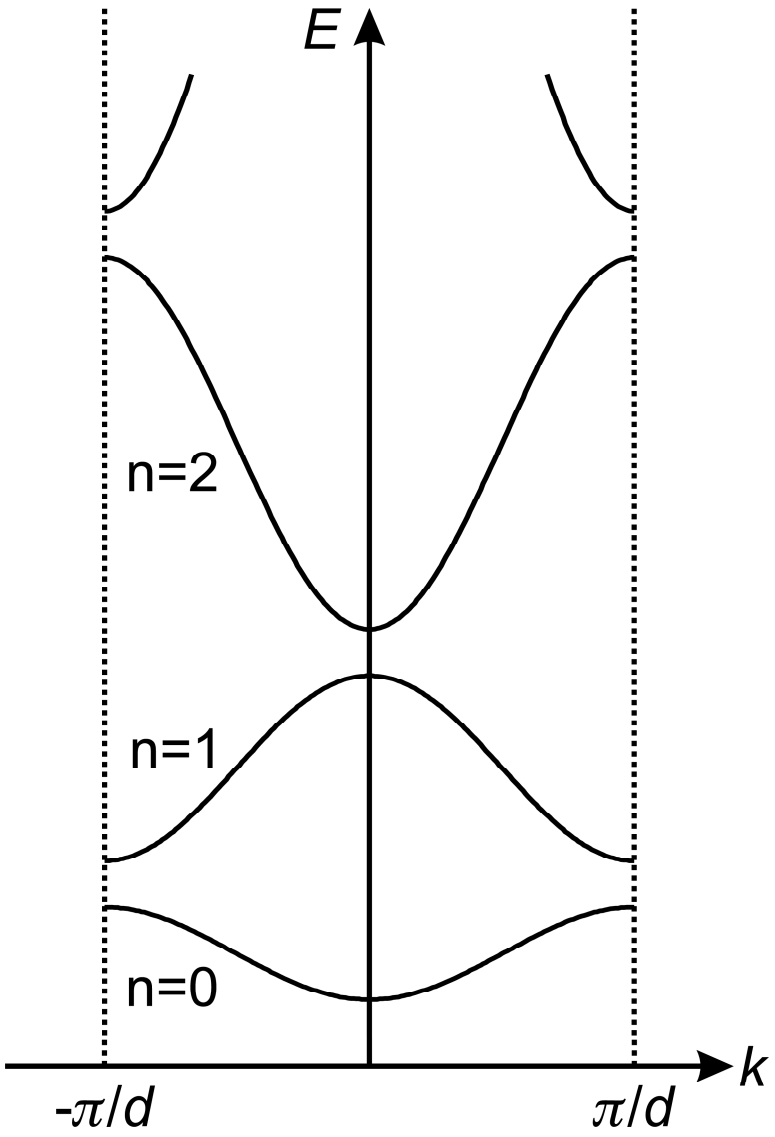

Figure 1.1: Typical dispersion relation in the reduced zone scheme, describing the band structure arising from a periodic potential.

(for a full derivation of this expression, refer to [3]).

There is a startling consequence arising directly from equation (1.13). Consider the case when the system is subjected to a constant force $F\hat{\mathbf{a}}_\mathbf{1}$. Equation (1.12) becomes

$$\hbar\frac{dk_1}{dt} = F. \tag{1.14}$$

Thus the effect of the force upon the wavevector is to push the particle through k-space in the positive direction. Now refer to the form of the typical dispersion relation illustrated in figure 1.1. It is clear that for a particle which starts at rest in the centre of the Brillouin zone, as k_1 begins to increase the gradient of the dispersion relation is increasingly positive and hence the particle accelerates in real space in the $\mathbf{a}_1$ direction, attaining a positive velocity. The velocity reaches its maximum when $\frac{dE}{dk_1}$ is maximal. As the particle is further accelerated through the band, the gradient of the dispersion becomes less and less steep and consequently the particle begins to decelerate and its velocity decreases. Eventually, the edge of the Brillouin zone is reached. Here the gradient of the dispersion relation is zero and the particle comes to a standstill.

However, the reader will recall that in the previous section it was demonstrated that any wavevector outside the first Brillouin zone has an equivalent wavevector within the range $\pm\frac{\pi}{d}$. Therefore upon reaching the edge of the Brillouin zone at $k_1 = +\frac{\pi}{d}$ the particle is imagined to reappear at the opposite boundary at $k_1 = -\frac{\pi}{d}$, where it continues to move through k-space at a constant speed in the positive direction. But now the dispersion curve has a negative gradient - resulting in a negative velocity in real space. Thus, when the particle passes through the Brillouin zone boundary, it changes direction in real space. This is known as *Bragg reflection*. The reflected particle continues to accelerate in the negative direction according to the increasingly negative gradient of the dispersion relation. Then as the gradient becomes less steep, the particle slows, until it reaches $k_1 = 0$ whereupon it arrives back at its original starting point in real space (due to the symmetry of the dispersion curve about $k_1 = 0$). This process is known as a *Bloch oscillation*.

Note that the amplitude, A_B, and time period, τ_B, of a Bloch oscillation are

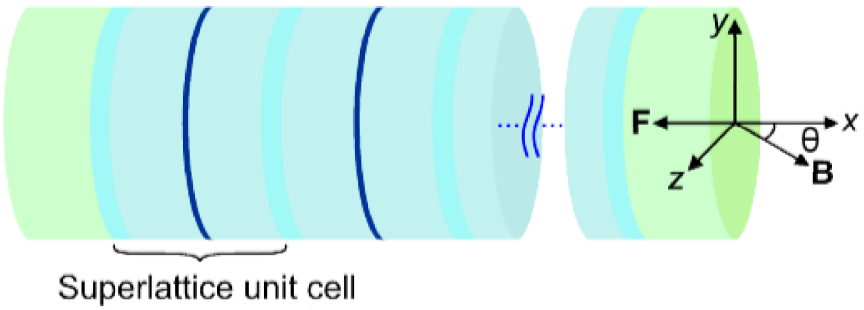

Figure 1.2: Schematic diagram of a semiconductor superlattice sample, showing the repeating layer structure in the x direction. The sample is biased by means of an electric field F applied in the opposite direction to the x-axis, and a magnetic field B is applied in the x-z plane.

easily determined by integration of equations (1.13) and (1.14):

$$A_B = \frac{\Delta}{F} \tag{1.15}$$

$$\tau_B = \frac{h}{Fd} \tag{1.16}$$

where Δ is the *bandwidth* of the occupied band.

1.3 Semiconductor superlattices

A *superlattice* is a semiconductor heterostructure. It is made of layers of different semiconductors sandwiched together in a regular arrangement (see figure 1.2). Each semiconductor material has a periodic crystal form implying the existence of electronic bands. However, the band structure varies between each layer. This leads to offsets in the conduction bands of the different constituent materials relative to one another. Hence we have a periodic variation of the conduction band edge which also gives rise to additional band structure. This superlattice is so called since its lattice period is much larger than in a conventional semiconductor (of order 30 times larger). Consequently, the bandwidth in reciprocal space is significantly smaller than ordinary band structures, therefore we refer to these bands as *minibands*.

A schematic diagram of a general superlattice is shown in figure 1.2. The x-axis of the system is defined perpendicular to the superlattice layers, whilst the y-z plane is parallel to the layers. Note also that all dopants in this discussion are n-type, and n_D is taken to be the doping density. Superlattice crystals are grown

by molecular beam epitaxy, which is carried out under ultra high vacuum (UHV) conditions to prevent the introduction of impurities into the sample. The samples generally take the form of an initial semiconductor substrate upon which layers of atoms are grown - firstly, highly doped layers ($n_D \sim 10^{18}$ cm^{-3}) which form the *emitter contact* whose thickness (of the order of hundreds of nanometers) is very large relative to that of the superlattice structure. This is followed by the superlattice itself, built up of alternating layers of lightly doped semiconductors (of the order of tens of nanometers thick, and with $n_D \sim 10^{16}$ cm^{-3}) that define barriers and wells in the profile of the conduction bands. It is usual to begin and end this section of the sample with a barrier layer, and to incorporate a minimum of roughly 15 periods to validate theoretical assumptions of an infinite periodic lattice. More highly doped thick layers are added to form the *collector contact* before the heterostructure is capped and processed into circular mesas of tens of μm in diameter. The purpose of the highly doped regions surrounding the lightly doped centre is to *modulation-dope* the superlattice. This technique avoids the problem of electron mobility being decreased at high doping concentrations due to scattering by the ionised dopants. The highly doped regions outside the superlattice provide a high density of charge carriers, some of which are transferred into the superlattice where the density of ionised dopants is much lower. Finally, the sample is completed by the addition of ohmic contacts to the substrate and capping layers. In this study, positive bias will be defined at the cap.

Two superlattice samples of differing structure will be considered in this thesis. The first, NU2299, consists of barriers of $Al_{0.3}Ga_{0.7}As$ separating quantum wells of GaAs. (The band gap in $Al_{0.3}Ga_{0.7}As$ is larger than that in GaAs, and hence the conduction band is higher causing it to act as a barrier.) The variation of the conduction band edge and the resultant dispersion relation are illustrated in figure 1.3. The conduction band edge in GaAs is defined to be the zero of the energy scale. The sample consists of 1000 nm of GaAs with a doping concentration of $n_D = 2.0 \times 10^{18}$ cm^{-3}, followed by a 30 nm layer of $Al_{0.03}Ga_{0.97}As$ with $n_D = 2.0 \times 10^{16}$ cm^{-3}. Next, 15 layers of $Al_{0.3}Ga_{0.7}As$ of thickness 2.5 nm ($n_D = 1.4 \times 10^{16}$ cm^{-3}) alternate with 10 nm sections of GaAs ($n_D = 2.0 \times 10^{16}$ cm^{-3}). There follows a 30 nm layer of $Al_{0.03}Ga_{0.97}As$ with $n_D = 2.0 \times 10^{16}$ cm^{-3}, and finally 600 nm of GaAs with $n_D = 2.0 \times 10^{18}$ cm^{-3}.

The second sample, NU2293, is shown in figure 1.4. The unit cell of this superlattice consists of AlAs, GaAs, InAs and GaAs layers whose respective thicknesses are 1 nm, 3.5 nm, 0.241 nm and 3.5 nm. The doping concentration is

$n_D = 3.0 \times 10^{16}$ cm^{-3} [4]. On each side of the 14-period growth are 50 nm GaAs layers with $n_D = 1.0 \times 10^{17}$ cm^{-3}, followed by 600 nm emitter and collector layers with $n_D = 2.0 \times 10^{18}$ cm^{-3}.

When designing superlattice structures, one of the challenges to overcome is the injection of electrons from the emitter contact into the superlattice itself. If the bottom of the first miniband in the superlattice lies at a higher energy than the Fermi energy of the emitter contact, the electrons are presented with a potential barrier which prevents direct injection from the emitter into the miniband [5]. The samples studied in this thesis employ different approaches to surmounting this problem. In NU2293, the introduction of an InAs niche in the centre of the GaAs wells has the effect of substantially lowering the energy of the first miniband so that it lies close to the Fermi level of the emitter (which is 12 meV above the conduction band edge of GaAs) [4]. Should a sample be fabricated which was identical except for the presence of the niche, the bottom of the first miniband would have an energy approximately 60 meV higher [6]. The second miniband, however, is virtually unchanged by the presence of the niche and consequently there is a large bandgap (∼240 meV) observed between minibands one and two in NU2293. This minimises the possibility of interminiband tunelling thus increasing the likelihood of agreement with the semiclassical model of transport in a single miniband presented previously in this section.

In sample NU2299, rather than focusing on the design of the superlattice, the emphasis is placed upon the emitter contact. By introducing a 3% Al content into the emitter, the energy of the conduction band edge is raised so that it becomes resonant with the lowest miniband in the superlattice. In contrast to the previous approach, the minigap in NU2299 is small (∼60 meV) and thus gives rise to a much greater probability of interminiband tunelling.

Unfortunately for theorists wishing to undertake full quantum transport in such systems rather than use a semiclassical model, the discontinuous nature of superlattice potentials can lead to great difficulties. In particular, modelling the motion of a wavepacket in a superlattice with the electric and magnetic fields shown in figure 1.2 requires solution of the full two-dimensional time-dependent Schrödinger equation, in which the superlattice potential must be explicitly included. To reproduce the discontinuities in the potential with satisfactory precision in a finite difference approximation to the Schrödinger equation requires a minimum of approximately seven points to define the smallest feature of the structure - in the case of NU2293 this is the niche, and in NU2299 the barrier.

Modelling a simple sinusoidally varying potential only calls for around ten points per whole lattice period. In view of the fact that the niche accounts for only 3% of the lattice period in NU2293, whilst in NU2299 the barrier is 20% of the period, it is clear that a much higher resolution is necessary to study transport in superlattices than in smoothly varying systems. In particular, simulations based upon NU2293 are severely limited by the huge increase in runtime, data storage and memory requirements.

1.3.1 Effective mass approximation

It is clear that the response of a particle in a Bloch state to an external force is very different to that of a free particle. An important concept employed in understanding this difference is the idea of *effective mass*. The effective mass is the mass a free particle would have if it were to respond to applied forces in the same way as a particle in a Bloch state. Consider the case of an applied constant force $F\hat{\mathbf{a}}_\mathbf{1}$ as described in the previous section. Equation (1.13) may be differentiated to obtain an expression for the acceleration:

$$\frac{dv}{dt} = \frac{1}{\hbar}\frac{d}{dt}\left(\frac{dE}{dk_1}\right) = \frac{1}{\hbar}\frac{d^2E}{dk_1^2}\frac{dk_1}{dt}. \tag{1.17}$$

Substituting from (1.14) and rearranging for F gives

$$F = \left(\frac{1}{\hbar^2}\frac{d^2E}{dk_1^2}\right)^{-1}\frac{dv}{dt} \tag{1.18}$$

and equating this to Newton's second law shows that the effective free mass of a Bloch particle is

$$m^* = \hbar^2 / \frac{d^2E}{dk_1^2}. \tag{1.19}$$

The effective mass is a measure of the forces exerted upon the particle by a periodic potential and takes negative values when the particle is demonstrating a negative acceleration in response to a force in the positive direction. A typical plot of the variation of the effective mass in **k**-space in shown in figure 1.5.

In the case of a superlattice, the electron is subject to two different periodic potentials: firstly, the rapidly varying potential due to the crystal structure, and secondly, the slow variation of the conduction band edge in different layers (see figures 1.3(a) and 1.4(a)). It is this second potential that we call the superlattice

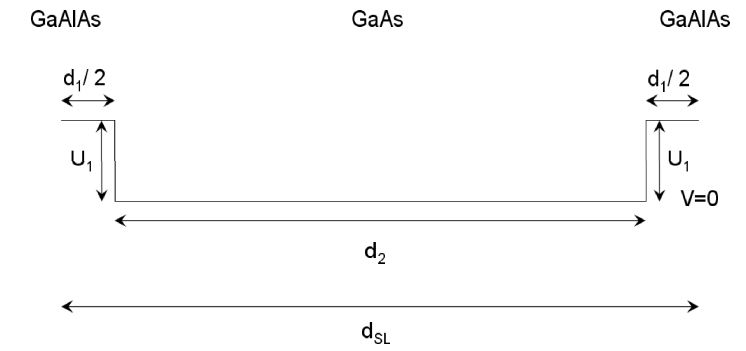

(a)

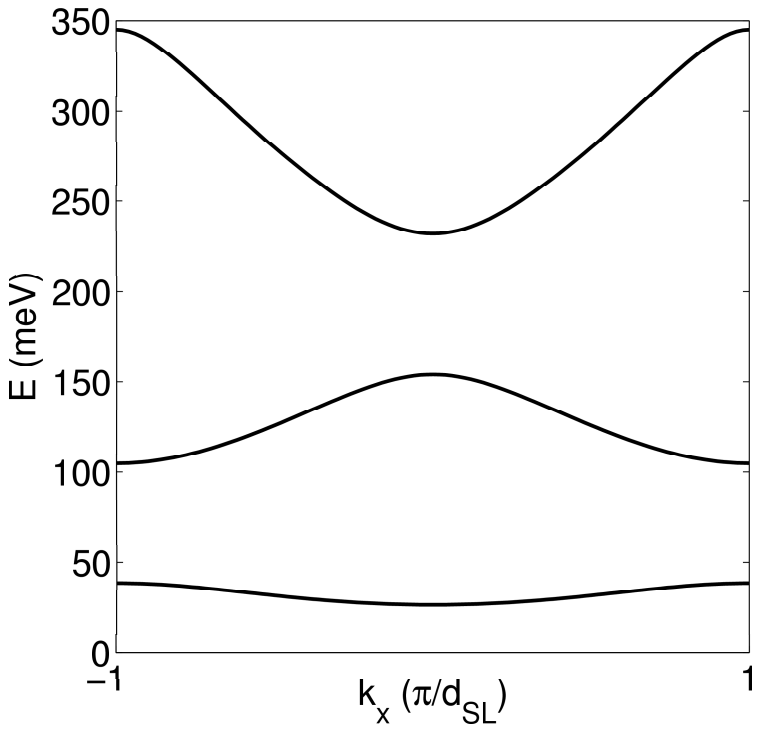

(b)

Figure 1.3: (a) Effective superlattice potential arising from the variation in conduction band edge energy in the different layers of sample NU2299, where $U_1 = 247$ meV, $d_1 = 25$ Å and $d_2 = 100$ Å (not to scale). (b) Dispersion relation of the first three minibands arising from the potential in (a).

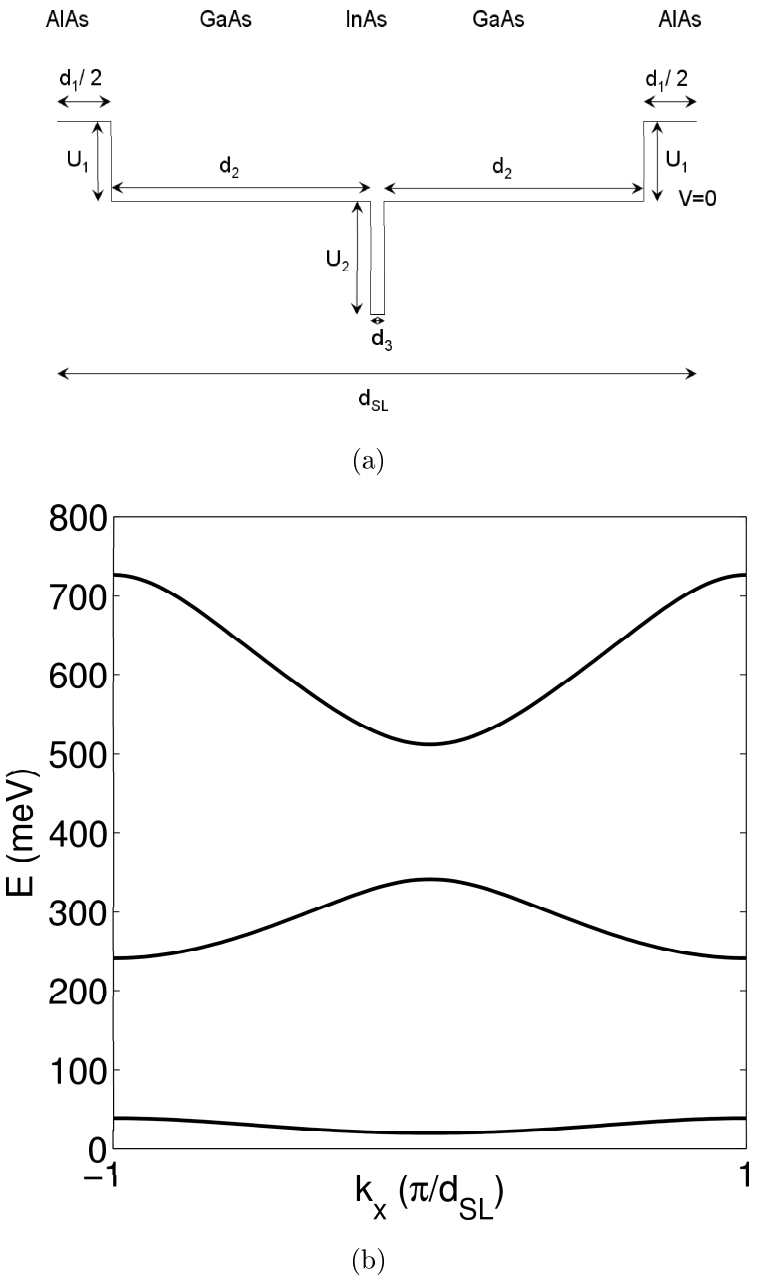

Figure 1.4: (a) Effective superlattice potential arising from the variation in conduction band edge energy in the different layers of sample NU2293, where $U_1 = 1064$ meV, $U_2 = -698$ meV, $d_1 = 10$ Å, $d_2 = 35$ Å and $d_3 = 2.41$ Å (not to scale). (b) Dispersion relation of the first three minibands arising from the potential in (a).

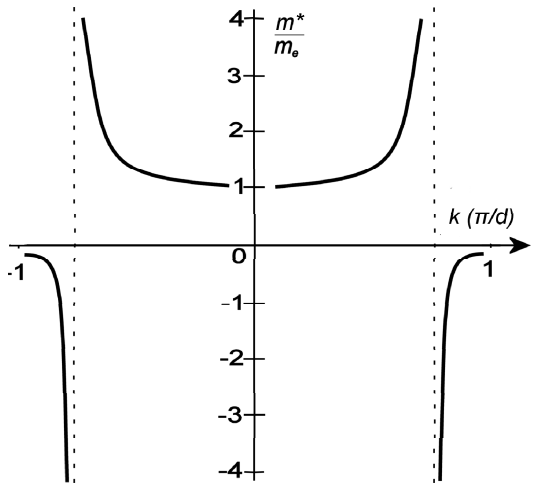

Figure 1.5: Ratio of the effective electron mass m^* to the bare electron mass m_e for a typical dispersion relation of the lowest energy band. The dotted lines represent the point in k-space for which the dispersion relation has $d^2E/dk^2 = 0$.

potential, V_{SL}, and it is the dynamics induced by this potential that are of interest. The purpose of the *effective mass approximation* is to take into account the crystal potential without the need to include it explicitly in the calculations. An effective Schrödinger equation is considered:

$$\left(-\frac{\hbar^2}{2}\frac{d}{dx}\frac{1}{m_e^*(x)}\frac{d}{dx} + V_{SL}\right)\phi(x) = E\phi(x) \tag{1.20}$$

where $m_e^*(x)$ is the effective electron mass (and is dependent upon position in the superlattice), whilst $\phi(x)$ is a so-called envelope function which satisfies the same Schrödinger equation as a free electron with mass $m_e^*(x)$. Thus the new kinetic energy operator term takes into account the variation in effective mass throughout the superlattice layers, with the envelope function describing the amplitude and phase modulation of the underlying Bloch functions [6]. This is illustrated in figure 1.6. Clearly the variation of the envelope function at any given point must be small in comparison with the variation of the Bloch functions enveloped.

Note that since GaAs forms the bulk of both superlattice samples studied in this thesis, it is reasonable to assume that $m_e^*(x)$ is constant with respect to x, and that $m_e^* = 0.067m_e$, the effective mass in GaAs. This will be assumed throughout, and hence the usual form of the kinetic energy operator is recovered in equation 1.20. Note also that the effective mass approximation is valid only when there is no interband mixing, that is, the external fields must be weak and slowly varying [6].

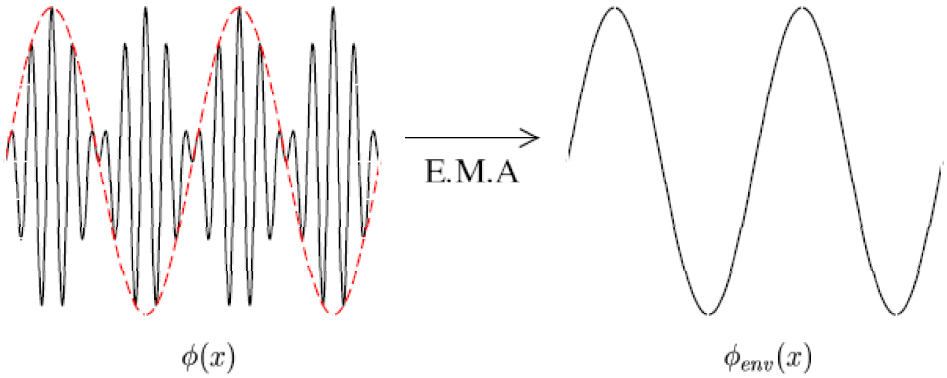

Figure 1.6: Effective mass approximation (EMA): the slowly varying envelope function $\phi_{env}(x)$ due to the changing conduction band edge is separated out from $\phi(x)$, the rapidly varying function due to the crystal structure.

1.3.2 Electronic drift velocity

The discussion of Bloch oscillations in section 1.2.2 suggests that when a DC electric field is applied to the superlattice samples, the electrons will simply oscillate about their initial position and no net current will be measured. In reality this is clearly not the case. A net current is observed because the electrons undergo collisions and are scattered before they have sufficient time to complete an entire Bloch oscillation. Thus the electrons have some net velocity induced by the field. This is known as the *drift velocity*.

The relaxation time approximation assumes that collisions occur in an infinitesimal time dt, and that the time taken for the momentum distribution to relax to an equilibrium configuration is given by τ. Relaxation taken place via scattering events, so τ is often known as the *scattering time*. This gives the mean time between scattering events. Inelastic scattering arises mainly from electron-phonon interactions. Sources of elastic scattering are ionised impurities, small concentrations of bulk impurities and roughness in the superlattice structure at the interfaces between different materials. In the case of NU2293, a further source is straining at the niche interface which arises due to the difference in the lattice constant of InAs and GaAs. Elastic scattering dominates since the elastic scattering time is so short ($\sim$20 fs) that miniband electrons don't gain enough kinetic energy to emit LO phonons before they scatter elastically.

Esaki and Tsu [1], in their famous 1970 paper, apply a path integration method to write the average drift velocity taking into account the scattering

time as

$$v_d = \frac{1}{\tau}\int_0^\infty v_x(t)e^{-t/\tau}dt. \tag{1.21}$$

$1/\tau$ is the scattering rate, and the decay term gives the probability of the electron remaining unscattered after time t. In the absence of a magnetic field the velocity, as stated previously, is

$$v_x = \frac{1}{\hbar}\frac{\partial E}{\partial k_x} \tag{1.22}$$

where the dispersion relation may be written as a Fourier series (see Appendix A:

$$E(k_x) = \frac{\Delta}{2}\left(a_0 - \sum_{n=1}^{\infty} a_n \cos(nk_x d_{SL})\right) \tag{1.23}$$

where d_{SL} is the superlattice period, n is an integer and a_n are the Fourier coefficients. Substituting equations (1.22) and (1.23) into equation (1.21) gives

$$v_d = \frac{\Delta d_{SL}}{2\hbar}\sum_{n=1}^{\infty} n a_n \int_0^\infty \sin(nk_x(t)d_{SL})e^{-t/\tau}dt/\tau \tag{1.24}$$

for an electron initially at the bottom of the miniband i.e. $k_x(0) = 0$. If the drift has been induced by an electric field of magnitude F applied in the negative x direction, then

$$k_x(t) = \frac{eF}{\hbar}t \tag{1.25}$$

and thus integrating equation (1.24) by parts results in

$$v_d = \frac{\Delta d_{SL}}{2\hbar}\sum_{n=1}^{\infty} n a_n \left(\frac{n\omega_B\tau}{1+(n\omega_B\tau)^2}\right) \tag{1.26}$$

where $\omega_B = eFd_{SL}/\hbar$ is the Bloch frequency. Applying a simple miniband approximation of $a_0 = a_1 = 1$, $a_{n>1} = 0$ such that

$$E(k_x) = \frac{\Delta}{2}\left(1 - \cos(k_x d_{SL})\right) \tag{1.27}$$

leads to the following simple expression for the drift velocity when $B = 0$:

$$v_d = \frac{\Delta d_{SL}}{2\hbar}\left(\frac{\omega_B\tau}{1+(\omega_B\tau)^2}\right). \tag{1.28}$$

The drift velocity - field relation described by this expression is known as the

Esaki-Tsu curve. It predicts a maximum in the drift velocity when $\omega_B = 1/\tau$. For $\omega_B << 1/\tau$ the behaviour is ohmic: the long Bloch period allows many scattering events to take place before a Bloch oscillation can be completed, therefore electron localisation is suppressed. However for $\omega_B > 1/\tau$ a surprising phenomenon is predicted: a region of so-called *negative differential velocity* (NDV). This arises because the Bloch oscillations become increasingly rapid at higher fields, thus allowing a manifestation of the localisation effects before scattering occurs.

In the samples studied, a_n falls off sharply as n increases therefore the simple miniband representation is a good guide to the $E(k_x)$ curve; however, when we consider the full quantum analysis of the transport we must consider higher terms to ensure accurate agreement between the semiclassical and quantum mechanical pictures. We find that including contributions up to $n = 10$ is more than sufficient.

1.4 Optical lattices

Crystal structures are not the only way to realise energy band transport. A pair of counter-propagating laser beams may be employed to create a standing light wave, providing another example of a periodic potential in which a band structure arises. In this case, instead of describing atomic positions, the primitive lattice vectors now describe the peaks in the standing wave. The electric field due to the lasers produces a periodic potential energy profile that may be used to act upon ultra-cold ($\lesssim 1$ μK) alkali atoms. For a clearer understanding of this, we will first consider the reaction of a single atom to a static electric field.

The presence of an electric field $\mathbf{E}_{las}$ induces an electric dipole moment, $\mathbf{d}$, in the atom by shifting its energy levels. The *polarisability*, α, of the atom is a measure of the tendency of its electron cloud to be distorted by external electric fields, and is defined as [7]:

$$\mathbf{d} = \alpha \mathbf{E}_{las}. \tag{1.29}$$

The resultant energy shift of the atom may be calculated by

$$dE = -\mathbf{d} \cdot d\mathbf{E}_{las}, \tag{1.30}$$

and hence

$$\Delta E = -\int \alpha \mathbf{E}_{las} \cdot d\mathbf{E}_{las} = -\frac{1}{2}\alpha E_{las}^2. \tag{1.31}$$

For the case of an electric field oscillating with frequency ω, $\mathbf{E}_{las}(t) = \mathbf{E}^0_{las}\cos(\omega t)$, this energy becomes a function of the *dynamical polarisability* $\alpha'(\omega)$:

$$\Delta E = -\frac{1}{2}\alpha'(\omega)\left\langle \mathbf{E}_{las}(\mathbf{r},t)^2\right\rangle_t \tag{1.32}$$

where the field has been time-averaged over the period of oscillation. If the time-average is spatially varying, the changing energy shift is equivalent to an externally varying potential and gives rise to a force:

$$\mathbf{F}_{dipole} = -\nabla V(\mathbf{r}) = \frac{\alpha'(\omega)}{2}\nabla\left\langle \mathbf{E}_{las}(\mathbf{r},t)^2\right\rangle_t . \tag{1.33}$$

This is known as the *dipole force* and is due to the interaction of the induced dipole moment with a spatially varying electric field [7].

In the case of a one-dimensional optical lattice, we consider two lasers whose beams are aligned in opposing directions along the x-axis of the system. We describe the electric fields associated with the two sources of wavelength λ as

$$\mathbf{E}^1_{las} = \frac{\mathbf{E}^0_{las}}{2}e^{i(kx-\omega t)} \tag{1.34}$$

and

$$\mathbf{E}^2_{las} = \frac{\mathbf{E}^0_{las}}{2}e^{i(-kx-\omega t)}, \tag{1.35}$$

where $k = 2\pi/\lambda$. The sum of equations (1.34) and (1.35) gives the overall field as [8]

$$\mathbf{E}_{las}(x,t) = \mathbf{E}^0_{las}\cos(kx)e^{-i\omega t} \tag{1.36}$$

of which we need consider only the real part:

$$\mathbf{E}^{Re}_{las}(x,t) = \mathbf{E}^0_{las}\cos(kx)\cos(\omega t). \tag{1.37}$$

Substitution of equation (1.37) into (1.32) yields the effective potential experienced by an atom due to the optical lattice:

$$\Delta E = -\frac{1}{2}\alpha'(\omega)(\mathbf{E}^0_{las})^2\cos^2(kx)\left\langle\cos^2(\omega t)\right\rangle_t = V_0\cos^2(kx) \tag{1.38}$$

where V_0 is a constant:

$$V_0 = -\frac{\alpha'(\omega)(\mathbf{E}^0_{las})^2}{4}. \tag{1.39}$$

Applying the trigonometric identity $\cos^2(A) = (1 + \cos(2A))/2$ and substituting for k in terms of λ we have

$$\Delta E = \frac{V_0}{2} + \frac{V_0}{2}\cos\left(2\pi\frac{x}{\lambda/2}\right) \tag{1.40}$$

so clearly the period of the optical lattice, d_{OL}, is $\lambda/2$.

It is essential to choose the wavelength of the lasers carefully depending on the species of atom to be studied. The main point of importance is making certain that the lasers are detuned from any atomic resonances that may result in excitation. Another factor is ensuring that the de Broglie wavelength of the atoms will be of the order of several lattice periods. This is to guarantee that the motion of the atomic wavepacket is indeed governed by quantum mechanical band dynamics and not simply the case of a classical particle in a single well. The period of the lattice is usually of the order of several hundreds of nanometres and so is roughly ten times that of the superlattices discussed in section 1.3, and a thousand times that of an atomic crystal. This, coupled with the fact that atomic masses are much larger than the mass of an electron, means that the dynamics occur on much longer timescales ($\sim$ ms) than is the case for electronic ($\sim$ ps) crystal dynamics (refer to equation (1.16)). Thus phenomena such as Bloch oscillations are far more accessible and easier to observe in optical lattices. Another major advantage over superlattice systems is the fact that optical lattices are free of defects [9] and are not subject to thermal vibrations, therefore essentially no scattering occurs. This means that it is possible to study dynamics whose Bloch periods are substantially longer than in superlattices [10].

Further advantages include the exact knowledge of the form of the potential [9] and indeed the ability to select a desirable potential, and hence choose the band structure, by careful selection of the period and depth of the lattice. Furthermore, by detuning the laser beams with respect to one another, the acceleration of the atoms may be controlled [11]. The depth of the potential wells is governed simply by the intensity of the beams. If switched off entirely, direct measurement of the momentum of the atoms is possible [12]. This is another huge advantage of optical lattices, since this is obviously not possible in a natural crystal.

Chapter 2

Cold atoms

2.1 Introduction

The study of cold atoms has applications in a diverse range of fields such as Bose-Einstein condensation, quantum fluids, atom and photon optics, coherence, spectroscopy, ultracold collisions and quantum devices, to name but a few. Indeed, the enormous scope of applications for cold atoms is one of the reasons why the 1997 Nobel Prize was awarded to Phillips, Chu and Cohen-Tannoudji for their work on laser cooling and trapping of atoms. This chapter will discuss the techniques required to trap and cool atoms to ultracold (μK and below) temperatures, focusing in particular upon their application to the attainment of Bose-Einstein condensation, which will be considered in detail in section 2.3.

2.2 Atomic trapping and cooling

2.2.1 The Zeeman effect

We begin this section by extending the previous discussion of atoms in electric fields to consider the effects of magnetic fields. We will consider the case of the alkali metals since later chapters study systems of sodium-23 atoms. In the ground state, the alkalis have a number of filled electron shells plus one single electron in the lowest available s-orbital. The net electronic orbital angular momentum, L, is zero, and the total electronic spin, S, is $1/2$. J is the quantum number of total electronic angular momentum, and is given by:

$$|L - S| \leq J \leq L + S \tag{2.1}$$

hence $J = 1/2$ for alkali atoms.

The *hyperfine interaction* describes the coupling between the nuclear spin, I, and the magnetic field produced at the nucleus by the electrons. This causes a splitting of the energy levels which is described in the Hamiltonian by a term [13]

$$H_{hf} = A_{hf}\hat{\mathbf{I}} \cdot \hat{\mathbf{J}} \tag{2.2}$$

where A_{hf} is a constant and $\hat{\mathbf{I}}$, $\hat{\mathbf{J}}$ are the operators for nuclear spin and total electronic angular momentum. These hyperfine levels are further split in the presence of an externally applied magnetic field. This is known as the *Zeeman effect* [7, 9, 13] and arises from the interaction of the applied field with the magnetic moments of both the nucleus and the outer electron. For a field $B\hat{\mathbf{z}}$ the contribution to the Hamiltonian due to spin is now

$$H_{spin} = A_{hf}\hat{\mathbf{I}} \cdot \hat{\mathbf{J}} + CJ_z + DI_z \tag{2.3}$$

where

$$C = g_J \mu_B B \tag{2.4}$$

and

$$D = -\frac{\mu}{I}B. \tag{2.5}$$

In equations (2.4) and (2.5) μ_B is the Bohr magneton, which is defined as

$$\mu_B = \frac{e\hbar}{2m_e}, \tag{2.6}$$

and μ is the magnetic moment of the nucleus, which is of the order of the nuclear magneton μ_N [7]:

$$\mu_N = \frac{e\hbar}{2m_p} = \left(\frac{m_e}{m_p}\right)\mu_B. \tag{2.7}$$

In equations (2.6) and (2.7) m_e, m_p represent the electron and proton masses respectively, thus it is clear that $\mu << \mu_B$ and hence D may be neglected. In equation (2.4) g_J is referred to as the *g-factor* of the electron and is defined as

$$g_J = 1 + \frac{J(J+1) + S(S+1) - L(L+1)}{2J(J+1)}. \tag{2.8}$$

For alkali atoms we recall that $L = 0$ and $S = 1/2$ thus $g_J = 2$. Note also that

the total spin, with quantum number F, is given by:

$$|I - J| \leq F \leq I + J \tag{2.9}$$

which for alkalis gives $F = I \pm 1/2$. In the specific case of ^{23}Na, $I = 3/2$ and thus $F = 2$ or 1.

Under the application of low-strength magnetic fields the Zeeman splitting is small compared with the hyperfine splitting, and the energy of the atom may be expressed by the following relationship to first order:

$$E(F, m_F) = E(F) + m_F g_F \mu_B B \tag{2.10}$$

where $E(F)$ is the energy of the atom in the absence of an external magnetic field and m_F is the quantum number relating to the z-component of the total angular momentum F. The reader should note that equation (2.10) will form the basis of the cold atom trapping techniques discussed in later sections. In this equation, g_F is the *Landé g-factor* given by:

$$g_F = g_J \frac{F(F+1) + J(J+1) - I(I+1)}{2F(F+1)}. \tag{2.11}$$

Since $J = 1/2$, $I = 3/2$ and $F = 1$ or 2 as detailed previously, $g_F = \pm 1$ for ^{23}Na.

2.2.2 Magnetic trapping

Neutral atoms may be trapped by the Zeeman effect [12]. Spatially varying magnetic fields can be engineered in order that an atom travelling through the field experiences a shift in its energy levels such that its kinetic energy is exchanged for an effective potential energy originating from the change in internal energy of the atom (see equation (2.10)). It is usual to select the field parameters such that states exist whose energy varies linearly with B. Thus we may write the energy of an atom in state i as

$$E_i = C_i - \mu_i B \tag{2.12}$$

(see equation (2.10)) where C_i is a constant and $\mu_i = -m_F g_F \mu_B$ is the magnetic moment of the state. If the magnetic moment of the atom is positive, it is known as a *high field seeker* since its energy is lowest in regions of high magnetic field. Conversely, if μ_i is negative the atom is a *low field seeker* and is attracted to

regions of low field in order to achieve the lowest possible energy configuration. This fact may be used to design a magnetic atom trap. Experimentalists cannot create a local maximum in the magnetic field in the absence of electric currents [14–16], therefore the trap must make use of a local minimum in a spatially varying field. Hence we can only trap neutral atoms whose magnetic moment is negative.

Still considering alkali atoms, we find that two states in particular are suitable for the trapping technique proposed: the *doubly polarised state* and the *maximally stretched state*. The doubly polarised state is characterised by $F = 2$ and $m_F = 2$, and the maximally stretched state by $F = 1$ and $m_F = -1$. For both states, we see from equation (2.10) that their energy is directly proportional to the magnetic field for small B, and provided the Zeeman splitting is much less than the hyperfine splitting, both have negative magnetic moments.

Another issue of importance is that of losses from the trap [7]. As the atom moves through the trap, it is subjected to an effective time-dependent magnetic field. If the temporal frequency at which the effective field changes is of the order of the frequency of transitions ($\propto B$) between Zeeman sublevels, a low field seeker may be flipped into a high field seeking state and consequently be ejected from the trap. The greater the temporal frequency of the field compared with the transition frequencies, the more appreciable the losses from the trap. The transition frequencies are of order $\mu_B B$, therefore if the field minimum is at $B = 0$ (as is the case for the *quadrupole trap*) there is a virtual hole in the trap which leads to serious losses.

Cornell and Wieman [17] overcame this problem by employing the *time-averaged orbiting potential (TOP) trap* which superimposes a rotating, spatially uniform magnetic field upon the quadrupole trap [7]. This has the effect of constantly repositioning the node of the trap. The frequency of the additional field must be chosen carefully - it must be low compared to the frequency of transitions between Zeeman sublevels ($\sim 10^6$ Hz), but must also be high in relation to the atomic motion ($\sim 10^2$ Hz). This ensures that the atoms experience an effective potential equal to the time average of the field over one period of rotation. Typically the frequency of rotation is chosen to be of order 10^3 Hz. An alternative solution is also offered by the *Ioffe-Pritchard trap* which employs a magnetic field profile whose minimum is non-zero [18, 19].

Another trap of great experimental importance is the *magneto-optical trap (MOT)*. This consists of a spatially-varying magnetic field supplemented by six

laser beams - two counter-propagating along each axis [7]. The MOT may also be used to cool atoms, and is often used to prepare the atoms before transferring them to alternative traps for further study.

2.2.3 Cooling techniques

Attaining the ultra-low temperatures necessary for cold atom experiments requires state of the art cooling techniques. We shall shortly proceed to a discussion of the processes employed by experimentalists in achieving μK temperatures. As alluded to previously, the MOT is instrumental in the initial stages of cooling. This is because the lasers exert *radiation pressure* upon atoms. When residing in the beam of a laser with wavevector $\mathbf{k}_p$ an atom may be excited and acquire a momentum $\hbar\mathbf{k}_p$ by absorbing a photon. The atom then relaxes to the ground state by spontaneously emitting a photon. The emission occurs in a random direction and there is therefore no net transfer of momentum to the atom when many such events are considered. The total force resulting from absorption processes is equal to

$$\mathbf{F}_{rad} = \hbar\mathbf{k}_p\Gamma_g \tag{2.13}$$

where Γ_g is the rate of excitation of the ground state. Radiation pressure forms the basis of both *Doppler* and *Sisyphus cooling*, which we will go on to describe in more detail. The final cooling step is a purely magnetic phenomenon and is known as *evaporative cooling*.

Doppler Cooling

When the alkali atoms are initially vaporised, they are at a temperature of several hundred kelvin. The first stage in the cooling process is Doppler cooling. This is carried out via a laser beam directed opposite the atom beam, which slows the atoms causing cooling in one dimension [20]. The atoms absorb photons which are on-resonance with an atomic transition, are excited into a higher energy state, then proceed to re-emit the absorbed photon. The absorption process provides a momentum kick opposing the direction of motion, however emission occurs in a random direction. Thus the net effect is to retard the atom beam in one direction. Due to the Doppler effect, the frequency of the atomic transition in the lab frame is not constant as the atoms slow. There are two possible methods employed to surmount this. This first is known as *chirping*, in which the laser frequency is

varied in a rapid sweep. The second is to employ a Zeeman slower, where the atoms travel along the axis of a tapered solenoid. The inhomogeneous magnetic field means that, due to the Zeeman effect, the spacing between the atomic levels varies with distance, cancelling out the Doppler effect. Such methods cool the atoms to temperatures of order 1 K.

Atoms are then loaded into a magneto-optical trap (MOT) which performs both trapping and cooling functions. A pair of Helmholtz coils with opposite currents generate the quadrupole profile which provides the magnetic effects, whilst three orthogonal pairs of counter-propagating lasers which intersect at the centre of the coils set up the optical potential. The inhomogeneous magnetic field means that the frequency of the atomic transition depends on position, thus efficient cooling is possible for a range of velocities [7]. The Zeeman splitting of the atomic levels depends on the position in the field and thus there is an imbalance in the radiation pressure due to absorption of photons from the lasers. The polarisation of the lasers may be chosen such that this imbalance acts to push atoms towards the centre of the trap from all sides.

An effect called *optical molasses* occurs, so called because the intersection of the laser beams causes the atoms to move as if they were in a viscous, treacle-type fluid. This is a three-dimensional slowing effect, as opposed to the one-dimensional cooling described earlier, achieved by detuning the three orthogonal standing waves to a few linewidths below the atomic resonance frequency. Since the Doppler effect means that the atom is always shifted towards the resonance of the beam opposing its motion, slowing is achieved regardless of the direction of motion. The limiting factor on the effectiveness of optical molasses is due to the random-directional recoil of the atoms as they re-emit photons. We model this diffusing effect as a random walk in momentum space, with step size $\hbar k$ equal to the photon momentum. To quantify the limiting effect upon the cooling process, we must consider the ratio of the diffusion coefficient to the damping coefficient of the force. Assuming low velocities and intensities and a saturated transition, and by taking into account fluctuations in the number of absorbed photons, a three-dimensional treatment of the diffusion [20] gives the minimum temperature attainable as

$$k_B T = \frac{\hbar}{2\tau_S} \tag{2.14}$$

where τ_S is the lifetime for spontaneous emission of photons. This is known as the Doppler cooling limit. It allows temperatures as low as 240 μK in sodium.

Sisyphus Cooling

Further cooling is achievable within the MOT, however this requires a more complex treatment than that so far. We know that in reality alkali atoms have degenerate sublevels in the ground and excited states, known as hyperfine states. When placed in a radiation field, these sublevels shift by amounts dependent upon the polarisation and intensity of the radiation. This may lead to a greater reduction in temperature via a process termed *optical pumping*. Consider a ground state which has split into two hyperfine levels. If the applied radiation is resonant with a transition from the higher energy of the two hyperfine ground states, to a hyperfine state of the excited level, atoms will be excited and then fall back. However they may decay into either of the hyperfine ground levels. Since there is no resonant excitation of the lower hyperfine ground level to a higher state, the net effect is to drop atoms into the lowest sublevel. Note that the timescale for optical pumping is greater than that for spontaneous emission, therefore considering equation (2.14), it is immediately clear that for an optical pumping time $\tau_P > \tau_S$, the temperatures that can be reached via this process are lower than in the previous discussion. The mechanism by which sub-Doppler cooling occurs in a MOT is known as the *Sisyphus effect*. It is dependent upon the fact that the radiation field of the lasers is inhomogeneous. If the lasers are linearly polarised in orthogonal directions, the polarisation of the resultant standing wave varies between circular and linear with a period of half the optical wavelength. The shift in energy of each sublevel depends on each of the circularly polarised components of the radiation field, which are spatially varying. It can be shown that for an atom with two substates of the ground level (g_+ and g_- say), the energies, V^+ and V^-, to which these substates shift vary out of phase with each other according to

$$V^{\pm} = V_0 \left(-2 \pm \sin 2kz\right), \tag{2.15}$$

where the value of V_0 depends upon the particular atom and substates in question, and we consider the variation along the z-axis. Note that V_0 is positive for red detuning [7]. It is found that at positions where the field is linearly polarised, no net pumping occurs. Pumping from g_+ to g_- is at a rate proportional to the intensity of circular polarisation in the negative sense, $\left(1 + \sin 2kz\right)/2$, whilst pumping from g_- to g_+ is proportional to the intensity of the positive circular polarisation componenent, $\left(1 - \sin 2kz\right)/2$. Hence, detuning the lasers to the red results in an increase in the population of the lower energy g_- state, and can lead

to temperatures of only a few μK. The limit of Sysiphus cooling is the photon recoil energy E_R [12], which corresponds to a temperature T_R given by:

$$E_R = k_B T_R = \frac{\hbar^2 k^2}{2m}. \tag{2.16}$$

Sisyphus cooling is so called because when it was described by Dalibard and Cohen-Tannoudji in 1989 [21], they compared it to the mythological Greek whom the Gods sentenced to an eternity of pushing a rock up a hill, only for it to roll down again when he reached the summit. Consider the case of an atom positioned at a point in the radiation field where the substates have equal energy. As the atom moves away from this point, its energy must shift due to the radiation field. If it moves into a higher energy region, conservation of energy dictates that its kinetic energy must decrease accordingly. Also, the probability that the atom is pumped into the lower energy state is increased. Alternatively, if it enters a region shifted to a lower energy and gains kinetic energy, the likelihood of pumping to a higher energy state decreases. Thus the overall effect is that the atoms tend to drop down into the lowest energy state, in the same way that the rock would always roll back into the valley.

Evaporative Cooling

The next step in the generation of ultra-cold atomic vapours is evaporative cooling. Evaporative cooling works on the principle that if we can selectively remove particles whose energy is greater than the average energy per particle, the temperature of the remaining particles will fall. For this stage, we confine the atoms in a purely magnetic trapping potential, and recall the conclusion in section 2.2.2 that magnetically trapped atoms *must* have a negative magnetic moment. Particles are removed by the application of a radio frequency pulse which flips the atomic spins from negative to positive, thus causing them to be ejected from the trap. Since the amount by which the Zeeman levels are shifted for a particular atom is a function of position in the trap, we can tune the rf pulse to the resonance of the most energetic atoms, namely those located in the regions of strongest magnetic field. When the gas rethermalises via elastic processes its temperature is lowered. As the atom vapour cools, the pulse frequency is adjusted to remove atoms of increasingly low energy. This way the temperature can be reduced to as little as roughly 1 μK. Note also that in order to attain densities high enough to make evaporative cooling effective, it is necessary to magnetically squeeze the vapour

whilst it is contained in the trap [22].

2.3 Bose-Einstein condensation

Bose-Einstein condensation (BEC) is a macroscopic quantum phenomenon first predicted by Einstein in 1925. Einstein recognised that if a non-interacting gas of bosons was cooled below a certain temperature, a quantum mechanical phase transition would occur in which a macroscopic fraction (approximately 99%) of the gas would fall into the ground state of the system. Note that in this case, the term condensation is used to describe not a localisation in real space but a localisation in phase space. No analogous effect is observed in a fermionic gas since fermions are subject to the Pauli exclusion principle, which dictates that two or more fermions may not exist in the same quantum state.

Despite the fact that this conceptually simple quantum mechanical effect was predicted in the 1920s, it was a further 60 years before it was produced experimentally. This delay was due to the technological innovation required for its realisation: it wasn't until relatively recently that the previously discussed cooling and trapping techniques that enable experimentalists to achieve the ultra-low temperatures required for BEC were refined. In June 1995, a research group at JILA led by Cornell and Wieman applied these techniques and became the first to generate a BEC using rubidium, followed closely by Ketterle's group at MIT in September with sodium. In the same year Hulet's group obtained indirect evidence of BEC in lithium. In 1998 Greytak and Kleppner added hydrogen to the growing list of condensates [23], and in 2001 the first helium-4 condensate was produced from metastable atoms in the lowest spin-triplet state [7]. Following these advances, Ketterle, Wieman and Cornell recieved the 2001 Nobel prize in physics for their work on BEC.

Wieman notes that the intuitive approach to obtaining the necessary conditions for BEC is to compress the atoms to reduce the inter-particle spacing - however this will obviously cause the atoms to form a solid [22]. Similarly, attempts to cool the atoms lead to solidification well before we even begin to approach the temperatures required, unless dilute gases (of typical density 10^{13}-10^{15} cm^{-3} [7]) are used to prevent this. However this means that the temperatures now required to achieve BEC are of order 100nK. Wieman's approach to attaining such low temperatures was a two-step process - first by laser cooling and trapping, followed by magnetic trapping and evaporative cooling. The tendency of

the system to solidify is overcome by creating a vapour that is quick to equilibrate to its proper thermal distribution as a spin-polarised gas, but which is slow to reach true equilibrium i.e. solidify. He worked with very dilute gases so that the formation time for a solid or liquid due to three-body collisions was of the order of seconds or minutes, whilst the elastic binary collision thermalisation time was of order 10 ms making BEC possible [23]. While the gas is in its metastable supersaturated-vapor the BEC is produced [22].

Originally the quest for a condensate began with hydrogen, but the laser cooling techniques which finally led to the realisation of BEC were not as well suited to hydrogen [24]. It was much more difficult to attain BEC in hydrogen due to dipole-dipole spin-flip collisions, which allow atoms to enter a lower-energy spin state and consequently escape from the trap [22]. Wieman knew that the key to successful evaporative cooling of a laser cooled sample is to attain a high elastic collision rate between the magnetically trapped atoms, therefore he decided to try the same approach with a heavy alkali gas (rubidium). He realised that although the rate of "bad" collisions was likely to be similar to that in hydrogen, the rate of two-body elastic collisions required to thermalise the gas for evaporative cooling was likely to be larger for alkalis due their larger cross section for "good" collisions. This is because the magnetic moments of hydrogen and rubidium are the same, but rubidium atoms are larger.

Since the attainment of BEC, the field has attracted worldwide interest. Motivations for research include the fact that BEC is known to be the basis of effects such as superconductivity and superfluidity. In addition, BECs offer experimentalists a robust and versatile platform for the study of mesoscopic many body physics [25]. The possibility of using BEC to create an atom laser is also a strong attraction. This would consist of an intense, highly directional, coherent atom beam [26]. A true continuous laser would require steady-state BEC formation and continuous replenishment - challenges which await physicists in the future. However, once achieved, the applications for such a system are manifold. Suggestions based on coherent atom optics range from use in precision measurements (of fundamental constants for example) to atom lithography, atom holography and non-linear atom optics, for which interactions are crucial. We may even find eventually that BEC (of nucleon pairs) is important inside neutron stars, which would have profound implications for current theories of supernovae and evolution of neutron stars [7].

2.4 Theoretical Discussion

In the following section, we will use the Bose distribution to explain why Bose-Einstein condensation occurs. We shall then proceed to a discussion of how the interatomic forces which are present in a non-ideal gas may be incorporated to provide a model suitable for practical application.

2.4.1 Statistical Mechanics

Einstein extended Bose's work on quantum statistics from photons to atoms to produce the now familiar Bose-Einstein distribution function. He considered the theory of a non-interacting, degenerate Bose gas with atoms of zero spin. Bowley [27] states that the chemical potential, μ, of such a system at high temperatures is approximately

$$\mu = k_B T \ln\left(n\lambda_{dB}^3\right), \tag{2.17}$$

where k_B is Boltzmann's constant, T is the temperature, n is atom density and λ_{dB} is the thermal de Broglie wavelength. Note that equation (2.17) is only true provided the condition $V >> N_A\lambda_D^3$ holds, where V is the volume and N_A the number of atoms. In this regime, μ is negative because $n\lambda_{dB}^3 < 1$. That is, equation (2.17) is valid for low-densities and high temperatures.

At this point, the number of particles in each single particle state is governed by the Maxwell-Boltzmann distribution. However as the temperature is reduced, the distribution narrows and takes the form of a Bose-Einstein distibution

$$f(E) = \frac{1}{e^{\frac{(E(k)-\mu)}{k_B T}} - 1} \tag{2.18}$$

where $f(E)$ is the mean occupation number of the single particle state having energy $E(k) = \hbar^2 k^2/2m$. For particles in a box of volume V, k is the wavevector labelling the plane wave state $V^{-1/2} exp(i\mathbf{k}\cdot\mathbf{r})$. Since the total number of atoms is given by

$$N = \sum_{allstates} f(k), \tag{2.19}$$

in order that N be conserved, μ must increase as the temperature falls. Eventually, some critical temperature is reached at which the chemical potential approaches zero. This is the upper limit of μ since a positive value of the chemical potential would cause low energy states to have a mean occupation number of

less than zero - clearly a physical impossibility. Now consider the occupation of the ground state, which we take to have zero energy, at this critical temperature:

$$f\left(k=0\right)=\frac{1}{e^{\frac{E(k=0)-\mu}{k_BT}}-1}\approx-\frac{k_BT}{\mu}. \tag{2.20}$$

It is clear that as the chemical potential tends to zero from negative values, the ground state of the system develops a macroscopic population. Atoms condense into the ground state with a uniform spread in real space - Bowley [27] confirms, as Einstein realised many years ago, that the appearance of such condensed particles indicates the presence of a new phase of matter.

Each atom is a quantum mechanical wavepacket. As the atoms are cooled, the wavepackets of neighbouring atoms begin to overlap. Indistinguishability then becomes important and Bose statistics must be applied. When the phase transition occurs, the de Broglie wavelength of the characteristic thermal motions is known to be of the order of the mean inter-particle spacing [25], i.e.

$$\lambda_{dB}\sim n^{-\frac{1}{3}} \tag{2.21}$$

where n is the atom density. This knowledge may be used to approximate the transition temperature. The thermal de Broglie wavelength of an atom of mass m is given by [7]

$$\lambda_{dB}\sim\sqrt{\frac{2\pi\hbar^2}{mk_BT}}, \tag{2.22}$$

so by substituting equation (2.22) into the condition for BEC given in equation (2.21) and rearranging, we obtain an estimate for the transition temperature, T_c

$$T_c\sim\frac{2\pi\hbar^2n^{\frac{2}{3}}}{mk_B}. \tag{2.23}$$

In order to determine a more accurate expression for T_c we need to consider the density of states. Kittel [28] derives the single-particle density of states in three dimensions, and finds that

$$D\left(E\right)dE=\frac{Vk^2}{2\pi^2}\left(\frac{dk}{dE\left(k\right)}\right)dE. \tag{2.24}$$

The total number of atoms present is given by

$$N_A = \int_0^\infty f(E)\, D(E)\, dE, \tag{2.25}$$

which reduces to

$$N_A = \frac{2\pi V (2m)^{3/2}}{h^3} \int_0^\infty \frac{E^{1/2}}{e^{\frac{E}{k_B T_c}} - 1} dE. \tag{2.26}$$

If we now change the variable of integration to $z = E/(k_B T_c)$, and substitute $n = N_A/V$ we obtain

$$n = \left(\frac{2\pi m k_B T_c}{h^2}\right)^{\frac{3}{2}} \left\{\frac{2}{\sqrt{\pi}} \int_0^\infty \frac{z^{1/2}}{e^z - 1} dz\right\}. \tag{2.27}$$

Thus, evaluating the standard integral using look-up tables, we find that

$$k_B T_c = 3.31 \frac{\hbar^2 n^{\frac{2}{3}}}{m}. \tag{2.28}$$

For a more rigorous derivation of T_c refer to [7]. We should note at this point that due to the finite volume of a real atomic gas, the transition temperatures are not precisely defined. In addition, inter-particle interactions shift the transition temperature by a few percent [25].

Another important parameter to derive is known as the condensate fraction. This tells us what proportion of the atoms present have condensed into the ground state. Recall that in order to derive the more accurate expression for the transition temperature, we began by integrating over all states to find the total number of particles. We should note that such an integral gives no weight to the ground state - what we actually calculate is the population of the excited states, N_{ex}. At temperatures above T_c, the proportion of particles in the ground state, N_0 is negligible, so the method is reliable for the determination of T_c. However, at temperatures below T_c, equation (2.25) should be written

$$N_{ex} = N_A - N_0 = \int_0^\infty f(E)\, D(E)\, dE. \tag{2.29}$$

Hence from equation (2.28) we can write

$$k_B T = 3.31 \frac{\hbar^2}{m} \left(\frac{N_{ex}}{V}\right)^{\frac{2}{3}}. \tag{2.30}$$

Dividing equation (2.28) by equation (2.30) and rearranging gives us

$$\frac{N_0}{N_A} = 1 - \left(\frac{T}{T_c}\right)^{\frac{3}{2}}. \tag{2.31}$$

Remember that this expression is not valid for $T > T_c$ since we have assumed $\mu = 0$.

2.4.2 Gross-Pitaevskii Equation

The treatment so far has not taken into account the fact that in a real system, interactions are present. BEC is a robust phenomenon - it is not destroyed despite the leading role that interactions play in the energetics of the system [25], however we must still give quantitative consideration to the effects of the interactomic forces. For instance, when we say that a dilute gas is required for the observation of BEC, what exactly is meant by this? As alluded to in section 2.3, for an atom vapour to be dilute requires that the dominant effects of interaction result from two-body scattering [7]. The strength of the interactions is characterised by a parameter a, known as the binary s-wave scattering length, which is of order $100a_0$ for alkali atoms (where a_0 is the Bohr radius). Therefore put quantitatively, we desire a ratio $a/r \approx 0.01$, where r is the inter-particle separation.

Once a dilute vapour is achieved, the atoms may be considered to be discrete interacting particles [25]. Pethick and Smith [7] show that at low energies the true interatomic potential can be replaced by a zero range (delta function) interaction of strength U_0 where

$$U_0 = \frac{4\pi\hbar^2 a}{m}. \tag{2.32}$$

Naturally, this term forms part of the equation governing the motion of the BEC. In constructing the BEC equation of motion, the atoms in the condensate are treated using a mean-field approximation, allowing us to write the wavefunction describing the N-particle system as

$$\Psi(\mathbf{r}_1, \mathbf{r}_2, \ldots, \mathbf{r}_N) = \prod_{i=1}^{N} \phi(\mathbf{r}_i) \tag{2.33}$$

where $\phi(\mathbf{r}_i)$ is the wavefunction describing the single particle ground state that all the atoms enter at $T = 0$. We assume that each atom experiences an additional potential due to the combined effect of all other atoms present [25] and write the

effective Hamiltonian as

$$H = \sum_{i=1}^{N} \left[\frac{\mathbf{p}_i^2}{2m} + V(\mathbf{r}_i) \right] + U_0 \sum_{i<j} \delta(\mathbf{r}_i - \mathbf{r}_j), \tag{2.34}$$

where $\mathbf{p}_i$ is the momentum of the ith atom, and $V(\mathbf{r})$ the external potential. From equation (2.34) it is possible to derive an expression for the energy of the state given in (2.33) [7]. Minimising the energy with respect to variation of Ψ yields a Schrödinger-type equation governing the evolution of the BEC wavefunction [7]:

$$i\hbar \frac{\partial \Psi(\mathbf{r})}{\partial t} = -\frac{\hbar^2}{2m} \nabla^2 \Psi(\mathbf{r}) + V(\mathbf{r}) \Psi(\mathbf{r}) + U_0 |\Psi(\mathbf{r})|^2 \Psi(\mathbf{r}). \tag{2.35}$$

This is known as the time-dependent Gross-Pitaevskii equation and is simply an extension of the usual time-dependent Schrödinger equation, where the first term relates to the kinetic energy of each particle present, and the second to the energy of each particle due to the trapping potential. The only difference is that the potential energy term has been extended to include a nonlinear term which takes into account the mean field due to interactions between each atom and the rest, described within the mean-field approximation.

Unsurprisingly there is also an analogue to the time-independent Schrödinger equation:

$$\mu \Psi(\mathbf{r}) = -\frac{\hbar^2}{2m} \nabla^2 \Psi(\mathbf{r}) + V(\mathbf{r}) \Psi(\mathbf{r}) + U_0 |\Psi(\mathbf{r})|^2 \Psi(\mathbf{r}). \tag{2.36}$$

Note that the eigenvalue of equation (2.36) is no longer the energy per particle as in the original linear form, but has been replaced by the chemical potential. In the case of non-interacting particles in the same quantum state, the chemical potential is simply equal to the energy per particle, however this is not so in the case where interactions are present.

It is useful to consider equation (2.36) in the case where the confining potential takes the form of a box with infinitely hard walls. Naturally, the wave function reduces to zero at the walls. We may estimate the distance over which the wave function approaches its bulk value from zero by considering the kinetic energy and interaction energy within the box. These two energies are equal when

$$\frac{\hbar^2}{2m\xi^2} = nU_0 \tag{2.37}$$

where ξ is the spatial scale of variations and n is the density as previously. Rearranging equation (2.37) gives

$$\xi^2 = \frac{\hbar^2}{2mnU_0}. \tag{2.38}$$

If we consider a sphere of radius r_s to have a volume equal to the average volume per particle, we may write n as

$$n = \frac{1}{(4\pi/3)r_s^3} \tag{2.39}$$

and can thus substitute equation (2.32) for U_0 to rewrite equation (2.38) as

$$\xi^2 = \frac{r_s^3}{6a}. \tag{2.40}$$

ξ is known as the *healing*, or *coherence*, *length*, and describes the distance over which the wave function tends to its bulk value when subjected to a localised perturbation [7]. Note that by substituting equation (2.32) directly into equation (2.37), the healing length may also be written as

$$\xi = \frac{1}{\sqrt{8\pi na}}. \tag{2.41}$$

Note that in this thesis, we consider BECs whose atoms experience repulsive interactions, i.e. $a > 0$. Condensates have however been created whose interactions are attractive - namely the lithium condensates studied by the Rice University group [29]. Negative s-wave scattering lengths prevent BEC in untrapped gases, however this is not so for trapped gases. Because the interaction energy decreases as the density increases, the condensate tends to collapse inwardly. However provided U_0 is small compared to the energy-level spacing of the confining potential, the tendency to implode is tempered by the kinetic pressure of the gas. Restricting U_0 necessitates that there is a maximum number of atoms for which a metastable BEC may form. The condensate number is limited to approximately 1000 for the case where $a < 0$.

2.4.3 Solitons and Vortices

Solitons and vortices are topological excitations characteristic of BECs [12, 30]. Solitons are one-dimensional waves that propagate without spreading [30]. They

are localised disturbances that arise from a combination of nonlinearity and dispersion [7]. Their behaviour is generally particle-like - for instance, they can interact with other solitons without altering their shape [30]. Strictly speaking, these features should be known as solitary waves rather than solitons [7], however the term "solitons" has been adopted throughout BEC literature, and will be used for the remainder of this thesis.

There are two types of soliton which may occur: *dark solitons*, which occur in repulsively interacting BECs, and *bright solitons*, which occur in attractively interacting BECs. A bright soliton is characterised by a peak in the condensate density, whilst dark solitons are distinguished by a local decrease in density and a macroscopic phase difference between each side of the soliton [31]. Dark solitons may be either black or grey: black solitons are stationary, have a minimum density of zero and exhibit a sharp π phase change; grey solitons can have non-zero velocity, have a non-zero minimum and display a smoother phase change, whose magnitude is less than π [12, 31].

Solitons are able to maintain their shape due to a balance between the dispersion and the nonlinearity. The kinetic energy term in the Gross-Pitaevskii equation, a function of the second derivative of the wavefunction, causes dispersion and is minimised by smoothing the wavefunction, i.e. broadening the soliton. Interactions (i.e. the nonlinearity factor in the medium) oppose this change and tend to narrow soliton. If $a > 0$, the interactions are repulsive therefore try to push particles into the minima causing the minima to narrow, and if $a < 0$ attractive interactions narrow the feature by pulling particles into the soliton resulting in a local density maximum [12]. Since this thesis is concerned with condensates whose interactions are repulsive, only dark solitons will be considered.

Solitons are exact solutions to the time-dependent Gross-Pitaevskii equation in 1D (assuming uniform density). For the case of a soliton propagating through a uniform condensate with velocity v_x, with boundary conditions $n \to n_0$ as $x \to \pm\infty$, the density, n, is found to be described by [32]

$$n\left(x,t\right) = n_{min} + \left(n_0 - n_{min}\right)\tanh^2\left[\frac{x - v_x t}{\sqrt{2}\xi'}\right], \tag{2.42}$$

where n_0 is the bulk density, n_{min} is the minimum density of the soliton, and ξ'

is the width of the soliton:

$$\xi' = \frac{\xi}{\sqrt{1 - \left(\frac{v_x}{v_s}\right)^2}}. \tag{2.43}$$

Here, v_s is speed of sound in the uniform BEC, and is given by

$$v_s = \sqrt{\frac{n_0 U_0}{m}}. \tag{2.44}$$

It is also possible to derive an expression for the phase offset Δ_ϕ between $x = \infty$ and $x = -\infty$:

$$\frac{v_x}{v_s} = \cos\left(\frac{\Delta_\phi}{2}\right) = \frac{n_{min}}{n_0}. \tag{2.45}$$

Note that for $v_x = 0$, equation (2.45) does indeed describe a black soliton, since we find $n_{min} = 0$ and $\Delta_\phi = \pi$.

Solitons moving in an applied potential behave as particles of mass $2m$ would if subjected to same potential. However, solitons are thought to be inherently dynamically unstable. Since the phase offset determines the soliton depth and velocity, any small perturbations of the depth or nonlinearity strength result in a nonuniform transverse velocity profile, causing it to preferentially form more stable structures [31]. Unlike solitons, vortices are stable in two and three dimensions, therefore if a one-dimensional soliton is subjected to perturbations in the other dimensions, this can cause the soliton to disintegrate into vortex pairs in a two-dimensional system or a vortex loop in a three-dimensional system [7]. Vortices are one-dimensional cores of vanishing density, around which the flow of a fluid is quantised. This can be shown as follows.

Consider integrating the phase, ϕ, of the condensate around a closed loop $\mathbf{l}$. Since the BEC has a single valued wavefunction, it must hold that

$$\Delta\phi = \oint \nabla\phi \cdot d\mathbf{l} = 2\pi q, \tag{2.46}$$

where q is an integer. The circulation is defined as

$$\Lambda = \oint \mathbf{v} \cdot d\mathbf{l}. \tag{2.47}$$

It can be shown the the velocity $\mathbf{v}$ of the condensate is related to the phase by

$$\mathbf{v} = \frac{\hbar}{m}\nabla\phi\left(\mathbf{r}, t\right), \tag{2.48}$$

thus it is trivial to show that

$$\Lambda = \frac{\hbar}{m} 2\pi q = q\frac{h}{m}. \tag{2.49}$$

Anderson et al. have observed the decay of dark solitons into vortex rings via the *snake instability* [31]. Vortices may also be generated by giving a BEC a degree of angular momentum [12]. Note that in general, a system prefers to form multiple singly-quantised vortices rather than a single vortex with large q. In real 3D condensates, vortices usually take the form of rings or lines, where the terms are used to describe the shape of the core [12].

Chapter 3

Stochastic dynamics

3.1 Introduction

Chaos theory is the study of nonlinear dynamical systems that give rise to unpredictable, seemingly random behaviour. Chaos is commonly summarised as an extreme sensitivity to initial conditions. This means that if we consider two sets of initial conditions for a given system, where these initial conditions differ only infinitesimally from one another, the resulting trajectories of the system will diverge exponentially.

Despite the fact that there may be no obvious order to the dynamics of a chaotic system, such systems may still be *deterministic* [33]. That is, the system's equations of motion are known and, given a set of initial conditions, one can predict the future motion of the system. Hypothetically, the behaviour at all times could be predicted. However, in practice, numerical errors are a limiting factor.

During the last 30 years, chaotic systems have been widely studied, and it has emerged that these apparently random dynamics often show common features [34], leading to general theories that are applicable in a diverse range of situations. In this chapter, both classical and quantum descriptions of chaos are summarised and the correspondence between the two regimes is addressed.

3.2 Classical chaos

3.2.1 Hamiltonian systems

This thesis limits itself to the study of Hamiltonian systems - that is to say, it considers only systems in which there is no dissipation [33]. Such systems are described in terms of the position, q_i, and momentum, p_i, of each particle in the system, where i is the co-ordinate axis of a specific particle. If a system requires N pairs of co-ordinates (q_i, p_i) to fully describe the motion of all its component particles, it is said to have N *degrees of freedom.* Hamilton's equations govern the dynamics of the system:

$$\frac{dq_i}{dt} = \frac{\partial H(\mathbf{q}, \mathbf{p}, t)}{\partial p_i} \tag{3.1}$$

$$\frac{dp_i}{dt} = -\frac{\partial H(\mathbf{q}, \mathbf{p}, t)}{\partial q_i} \tag{3.2}$$

therefore a Hamiltonian system is defined by $2N$ coupled differential equations.

We can apply the chain rule to determine the temporal derivative of the Hamiltonian:

$$\frac{dH(\mathbf{q}, \mathbf{p}, t)}{dt} = \sum_i \left\{ \frac{\partial H}{\partial p_i}\frac{dp_i}{dt} + \frac{\partial H}{\partial q_i}\frac{dq_i}{dt} \right\} + \frac{\partial H}{\partial t}. \tag{3.3}$$

Substituting equations (3.1) and (3.2) into equation (3.3) gives

$$\frac{dH(\mathbf{q}, \mathbf{p}, t)}{dt} = \sum_i \left\{ \frac{\partial H}{\partial p_i}\left(\frac{-\partial H}{\partial q_i}\right) + \frac{\partial H}{\partial q_i}\left(\frac{\partial H}{\partial p_i}\right) \right\} + \frac{\partial H}{\partial t} \tag{3.4}$$

which reduces to

$$\frac{dH(\mathbf{q}, \mathbf{p}, t)}{dt} = \frac{\partial H}{\partial t}. \tag{3.5}$$

Hamiltonian systems are also described as *conservative* systems since they often have physical properties that are constant in time, known as *conserved quantities.* The systems studied in later chapters have time-independent Hamiltonians and, since H is the total energy, it follows from equation (3.5) that the total energy is conserved throughout.

A useful tool employed when exploring the dynamics of such systems is a concept known as *phase space.* Rather than plotting the motion in real space, axes of $q_i(t)$, $p_i(t)$ are considered. It follows therefore that phase space is $2N$

dimensional. Plotting the dynamics in phase space often gives more information about a system than may be easily apparent in a simple real space plot. It is clear that if energy is conserved, a particle may only move through points in phase space whose energy is equal to that of the initial condition. Thus the conservation of energy limits the particle trajectories to a $2N-1$ dimensional surface in phase space. Similarly, the trajectories are restricted to a $(2N-k)$ dimensional surface in phase phase if k quantities are conserved.

We calculate an expression known as the *Poisson bracket* in order to determine whether a quantity is conserved. Consider the temporal derivative of some quantity $f(\mathbf{q},\mathbf{p},t)$ which we suspect may be conserved:

$$\frac{df}{dt} = \frac{\partial f}{\partial t} + \frac{\partial f}{\partial \mathbf{q}}\frac{d\mathbf{q}}{dt} + \frac{\partial f}{\partial \mathbf{p}}\frac{d\mathbf{p}}{dt}. \tag{3.6}$$

Assuming the Hamiltonian is time-independent and using Hamilton's equations (3.1) and (3.2) to substitute for time derivatives of $\mathbf{q}$ and $\mathbf{p}$ in equation (3.6) gives

$$\frac{df}{dt} = \frac{\partial f}{\partial t} + \frac{\partial f}{\partial \mathbf{q}}\frac{\partial H}{\partial \mathbf{p}} - \frac{\partial f}{\partial \mathbf{p}}\frac{\partial H}{\partial \mathbf{q}} = \frac{\partial f}{\partial t} + [f,H]. \tag{3.7}$$

If f does not depend explicitly on time, so that $\partial f/\partial t = 0$, and in addition the Poisson bracket $[f,H]=0$, then we can say that f is a *constant of the motion.*

3.2.2 Integrability of a system

A constant of motion is also known as an *integral of motion* since it allows a reduction in the number of equations to be solved [35]. A Hamiltonian system with N degrees of freedom requires N integrals of motion if it is to be fully solved analytically. Thus we say a system is *integrable* if the number of independent conserved quantities is *equal to* the number of degrees of freedom ($k=N$). A conserved quantity is only independent if it may not be expressed as a function of other conserved quantities. This condition is known as being *in involution* [33] and is satisfied if the Poisson bracket

$$[f_i, f_j] = 0 \tag{3.8}$$

for all constants of motion f_i. If a system is found to be integrable then all possible trajectories of the system lie on the surface of an N-dimensional torus in phase space, and the motion is periodic with N characteristic frequencies that are

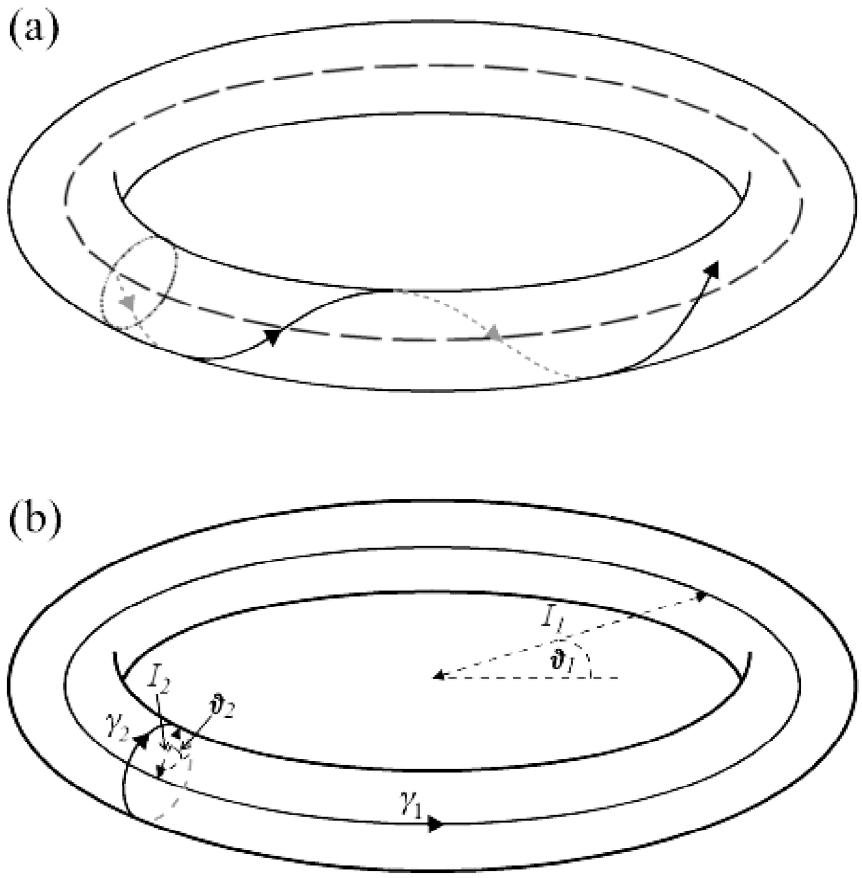

Figure 3.1: (a) Schematic representation of a phase space trajectory which lies on the surface of a torus. (b) The irreducible paths γ_i defined by action-angle variables I_i and ϑ_i.

defined by $\omega_i = \omega_i(f_1, \ldots, f_N)$ $(i = 1, 2, 3, \ldots, N)$ [35]. For example, figure 3.1(a) depicts a possible phase space trajectory around a two-dimensional torus. The two characteristic frequencies in this case would relate to motion around the small cross-section of the torus (dotted line in figure 3.1(a)) and around the ring of the torus (dashed line in figure 3.1(a)). The ratio of these frequencies is referred to as the *winding number* and tells us how many small circuits a trajectory completes in a single circuit of the whole torus.

It is possible to make a canonical change of variables as follows:

$$I_i = \frac{1}{2\pi} \oint_{\gamma_i} \mathbf{p} \cdot d\mathbf{q} \tag{3.9}$$

$$\theta_i(t) = \omega_i t + \theta_i(0) \tag{3.10}$$

where $\omega_i = \partial H / \partial I_i$. These new variables are known as *action-angle variables*, I_i

being the action and θ_i the angle. All points on the torus may now be defined by a sum of I_i vectors. The θ_i determine the orientation of the path traversed when calculating each I_i. Varying one value of θ_i whilst all the others remain constant defines the so called *irreducible paths*, γ_i, referred to in equation (3.9) in the definition of each action variable. Each angle variable defines a path upon the torus in phase space, and hence the entire motion is defined by N irreducible paths. This is illustrated in figure 3.1(b).

The surface of a given torus represents a particular set of values of conserved quantities. For a different set of initial values, the surface of a different torus is defined. Trajectories on the tori lead to periodic motion when the paths have commensurate frequencies (i.e. rational winding numbers), and quasi-periodic motion occurs where an irrational ratio of frequencies occurs [36]. Quasi-periodic motion allows a trajectory to explore the entire surface of the torus, returning arbitrarily close to the original start point after some time t [12]. (Note that if a trajectory in phase space returns to its original start point after some time τ_M, then the motion in real space is also periodic with period τ_M, and similarly, if the motion is quasi-periodic in phase space then it is also quasi-periodic in real space.) Since these possibilities account for all values the winding number may take, it is obvious that integrable systems do not display chaotic behaviour.

Now consider the situation where a perturbation is applied to an integrable system so that it becomes non-integrable. Non-integrable systems are those where the number of conserved quantities k is *less than* N. The perturbation removes constraints from trajectories so that they are no longer confined to the torus [36]. Non-integrability is a necessary condition for a system to exhibit chaotic motion. However, it is important to remember that whilst a chaotic system *must* be non-integrable, non-integrable systems are not necessarily chaotic. Trajectories in a chaotic system are mostly aperiodic. Any periodic orbits which may exist tend to be unstable. This is very different from the case of an integrable system where all the trajectories are stable [36], and it is this instability of orbits which is used to differentiate between chaotic and non-chaotic systems, as is now shown.

Chaos is often described as extreme sensitivity to initial conditions. The extent to which two trajectories diverge when starting from infinitesimally close initial points in phase space is used as a measure of the degree of instability. The separation of the trajectories as a function of time is given approximately by

$$d(t) = d_0 e^{\lambda t} \tag{3.11}$$

where d_0 is the initial separation. The constant λ is known as the Lyapunov exponent and must be a real positive number for a chaotic region to exist. The reader should note that the introduction of a perturbation may not necessarily cause the Lyapunov exponent to become real and positive in all parts of phase space - regions may remain where motion is still stable, although the tori in these regions will still be distorted by the perturbation.

A final important point to note is that chaotic systems are still *deterministic* despite their random-seeming nature - all motion is governed by well-defined equations. However they are still unpredictable even though we have access to the equations of motion: since we can only specify the initial conditions with finite accuracy, once some sufficiently long time has elapsed, any predicted solutions will have diverged from the real behaviour.

3.2.3 Poincaré sections

Poincaré sections [33] are used to gain an overview of specific regions of phase space. Rather than attempting to imagine the entire multi-dimensional phase space which has been described so far, the situation is greatly simplified by considering a single plane or cross-section of the space. An image of the cross-section is constructed by selecting two phase space variables of interest which are plotted every time a trajectory crosses some plane that has been defined to intersect the phase space. This concept is illustrated in figure 3.2(a) for the idea of the nested tori introduced in section 3.2.2: we imagine defining some plane in phase space which cuts a section through the tori.

A point is added to the Poincaré section each time the motion of the system causes it to cross this imaginary plane. From this we can gain information about whether chaotic or stable regions are present. Figure 3.2 shows typical Poincaré sections for (b) periodic motion, (c) quasi-periodic motion, (d) mixed stable and chaotic motion (where both stable and chaotic regions appear in the phase space) and (e) strong chaos (where the Lyapunov exponent is positive throughout the whole of phase space, hence there are no stable regions). The concepts of weak and strong chaos will be discussed in section 3.2.4.

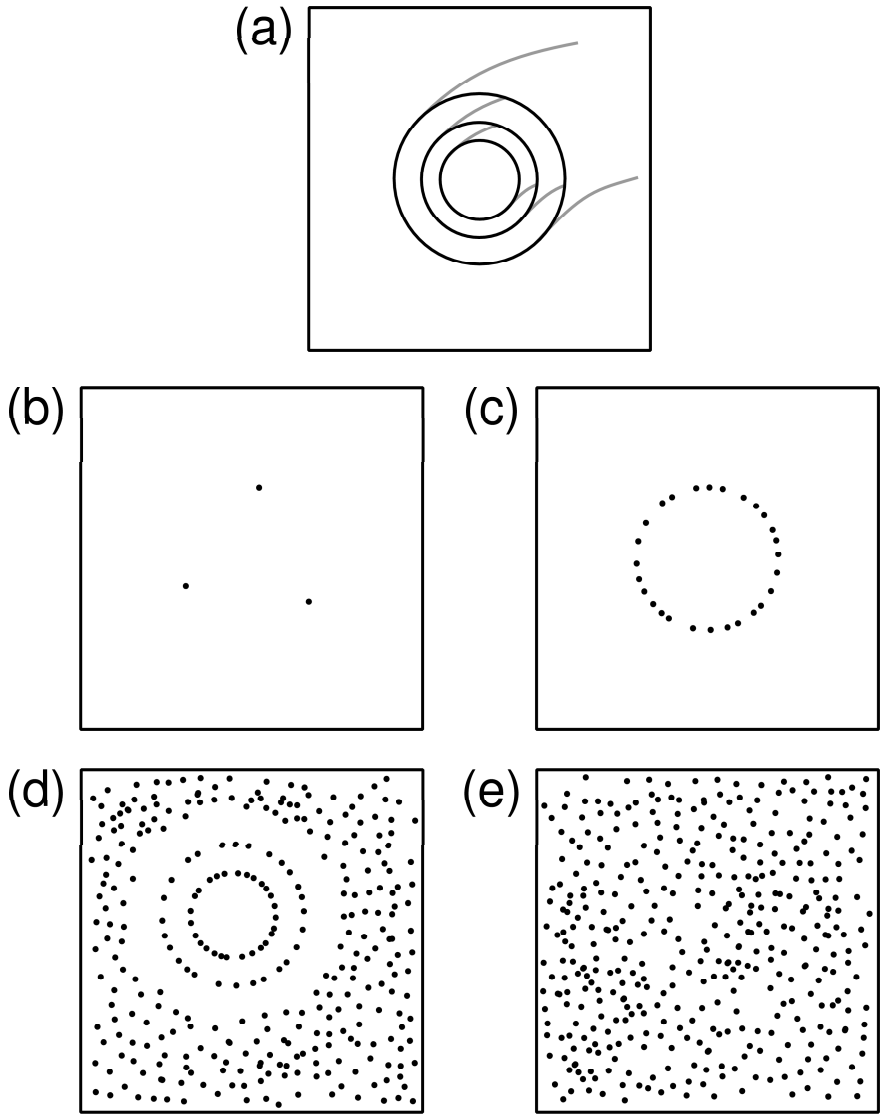

Figure 3.2: Schematic representation of (a) nested tori intersecting a plane in phase space (b) Poincaré section of a periodic orbit (c) Poincaré section of a quasi-periodic orbit (d) Poincaré section of mixed stable/chaotic phase space (e) Poincaré section of a strongly chaotic phase space

3.2.4 The KAM theorem and non-KAM chaos

Kolmogorov, Arnold and Moser [35, 37] studied an integrable system perturbed by some non-integrable function so that the total Hamiltonian is

$$H_0(\mathbf{I}) + \epsilon H_1(\mathbf{I}, \theta) \tag{3.12}$$

where the parameter ϵ determines the magnitude of the perturbation. The KAM theorem states that for small perturbations of a *non-degenerate* Hamiltonian system, most of the tori corresponding to H_0 are not destroyed but instead remain in a slightly distorted form [35]. The tori whose winding numbers are rational (i.e. *resonant* tori) are destroyed, whilst those with irrational winding numbers (*non-resonant* tori) survive and are known as KAM tori. As the strength of the perturbation is increased, the KAM tori are also gradually destroyed. This results in two possible descriptions of the chaotic motion observed in such systems: *mixed stable-chaotic behaviour*, in which there are remaining KAM tori, and *strong chaos* where all KAM tori have disappeared. Thus in a KAM system, a gradual descent into chaos occurs with increasing strength of the perturbation.

In a $2N$-dimensional phase space, the constant energy surface is $2N-1$ dimensional. Therefore if the phase space is to be divided into separate regions by the invariant tori, such tori must have dimensionality $2N-2$. Hence, N-dimensional tori may only divide phase space if

$$N \geq 2N - 1, \tag{3.13}$$

i.e. if $N \leq 2$. Therefore when $N = 2$ as in the example system studied in section 3.2.2, the different tori cannot intersect and the phase space is filled with nested tori. However, in systems with $N > 2$, the tori may intersect. The resonant trajectories is the case where $N = 2$ are those which satisfy

$$\frac{\omega_1}{\omega_2} = \frac{n_1}{n_2}, \tag{3.14}$$

that is, the ratio between the frequencies is rational. In the general case, the resonance condition is given by

$$\sum_{i=1}^{N} n_i \omega_i = 0, \tag{3.15}$$

where the n_i are integers (not all zero). In a system such as (3.12), if H_0 is non-degenerate, such that

$$\det\left|\frac{\partial\omega_i}{\partial I_j}\right| = \det\left|\frac{\partial^2 H_0}{\partial I_j \partial I_i}\right| \neq 0, \tag{3.16}$$

then when the condition (3.15) is satisfied, the perturbation acts to destroy tori that lie close to the resonance tori. Provided $N > 2$, the invariant tori intersect, therefore under this condition the destroyed tori may join together forming a web-like network of so-called *stochastic layers* which extends infinitely through phase space. Zaslavsky describes a stochastic layer as *a region of many overlapping trajectories whose width varies linearly with the perturbation strength* [38]. A trajectory located in this region of phase space has the potential to spread arbitrarily far along this web. This is known as *Arnold diffusion* [35] and the unique form of the phase space under such conditions is described as a *stochastic web.*

The following dimensionless Hamiltonian governs the nonlinear pendulum and obeys the KAM theorem:

$$H_0 = \frac{1}{2}p^2 - \cos x \tag{3.17}$$

where the mass and frequency have been set to 1. The potential energy profile and phase space of the system are illustrated in figure 3.3.

The trajectory of an oscillator is determined by its energy. There are three types of trajectory possible: if the oscillator does not have enough energy to escape the potential well in which it is contained, it follows a *closed* orbit trajectory (which lies on an *invariant torus* in phase space). If it has sufficient energy to escape, its trajectory is *open.* However if it has just enough energy to reach the maximum of the potential well in the $\cos x$ part of equation (3.17) it remains indefinitely in an unstable state. Such a trajectory is known as a *separatrix.* Points corresponding to maxima in the potential are unstable and are known as *hyperbolic* points, whilst the potential minima are stable and are referred to as *elliptic* points.

If the Hamiltonian H_0 is subjected to a perturbation such that a new Hamiltonian

$$H = H_0 + \epsilon V(I, \theta)\cos\nu t \tag{3.18}$$

may be written, where $V(I, \theta)$ and ϵ govern the amplitude and strength of the perturbation respectively and ν is the frequency of the oscillation. When $\nu =$

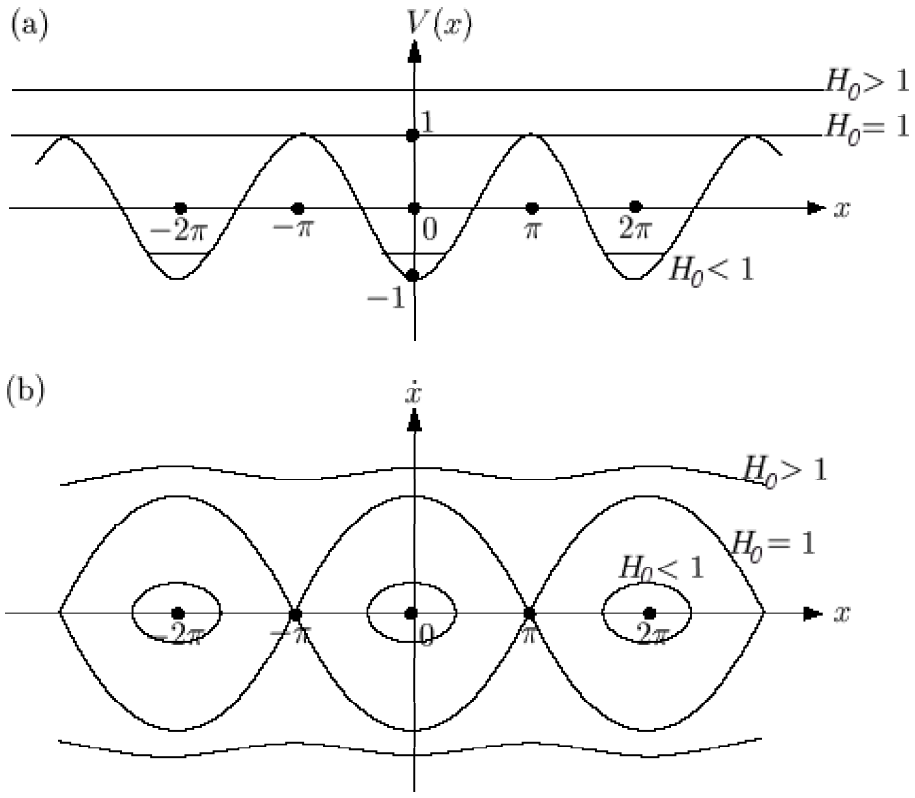

Figure 3.3: (a) Periodic potential and (b) phase space plots for the Hamiltonian in equation 3.17. The different curves in (b) correspond to different values of H_0: closed orbits correspond to the case when $H_0 < 1$, the separatrix applies when $H_0 = 1$, and for $H_0 > 1$ there are open orbits. Corresponding plots are shown in (a). Reproduced from [6].

$\omega, 2\omega, 3\omega, \ldots$ (where $\omega = 1$) a nonlinear resonance is induced in the system, that in turn leads to the destruction of the separatrix and to the formation of a stochastic layer, whose width is proportional to the strength of the applied perturbation [6]. Trajectories close to the hyperbolic points are highly perturbed, whilst the unperturbed resonant tori fill the remaining phase space away from resonant points, albeit in a somewhat distorted form.

In the case of *degenerate* systems, the KAM theorem breaks down. In this instance we find that providing the applied perturbation is time-dependent, stochastic webs can form for $N = 1$. In such a non-KAM system, chaos switches on abruptly throughout the entire phase space when the temporal frequency of the perturbation reaches certain critical values (see below). Chaos switches on globally rather than locally, making the system attractive as a switching mechanism [39]. By contrast, in a KAM system the appearance of chaos in the system occurs gradually in small parts of the phase space.

3.2.5 Prediction of the stochastic web

The one-dimensional driven harmonic oscillator is an example of a non-KAM system - since its frequency is independent of energy, $H_0 = I\omega$ and, from equation (3.16), it is degenerate. Consequently the KAM theorem does not apply. It follows that any system which reduces to a one-dimensional oscillator perturbed by set of plane waves is also non-KAM. It will be shown that the semiclassical Hamiltonian for the systems studied in chapters 4 and 5 may be reduced to an equation of this form. In the cases studied, the perturbation is generated by the sinusoidal form of the dispersion relation of the band structure caused by the periodic lattice potential.

We begin by constructing the semiclassical Hamiltonian, H, for a particle in a band. The kinetic energy of the particle is given by

$$K_E = E(p_x) + \frac{p_y^2}{2m} + \frac{p_z^2}{2m}, \tag{3.19}$$

assuming the lattice potential is in the x-direction. To determine $E\left(p_x\right)$ we must consider the dispersion relation of the band. This may be described by a Fourier series:

$$E(k_x) = \frac{\Delta}{2}\left(a_0 - \sum_{n=1}^{\infty} a_n \cos\left(nk_x d\right)\right) \tag{3.20}$$

where d is the lattice constant, Δ is the width of the first energy band and $k_x = p_x/\hbar$. Appendix A shows how the a_n coefficients are determined. Thus $E(p_x)$ is given by

$$E(p_x) = \frac{\Delta}{2}\left(a_0 - \sum_{n=1}^{\infty} a_n \cos\left(n\frac{p_x d}{\hbar}\right)\right) \tag{3.21}$$

We now consider the potential energy. A tilted magnetic field is applied to confine the particle in the x-z plane within a gutter-shaped potential. This can be done both for electrons in a superlattice using a tilted *uniform* B-field (see figure 1.2), and for neutral atoms in an optical lattice with an *inhomogeneous* B-field (refer to section 2.2.2 for details on trapping neutral atoms magnetically). If we choose a magnetic gauge

$$\mathbf{A} = (0, B(x\sin\theta - z\cos\theta), 0) \tag{3.22}$$

and define new variables x_t, z_t along the axes of the trap:

$$x_t = x\cos\theta + z\sin\theta \tag{3.23}$$

$$z_t = -x\sin\theta + z\cos\theta \tag{3.24}$$

where θ is the tilt angle of the field, recalling that the canonical momentum p_y may be replaced with linear momentum q_y, where

$$q_y = p_y + eA_y(x,z) = p_y + eB(x\sin\theta - z\cos\theta), \tag{3.25}$$

we find that the gutter potential due to the tilted field may be written

$$\frac{1}{2}m\omega^2 z_t^2 \tag{3.26}$$

where ω is the frequency characterising the curvature of the gutter potential.

A single atom in a harmonic trap is also confined by a harmonic potential in the y-direction. By contrast, an electron in a superlattice with a tilted magnetic field moves freely along the y-direction (see section 4.2). Consequently, for both the single atom and electronic systems, we may write

$$V_{trap} = \frac{\alpha_s}{2}m\omega_y^2 y^2 + \frac{1}{2}m\omega^2 z_t^2, \tag{3.27}$$

where $\alpha_s = 0$ for the electronic system and $\alpha_s = 1$ for the single atom system.

A linear accelerating force ξ_s is also applied to the particle in the x direction to push it through the lattice. The full semiclassical Hamiltonian is now

$$H = E(p_x) + \frac{1}{2m}\left(p_y^2 + p_z^2\right) + \frac{\alpha_s}{2} m\omega_y^2 y^2 + \frac{1}{2} m\omega^2 z_t^2 - \xi_s x. \tag{3.28}$$

To determine the semiclassical dynamics we consider Hamilton's equations of motion:

$$\dot{x} = \frac{\partial H}{\partial p_x} \tag{3.29a}$$

$$\dot{p}_x = -\frac{\partial H}{\partial x} \tag{3.29b}$$

$$\dot{y} = \frac{\partial H}{\partial p_y} \tag{3.30a}$$

$$\dot{p}_y = -\frac{\partial H}{\partial y} \tag{3.30b}$$

$$\dot{z} = \frac{\partial H}{\partial p_z} \tag{3.31a}$$

$$\dot{p}_z = -\frac{\partial H}{\partial z}. \tag{3.31b}$$

Applying Hamilton's equations to (3.28) results in the following:

$$\dot{x} = \frac{\Delta d}{2\hbar} \sum_{n=1}^{\infty} n a_n \sin\left(\frac{n p_x d}{\hbar}\right) \tag{3.32}$$

$$\dot{p}_x = -m\omega^2 (x \sin^2\theta - z \sin\theta \cos\theta) + \xi_s \tag{3.33}$$

$$\dot{y} = \frac{p_y}{m} \tag{3.34}$$

$$\dot{p}_y = -m\omega_y^2 y \alpha_s \tag{3.35}$$

$$\dot{z} = \frac{p_z}{m} \tag{3.36}$$

$$\dot{p}_z = -m\omega^2 (z \cos^2\theta - x \sin\theta \cos\theta) \tag{3.37}$$

It is a simple matter to show that, for both the electronic and single atom systems, the motion in the y-direction separates from motion in the x-z plane. Differentiating equation (3.34) with respect to t and substituting equation (3.35) into the

result gives

$$\ddot{y} = -\omega_y^2 y \alpha_s \tag{3.38}$$

which, for the single atom system, describes simple harmonic motion [40] in the y-direction.

Having ascertained that the motion is indeed separable, we will continue by only considering motion in the x-z plane, which is described by the same equation of motion in both the electron and single atom cases. We begin by showing that equations (3.32), (3.33), (3.36) and (3.37) may be reduced to a single second-order differential equation in p_z. Firstly, differentiate equation (3.37) with respect to t. Thus

$$\ddot{p}_z = -m\omega^2 \left(\dot{z} \cos^2\theta - \dot{x} \sin\theta \cos\theta \right). \tag{3.39}$$

Secondly, substitute for $\dot{x}$ and $\dot{z}$ using equations (3.32) and (3.36) to give

$$\ddot{p}_z = -m\omega^2 \cos^2\theta \left(\frac{p_z}{m} \right) + m\omega^2 \sin\theta \cos\theta \frac{\Delta d}{2\hbar} \sum_{n=1}^{\infty} n a_n \sin\left(\frac{n p_x d}{\hbar} \right). \tag{3.40}$$

It still remains to eliminate p_x from equation (3.40). This is achieved via the following steps. Combining equations (3.33) and (3.37) gives

$$\dot{p}_x = -\dot{p}_z \tan\theta + \xi_s. \tag{3.41}$$

Integrating the above equation with respect to time and rearranging results in an expression for p_x in terms of p_z we find

$$p_x = p_x(0) + \xi_s t - (p_z - p_z(0)) \tan\theta \tag{3.42}$$

where $p_x(0)$ and $p_z(0)$ are the values of p_x and p_z at $t = 0$. Finally we can substitute equation (3.42) to write (3.40) as

$$\ddot{p}_z + \omega_{\|}^2 p_z = A \sum_{n=1}^{\infty} n a_n \sin\left(n \left(K p_z - \omega_B t - \phi \right) \right) \tag{3.43}$$

where terms are defined as follows:

$$\omega_{\|} = \omega \cos\theta \tag{3.44}$$

$$A = \frac{-m\omega^2 d\Delta \sin\theta\cos\theta}{2\hbar} \tag{3.45}$$

$$K = \frac{d\tan\theta}{\hbar} \tag{3.46}$$

$$\omega_B = \frac{d\xi_s}{\hbar} \tag{3.47}$$

$$\phi = \frac{d}{\hbar}\left(p_x(0) + p_z(0)\tan\theta\right). \tag{3.48}$$

This non-linear equation has the form of a driven simple harmonic oscillator. The natural frequency of the oscillator is $\omega_{\|}$, whilst the driving term has the form of a series of plane waves with frequency $n\omega_B$ and wave vector nK, where the amplitude of the nth wave decreases rapidly with increasing n. This set of plane waves is determined by the dispersion relation of the band through which the particle is moving.

When the tilt angle is zero, the driving term is also zero. Under these conditions we have a separable Hamiltonian and expect to observe the particle Bloch oscillating along the lattice with frequency ω_B whilst performing simple harmonic oscillations with frequency ω in the z direction. As θ is increased from zero, the motion of the particle in the z direction plays a dominant role in determining the overall behaviour. Equation (3.42) shows that the relation between p_x and p_z depends on $\tan\theta$, implying an increasingly large exchange in momentum between p_x and p_z as the tilt angle becomes greater. The effect of changing θ on the single-particle motion is more apparent if we rewrite equation (3.43) as follows:

$$\ddot{p}_z + \omega_{\|}^2\left(p_z + \frac{m\Delta d\sin 2\theta}{4\hbar}\sum_{n=1}^{\infty} n a_n \sin\left(n\left(Kp_z - \omega_B t - \phi\right)\right)\right) = 0. \tag{3.49}$$

It is clear from this form that the amplitude of the plane-wave perturbation will be strongest for systems with tilt angles of $\theta = 45°$, and will also be increased by the existence of wide bands (large Δ) and long lattice periods (large d).

The motion of the particle is entirely determined by solving equation (3.43) for p_z, since we can subsequently solve (3.42) to obtain p_x, (3.32) to obtain x and (3.36) to obtain z. The system is on resonance when the frequency of motion associated with the magnetic potential, $\omega_{\|}$, is commensurate with the

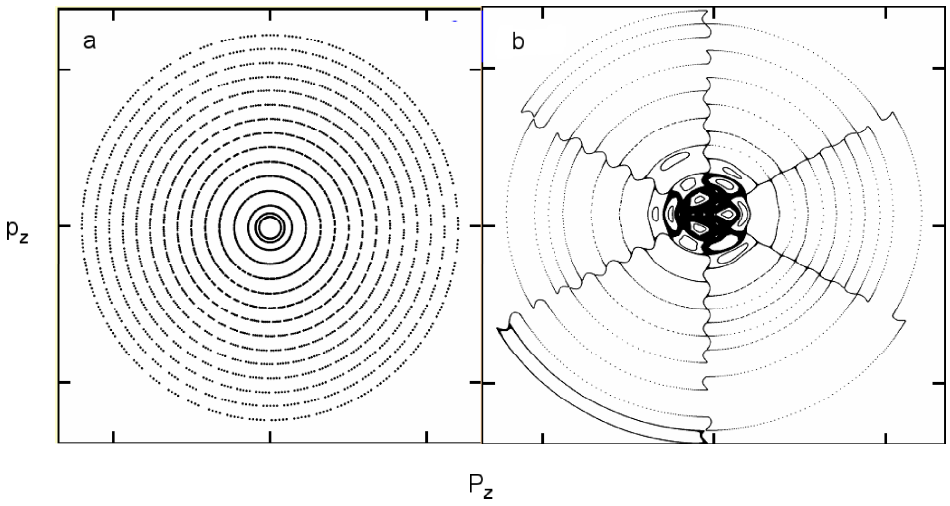

Figure 3.4: Poincaré sections of the (P_z, p_z) phase space (where $P_z = \dot{p}_z/\omega_{||}$) for (a) r is non-integer and (b) r is an integer value ($r = 3$ in this case). Where the system is off resonance in (a), the phase space is filled with concentric rings, whereas when the resonance condition is fulfilled in (b), the rings become linked by filaments and a stochastic web is formed. A chaotic region can be seen in the centre of the web.

Bloch frequency, ω_B. Therefore when the ratio

$$r = \frac{\omega_B}{\omega_{||}} \tag{3.50}$$

is an integer we expect to observe an increase in the delocalisation of the particle in real space, and the formation of a stochastic web in phase space in accordance with the theory of non-KAM chaos as discussed in section 3.2.4. To view such a stochastic web we construct a stroboscopic Poincaré section; that is, the points are plotted at equally spaced times. In this case, (P_z, p_z) are sampled every time that the time elapsed since the last point was plotted satisfies

$$\Delta t = \frac{2\pi}{\omega_{||}}, \tag{3.51}$$

where $P_z = \dot{p}_z/\omega_{||}$. Examples of the phase space for on and off resonance conditions are shown in figure 3.4.

The geometric form of the stochastic web

It will now be shown how the form of stochastic webs such as that shown in figure 3.4(b) can be predicted by analysing the form of the Hamiltonian for the

driven harmonic oscillator described by equation (3.43). The derivation follows that described in [38].

We have seen how the system is described by a single semiclassical equation of motion, given in (3.43). Here we will consider only the $n = 1$ term (known as the tight binding approximation in solid state physics). We effectively assume a simple cosinusoidal dispersion relation equivalent to a single plane wave perturbation, so equation (3.43) becomes

$$\ddot{p}_z + \omega_{\|}^2 p_z = \frac{-m\omega^2 d\Delta \sin\theta\cos\theta}{2\hbar} a_1 \sin\left(Kp_z - \omega_B t - \phi\right). \tag{3.52}$$

Defining a dimensionless parameter

$$\epsilon = \frac{1}{2} m\Delta K^2 a_1 \tag{3.53}$$

as a measure of the strength of perturbation and substituting this into equation (3.52) gives

$$\ddot{p}_z + \omega_{\|}^2 p_z = -\frac{\epsilon}{K}\omega_{\|}^2 \sin\left(Kp_z - \omega_B t - \phi\right). \tag{3.54}$$

The Hamiltonian corresponding to this driven harmonic oscillator, with an effective displacement p_z from equilibrium is

$$H = \frac{1}{2}\left(\dot{p}_z^2 + \omega_{\|}^2 p_z^2\right) - \frac{1}{K^2}\omega_{\|}^2 \epsilon \cos\left(Kp_z - \omega_B t - \phi\right). \tag{3.55}$$

Although this Hamiltonian does not have units of energy, it can still be used to analyse the structure of the phase space with variables (P_z, p_z). To see this, we begin by making a change of variables:

$$p_z = \rho \sin\varphi \tag{3.56a}$$

$$P_z = \rho \cos\varphi \tag{3.56b}$$

recalling that $P_z = \dot{p}_z/\omega_{\|}$. Therefore a Poincaré section of p_z versus P_z can be described by the polar co-ordinates:

$$\rho = \sqrt{p_z^2 + P_z^2} \tag{3.57a}$$

$$\varphi = \tan^{-1}\left(\frac{p_z}{P_z}\right) \tag{3.57b}$$

where ρ is the radial distance of a point in phase space from $(0, 0)$ and φ is the an-

gle that such a line makes in phase space with the $(1,0)$ direction. Implementing our new variables in equation (3.55) results in

$$H = \frac{1}{2}\left(\omega_{\|}^2\rho^2\cos^2\varphi + \omega_{\|}^2\rho^2\sin^2\varphi\right) - \frac{1}{K^2}\omega_{\|}^2\epsilon\cos\left(K\rho\sin\varphi - \omega_B t - \phi\right). \quad (3.58)$$

The cosine term may then be rewritten in the form of a Bessel function of the first kind:

$$\cos\left(K\rho\sin\varphi - \omega_B t - \phi\right) = \sum_{l=-\infty}^{\infty} J_l\left(K\rho\right)\cos\left(l\varphi - \omega_B t - \phi\right). \quad (3.59)$$

Substituting equation (3.59) into the modified Hamiltonian (3.58), and simplifying gives:

$$H = \frac{1}{2}\omega_{\|}^2\rho^2 - \frac{1}{K^2}\omega_{\|}^2\epsilon\sum_{l=-\infty}^{\infty} J_l\left(K\rho\right)\cos\left(l\varphi - \omega_B t - \phi\right). \quad (3.60)$$

Next we expand a term $l = r$ to give:

$$\begin{aligned} H = \frac{1}{2}\omega_{\|}^2\rho^2 - \frac{1}{K^2}\omega_{\|}^2\epsilon J_r\left(K\rho\right)\cos\left(r\varphi - \omega_B t - \phi\right) \\ -\frac{1}{K^2}\omega_{\|}^2\epsilon\sum_{l\neq r} J_l\left(K\rho\right)\cos\left(l\varphi - \omega_B t - \phi\right) \end{aligned} \quad (3.61)$$

before introducing a second change of variables:

$$I = \frac{\omega_{\|}\rho^2}{2r} \quad (3.62a)$$

$$\theta = r\varphi - \omega_B t. \quad (3.62b)$$

If we define a new Hamiltonian

$$\widetilde{H} = H - \omega_B I \quad (3.63)$$

and substitute for ρ^2 and φ in equation (3.63) using equations (3.62a) and (3.62b), we have:

$$\begin{aligned} \widetilde{H} &= \left(r\omega_{\|} - \omega_B\right) I - \frac{1}{K^2}\omega_{\|}\epsilon J_r\left(K\rho\right)\cos\left(\theta - \phi\right) \\ &- \frac{1}{K^2}\omega_{\|}\epsilon\sum_{l\neq r} J_l\left(K\rho\right)\cos\left(\frac{l}{r}\theta - \left(1 - \frac{l}{r}\right)\omega_B t - \phi\right). \end{aligned} \quad (3.64)$$

This new Hamiltonian is then rewritten as

$$\widetilde{H} = \widetilde{H}_0 (I) + \widetilde{V} (I, \theta; t) \tag{3.65}$$

where

$$\widetilde{H}_0 (I) = \left(r\omega_{\|} - \omega_B\right) I - \frac{1}{K^2}\omega_{\|}^2 \epsilon J_r (K\rho) \cos(\theta - \phi) \tag{3.66}$$

$$\widetilde{V} (I, \theta; t) = -\frac{1}{K^2}\omega_{\|}\epsilon \sum_{l \neq r} J_l (K\rho) \cos\left(\frac{l}{r}\theta - \left(1 - \frac{l}{r}\right)\omega_B t - \phi\right). \tag{3.67}$$

Here, we consider $\widetilde{H}_0$ to be the unperturbed part of $\widetilde{H}$ and $\widetilde{V}$ to be the perturbation [38]. When $r\omega_{\|} = \omega_B$, i.e. the system is on resonance, we have

$$\widetilde{H}_0 = -\frac{1}{K^2}\omega_{\|}^2 \epsilon J_r (K\rho) \cos(\theta - \phi), \tag{3.68}$$

and substituting for ρ in terms of I gives

$$\widetilde{H}_0 = -\frac{1}{K^2}\omega_{\|}^2 \epsilon J_r \left(K \left(\frac{2rI}{\omega_{\|}}^{1/2}\right)\right) \cos(\theta - \phi) \tag{3.69}$$

Thus we can see that when the system is on resonance $\widetilde{H}_0$ and $\widetilde{V}$ are proportional to the perturbation strength, which means that the stationary component is induced by the perturbation [6]. In order to locate the separatrices in phase space corresponding to the unperturbed Hamiltonian, we must determine the singularities of $\widetilde{H}_0$. Therefore we solve simultaneously the following:

$$\frac{\partial \widetilde{H}_0}{\partial I} = 0 \tag{3.70a}$$

$$\frac{\partial \widetilde{H}_0}{\partial \theta} = 0. \tag{3.70b}$$

Performing the differentials in equations (3.70a) and (3.70b) gives

$$J_r' (K\rho) \cos(\theta - \phi) = 0 \tag{3.71a}$$

$$J_r (K\rho) \sin(\theta - \phi) = 0 \tag{3.71b}$$

whose solution yields a set of hyperbolic points (potential maxima):

$$J_r\left(K\rho_h\right) = 0 \tag{3.72a}$$

$$\theta_h - \phi = \pi/2, 3\pi/2, \ldots \tag{3.72b}$$

and a set of elliptic points (potential minima):

$$J_r'\left(K\rho_e\right) = 0 \tag{3.73a}$$

$$\theta_e - \phi = 0, \pi, \ldots \tag{3.73b}$$

When plotting a stroboscopic Poincaré section we find that the phase angle of the hyperbolic points is given by

$$\varphi_h = \frac{\phi}{r} + \frac{\pi}{2r}, \frac{\phi}{r} + \frac{3\pi}{2r}, \ldots \tag{3.74}$$

and that of the elliptic points is

$$\varphi_e = \frac{\phi}{r}, \frac{\phi}{r} + \frac{\pi}{r}, \ldots \tag{3.75}$$

Hyperbolic points are the unstable points in phase space which represent the potential maxima of the system. Elliptic points are the potential minima and are stable. Therefore for a given resonance equations (3.71a) and (3.71b) predict the characteristics of the Poincaré section. The position of the hyperbolic and elliptic points may be determined from the roots of the Bessel functions (refer to table 3.1 for a selection of solutions). We find that the hyperbolic points define radial filaments in the (P_z, p_z) plane of phase space, and that consequently the separatrices define a web of cells, each containing an elliptic point. This is illustrated for the case $r = 3$ and $\phi = 0°$ in figure 3.5.

When there is no perturbation (as is the case so far) particles can diffuse along the radial filaments as far as the hyperbolic points, whereupon all of the particle's kinetic energy becomes potential energy. However, once the perturbation $\widetilde{V}(I, \theta; t)$ is introduced the separatrices are destroyed in accordance with the theory of non-KAM chaos outlined in section 3.2.4. They are replaced by channels of chaotic trajectories which allow the particle to diffuse past the unperturbed hyperbolic points: these channels make up the stochastic web. In theory, the presence of the web allows for the possibility of unbounded diffusion in both phase space and hence real space. In practice this is not so since the thickness of

i	$r=1$		$r=2$		$r=3$	
	$K\rho_h$	$K\rho_e$	$K\rho_h$	$K\rho_e$	$K\rho_h$	$K\rho_e$
1	0.00000	1.84118	0.00000	3.05424	0.00000	4.20119
2	3.83171	5.33144	5.13562	6.70613	6.38016	8.01524
3	7.01559	8.53632	8.41724	9.96947	9.76102	11.3459
4	10.1735	11.7060	11.6198	13.1704	13.0152	14.5858
5	13.3237	14.8636	14.7960	16.3475	16.2235	17.7887

Table 3.1: The first five roots of equations (3.72a) and (3.73a). These may be used to predict the locations of features in the stochastic web.

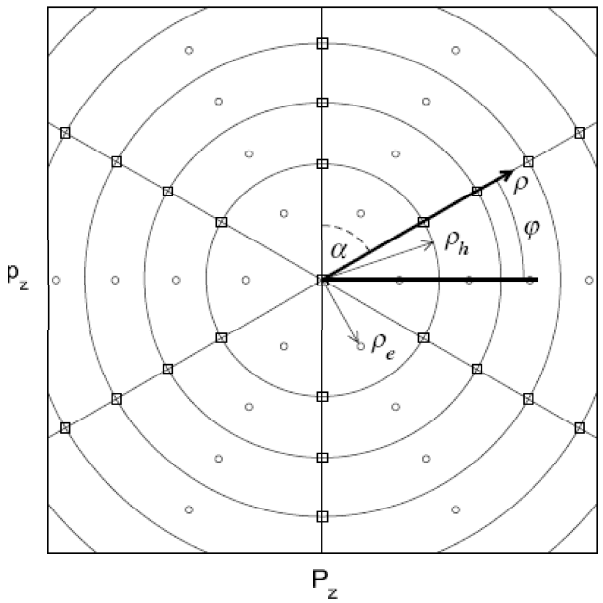

Figure 3.5: A schematic diagram of the stochastic web predicted in the case when $r = 3$. Circles and squares indicate the positions of elliptic and hyperbolic points respectively. The quantity p_z is the z component of momentum, whilst $P_z = \dot{p}_z/\omega_{||}$. The labels ρ_h, ρ_e depict the radial distances of hyperbolic and elliptic points from the origin respectively. The polar coordinates satisfy $\rho = \sqrt{p_z^2 + P_z^2}$ and $\phi = \tan^{-1}(p_z/P_z)$. Radial filaments are separated by an angle $\alpha = 2\pi/2r = \pi/3$.

the channels is proportional to $e^{-\sqrt{\rho}}$ [35]. Thus, the further the particle travels from the centre of the web, the more constricted the channel down which it is diffusing, leading to a very low probability of traversing an infinite path. Yet we do still expect to see a marked increase in the delocalisation of a particle when the system is on resonance.

We find that for a resonance r, we expect the hyperbolic points to define $2r$ radial filaments in the stochastic web. These are linked together by circular filaments - so each root, S_r ($r = 1, 2, 3, \ldots$), of the Bessel function of order r defines a ring of radius $\rho_r = S_r/K$ in the web. If the initial state of a particle lies upon the web, it will diffuse along the web indefinitely, following a chaotic trajectory. Note that the probability of radial diffusion is also proportional to the strength of the driving term. If the initial conditions define a point within one of the islands marked out by the web, the particle will follow a stable trajectory centred around the elliptic point. It should also be noted from equations (3.74) and (3.75) that if the initial phase of the particle is non zero we expect to observe a rotation of the web pattern through an angle ϕ/r [6].

When the band through which the particle is moving is not a simple cosinusoidal function (which is typically the case in real systems), providing that the coefficients a_l ($l > 1$) are rapidly decreasing, the behaviour is very similar to that described above. The additional plane waves present in the Fourier expression for the band will cause a slight deviation in the positions of the elliptic and hyperbolic points from those predicted by table 3.1, but the web will still retain the same general appearance described above.

3.3 Quantum chaos

In quantum mechanics, our knowledge of the properties of a system is always limited by Heisenberg's Uncertainty Principle, which states that

$$\Delta x \Delta p \geq \frac{\hbar}{2}. \tag{3.76}$$

The classical definition of chaos is in terms of the diverging separation of two initially arbitrarily close points (see section 3.2.2), and since uncertainty prevents us from defining two such points the definition of chaos must break down in the quantum mechanical regime [41].

Indeed we find that two "nearby" wavefunctions cannot diverge exponentially

[36]. If we specify two wavefunctions, Ψ and Ψ' whose initial form is:

$$\Psi(t=0) = \sum_n c_n u_n \tag{3.77a}$$

$$\Psi'(t=0) = \sum_n c_n u_n + \delta c_1 u_1 \tag{3.77b}$$

where $\{u_n\}$ are the eigenstates of the system and $\{c_n\}$ the respective expansion coefficients, we find that at some subsequent time they are given by:

$$\Psi(t) = \sum_n c_n u_n e^{-iE_n t/\hbar} \tag{3.78a}$$

$$\Psi'(t) = \sum_n c_n u_n e^{-iE_n t/\hbar} + \delta c_1 u_1 e^{-iE_1 t/\hbar} \tag{3.78b}$$

where $\{E_n\}$ are the eigenvalues associated with $\{u_n\}$. Thus the difference between the two clearly does not grow exponentially therefore it is impossible for a wavefunction to evolve chaotically according to our classical definiton.

Yet according to the Correspondence Principle, which states that quantum mechanics tends to classical mechanics as $\hbar \to 0$, the classical and quantum descriptions must converge. So although the evolution of the wavefunction itself may not fit the classical description of chaos, the mean positions of two wavefunctions may diverge exponentially in the same way that the corresponding classical paths might. The field of quantum chaos is concerned with the study of this connection. So although the term quantum chaos may seem misleading, it is the title given to the study of quantum systems whose classical analogue is chaotic [12].

3.3.1 The Wigner function

Much of the classical theory of chaos discussed in section 3.2 is concerned with the stability of a particle occupying some given point $(\mathbf{p}, \mathbf{q})$ in phase space, with the Poincaré section being employed to provide an insight into the possible dynamics for a particular plane in phase space. Classically, one can define a distribution for the probability $f(\mathbf{p}, \mathbf{q})d\mathbf{p}d\mathbf{q}$ that a particle has momentum in the small volume $d\mathbf{p}$ near $\mathbf{p}$ and position in the small volume $d\mathbf{q}$ near $\mathbf{q}$. This requires the ability to define a point in phase space with precision, which in turn relies on the trajectories being continuous. In particular, since a continuous chaotic trajectory may pass arbitrarily close to some given point in phase space, it follows that the classical phase space must be infinitely detailed in order to represent this. At the quantum

scale, the level of detail is limited by the uncertainty principle, and it is hence impossible to define a true quantum mechanical phase space.

However, in 1932, Wigner [42,43] derived an expression for $f(\mathbf{p},\mathbf{q})d\mathbf{p}d\mathbf{q}$ based upon the wavefunction of the particle, $\Psi(\mathbf{q})$ of an N-dimensional system at time t:

$$W(\mathbf{p},\mathbf{q}) = \frac{1}{h^N}\int \Psi^*\left(\mathbf{q}+\frac{\boldsymbol{\lambda}}{2}\right)\Psi\left(\mathbf{q}-\frac{\boldsymbol{\lambda}}{2}\right)\times\exp\left(-i\frac{\mathbf{p}\cdot\boldsymbol{\lambda}}{\hbar}\right)d^N\boldsymbol{\lambda}. \qquad (3.79)$$

where $\boldsymbol{\lambda}$ represents a spatial displacement from the point $\mathbf{q}$. The quantity $W(\mathbf{p},\mathbf{q})$ is known as the Wigner function and is a quantum mechanical analogue of the classical phase space plot.

One of the initial objections raised in response to Wigner's function is that it can take negative values, and therefore appears to be at odds with our fundamental understanding of the idea of probabilities. Wigner's response to this was to demonstrate that (i) the integral of $W(\mathbf{p},\mathbf{q})$ over all *momentum* space is equal to the squared modulus of the wavefunction; (ii) the integral of $W(\mathbf{p},\mathbf{q})$ over all *real* space is equal to the squared modulus of the wavefunction in momentum space (which is equal to the Fourier transform of the wavefunction); and (iii) the integral of $W(\mathbf{p},\mathbf{q})$ *with any function of* $(\mathbf{p},\mathbf{q})$ over *all* space is equal to the expectation value (which is always positive) of the function of $(\mathbf{p},\mathbf{q})$. Moreover, he proved that there is no *simple* function satisfying all of the above which is always positive. Other functions can satisfy the criteria, but require further terms in Ψ to be included. Wigner's function was therefore accepted as the simplest to work with. An alternative to the Wigner function is the Husimi function, a Gaussian-smoothed form of the Wigner, but it has been shown in studies of chaotic quantum systems that the Wigner function reproduces the Poincaré section with greater sharpness [44].

Like the classical phase space, the full Wigner function is $2N$ dimensional, so it is usual to study a two-dimensional projection of the function, which can be compared with the classical Poincaré section. The correlation between Wigner functions and Poincaré sections was verified in a study by Hutchinson and Wyatt in 1980 [45]. The reader should recall that section 3.2.5 predicts the occurrence of a stochastic web when plotting a stroboscopic Poincaré section for the systems studied in later chapters. An analogous quantum mechanical distribution may be plotted for a time-dependent system by averaging Wigner functions calculated at times $t = 2m_v\pi/\omega_{||}$ where m_v is an integer. Similar approaches have been imple-

mented successfully by Gardiner [46] and Korsch and Wiescher [47]. The reader should note that although the time-averaging idea is relatively straightforward in principle, in practice it is daunting due to the enormous computational demands, with a single time-averaged Wigner function often requiring hundreds of hours of processor time to generate.

Chapter 4

Semiclassical and quantum electron transport in a superlattice with an applied bias voltage and a tilted magnetic field

4.1 Introduction

As discussed in section 3.2.4, chaotic systems may display nonlinear resonances that lead to the formation of a connecting network of stochastic layers in phase space. These networks are called stochastic webs and provide a mechanism that enables a particle to diffuse through the system. Theoretically, there is the potential for unbounded diffusion throughout phase space along a stochastic web. However, in reality, the probability of this is very small. In practice one expects to see an increase in the delocalisation of the particle in phase space, which corresponds to an increasing delocalisation in real space as shown in section 3.2.5.

In non-degenerate systems, the KAM theorem applies and the onset of chaos in the system occurs gradually. However, in the case of degenerate systems, the KAM theorem breaks down. Chaos switches on abruptly throughout the entire phase space when the perturbation satisfies certain conditions. Previous studies of chaotic electron transport have explored KAM dynamics in systems such as quantum dots [48], resonant tunnelling diodes [49,50] and doped [51,52] or driven

[53] superlattices. Non-KAM chaos has only recently been created experimentally by Fromhold et al. [39], who showed that the formation of stochastic webs has a profound effect on the current-voltage (I-V) characteristics of semiconductor superlattices. Non-KAM systems are not yet well understood, so the motivation for studying them is strong [54]. There is much interest in their dynamics due to applications in the theory of plasma physics and tokamak fusion [35, 55–57], turbulent fluid dynamics [35, 57], ion traps [55] and quasicrystals [35, 57].

In this chapter, we consider systems of the same type as that studied by Fromhold et al. [39]: namely, the dynamics of a single electron in a semiconductor superlattice. The superlattice bias voltage creates an electric field F antiparallel to the axis of the superlattice (which is taken to be in the x direction, as illustrated in figure 1.2). A magnetic field B is also applied to the system, and can be tilted in the x-z plane by an angle θ relative to the x axis. We consider dynamics created by a range of F, B and θ values. By numerically modelling the electron response to the fields, predictions of the electronic drift velocity in the system may be made. When the electric and magnetic fields meet the conditions for resonance, the formation of a stochastic web in phase space facilitates enhanced electron transport through the superlattice. We expect to see this effect reflected in the variation of electronic drift velocity with electric field.

When the orientation of the magnetic field is 0° or 90°, a semiclassical analysis of the motion of the electron predicts stable behaviour [6]. In both cases, the motion along each axis has been shown to be separable [6]. For electric and magnetic fields parallel to the superlattice axis, Bloch oscillations are induced in the x direction by the electric field and cyclotron orbits in the orthogonal (y-z) plane result from the magnetic field. When the magnetic field is perpendicular to the electric field (i.e. is aligned along the z axis), motion is bounded in the x direction but unbounded along z. However, tilting the magnetic field away from these values leads to coupled motion. In this case, where $0° < \theta < 90°$, the motion remains strongly localised *unless* the Bloch and cyclotron frequencies are commensurate. We show that when the strength of the electric field is such that the Bloch and cyclotron frequencies are commensurate (the system is on resonance), the extent of the predicted semiclassical trajectories shows a marked increase. Consequently, the drift velocity also increases, giving rise to resonant peaks in plots of drift velocity versus electric field. Stroboscopic Poincaré sections confirm the presence of the stochastic web in phase space.

A full quantum mechanical analysis of the wavepacket dynamics is also pre-

NU2293			
Miniband (eV)		Minigap (eV)	
Δ_{SL}^1	0.019	G_{SL}^1	0.202
Δ_{SL}^2	0.101	G_{SL}^2	0.170
Δ_{SL}^3	0.215	G_{SL}^3	0.259

Table 4.1: The properties of the miniband structure in NU2293. Δ_{SL}^n is the bandwidth of the nth miniband and G_{SL}^n is the width of the nth minigap.

NU2299			
Miniband (eV)		Minigap (eV)	
Δ_{SL}^1	0.012	G_{SL}^1	0.066
Δ_{SL}^2	0.049	G_{SL}^2	0.078
Δ_{SL}^3	0.113	G_{SL}^3	0.066

Table 4.2: The properties of the miniband structure in NU2299. Δ_{SL}^n is the bandwidth of the nth miniband and G_{SL}^n is the width of the nth minigap.

sented here. The evolution of a single electron wavefunction is determined numerically and, from this, the expectation values of position and velocity are calculated. Thus, plots of the mean position of the wavefunction may be made and compared to the semiclassical trajectories. The correspondence between the Poincaré sections and Wigner functions calculated at stroboscopic times is also investigated. In addition, drift velocity-field curves may be generated. Since the quantum analysis explicitly includes the full superlattice potential, interminiband tunnelling effects may be observed in this model. Furthermore, knowledge of the variation of the drift velocity as a function of the field enables current - voltage (I-V) characteristics of the samples to be predicted which may be scrutinised for agreement with experimental results.

Two semiconductor superlattice samples are considered: NU2293 and NU2299. Both are real samples that have been fabricated and used in experiments [4, 5]. A brief review of their characteristics is included here, but for a more detailed discussion of their construction, see section 1.3. Sample NU2293 is a repeating

structure of AlAs/GaAs/InAs/GaAs (see figure 1.4(a)). The overall period of the superlattice is $d_{SL} = 82.41$ Å, and the thicknesses of the individual semiconductor layers are 10, 35, 2.41 and 35 Å respectively. The potential in GaAs is taken to be zero, and hence the potentials in the barriers and niches are given by $U_1 = 1.064$ eV and $U_2 = -0.698$ eV. It is the presence of the InAs niche that makes this design novel compared to the more usual bi-layer repeating samples. The inclusion of the niche lowers the first miniband to facilitate electron injection and causes the large minibandgap (G^1_{SL} ~200 meV) observed between the first and second minibands (see figure 4.1). As a result of this large minibandgap, it is expected that interminiband tunnelling effects will be suppressed in this sample.

Sample NU2299 is a simple bi-layer structure consisting of alternating layers of AlGaAs/GaAs (see figure 1.4(b)). The superlattice period is 125 Å, where the AlGaAs barriers are 25 Å thick and the GaAs wells 100 Å. Again, the potential in GaAs is taken to be zero and the potential in the barriers is 0.247 eV. In this sample, the lowest minibandgap is small (G^1_{SL} ~60 meV, see figure 4.2) and so there is significant interminiband tunnelling. This allows the electrons to move more easily between minibands and so suppresses charge build up in the sample. This is reflected in the quantum mechanical calculations of the drift velocity - field curves reported in section 4.3. Tables 4.1 and 4.2 show the widths of the three lowest minibands (Δ^1_{SL}, Δ^2_{SL} and Δ^3_{SL}) and corresponding gaps (G^1_{SL}, G^2_{SL} and G^3_{SL}) for samples NU2293 and NU2299 respectively.

4.2 The semiclassical mechanics of the system

Since both superlattice structures consist of approximately 15 periods, incoherent (diffusive) transport may be assumed [58]. This can be described by a semiclassical model of miniband transport as shown by Easki and Tsu [1]. Note that this model assumes that inhomogeneities have no effect on the miniband structure but cause electrons to scatter with a characteristic scattering time τ. In addition, the conduction electron density is also assumed to be constant. The reader should refer to sections 1.2.1 and 1.3.2 for an in depth treatment of semiclassical band transport and the Esaki-Tsu model.

A semiclassical model assumes knowledge of the band structure of a system.

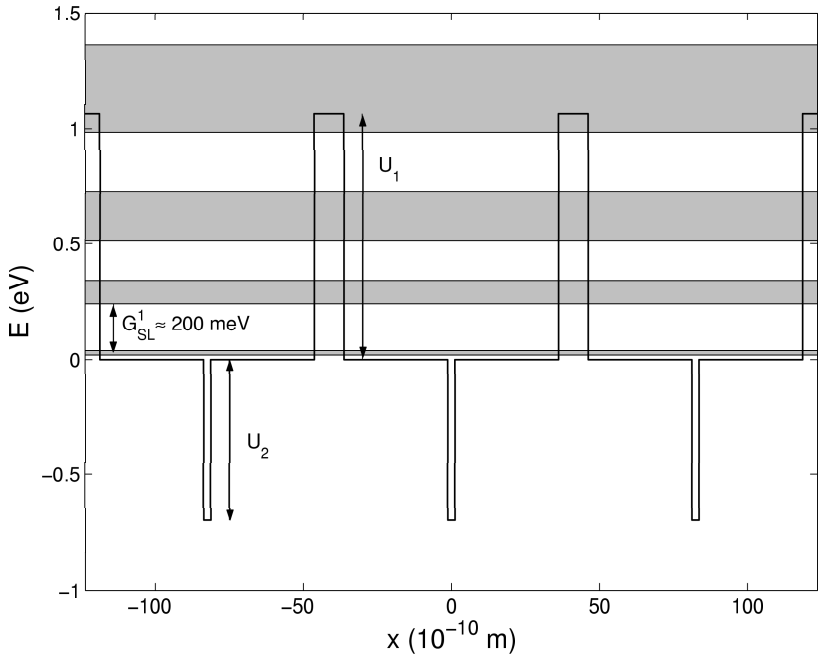

Figure 4.1: Miniband structure of NU2293 superimposed upon the superlattice potential. The shaded areas represent minibands, whilst the areas between minibands are minibandgaps.

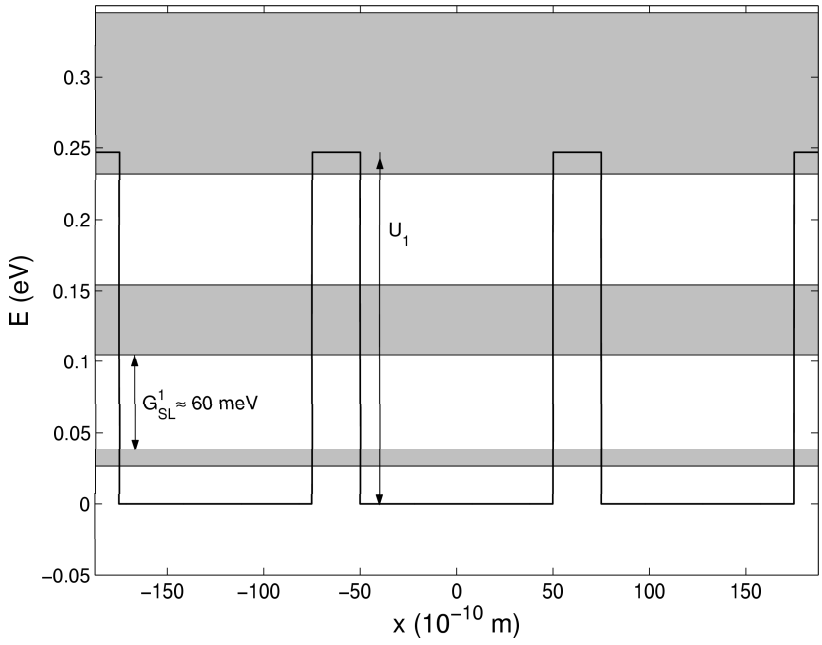

Figure 4.2: Miniband structure of NU2299 superimposed upon the superlattice potential. The shaded areas represent minibands, whilst the areas between minibands are minibandgaps.

The velocity $\mathbf{v}$ of an electron in the band is

$$\mathbf{v} = \frac{\partial E}{\partial \mathbf{p}} = \frac{1}{\hbar}\frac{\partial E(\mathbf{k})}{\partial \mathbf{k}} \tag{4.1}$$

where E is the energy of the dispersion relation for the first miniband in this case, and $\mathbf{p} = \hbar\mathbf{k}$. The crystal momentum $\hbar\mathbf{k}$ (see section 1.2.1) obeys Newton's second law, such that

$$\hbar\dot{\mathbf{k}} = -e\left(\mathbf{F} + \mathbf{v} \times \mathbf{B}\right). \tag{4.2}$$

where $\mathbf{F}$ and $\mathbf{B}$ are the externally applied electric and magnetic fields. Strictly speaking, the semiclassical model is only valid in the low field regime.

As a result of equations (4.1) and (4.2) we can write down a semiclassical Hamiltonian. The effective mass approximation (see section 1.3.1) means one can simply replace m with m^* in all equations. The Hamiltonian H_0 before externally applied fields are taken into account is

$$H_0 = E(p_x) + \frac{p_y^2}{2m^*} + \frac{p_z^2}{2m^*}. \tag{4.3}$$

The effective mass is taken to be that of an electron in GaAs, $m^* = 0.067m_e$ (where m_e is the electron mass) [59], since in both samples the electron is most likely to be found in a GaAs layer. In a semiclassical model, we describe the dispersion relation of the lowest miniband by a Fourier series as previously stated in equation (3.21), but restated here for convenience:

$$E(p_x) = \frac{\Delta_{SL}^1}{2}\left(a_0 - \sum_{n=1}^{\infty} a_n \cos\left(n\frac{p_x d_{SL}}{\hbar}\right)\right) \tag{4.4}$$

where Δ_{SL}^1 is the width of the first miniband, n is an integer and the coefficients a_n are determined in Appendix A.

To include the effect of the magnetic field, we first choose a gauge $\mathbf{A}$

$$\mathbf{A} = \left(0, B\left(x\sin\theta - z\cos\theta\right), 0\right), \tag{4.5}$$

and then replace the canonical momentum p_y with linear momentum q_y, where

$$q_y = p_y + eA_y\left(x, z\right) = p_y + eB\left(x\sin\theta - z\cos\theta\right). \tag{4.6}$$

The potential energy of the electron in the electric field is $-eFx$. The full semi-

classical Hamiltonian H is thus:

$$H = E(p_x) + \frac{1}{2}m^*\omega_c^2\left(x\sin\theta - (z-z_0)\cos\theta\right)^2 + \frac{p_z^2}{2m^*} - eFx \tag{4.7}$$

where the cyclotron frequency $\omega_c = eB/m^*$ and $z_0 = p_y/eB\cos\theta$.

It was shown in section 3.2.5 that, for a general system of the form given in equation (4.7), the motion in the y direction is separable and, in this case, the chosen gauge (4.5) corresponds to free electron motion along y. Thus, we consider Hamilton's equations for motion only in the x and z directions:

$$\dot{x} = \frac{\partial H}{\partial p_x} = \frac{\Delta_{SL}^1 d_{SL}}{2\hbar}\sum_{n=1}^{\infty} n a_n \sin\left(\frac{n p_x d_{SL}}{\hbar}\right) \tag{4.8}$$

$$\dot{p}_x = -\frac{\partial H}{\partial x} = -m^*\omega_c^2\sin\theta(x\sin\theta - (z-z_0)\cos\theta) + eF \tag{4.9}$$

$$\dot{z} = \frac{\partial H}{\partial p_z} = \frac{p_z}{m^*} \tag{4.10}$$

$$\dot{p}_z = -\frac{\partial H}{\partial z} = -m^*\omega_c^2\cos\theta\left((z-z_0)\cos\theta - x\sin\theta\right). \tag{4.11}$$

For the simple case when $\theta = 0°$, equations (4.9) and (4.11) become

$$\dot{p}_x = eF \tag{4.12}$$

$$\dot{p}_z = -m^*\omega_c^2(z-z_0) \tag{4.13}$$

respectively. Integrating equation (4.12) gives

$$p_x(t) = eFt + p_x(0), \tag{4.14}$$

and, substituting this into equation (4.8) and integrating again, yields

$$x(t) = x(0) + \frac{\Delta_{SL}^1 d_{SL}}{2\hbar\omega_B}\sum_{n=1}^{\infty} a_n\left(\cos(n\phi) - \cos(n(\omega_B t + \phi))\right) \tag{4.15}$$

where $\phi = p_x(0)d_{SL}/\hbar$ and we have substituted for the Bloch frequency, $\omega_B = eFd_{SL}/\hbar$. Thus, the electron performs Bloch oscillations in the x direction. To determine the nature of motion in the z direction, we differentiate equation (4.10)

with respect to time and substitute equation (4.11) into the result, giving

$$\ddot{z} = -\omega_c^2(z - z_0) \tag{4.16}$$

which has the general form of a simple harmonic oscillator. So when $\theta = 0°$, motion in the x and z directions is separable, and oscillations are due to the periodic miniband potential in the x direction, and to the Lorentz force in the z direction. Note that the value of z_0 is proportional to p_y and determines the centre position for the oscillations but not the actual dynamics.

When $\theta = 90°$, equation (4.9) becomes

$$\dot{p}_x = -m^*\omega_c^2 x + eF \tag{4.17}$$

and $\dot{p}_z = 0$. Here, the motion along z is simply obtained by integrating equation (4.10):

$$z(t) = z(0) + \frac{p_z}{m^*}t. \tag{4.18}$$

Since $\dot{p}_z = 0$, p_z must be constant and so the motion in the z direction is unbounded. In the x direction, differentiating equation (4.12) gives

$$\ddot{p}_x = -m^*\omega_c^2\dot{x}, \tag{4.19}$$

and substituting equation (4.8) into the above results in

$$\ddot{p}_x = -\frac{m^*\omega_c^2\Delta_{SL}d_{SL}}{2\hbar}\sum_{n=1}^{\infty} n a_n \sin\left(\frac{n p_x d_{SL}}{\hbar}\right). \tag{4.20}$$

This nonlinear equation is similar in form to that of the nonlinear pendulum, and shows that motion in the x direction is bounded when $\theta = 90°$.

However, the case of interest is when $0° < \theta < 90°$. We showed in section 3.2.5 how it is possible to reduce the dynamics in this case to a single equation, whose form is that of a driven harmonic oscillator. Thus for an electron in our given superlattice system we have

$$\ddot{p}_z + \omega_{\|}^2 p_z = -\frac{m^*\omega_c^2\Delta_{SL}^1 d_{SL}\sin\theta\cos\theta}{2\hbar}\sum_{n=1}^{\infty} n a_n \sin\left(n\left(Kp_z - \omega_B t - \phi\right)\right) \tag{4.21}$$

where $\omega_{\|} = \omega_c\cos\theta$, $K = d_{SL}\tan\theta/\hbar$ and $\phi = d_{SL}\left(p_x(0) + p_z(0)\tan\theta\right)/\hbar$. The Bloch frequency, $\omega_B = eFd/\hbar$, associated with the motion of the electron through

the superlattice potential is the frequency of the effective driving terms resulting from the plane wave form of the dispersion relation.

The full electron dynamics may be determined by solving equation (4.21) for p_z, and simultaneously solving the following equations (also obtained in section 3.2.5):

$$p_x(t) = p_x(0) + eFt - (p_z(t) - p_z(0)) \tan\theta \tag{4.22a}$$

$$\dot{x} = \frac{\partial E(p_x)}{\partial p_x} = -\frac{\Delta^1_{SL} d_{SL}}{2\hbar} \sum_{n=1}^{\infty} n a_n \sin\left(n(Kp_z - w_B t - \phi)\right) \tag{4.22b}$$

$$\dot{z} = \frac{p_z}{m^*} \tag{4.22c}$$

for p_x, x and z. To do this, we used a 4th/5th order implementation of the Runge-Kutta method [6, 60], as described in Appendix B. Note that inclusion of terms up to $n = 10$ in the dispersion relation was found to be more than sufficient to accurately model the band structure and that initial conditions were specified such that $\phi = 0$.

We consider electrons injected at the bottom of the first miniband, with $p_x = q_y = p_z = 0$ so that the electron is at rest, and at position $x = z = 0$ at $t = 0$. The magnetic fields studied are in the range 8-14 T, and are tilted through angles of 0°-75°. Electric fields range between 0-10 MVm^{-1}. Although experimentalists do not produce I-V characteristics for fields as high as 10 MVm^{-1}, it is necessary for theorists to model dynamics up to very high fields due to the numerical techniques employed in determining an I-V plot from a drift velocity - field (v_d-F) curve. The theoretical data set must truncate at field values higher than those required for comparison with experiment to ensure that the predicted I-V curve remains accurate over the entire voltage.

It was discussed previously in section 3.2.5 that the nonlinear resonance condition necessary for the formation of stochastic webs is

$$r = \frac{\omega_B}{\omega_{||}} \tag{4.23}$$

where r is an integer. The presence of a stochastic web in the phase space provides a mechanism by which the delocalisation of the electron may be greatly increased. Therefore we expect to see this reflected in the extent of the electron trajectories when the frequencies ω_B and $\omega_{||}$ are commensurate. Substituting for ω_B and $\omega_{||}$ in equation (4.23), we find that an increase in delocalisation is predicted for fields

which satisfy

$$F = \frac{r\hbar B \cos\theta}{m^* d_{SL}}. \tag{4.24}$$

Note that this condition will only apply when $\theta \neq 0°$ and $B \neq 0$ T.

4.2.1 Stroboscopic Poincaré sections

Stroboscopic Poincaré sections that demonstrate the existence of stochastic webs in phase space (generated via the Runge-Kutta method referred to previously) will be shown in this section for sample NU2293, with an applied magnetic field of $B = 11$ T. It is sufficient to present results for only one magnetic field as it has been previously shown that the effect of the magnetic field magnitude is only to set the scale of the motion [6]. The actual structure of the web is unchanged by altering the magnetic field strength. A field of 11 T was selected since good agreement between experimental and theoretical results has been demonstrated in previous work [6]. Also, since the appearance of the webs for both superlattice samples is very similar, we have chosen to present Poincaré sections only for NU2293 here, since a selection of results using sample NU2299 are featured in a later comparison of the quantum mechanical phase space with the semiclassical one.

For the general case considered in section 3.2.5, the radius of the rings in the stochastic web was predicted by determining the location of the hyperbolic points in the (P_z, p_z) phase space of the system (where $P_z = \dot{p}_z/\omega_{||}$). Applying those solutions to sample NU2293 for $B = 11$ T, we can calculate the expected scale of the stochastic webs for each tilt angle (recalling that the ring radii were calculated for an unperturbed driven oscillator system and will therefore only approximate those found by solving the full equations of motion). The unperturbed solutions are presented in table 4.3.

In the case of the superlattice system, we find that the quantity $\dot{p}_z/\omega_{||}$ is equal to the linearised momentum q_y defined in equation (4.6). This is shown as follows. First, we substitute from equation (4.11) for $\dot{p}_z$

$$\frac{\dot{p}_z}{\omega_{||}} = \frac{m^*\omega_c^2 \cos\theta}{\omega_{||}} \left(x \sin\theta - (z - z_0)\cos\theta\right). \tag{4.25}$$

Recalling that $\omega_c = eB/m^*$ and $\omega_{||} = \omega_c \cos\theta$, and separating the z_0 term out,

Ring radii	$r=1$	$r=2$	$r=3$
	$\theta = 30^\circ$		
1	0.85	1.14	1.41
2	1.55	1.87	2.16
	$\theta = 45^\circ$		
1	0.49	0.66	0.82
2	0.90	1.08	1.25
	$\theta = 60^\circ$		
1	0.28	0.38	0.47
2	0.52	0.62	0.72

Table 4.3: Expected radii of the stochastic web rings predicted in the NU2293 $(\dot{p}_z/\omega_{\|}, p_z)$ phase space. All radii are in units of 10^{-25} kg ms^{-1}.

we have

$$\frac{\dot{p}_z}{\omega_{\|}} = eBz_0\cos\theta + eB\left(x\sin\theta - z\cos\theta\right), \tag{4.26}$$

and since $z_0 = p_y/eB\cos\theta$,

$$\frac{\dot{p}_z}{\omega_{\|}} = p_y + eB\left(x\sin\theta - z\cos\theta\right), \tag{4.27}$$

which is the original definition of q_y. Hence, the Poincaré sections presented in this section (and the Wigner functions in later sections) will be labelled in terms of (q_y, p_z). Note that because in this case $q_y = \dot{p}_z/\omega_{\|}$, equation (3.57a) gives $\rho^2 = q_y^2 + p_z^2$. Therefore, since

$$H = E(p_x) + \frac{q_y^2 + p_z^2}{2m} - eFx, \tag{4.28}$$

if $H = 0$ and a Poincaré section is plotted when the condition $E(p_x) = 0$ is satisfied, i.e. when $p_x = 0$, it follows that

$$\frac{q_y^2 + p_z^2}{2m} = eFx \tag{4.29}$$

and thus we can say that ρ is proportional to $\sqrt{x}$. That is, the delocalisation of the electron in real space is directly proportional to its displacement in phase space.

For a stroboscopic Poincaré section, this relationship holds when $\rho^2/2m \gg \Delta^1_{SL}$, so that the $E(p_x)$ term in H is negligible.

Figure 4.3 shows stroboscopic Poincaré sections (in which points are plotted at multiples of the period $2\pi/\omega_{||}$) for the case when $r = 1$ and (a) $\theta = 30°$, (b) $\theta = 45°$ and (c) $\theta = 60°$. We predicted in chapter 3 that the phase space should display $2r$ radial filaments intersecting the rings with a π rotational symmetry, and clearly for $\theta = 30°$ there is good agreement with the predicted structure despite the effects of the perturbation. The rings are at the radii calculated in table 4.3, and the stable islands bounded by the web are clearly visible. Also, if attention is paid to the decreasing axis scales for $\theta = 45°$ and $\theta = 60°$, it is also clear that the radius of the rings is decreasing as θ is increased. However, another result of the increasing tilt angle is that the centre of the web becomes increasingly chaotic, as the amplitude of the plane wave in equation (4.21) increases, and the rings begin to deform from the predictions of table 4.3. The stable orbits also become deformed, and many are swallowed up in the central chaotic sea. In addition, the web filaments bend away from the straight or circular paths they follow at low tilt angles.

Figures 4.4 and 4.5 show stochastic webs for $r = 2$ and $r = 3$ respectively, for (a) $\theta = 30°$, (b) $\theta = 45°$ and (c) $\theta = 60°$. Both display similar trends to those highlighted in the $r = 1$ case. There are $2r$ radial filaments once more, as expected, and there is also rotational symmetry of $\pi/2$ in figure 4.4 and $\pi/3$ in figure 4.5. The central chaotic sea develops as the tilt angle becomes large, causing the plane wave in equation (4.21) to drive the harmonic oscillator harder, and the web filaments become progressively more distorted.

4.2.2 Semiclassical electron trajectories

Presented in this section are the real-space semiclassical trajectories predicted for both samples when on resonance. The formation of a stochastic web in phase space under resonant conditions leads to an increase in the degree of delocalisation of the electron. This delocalisation should be apparent in the motion of the electron through real space.

Figure 4.6 compares trajectories for both on and off resonance conditions for sample NU2293, for $B = 11$ T and $\theta = 45°$. The upper figure compares the case when $r = 1$ (black) to the case when $r = (1 + \sqrt{5})/4 \approx 0.809$ (red). The lower figure shows $r = 2$ (black) and $r = \pi/2 \approx 1.57$ (red). All trajectories presented

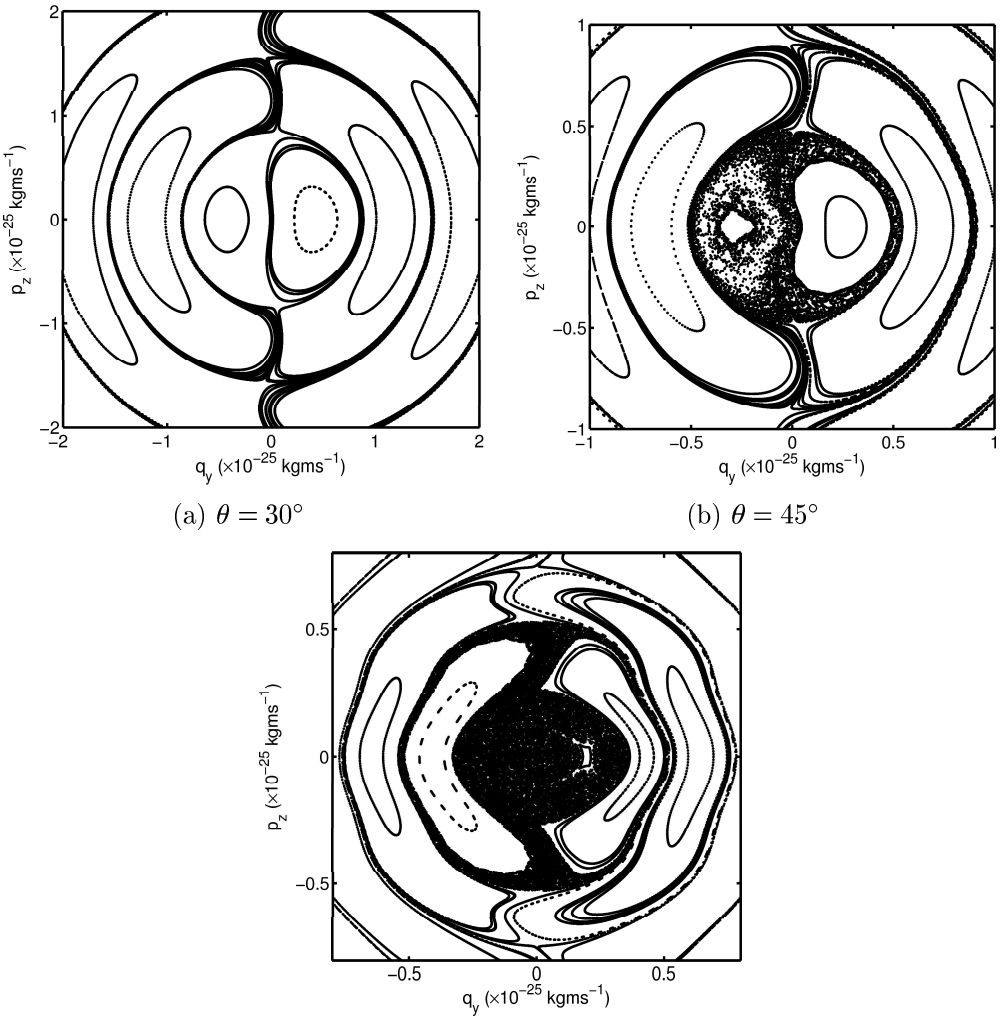

(a) $\theta = 30°$

(b) $\theta = 45°$

(c) $\theta = 60°$

Figure 4.3: Stroboscopic Poincaré sections calculated when $B = 11$ T, $r = 1$ and (a) $\theta = 30°$, (b) $\theta = 45°$ and (c) $\theta = 60°$ for sample NU2293.

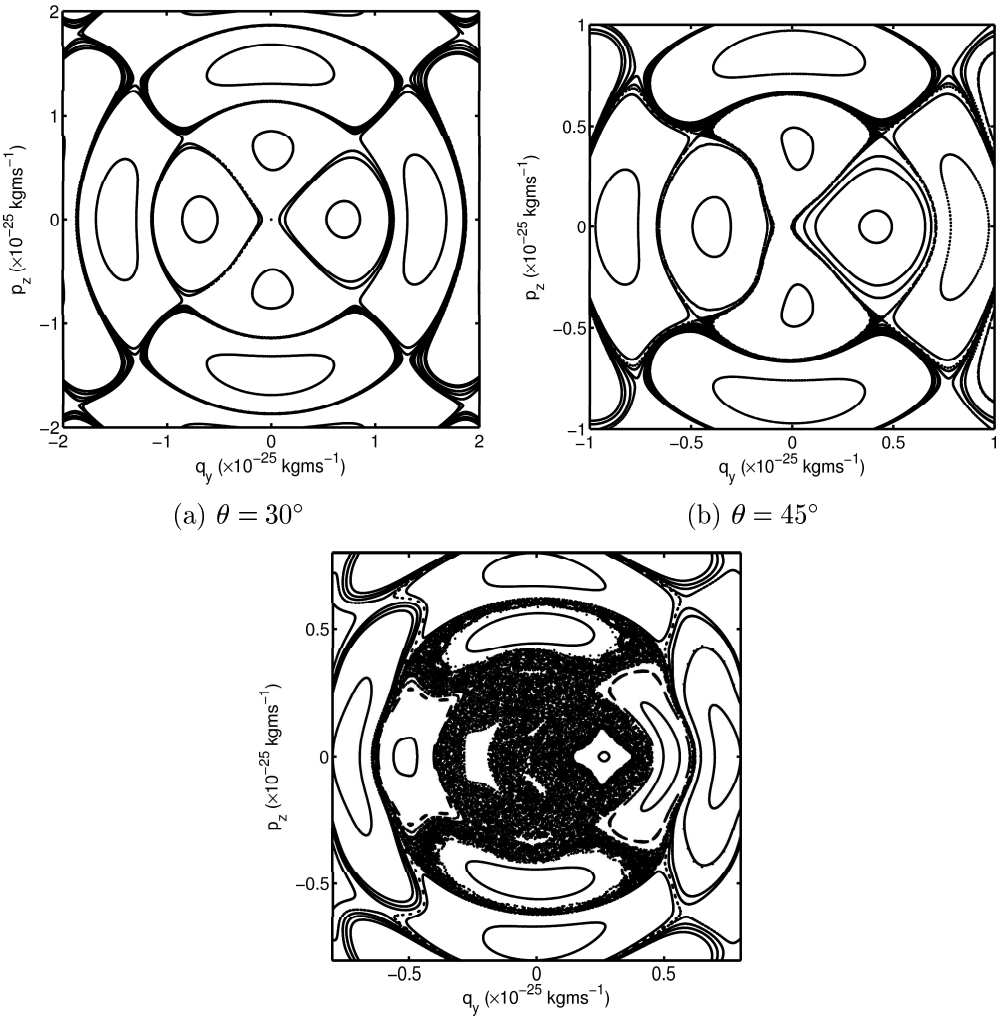

(a) $\theta = 30°$

(b) $\theta = 45°$

(c) $\theta = 60°$

Figure 4.4: Stroboscopic Poincaré sections calculated when $B = 11$ T, $r = 2$ and (a) $\theta = 30°$, (b) $\theta = 45°$ and (c) $\theta = 60°$ for sample NU2293.

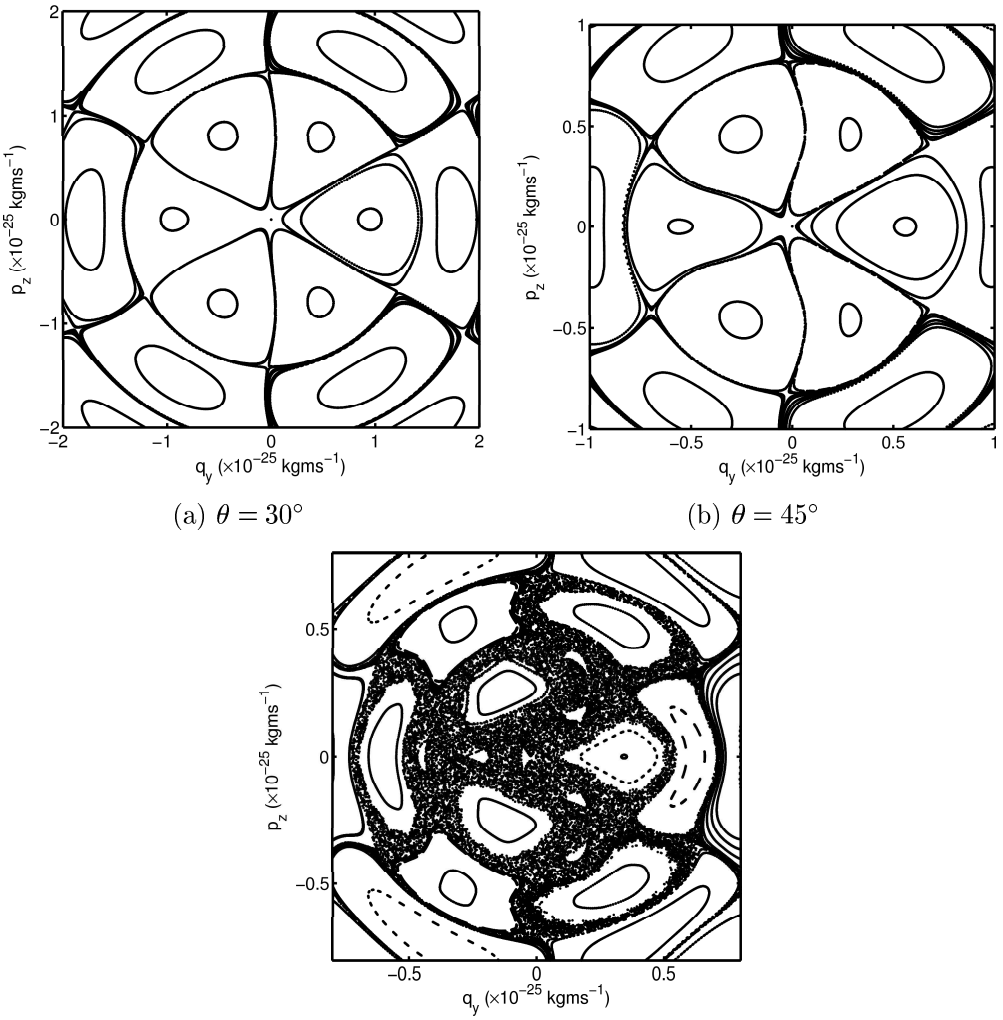

(a) $\theta = 30°$

(b) $\theta = 45°$

(c) $\theta = 60°$

Figure 4.5: Stroboscopic Poincaré sections calculated when $B = 11$ T, $r = 3$ and (a) $\theta = 30°$, (b) $\theta = 45°$ and (c) $\theta = 60°$ for sample NU2293.

in this section are plotted over a time of 1.6 ps. It is clear in both cases that the path of the electron when r takes integer values is much more delocalised than when r is non-integer. Similar plots are shown in figure 4.7 for sample NU2299, with $B = 14$ T and $\theta = 30°$. As before, the upper figure shows $r = 1$ (black) and $r = (1 + \sqrt{5})/4$ (red), and the lower figure is $r = 2$ (black) and $r = \pi/2$ (red). Once more, the increase in delocalisation that takes place when the system is on resonance is clear to see. For both samples however, note that the extent of the resonant trajectories decreases as the order of the resonance increases. This is despite the fact that the web radii increase with increasing r. However, it can be understood in terms of two factors. Firstly, the web filaments which facilitate the increased delocalisation appear to become narrower as r increases (as can be seen by comparing figures 4.3(a), 4.4(a) and 4.5(a)). This means that the probability of diffusion along the filaments is reduced, and so the expected degree of delocalisation would not be as great. Intuitively, however, it makes sense to consider the motion in terms of the Bloch oscillations contributing to the motion in the x direction. As the resonance is increased, the electric field F must also increase and so the Bloch amplitude, Δ_{SL}^{1}/eF, will decrease. So whilst the electron undergoes an increase in delocalisation due to the presence of the stochastic web, this is counteracted slightly by the localising effect of the electric field.

Figures 4.8 and 4.9 give an overview of the effects of the strength and tilt angle of the magnetic field upon the electron trajectories for samples NU2293 and NU2299 respectively. Trajectories are shown for $r = 1$, with $B = 8$, 11 and 14 T going down the page, and $\theta = 30°$, $45°$ and $60°$ from left to right. It is immediately apparent that as θ increases, the trajectories become less regular due to the formation of the chaotic sea in phase space. In addition, as B is increased, trajectories for a given value of θ usually become more confined in the z direction and also in the x direction. Increasing B is equivalent to increasing the harmonic potential barrier (by increasing the steepness of the gutter potential) that the electron is faced with as it oscillates in the z direction. And also, by our definition of the electric field required for resonance in equation (4.24), it is clear that increasing B also increases F, leading to a localising effect due to Bloch-type oscillations, counteracting the resonance as discussed previously.

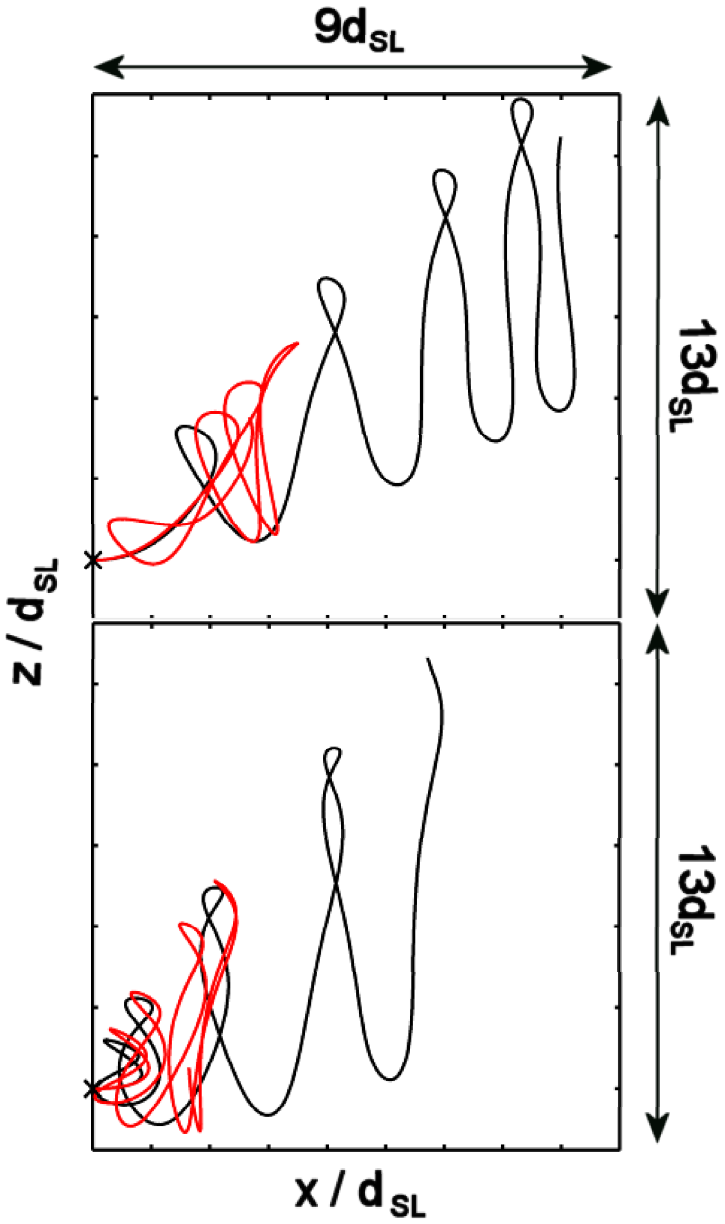

Figure 4.6: Comparison of on (black) and off (red) resonance semiclassical electron trajectories in the first miniband of sample NU2293, for $B = 11$ T and $\theta = 45°$. The upper plot shows $r = 1$ and $r = (1 + \sqrt{5})/4$, whilst the lower plot shows $r = 2$ and $r = \pi/2$. The electron was initially at rest in all cases.

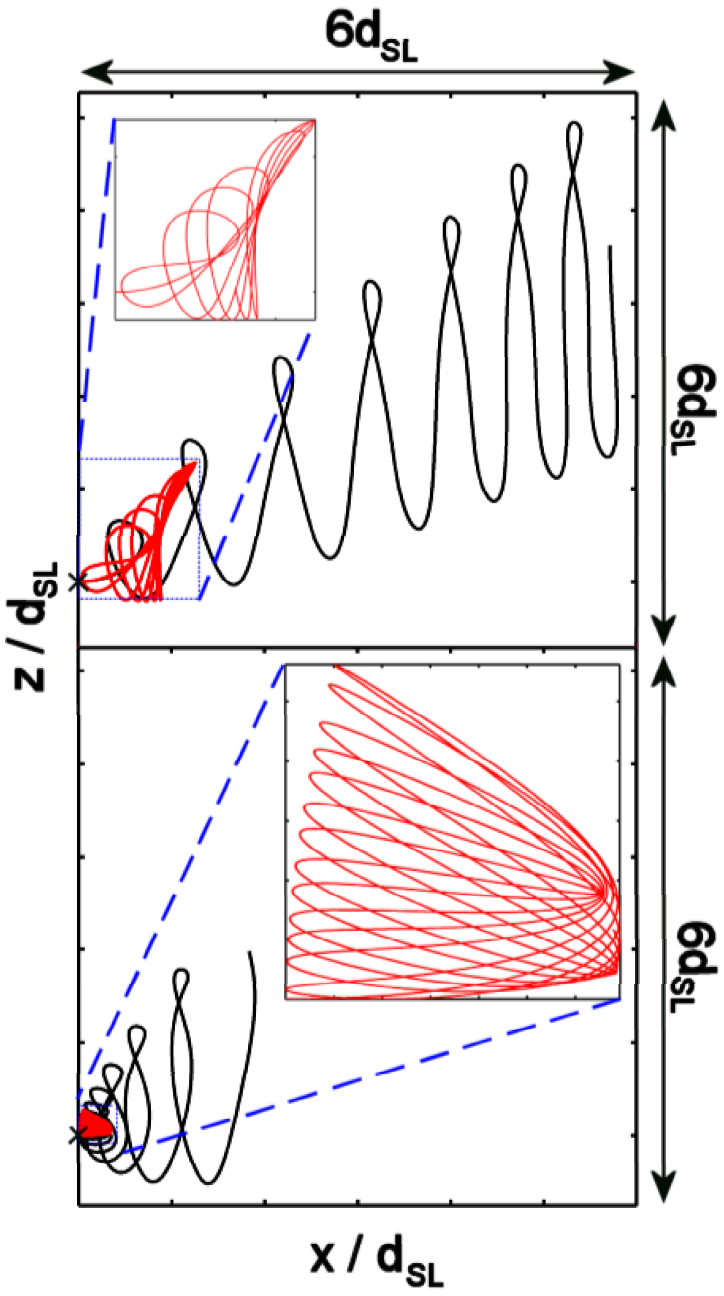

Figure 4.7: Comparison of on (black) and off (red) resonance semiclassical electron trajectories in the first miniband of sample NU2299, for $B = 14$ T and $\theta = 30°$. The upper plot shows $r = 1$ and $r = (1 + \sqrt{5})/4$, whilst the lower plot shows $r = 2$ and $r = \pi/2$. Insets show the enlarged off resonance trajectories to allow the reader to appreciate the detail of the motion. The electron was initially at rest in all cases.

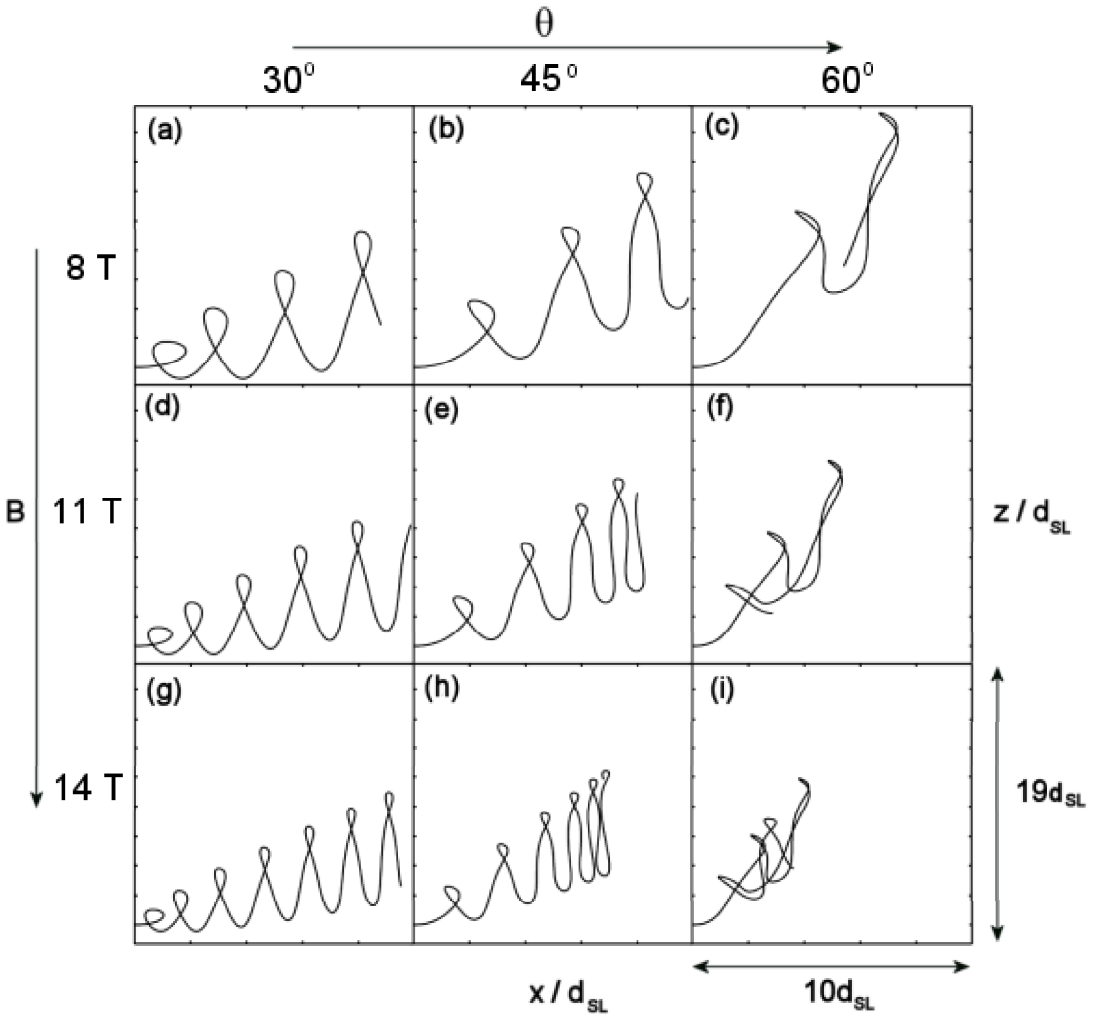

Figure 4.8: Comparison of on resonance ($r = 1$) semiclassical electron trajectories in the first miniband of sample NU2293 for varying values of B and θ. In (a) to (c) $B = 8$ T, (d) to (f) $B = 11$ T and (g) to (i) $B = 14$ T. From left to right, θ takes values of 30°, 45° and 60°. The electron was initially at rest in all cases.

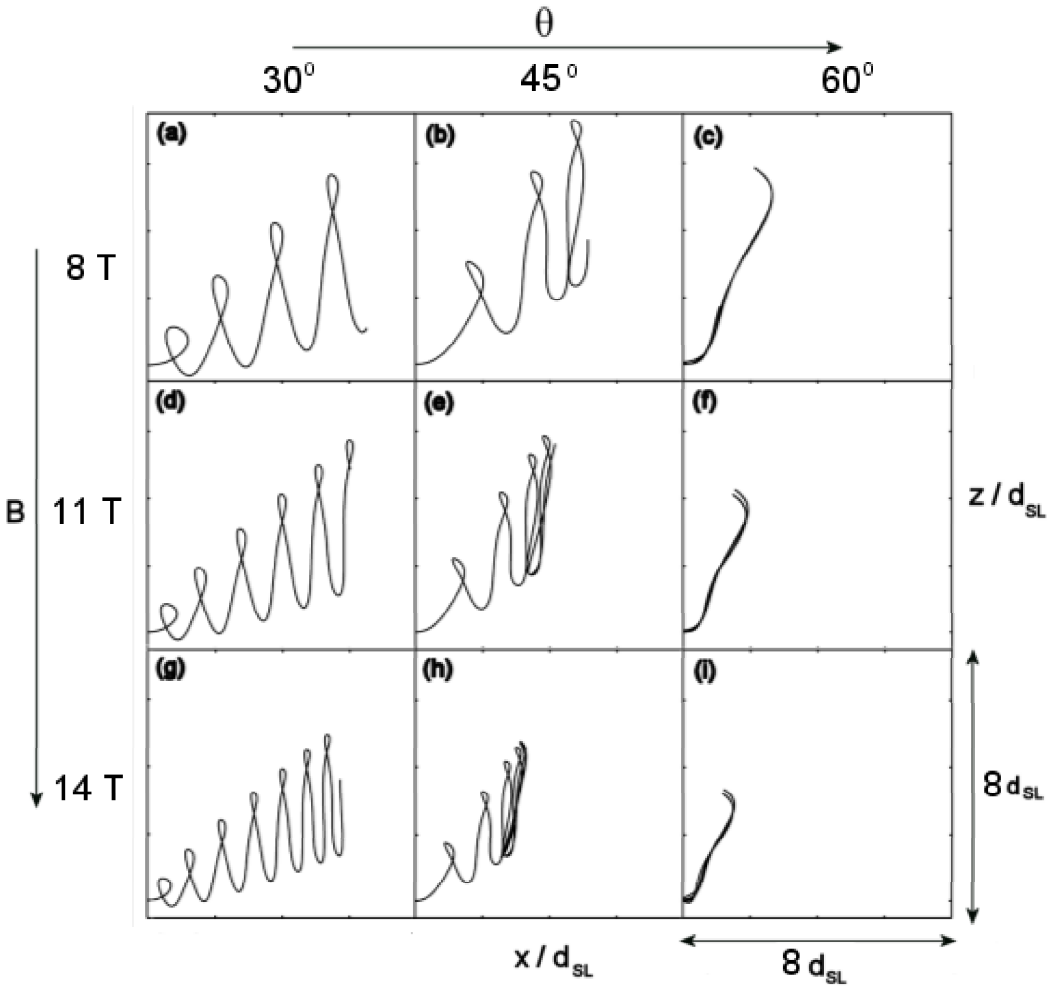

Figure 4.9: Comparison of on resonance ($r = 1$) semiclassical electron trajectories in the first miniband of sample NU2299 for varying values of B and θ. In (a) to (c) $B = 8$ T, (d) to (f) $B = 11$ T and (g) to (i) $B = 14$ T. From left to right, θ takes values of 30°, 45° and 60°. The electron was initially at rest in all cases.

4.2.3 Semiclassical drift velocity field curves

A useful way to compare the delocalisation of the electron at different field strengths is to consider the drift velocity. Having used the Runge-Kutta method [6, 60] to determine the real space trajectories of the electron for a variety of applied field strengths, the knowledge of $p_z(t)$ may be used to determine $v_x(t) = \dot{x}$ via equation (4.22b). Then for any given field strength, one calculates the drift velocity v_d from

$$v_d(F) = \frac{1}{\tau}\int_0^\infty v_x(F,t)\, e^{-t/\tau} dt \tag{4.30}$$

where τ is the scattering time [1]. For the purposes of this model, a time interval of 4τ sufficiently approximates an infinite time, since calculations of the scattering probability $P(t) = e^{-t/\tau}/\tau$ indicate that the probability of an electron remaining unscattered after that time is negligible.

The scattering time is given by the following formula [39, 61]:

$$\tau = \left(\frac{\tau_e}{\tau_e + \tau_i}\right)^{\frac{1}{2}} \tau_i, \tag{4.31}$$

where τ_e and τ_i are the elastic and inelastic scattering times respectively. In the case of NU2293, $\tau_e = 21$ fs and $\tau_i = 1.5$ ps [39], therefore the scattering time is taken to be $\tau = 176$ fs. In NU2299, $\tau_e = 27.78$ fs and $\tau_i = 1.26$ ps and consequently $\tau = 185$ fs.

From section 1.3.2, which describes the Esaki-Tsu model [1], we recall that for $\theta = 0°$, the expression that the drift velocity of an electron in a band described by n terms of a Fourier series is given by

$$v_d = \frac{\Delta^1_{SL} d_{SL}}{2\hbar} \sum_{n=1}^{\infty} n a_n \left(\frac{n\omega_B \tau}{1 + (n\omega_B \tau)^2}\right). \tag{4.32}$$

So, substituting for $\omega_B = edF/\hbar$, we see that the theoretical drift velocity field curve is defined by

$$v_d(F) = \frac{\Delta^1_{SL} d_{SL}}{2\hbar} \sum_{n=1}^{\infty} n a_n \left(\frac{n\tau\hbar e d_{SL} F}{\hbar^2 + (n\tau e d_{SL} F)^2}\right). \tag{4.33}$$

Remember that the Esaki-Tsu model is only valid when $B = 0$ or $\theta = 0°$, when the magnetic field should not affect the dynamics in the x direction.

Figures 4.10 and 4.11 show drift velocity field plots for samples NU2293 and

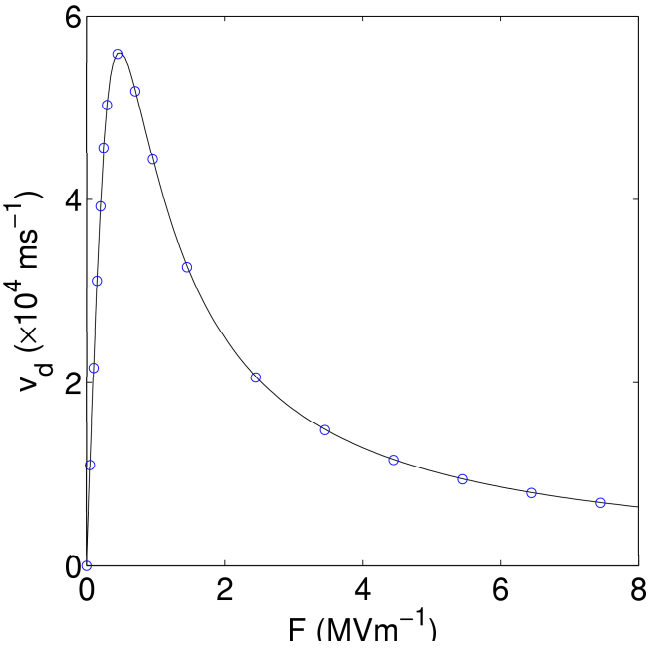

Figure 4.10: Comparison of the exact Esaki-Tsu drift velocity field curve (blue circles) and the curve (black) obtained by numerical solution of equation (4.22b) for sample NU2293. The plots are indistinguishable. Both are calculated using the first 10 terms in the Fourier expansion of the dispersion relation of the first miniband.

NU2299 respectively overlaid with the Esaki-Tsu relationship specified in equation (4.33). Clearly, since the curves are indistinguishable by eye, the agreement between numerical calculations of the semiclassical regime at $\theta = 0°$ and the theoretical Esaki-Tsu curve are ideal.

When the orientation of the magnetic field is no longer parallel to the electric field the Easki-Tsu model no longer applies, and we expect to see resonant peaks appearing in the v_d-F curves at electric field strengths that meet the condition specified in equation (4.24). Figure 4.12 shows cascade plots of the drift velocity in NU2293 as a function of electric field for $\theta = 0 - 75°$, for $B = 8$ T (a), 11 T (b) and 14 T (c). Figure 4.13 shows equivalent plots for sample NU2299. Resonances that can be clearly identified are marked on each plot. Note that as the strength of the magnetic field is increased, resonances may also be observed for non-integer rational values of r. The $r = 1/2$ resonance is highlighted in some cases to draw attention to this.

As the tilt angle increases, higher order resonances become apparent in the drift velocity - indeed, for sample NU2299 at $\theta = 75°$ and $B = 14$ T - it is almost impossible to separate out the peaks due to different resonances (figure 4.13(c)).

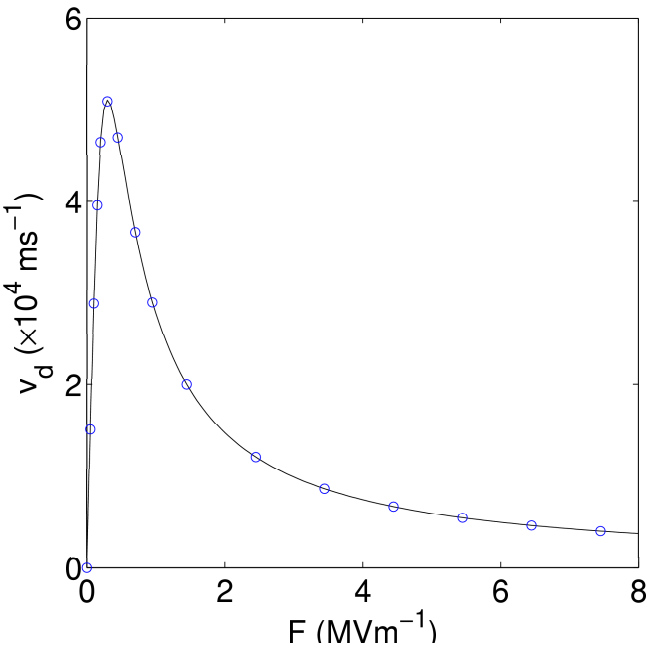

Figure 4.11: Comparison of the exact Esaki-Tsu drift velocity field curve (blue circles) and the curve (black) obtained by numerical solution of equation (4.22b) for sample NU2299. The plots are indistinguishable. Both are calculated using the first 10 terms in the Fourier expansion of the dispersion relation of the first miniband.

Increasing the magnetic field strength enables us to observe the resonances more clearly. This may seem counter-intuitive since it was seen in the previous section that increasing B led to a slight decrease in the extent of the electron delocalisation. However, whilst higher electric fields have a localising effect on electrons, they also increase the frequency at which the electrons oscillate. Thus, by increasing both ω_c and ω_B, the electron is able to complete more periods of the resonant motion before it is scattered (as is apparent in figures 4.8 and 4.9), and hence the resulting drift velocity is increased. In addition, because increasing B causes the resonance condition to occur at higher F, the resonant peaks in the drift velocity are superimposed upon lower background levels and therefore appear much more prominent than peaks occurring near the high initial Esaki-Tsu-like peak. Also note that for a given value of B, the observed resonances tend to be stronger in NU2299 than NU2293. This is because of the longer scattering time in NU2299, which again allows the electron to complete more periods of delocalised motion before scattering.

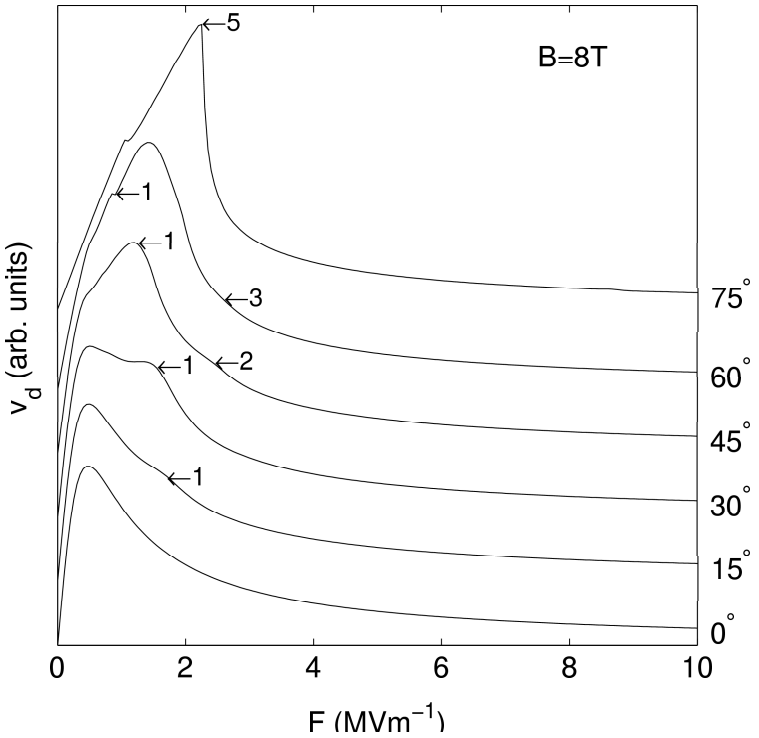

Figure 4.12: (a) Cascade plot of the drift velocity field relationship, numerically calculated using a semiclassical model, for sample NU2293 when $\theta = 0°$-$75°$ and $B = 8$ T. Similar plots are shown for (b) $B = 11$ T and (c) $B = 14$ T. The locations of a number of predicted resonance peaks are highlighted.

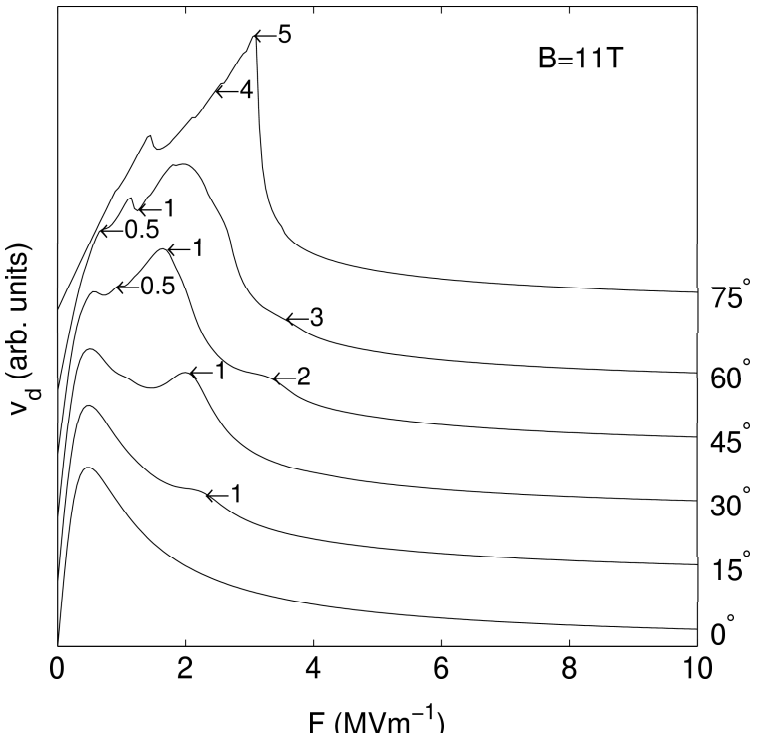

Figure 4.12: (b) Sample NU2293 when $B = 11$ T.

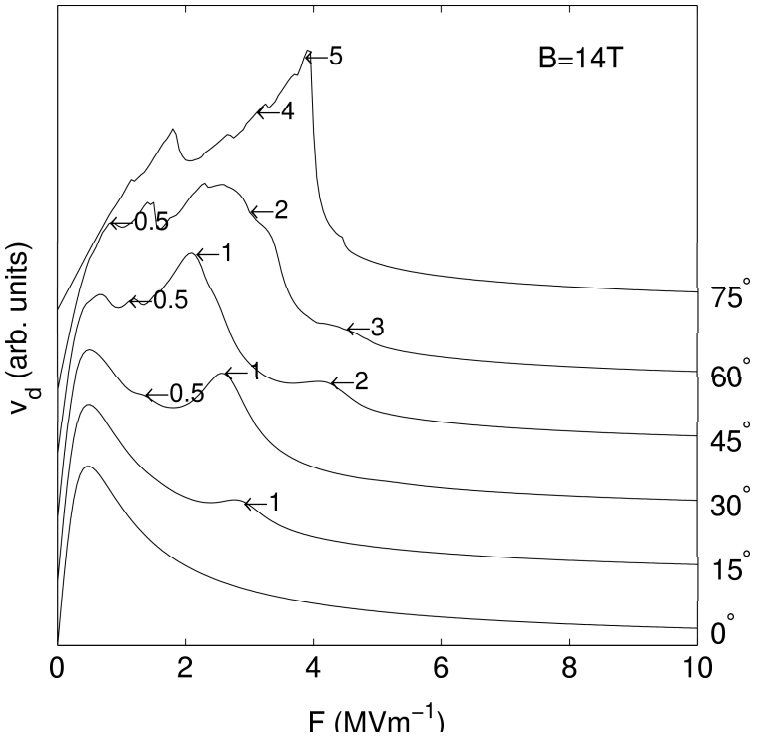

Figure 4.12: (c) Sample NU2293 when $B = 14$ T.

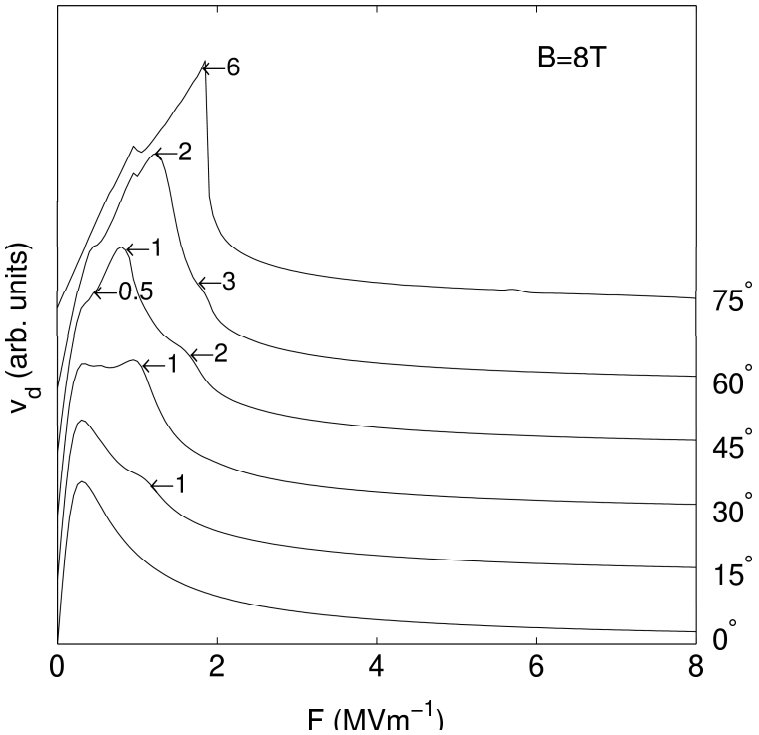

Figure 4.13: (a) Cascade plot of the drift velocity field relationship, numerically calculated using a semiclassical model, for sample NU2299 when $\theta = 0°$-$75°$ and $B = 8$ T. Similar plots are shown for (b) $B = 11$ T and (c) $B = 14$ T. The locations of a number of predicted resonance peaks are highlighted.

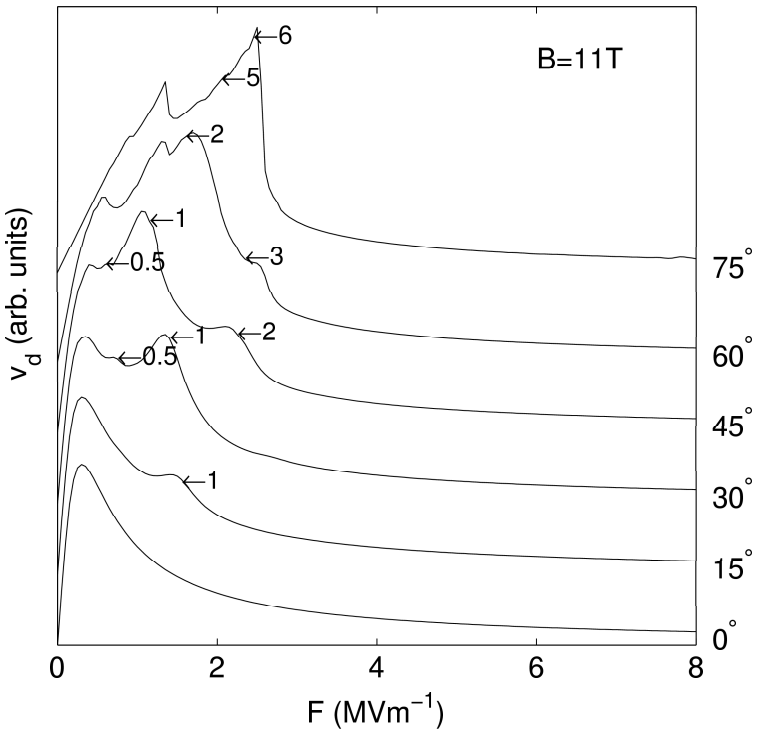

Figure 4.13: (b) Sample NU2299 when $B = 11$ T.

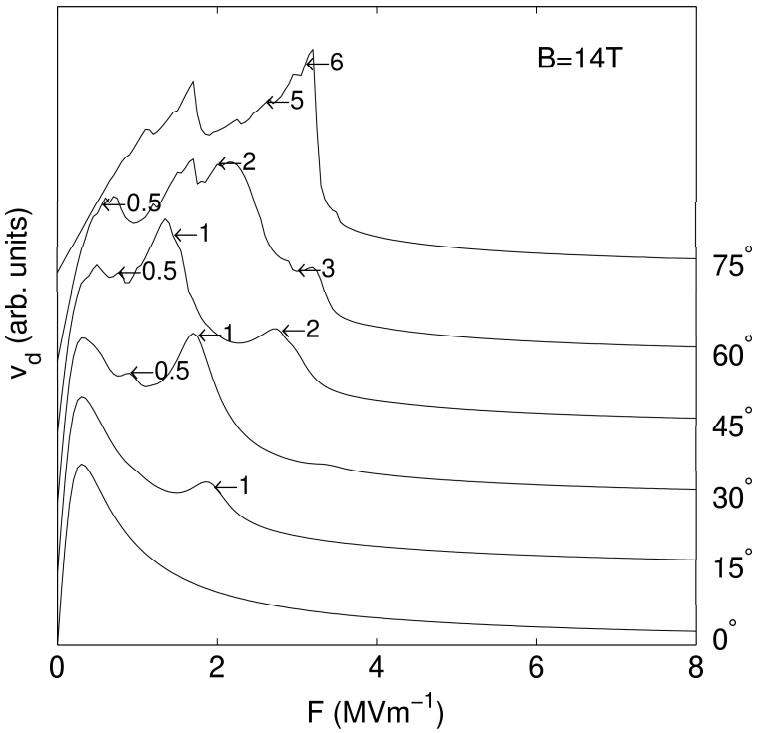

Figure 4.13: (c) Sample NU2299 when $B = 14$ T.

4.3 The quantum mechanics of the system

The two-dimensional quantum mechanical Hamiltonian of an electron in a one-dimensional superlattice with an applied bias and tilted magnetic field is

$$H = -\frac{\hbar^2}{2m^*}\left(\frac{\partial^2}{\partial x^2} + \frac{\partial^2}{\partial z^2}\right) + V_{SL}(x) + V_B(x,z) + V_F(x) \tag{4.34}$$

where V_{SL} is defined by the variation of the conduction band edge in the superlattice structure in question. The potential energy due to the magnetic field is

$$V_B(x,z) = \frac{1}{2}m^*\omega_c^2\left(x\sin\theta - (z-z_0)\cos\theta\right)^2 \tag{4.35}$$

and the potential energy due to the electric field, is

$$V_F(x) = -eFx. \tag{4.36}$$

The electron wavefunction, $\Psi(x,z)$, is governed by the time-dependent Schrödinger equation:

$$i\hbar\frac{\partial\Psi(x,z)}{\partial t} = H\Psi(x,z) \tag{4.37}$$

In order to compare the quantum regime with the semiclassical analysis in the previous section, one must solve equation (4.37) numerically. The evolution of the wavefunction at finite times is determined via the Crank-Nicolson method [60]. Appendix C describes this powerful technique in detail. The parameter range modelled in this section is the same as that considered in the semiclassical case. The choice of the initial wavefunction is discussed in section 4.3.1.

4.3.1 Determination of the initial wavefunction

It became clear during preliminary investigations that the choice of the initial wavefunction, Ψ_0, is important, since the observed behaviour in the quantum mechanical regime depends strongly upon the probability distribution of the initial state. This is because the initial form of the wavefunction determines which of the system's minibands are populated.

For example, considering the case where $\theta = 0°$ for simplicity, the first approach to the modelling problem was to define a simple Gaussian probability density function as the starting point for the simulation. We chose a normalised

initial state:

$$\Psi_0(x,z) = \left[\frac{1}{2\pi\sigma_x\sigma_z}\exp\left(\frac{-(x-x_c)^2}{2\sigma_x^2} - \frac{(z-z_c)^2}{2\sigma_z^2}\right)\right]^{\frac{1}{2}} \tag{4.38}$$

where (x_c, z_c) are the co-ordinates of the point in real space about which the Gaussian is centred (taken to be $(0,0)$) and σ_x, σ_z represent the standard deviation of the Gaussian in the x and z directions. The standard deviation was defined in terms of the full-width half-maximum (FWHM), f_i, of the wavefunction by the following relationship:

$$f_i = 2\sqrt{2\ln 2}\sigma_i \tag{4.39}$$

where i may represent either x or z. The FWHM was chosen to be a multiple of the superlattice period in the x direction, such that $f_x = 6d_{SL}$, whilst in the z direction $f_z = 2r_c$ where r_c is the cyclotron radius associated with the applied magnetic field:

$$r_c = \sqrt{\frac{\hbar}{Be}}. \tag{4.40}$$

This choice of initial wavefunction was based upon the desire to ensure that the position of the electron was delocalised over a number of superlattice periods so that the periodic potential induces band-like dynamics.

The dynamics resulting from an initial wavefunction of the form (4.38) leads to the population of multiple minibands. We find that although the initial wavepacket is a superposition of states mainly from the first miniband, a small fraction of the admixture involves states in a higher miniband. Figures 4.14 and 4.15 illustrate this for superlattices NU2293 and NU2299 subjected to a low bias. The plots show the change in the probability density profile $|\Psi(x, z=0, t)|^2$ along the x direction as a function of time. Only the x direction is shown for clarity, since motion in the z direction is not significant when $\theta = 0°$. It is clear that the wavefunction splits into two unequal fractions which oscillate with the same frequency but different amplitudes. Note that in the colourmap for figures 4.14 and 4.15, red indicates areas of high probability density, going through yellow, green and blue to white for zero probability density. This colourmap will be applied throughout this thesis and its scale is displayed in Appendix D should the reader wish to refer to it for further information.

Referring back to section 1.2.2, we recall that the amplitude A_B and period

τ_B of Bloch oscillations in band i are given by the following equations:

$$A_B = \frac{\Delta^i_{SL}}{eF} \tag{4.41}$$

$$\tau_B = \frac{h}{eFd_{SL}}. \tag{4.42}$$

Therefore, the time period of the oscillations is unaffected by which miniband the wavefunction is populating, whilst the amplitudes of oscillation for different minibands are related by the ratio:

$$\frac{A_{B_a}}{A_{B_b}} = \frac{\Delta^a_{SL}}{\Delta^b_{SL}} \tag{4.43}$$

where a and b represent the index of the miniband in question. Thus the data in table 4.1 predicts that for NU2293, oscillations in the second miniband will be approximately 5 times larger in amplitude than oscillations in the first miniband, whilst oscillations in the third miniband will be around 11 times larger than in miniband one. Similarly, the data presented in table 4.2 predicts amplitudes of approximately 4 and 9 times the amplitude of first miniband oscillations for the second and third minibands in NU2299 respectively.

Bearing in mind these values, it is clear from figures 4.14 and 4.15 that the majority of the wavefunction is indeed residing in the first miniband whilst a small but significant component appears to be in the third miniband. This confirms that taking a simple Gaussian as the form of the initial wavefunction populated both the first and third minibands. Since both fractions of the wavepacket are at the same point in k_x-space, and both bands have the same shape, both Bloch oscillate in the same manner. However the amplitude of the Bloch oscillations is governed by the width of the miniband, so the greater width of the third miniband leads to a small fraction of the wavepacket performing oscillations with large amplitude in comparison to the main body. The wavepacket dynamics in cases of this nature have been discussed in more detail by Hartmann et al. [62].

The reader may find it surprising that the wavefunction populates the first and third minibands rather than the first and second, yet a few moments thought should convince one that this is reasonable. Firstly, there is the simple evidence that the breakaway fraction is oscillating in the same sense as the first miniband fraction. The form of the dispersion relation depicted in figure 1.3 (in particular the gradient, which determines the electron's direction of motion) shows that any

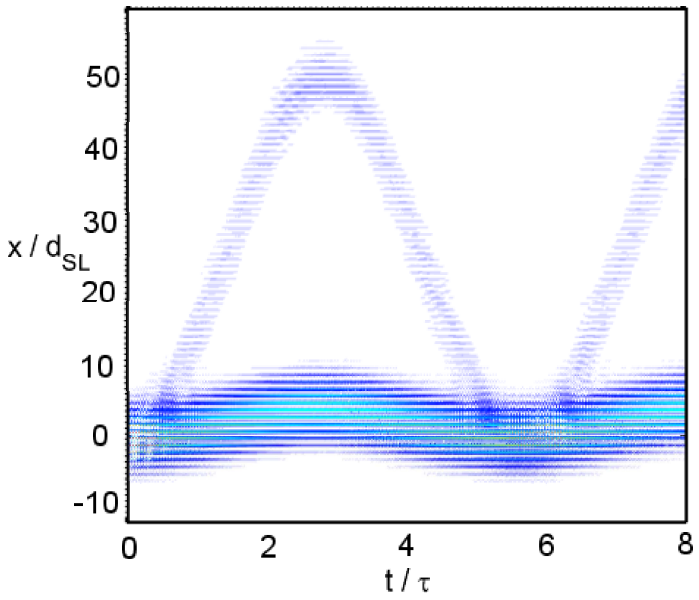

Figure 4.14: Surface plot showing the variation in the probability density function as a function of time, in sample NU2293 when $\theta = 0°$. The initial state of the electron is represented by a Gaussian wavefunction, for which the electron is at rest. The vertical axis shows the changing cross-section of the probability density (along $z = 0$); time is represented on the horizontal axis.

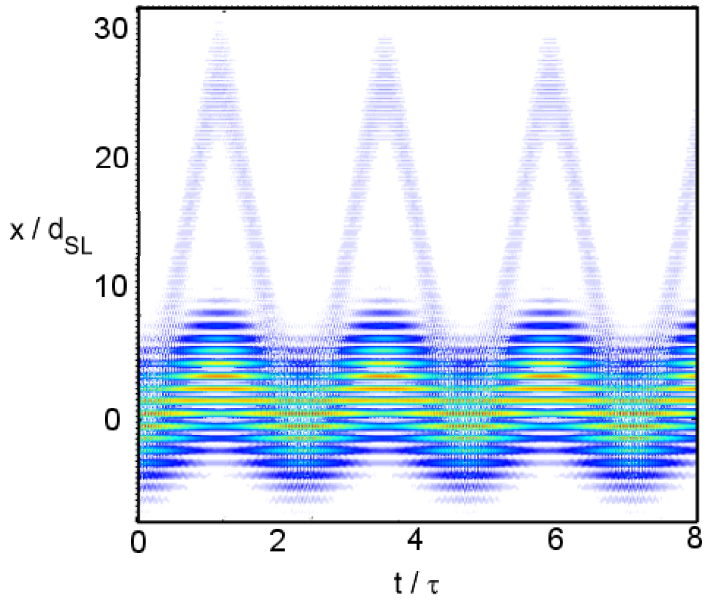

Figure 4.15: Surface plot showing the variation in the probability density function as a function of time, in sample NU2299 when $\theta = 0°$. The initial state of the electron is represented by a Gaussian wavefunction, for which the electron is at rest. The vertical axis shows the changing cross-section of the probability density (along $z = 0$); time is represented on the horizontal axis.

fragments populating the second miniband should Bloch oscillate in the opposite sense to that of the first miniband, whilst fragments in the third miniband should indeed follow the component in the first miniband. However, it is also intuitive to realise that a physically reasonable wavepacket for an electron in this system would be spatially modulated, with peaks in the regions of the superlattice wells, and troughs in the barrier regions. In defining a Gaussian probability density function across the system, we have ignored this tendency of the electron to reside in low energy regions of the potential. We see from figure 4.2 that for sample NU2299, the height of the potential barriers coincides with the energy of the third miniband, therefore it is logical that in forcing the electron to reside in such high energy regions we cause a fraction of the wavefunction to populate the third miniband. In NU2293, the barrier height coincides with the energy of the fourth miniband. But the barrier is a smaller fraction of the unit cell width than in NU2299 and its tendency to increase the electron energy is partially compensated by the InAs notch layer. Consequently, the effect of the barrier seems to be to populate the third miniband, just as in NU2293.

In order to ensure that the quantum dynamics is truly analagous to the semiclassical case, an alternative definition of the initial wavefunction had to be found to avoid the issue of populating higher minibands. Populating only the first miniband would be directly comparable to the semiclassical model, which considers just the first miniband, and would also make the two dimensional wavefunction dynamics in a tilted magnetic field easier to interpret than if the wavefunction contains an admixture of Bloch states from different minibands, which evolves in a complex way. In addition, it would then be clear that if fractions were observed to be moving in higher minibands, this must be a consequence of tunnelling, making such phenomena easier to identify.

The new initial wavefunction was defined as a product of two terms: one, Ψ_0^X, a function of x and the other, Ψ_0^Z, a function of z. The function Ψ_0^X was written in terms of Bloch functions, $\Phi_{k_x}^n(x)$, where k_x specifies the wavenumber and n the miniband index to which a given Bloch state corresponds. Since Bloch functions are completely delocalised, they are not practical to work with directly, so Ψ_0^X was defined as a weighted sum over all states in the first miniband:

$$\Psi_0^X = \frac{d_{SL}}{2\pi} \int_{-\pi/d_{SL}}^{+\pi/d_{SL}} \Phi_{k_x}^{n=1}(x)\zeta(k_x)dk_x. \tag{4.44}$$

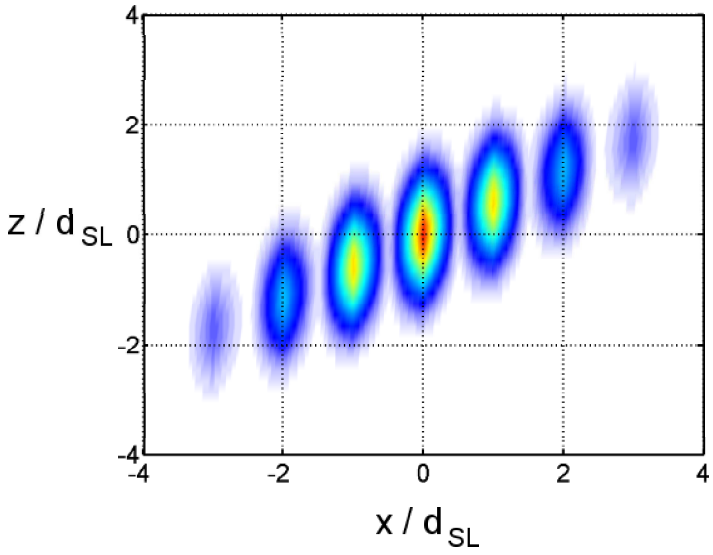

Figure 4.16: Surface plot illustrating the probability density function at $t = 0$ used in calculations of the quantum mechanical behaviour of an electron in sample NU2293. In this plot, $\theta = 30°$, and as θ varies so does the orientation of the initial state.

In equation (4.44) $\zeta(k_x)$ is the weighting function, of the form

$$\zeta(k) = Ce^{-Ak_x^2} \tag{4.45}$$

where A and C are constants that determine the spread and normalise the function respectively. The function Ψ_0^Z is a Gaussian with σ_z as defined previously. Here, however, we consider the case when $\theta \neq 0°$. In this situation, we wish the wavefunction to be tilted with the magnetic field, so we write the Gaussian in terms of the tilted axes coordinates which were defined earlier in equations (3.23) and (3.24). The wavefunction is centred on $z_t = 0$, and is written as

$$\Psi_0(x, z) = \Psi_0^X \times \frac{1}{2\pi\sqrt{\sigma_z}} \exp\left(-\frac{z_t^2}{2\sigma_z^2}\right). \tag{4.46}$$

Examples of the initial wavefunction probability densities used for studying each sample are displayed as surface plots in figures 4.16 and 4.17. For $\theta = 0°$, this new initial state Bloch oscillates in a single band.

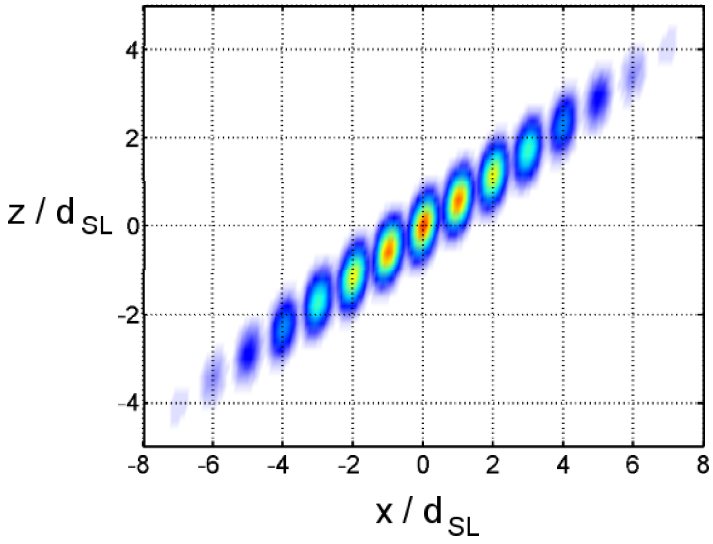

Figure 4.17: Surface plot illustrating the probability density function at $t = 0$ used in calculations of the quantum mechanical behaviour of an electron in sample NU2299. In this plot, $\theta = 30°$, and as θ varies so does the orientation of the initial state.

4.3.2 Quantum mechanical electron trajectories

To determine the quantum mechanical trajectory of the electron when subjected to any given combination of fields, at discrete times we calculate the expectation values of position in both the x and z directions:

$$\langle x \rangle = \frac{\int\int_{-\infty}^{\infty} \Psi^* x \Psi dx dz}{\int\int_{-\infty}^{\infty} \Psi^* \Psi dx dz} \tag{4.47a}$$

$$\langle z \rangle = \frac{\int\int_{-\infty}^{\infty} \Psi^* z \Psi dx dz}{\int\int_{-\infty}^{\infty} \Psi^* \Psi dx dz}. \tag{4.47b}$$

Although in theory the denominator is not required in equations (4.47a) and (4.47b) since the wavefunction is initially normalised to unity, it is included in calculations to guard against inaccuracies that might be caused by numerical errors at the boundary, where tiny fractions of the wavefunction may "leak" away and be lost from the simulation. To minimise the possibility of such leakage, the extent of each quantum mechanical simulation is carefully calculated from the extent of the corresponding semiclassical trajectory, with a further significant margin of error allowed as a precaution.

Figure 4.18 illustrates the results of a full quantum mechanical simulation of the electron dynamics in sample NU2293 for conditions $B = 11$ T, $\theta = 30°$ and $r = (1+\sqrt{5})/4$. Figure 4.18(a) is an enlargement of a plot of mean wavefunction position, $\langle x \rangle$ versus $\langle z \rangle$. It is clear that this off resonance trajectory is bounded, and that the path is simply traversed backwards and forwards repeatedly. Figures 4.18(b) to (f) are all snapshots of the probability density function at various times during the simulation, viewed as a two dimensional surface plot. These confirm that the mean position of the wavefunction oscillates back and forth along the trajectory, and also demonstrate that the wavefunction remains largely unchanged by the motion. There are no obvious changes in the structure of the wavefunction, although it does show a tendency to spread along the gutter potential created by the magnetic field. This is only very slight though, as comparison of figures 4.18(b) and 4.18(e) illustrates, where the expected positions are very close. The reader should note that although the probability density function is not shown in its entirety, at no point does it come close to the edges of the simulation "box". The diffuse nature of the wavefunction (the need for which is addressed in the previous section) simply makes it unfeasible to show the entire extent of the plot whilst retaining reasonable resolution of the path it is following. Note also that to avoid confusion by displaying too many details in each figure, the comparison between mean quantum mechanical trajectories and the semiclassical paths will be considered later in section 4.3.4.

Figure 4.19 shows the quantum mechanical trajectory (enlarged in 4.19(a)) and probability density function for sample NU2293 for the $r = 1$ resonance under an applied field of $B = 11$ T at an angle of $\theta = 30°$. Again, it is impossible to show the entire probability density whilst also conveying a sense of its movement through real space because it is so diffuse. If the reader takes a moment to compare figures 4.19(b) and 4.19(i), it should be apparent that the scale necessary to display the full extent of both these probability densities on the same axes would fail to show the detail of the quantum mechanical trajectory.

It is clear that the quantum mechanical trajectory is of the same form as the $r = 1$ semiclassical trajectories highlighted in the left-hand ($\theta = 30°$) column of figure 4.8, and that furthermore, it is much greater in extent than the quantum mechanical path in the off resonance case shown in figure 4.18. The probability density clearly follows the trajectory, oscillating in the z direction as it progresses in the x direction, without undergoing any significant changes in structure, other than a slight tendency of the wavefunction to become elongated

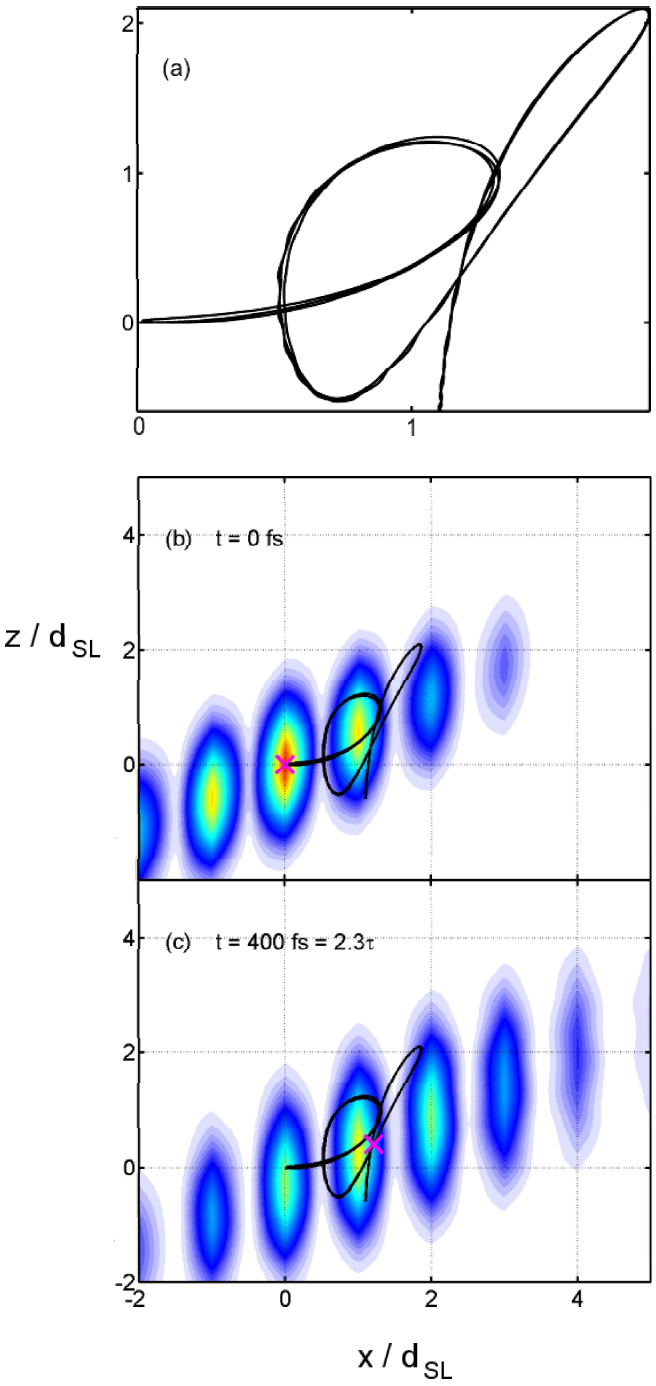

Figure 4.18: Snapshots of the time-evolution of the electron probability distribution in sample NU2293, for $r = (1+\sqrt{5})/4$, $B = 11$ T and $\theta = 30°$. In (a) the mean trajectory of the electron wavefunction is enlarged. Surface plots of the probability distribution at times (b) $t = 0$ fs, (c) $t = 400$ fs, (d) $t = 800$ fs, (e) $t = 1200$ fs and (f) $t = 1600$ fs are shown. The mean trajectory is overlaid in black, whilst the magenta cross marks the point on the trajectory corresponding to the current frame.

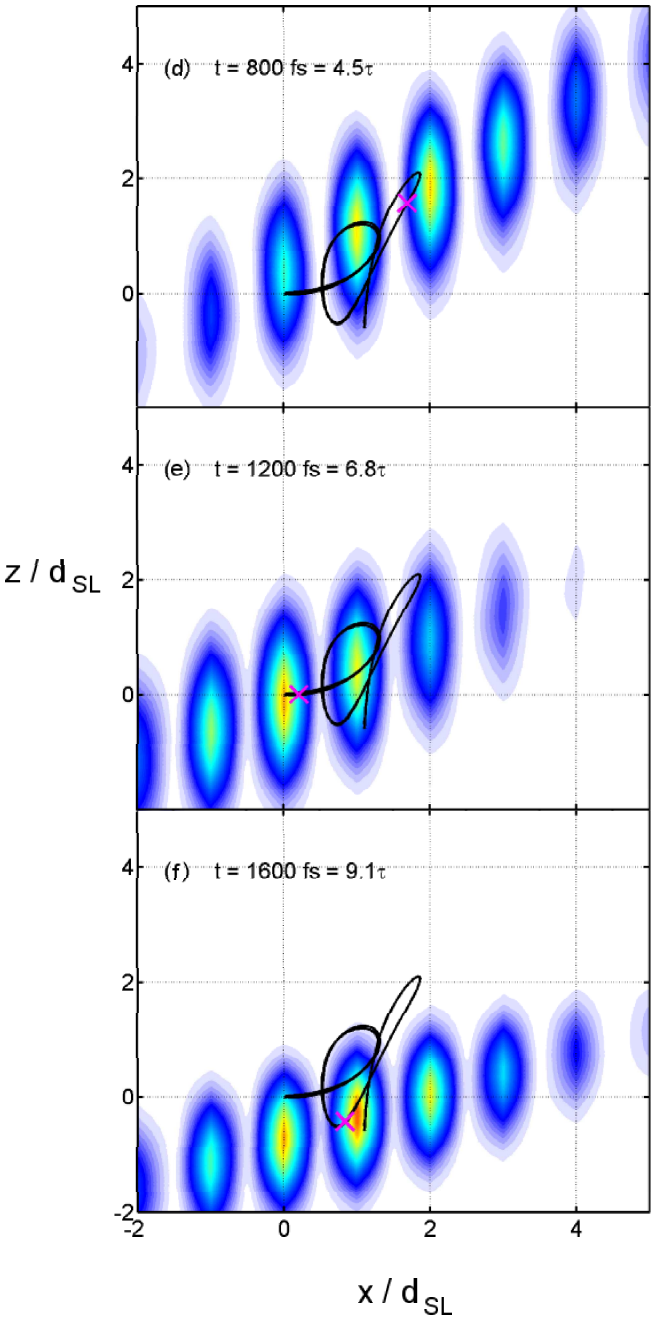

Figure 4.18: Continued.

along the magnetic gutter potential.

The reader may be concerned that the mean quantum mechanical position (marked by a magenta cross) is not always coincident with the peak in probability density, for example in figure 4.19(g). The maximum probability density is highlighted with a dotted arrow, and each of the leading peaks has been paired up with the corresponding trailing peak (as shown by the solid arrows). In this case, the spreading appears to be more pronounced in the negative x direction, and the mean position is to the left of the maximum. However, the opposite is true in figure 4.19(i): the mean position is to the right of the maximum, and the intensity of the leading peaks is greater than that of corresponding trailing peaks. This shifting of the maximum around the mean position is due simply to the nature of the quantum transport through the superlattice barriers. Note that in every frame in figure 4.19, the peaks are always located along the same positions in the x direction - that is, the wavepacket always localises away from the superlattice barriers, in the niche and well regions of the superlattice potential. (Each niche is centred upon nd_{SL}, where n is an integer.) Therefore in order to progress in the x direction, the probability shows a gradual transfer of intensity between adjacent peaks, without the peaks ever actually being physically displaced to the right. Thus there is a shift of the mean position along the superlattice, across the barriers, and whilst the mean position is moving across a barrier (as is the case in figure 4.19(g)), it can never be coincident with a peak in the probability density function. When crossing the niches in the superlattice potential however, the maximum and mean position are able to coincide (figure 4.19(h)).

Figure 4.20 shows the $r = 2$ resonance of sample NU2293 for $B = 11$ T and $\theta = 45°$. In this case, whilst the general features of the quantum mechanical trajectory in figure 4.20(a) are similar to those seen in the semiclassical case (inset) - the trajectory is much longer in extent that in the off resonance case, and there is a comparable structure to the shape of the path - only the first "figure of eight" loop in the trajectory is a good match. Study of the later frames of the evolution of the probability density offer the key to this mismatch. It is clear - and this is particularly visible in figures 4.20(e) and (f) - that the wavefunction has split into two roughly equal parts oscillating in opposing directions (in the z direction). These meet, forming an interference pattern as they pass through one another (as seen in figures 4.20(d) and (g)), before emerging relatively intact (as seen in figures 4.20(e), (f) and (i)).

This effect is caused by a combination of two factors. Firstly, as explained

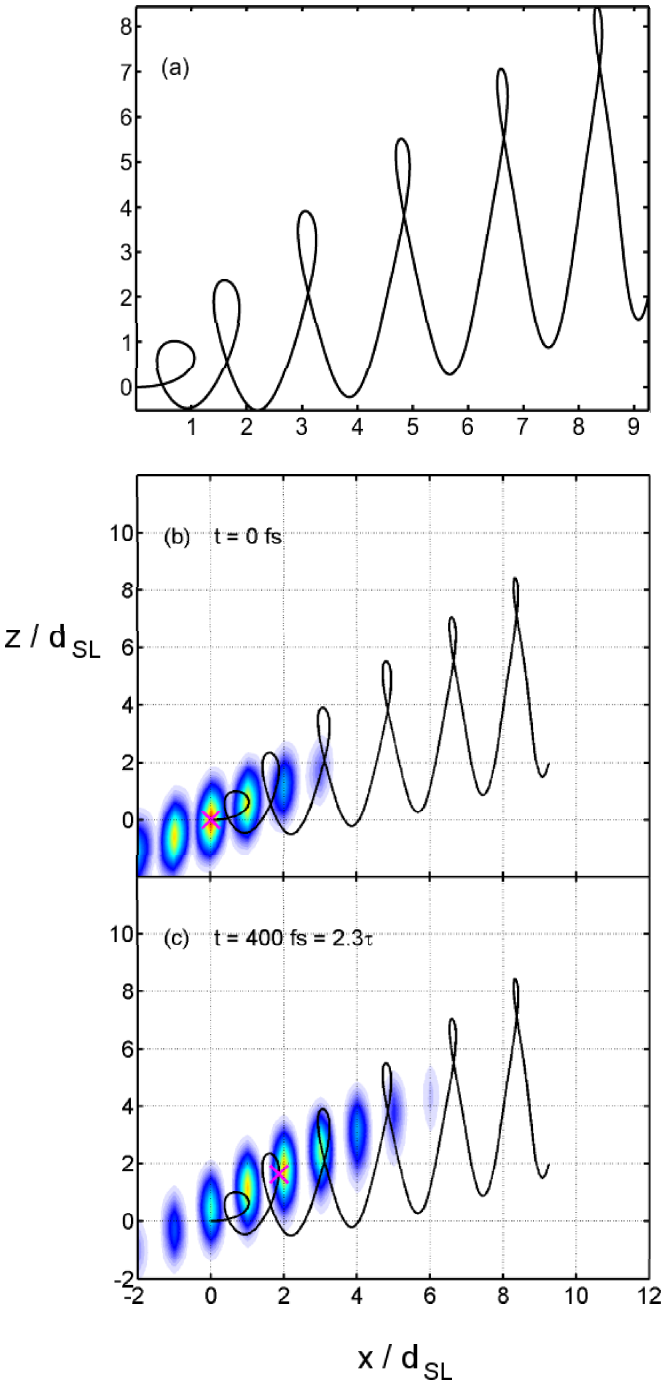

Figure 4.19: Snapshots of the time-evolution of the electron probability distribution in sample NU2293, for $r = 1$, $B = 11$ T and $\theta = 30°$. In (a) the mean trajectory of the electron wavefunction is enlarged. Surface plots of the probability distribution at times (b) $t = 0$ fs, (c) $t = 400$ fs, (d) $t = 600$ fs, (e) $t = 800$ fs, (f) $t = 1000$ fs, (g) $t = 1200$ fs, (h) $t = 1400$ fs and (i) $t = 1600$ fs are shown. The mean trajectory is overlaid in black, whilst the magenta cross marks the electron's position on the trajectory at the time corresponding to the current frame.

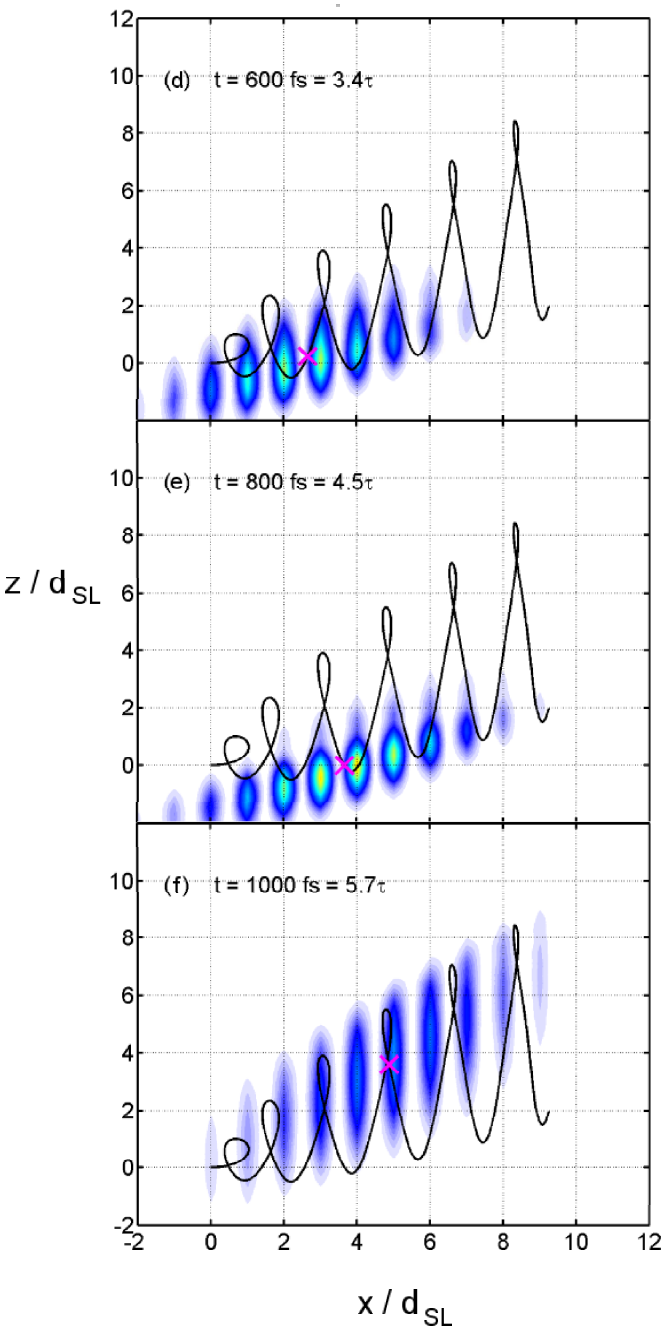

Figure 4.19: Continued.

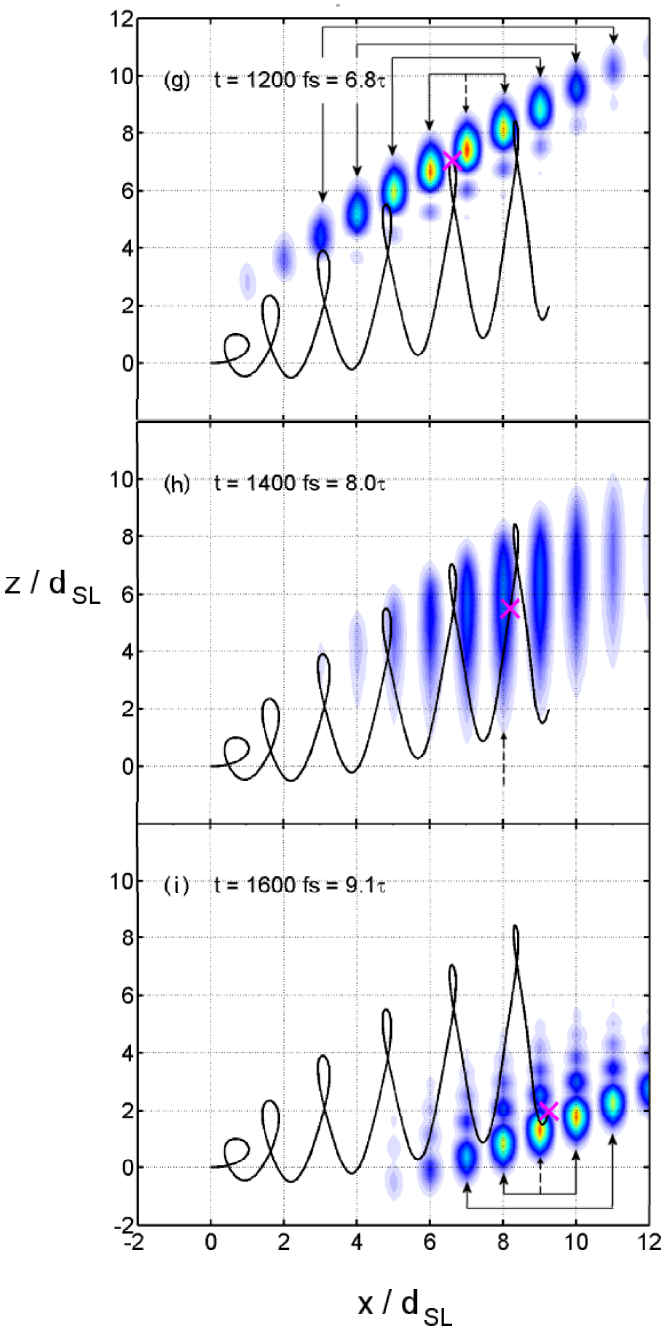

Figure 4.19: Continued.

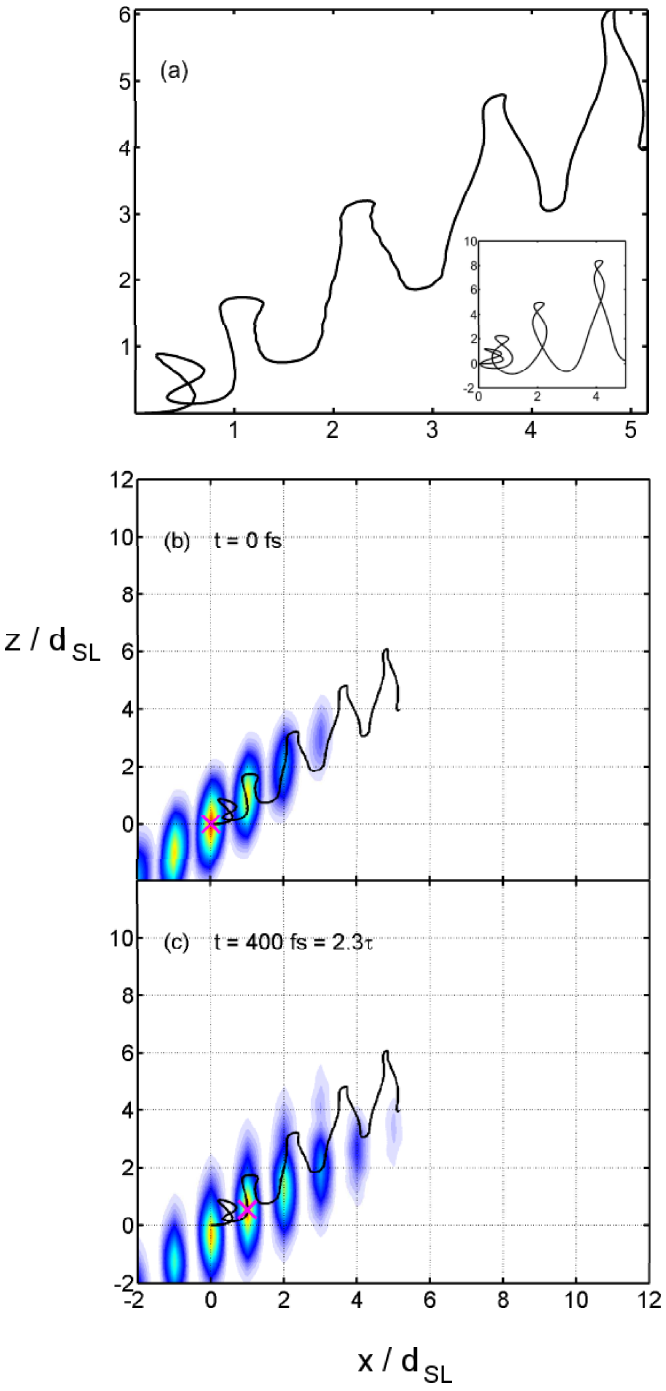

Figure 4.20: Snapshots of the time-evolution of the electron probability distribution in sample NU2293, for $r = 2$, $B = 11$ T and $\theta = 45°$. In (a) the mean trajectory of the electron wavefunction is enlarged. Surface plots of the probability distribution at times (b) $t = 0$ fs, (c) $t = 400$ fs, (d) $t = 600$ fs, (e) $t = 800$ fs, (f) $t = 1000$ fs, (g) $t = 1200$ fs, (h) $t = 1400$ fs and (i) $t = 1600$ fs are shown. The mean trajectory is overlaid in black, whilst the magenta cross marks the electron's position on the trajectory at the time corresponding to the current frame.

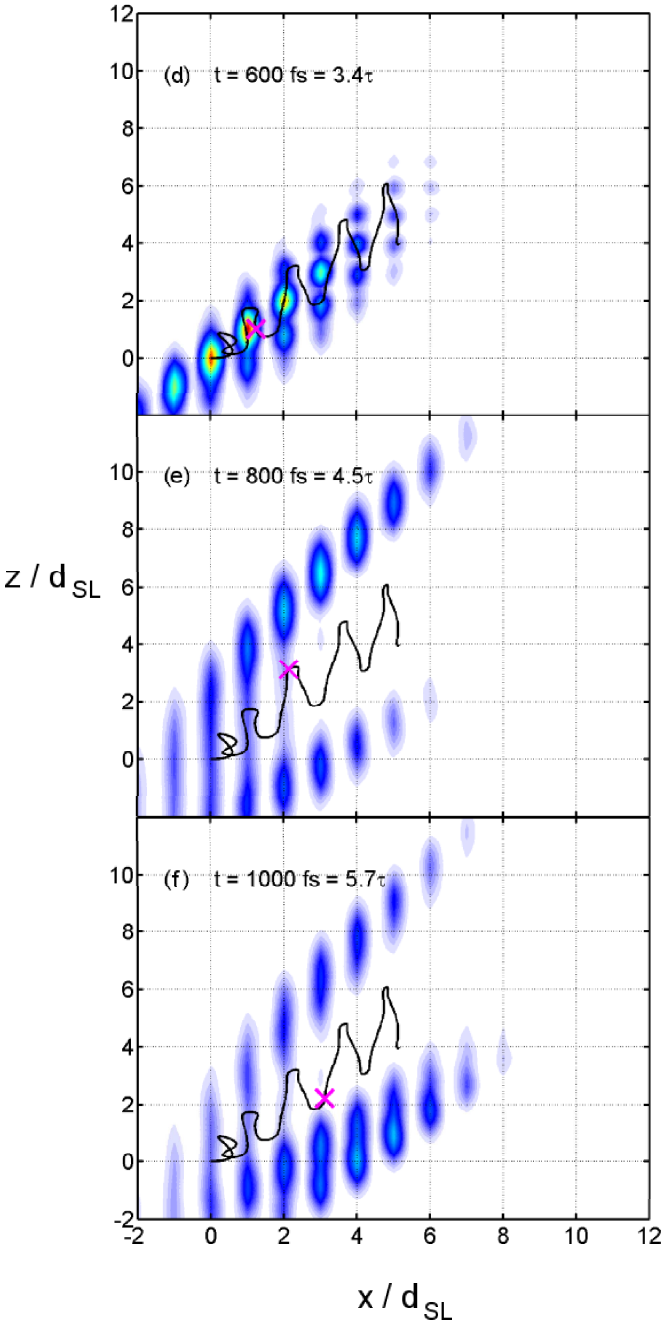

Figure 4.20: Continued.

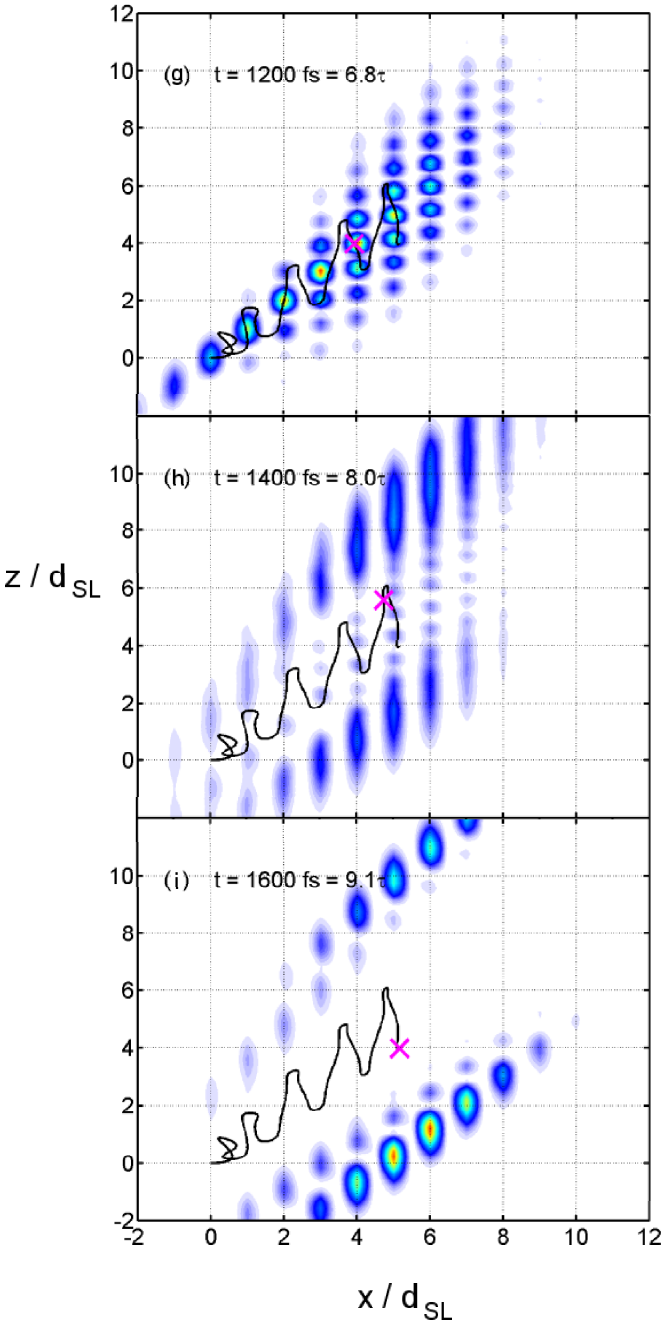

Figure 4.20: Continued.

below, it is due to the symmetry of the stochastic web for the case when $r = 2$. Secondly, it is also partially due to the diffuse nature of a wavefunction, which encompasses a spread of position and momentum values, in contrast to a semiclassical trajectory corresponding to a *single* initial condition. If the reader considers the Poincaré section corresponding to this system, shown in figure 4.21(a), it can be seen that there are four filaments of the web extending from the centre of phase space. In the semiclassical case, where the position and momentum may be *explicitly* defined, the initial motion occurs along the positive x and z directions and the electron traverses a single radial filament outwards from the centre of phase space leading to the path displayed in figure 4.22. The electric field forces the electron motion to begin in the positive x direction, and rearranging the semiclassical Hamiltonian we can write

$$x\left(t\right) = \frac{1}{eF}\left(E(p_x) + \left(\frac{q_y^2\left(t\right) + p_z^2\left(t\right)}{2m^*}\right) - H\right). \tag{4.48}$$

Since both q_y and p_z are squared, any combination of these can generate a positive displacement in the x direction, depending only on the values of $E(p_x)$ and H. If we then also rearrange the magnetic gauge chosen earlier to give

$$z\left(t\right) = \frac{1}{\cos\theta}\left(-\frac{q_y\left(t\right)}{eB} + x\left(t\right)\sin\theta\right), \tag{4.49}$$

we can see that z depends upon the sign of q_y. When $r = 1$ (figure 4.21(b)), the symmetry of the web means that there is only one way in which q_y can vary after an electron is launched at the web centre, $(q_y, p_z) = (0, 0)$, and that is to decrease. When q_y decreases (i.e. becomes negative), equation (4.49) dictates that z must increase (since x increases initially due to F). Thus if z is increasing, the electron is moving with positive p_z, and hence the only radial filament it can travel along is vertically upwards from the centre, marked by the solid blue arrow in figure 4.21(b). The electron loops around the inner cells of the web, along the first ring-shaped filament and then returns to the centre of phase space along the dotted arrow. The sense in which it traverses the $r = 1$ filament is always the same, as indicated by the arrows. When $r = 2$, the semiclassical electron starting from rest initially travels along the filament shown by the blue arrow in figure 4.21(a), so that q_y becomes more positive, and p_z becomes more negative. The reason for this can be seen from figure 4.23, where z, x, p_z and q_y are plotted as a function of time. The black curves relate to the original semiclassical initial

conditions, where both position and momentum are zero. In 4.23(c) and (d), blue circles are marked on the plots of momentum (at times that are multiples of $2\pi/\omega_{||}$) to indicate which values of p_z and q_y are plotted on the stroboscopic Poincaré section, and it is clear that these do indeed correspond to the blue arrow in figure 4.21(a) (i.e. $q_y > 0$, $p_z < 0$).

In the quantum mechanical regime, the initial conditions cannot be exactly specified, so the diffuse nature of the wavefunction means that a range of points in phase space are occupied initially, as illustrated by the magenta ring in figure 4.21(a). When $r = 2$, the range of initial conditions encompassed in the quantum mechanical case means that q_y can increase *or* decrease as t increases, corresponding to motion in either the negative or positive z direction respectively, whilst still moving in the positive x direction. When q_y decreases, the result is the same as in the semiclassical case, however when q_y increases, z decreases, and consequently p_z is negative (indicated by the magenta arrow in figure 4.21(a)). True to the nature of quantum mechanics, the wavefunction follows both possibilities simultaneously, with two fractions travelling out through phase space along the two radial filaments highlighted by arrows in figure 4.21(a), and returning via the remaining filaments. Another set of semiclassical plots are shown in red in figure 4.23, which start very close to the centre of phase space ($(q_y, p_z) = (0, 0.08 \times 10^{-25})$), and illustrate one of the possible alternative trajectories available in the quantum mechanical regime. In figure 4.23(a), the electron is clearly oscillating in the opposite sense to the case when the initial conditions are zero, deviating by as much as $10d_{SL}$ at times of order 1400 fs (corresponding to figure 4.20(h)), yet 4.23(b) shows that the trajectories do not deviate by more than $\sim 2d_{SL}$ in the x direction. The magenta crosses in figures 4.23(c) and 4.23(d) confirm that this alternative motion does indeed equate to following the magenta arrow in figure 4.21(a) through phase space.

The result of such dual motion is that the expectation value of the position reflects the oscillatory nature of the motion of both fractions of the wavepacket, but, since the two fractions are roughly equal, the full amplitudes of the opposing oscillations cancel each other out in the mean position. So the amplitude of the resultant path is restricted to the spread of the probability density function when both fractions meet and interfere, as seen in figures 4.20(d) and 4.20(g). Figure 4.22 presents the probability density at time $t = 800$ fs (as shown in figure 4.20(e)) with the corresponding semiclassical path overlaid, demonstrating visually that there is clearly a good match of both the maximum z-amplitude

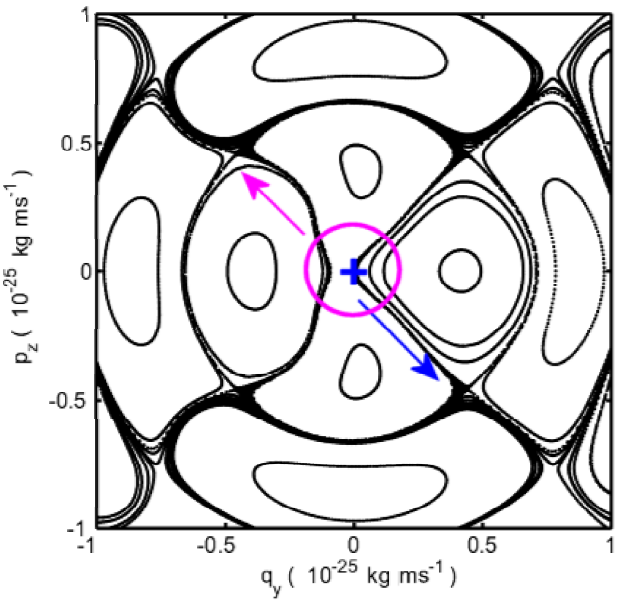

(a)

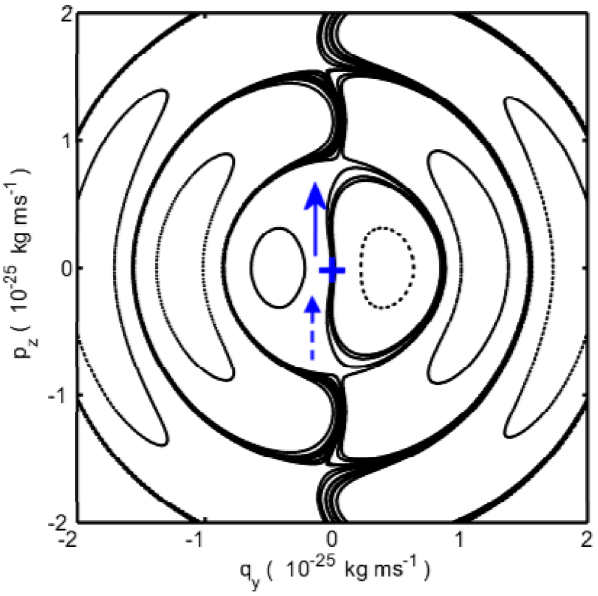

(b)

Figure 4.21: Stroboscopic Poincaré sections calculated when $B = 11$ T for sample NU2293. (a) corresponds to $r = 2$ and $\theta = 45°$. The magenta circle represents the multiple initial conditions occupied by a quantum mechanical wavepacket. The blue arrow is the filament traversed by the semiclassical electron, starting from rest, and the magenta arrow is the alternative direction which is followed simultaneously in the quantum mechanical case. (b) corresponds to $r = 1$ and $\theta = 30°$. The blue cross and solid arrow mark the starting point of the semiclassical electron trajectory and its initial direction in phase space. The dotted arrow marks the return trajectory of the electron.

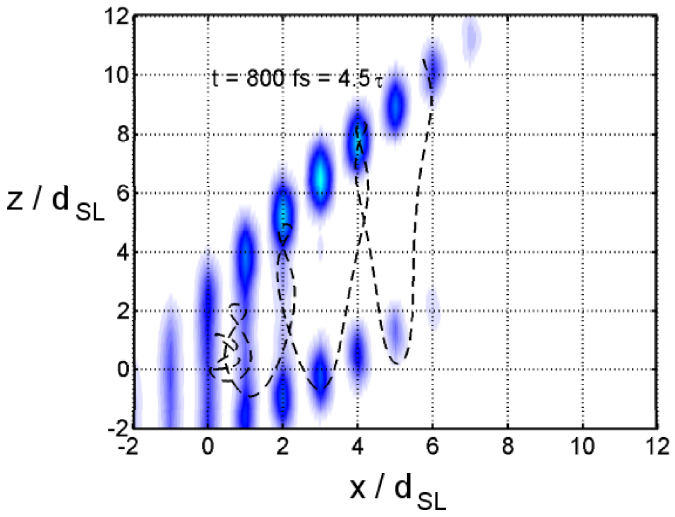

Figure 4.22: Snapshot of the time-evolution of the electron probability distribution in sample NU2293, for $r = 2$, $B = 11$ T and $\theta = 45°$, at time $t = 800$ fs (as in figure 4.20(e)) with the semiclassical path overlaid.

and spatial extent along the x direction between the two.

Figure 4.24 depicts the $r = 1$ resonance of sample NU2299 when $B = 14$ T and $\theta = 30°$. Note that whilst fields of $B = 11$ T tend to be presented for sample NU2293 since the best match between experimental and theoretical results has previously been observed in this regime, fields of $B = 14$ T tend to be studied for sample NU2299 for similar reasons. (As has been discussed previously, adjusting the strength of the magnetic field should, in theory, serve only to alter the scale of the motion.)

Comparison of the quantum mechanical trajectory in figure 4.24(a) with the corresponding semiclassical orbit in figure 4.25 shows that the nature of the path is broadly similar, although the extent of both quantum and semiclassical trajectories differs. Figure 4.25 shows the probability density at time $t = 1334$ fs, illustrating that the motion of the probability density function still follows the semiclassical path in a clearly recognisable way, despite the differing extent of the paths. As stated previously, we will make a detailed comparison between these paths in section 4.3.4.

Considering the sequence of snapshots in figure 4.24, we see that again, as observed in NU2293, the maximum probability density oscillates about the mean position (marked by the dotted arrow and magenta cross respectively in figure 4.24(g)). It can also be seen that for $t \gtrsim 1000$ fs (figures 4.24(g), (h) and (i)) the

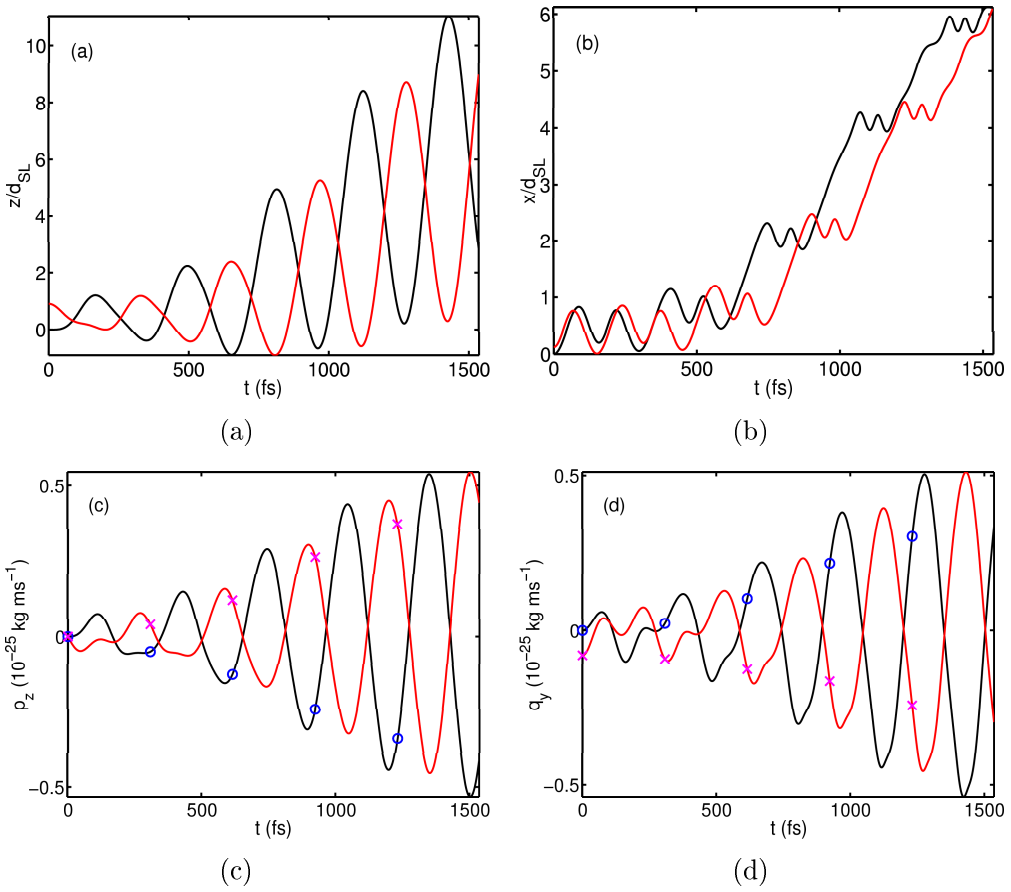

Figure 4.23: Semiclassical plots calculated for different initial conditions when $B = 11$ T, $r = 2$ and $\theta = 45°$ for sample NU2293. Black curves correspond to the original semiclassical case when the initial position and momentum are set to zero. Red curves correspond to an alternative semiclassical trajectory whose initial conditions in real space are encompassed by the quantum mechanical wavepacket, and in phase space lie within the magenta circle in figure 4.21(a). In (a), (b), (c) and (d), values of z, x, p_z and q_y respectively are plotted as a function of time. In (c) and (d), values of p_z and q_y are highlighted at times which are plotted on the stroboscopic Poincaré section. Blue circles relate to the blue arrow in figure 4.21(a), and similarly, magenta crosses relate to the magenta arrow.

wavefunction develops some fragmentation in the z direction as time progresses. This is probably due to the increased B field in the NU2299 studies, since increasing B leads to an increase in the speed of motion in the z direction. This is because the cyclotron radius is proportional to $1/\sqrt{B}$, whilst the time period for cyclotron oscillations is proportional to $1/B$, therefore the mean speed of the electron is proportional to $\sqrt{B}$. This combination of increasing the speed of the motion whilst decreasing the distance travelled (in the z direction) means that the leading edge (along z) of the diffuse wavefunction has already changed direction before the trailing edge has reached the turning point, and thus the wavefunction interferes with itself. If we compare figure 4.24(g) to figure 4.24(b) we see that the overall spread of the wavepacket in the z direction has only increased by a very small amount in figure 4.24(g) despite its seemingly fragmented nature.

Figure 4.26 shows the $r = 2$ resonance of sample NU2299 at $B = 14$ T, $\theta = 45°$. We see from figures 4.26(c) and (d) that the wavefunction splits into two fractions that counter-oscillate in the z direction due to the doubling in the number of radial filaments in phase space, as was the case for the $r = 2$ resonance in NU2293. However, not only is an interference pattern produced when these two fractions pass through one another in the central region of the trajectory (considering the z direction), but interference patterns also develop at the extremes of the z direction as the rapid change in direction of the diffuse fractions leads to self-interference (as discussed previously for NU2299 when $r = 1$ and $\theta = 30°$). Both of these factors lead to the highly fragmented appearance of the probability density in the z direction seen in figures 4.26(e) and (f). Consequently, the amplitude of oscillation observed in the mean position is very low, and at early times is roughly equal to the spread of the probability density function (figure 4.26(b)). Also, the amplitude (in the z direction) of the oscillating wavepacket fractions coincides with the amplitude of the semiclassical path (figure 4.27(a)).

Apart from such effects, however, it is immediately obvious that at later times $\gtrsim 1000$ fs, such as in figure 4.26(f), the almost linear form of the trajectory followed by the expectation value of the wavepacket's position does not have the same form as any of the resonant trajectories considered thus far. Whereas previously the mean position has been located near to the maximum in the probability density, in this case the mean position (magenta crosses in figure 4.26) is located much further along the x direction than the maximum probability density (arrowed in figure 4.26(f)). The major peaks in the probability density remain in the region one would expect for an $r = 2$ resonance in the first miniband, yet

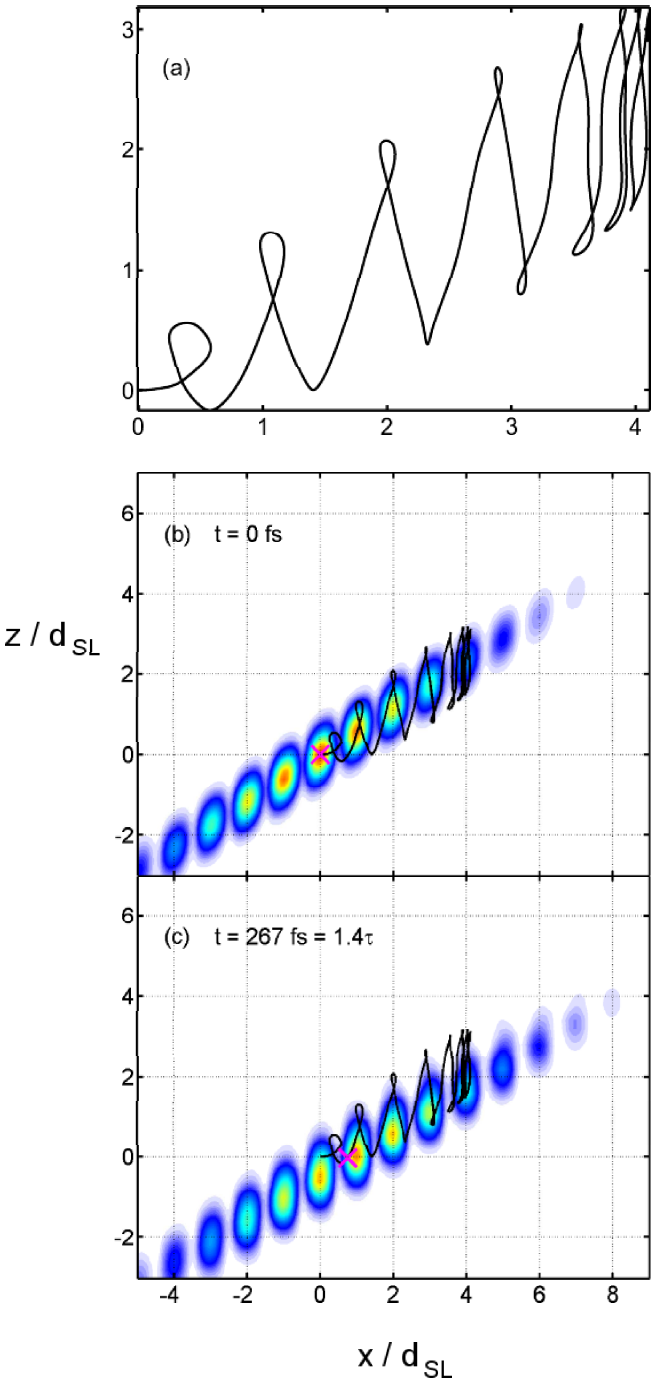

Figure 4.24: Snapshots of the time-evolution of the electron probability distribution in sample NU2299, for $r = 1$, $B = 14$ T and $\theta = 30°$. In (a) the mean trajectory of the electron wavefunction is enlarged. Surface plots of the probability distribution at times (b) $t = 0$ fs, (c) $t = 267$ fs, (d) $t = 533$ fs, (e) $t = 667$ fs, (f) $t = 800$ fs, (g) $t = 1067$ fs, (h) $t = 1334$ fs and (i) $t = 1467$ fs are shown. The mean trajectory is overlaid in black, whilst the magenta cross marks the electron's position on the trajectory at the time corresponding to the current frame.

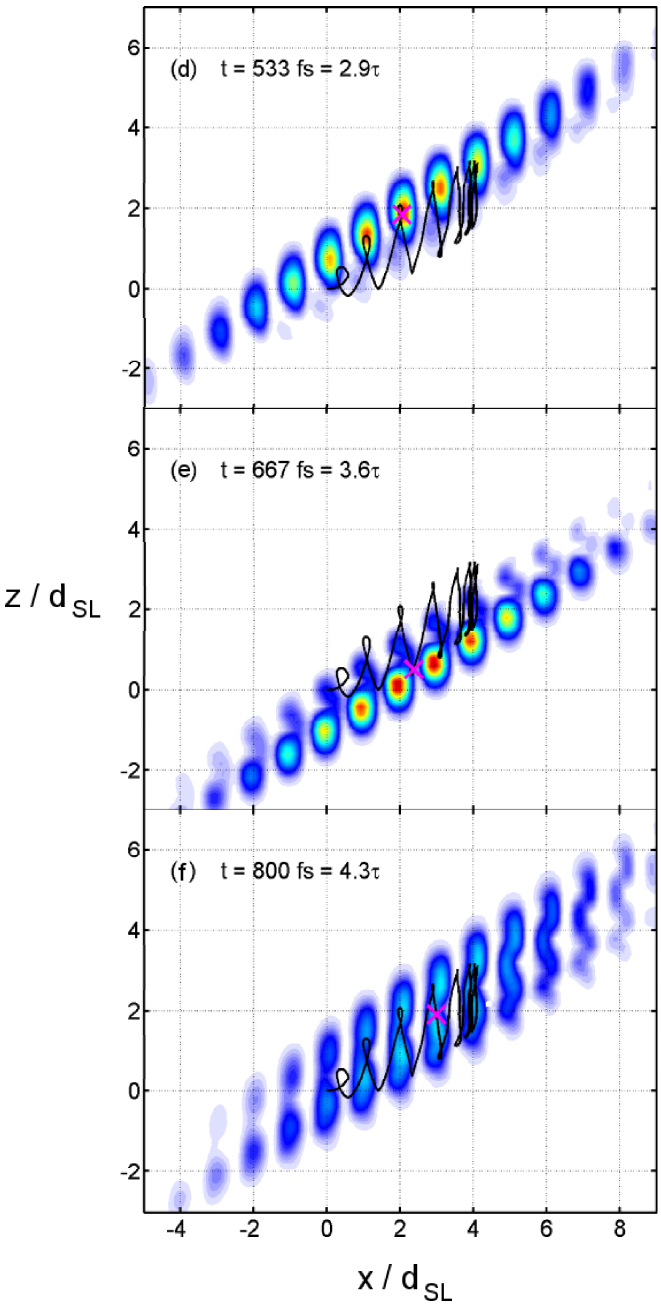

Figure 4.24: Continued.

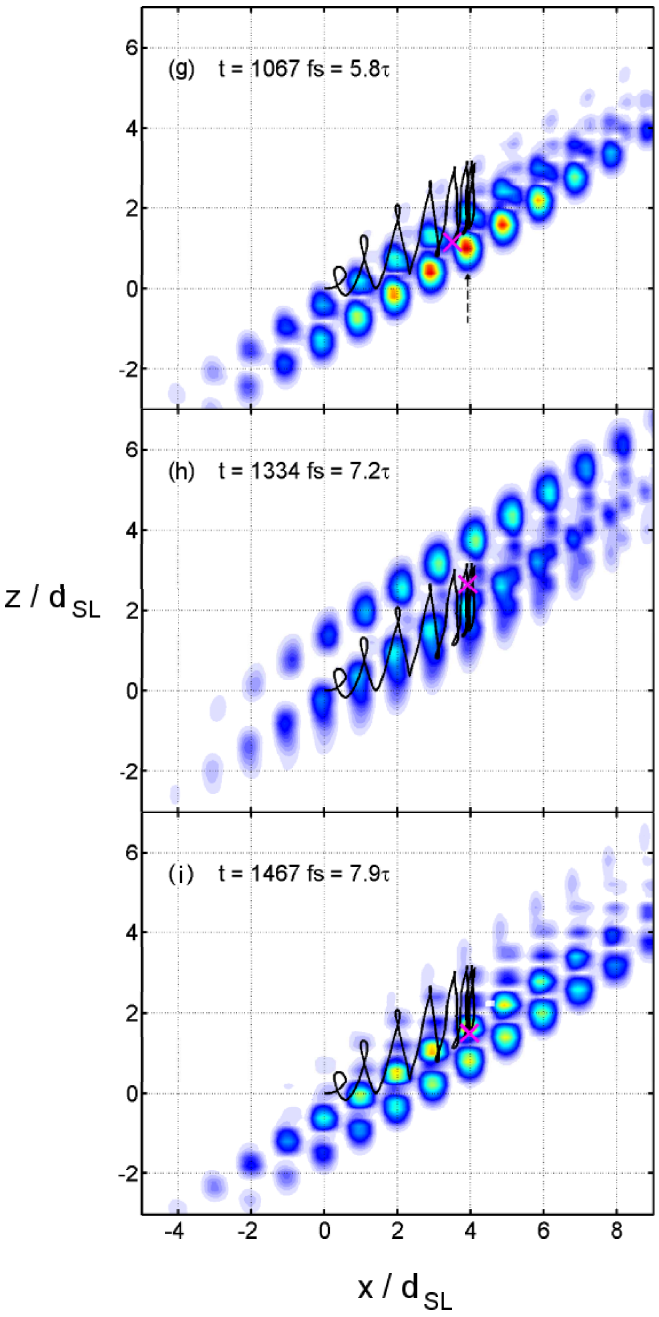

Figure 4.24: Continued.

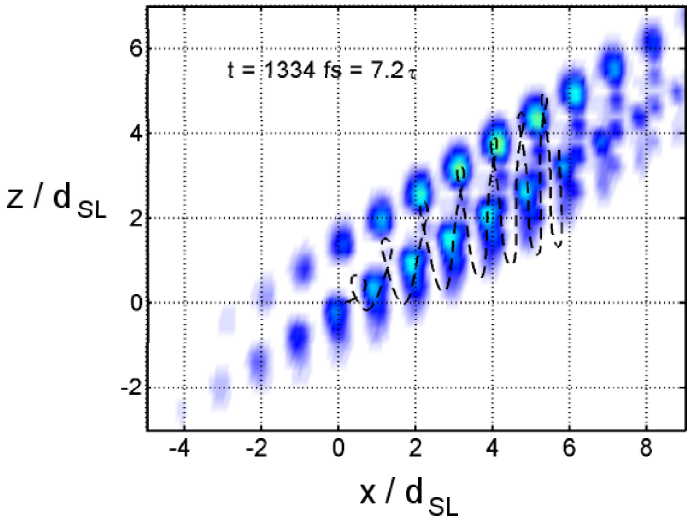

Figure 4.25: Snapshot of the time-evolution of the electron probability distribution in sample NU2299, for $r = 1$, $B = 14$ T and $\theta = 30°$, at time $t = 1334$ fs (as in figure 4.24(h)) with the semiclassical path, starting from rest, overlaid.

the wavefunction is smeared out enormously along the gutter in the positive x direction. We find that this is due to the ability of the wavefunction to tunnel into higher minibands (both second and third). In this case, due to the coincidence of the third band in NU2299 with the top of the potential barriers, the electron becomes effectively free. Tunnelling between minibands in this way will be discussed in greater detail in section 4.3.4. This leads to the straighter portion of the quantum mechanical trajectory (e.g. for $x/d_{SL} \gtrsim 4$ in figure 4.26(f)) which corresponds to the linear motion of a free electron under the action of $\mathbf{F}$ and $\mathbf{B}$). Figure 4.27(b) shows the probability density at $t = 1600$ fs upon axes that extend 3 times further in the positive x and z directions than in figure 4.26 in order to illustrate the extent of this dramatic delocalisation along the direction of the magnetic gutter potential. Some fragments of the wavepacket are moving with constant acceleration due to the electric field, without the hindering effects of the superlattice potential. However, it can be seen by comparing figures 4.26(f), 4.27(a) and 4.27(b), that the peaks in the wavefunction (light blue in figure 4.26(f)) tend to be confined within the extent of the semiclassical trajectory ($x \lesssim 3d_{SL}$ in figure 4.27(a)).

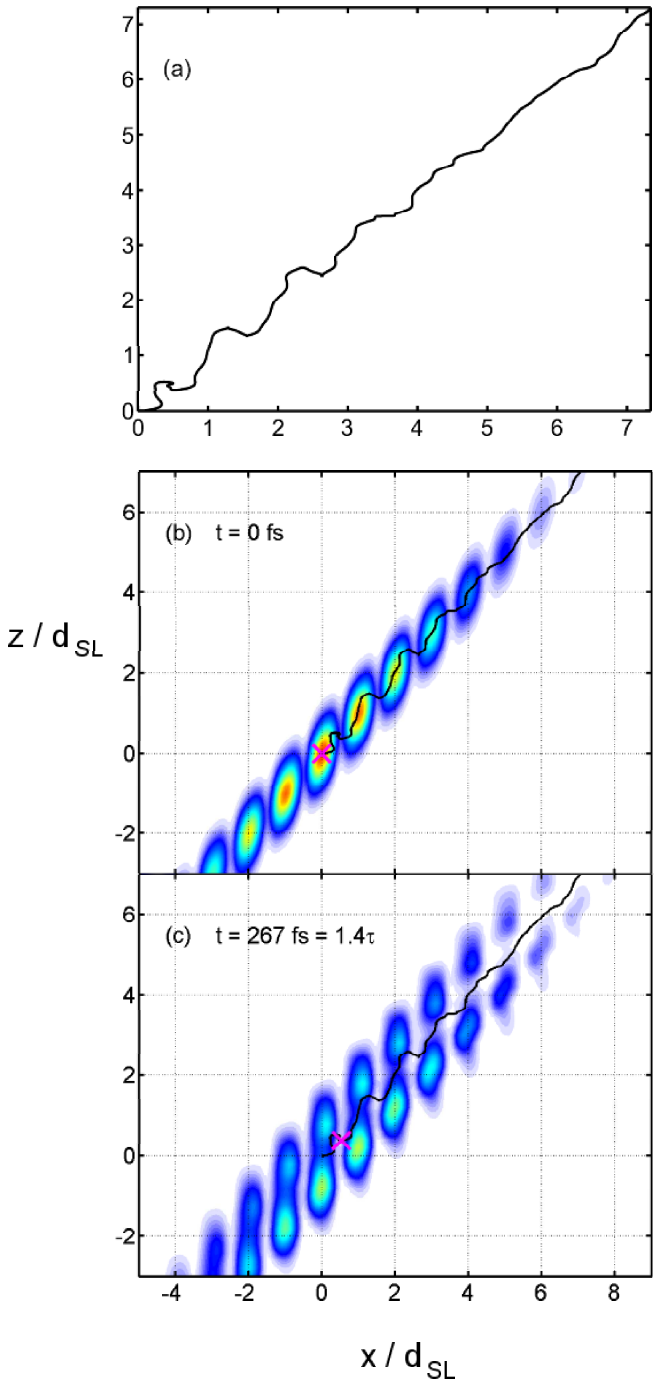

Figure 4.26: Snapshots of the time-evolution of the electron probability distribution in sample NU2299, for $r = 2$, $B = 14$ T and $\theta = 45°$. In (a) the mean trajectory of the electron wavefunction is enlarged. Surface plots of the probability distribution at times (b) $t = 0$ fs, (c) $t = 267$ fs, (d) $t = 533$ fs, (e) $t = 800$ fs and (f) $t = 1067$ fs are shown. The mean trajectory is overlaid in black, whilst the magenta cross marks the electron's position on the trajectory at the time corresponding to the current frame.

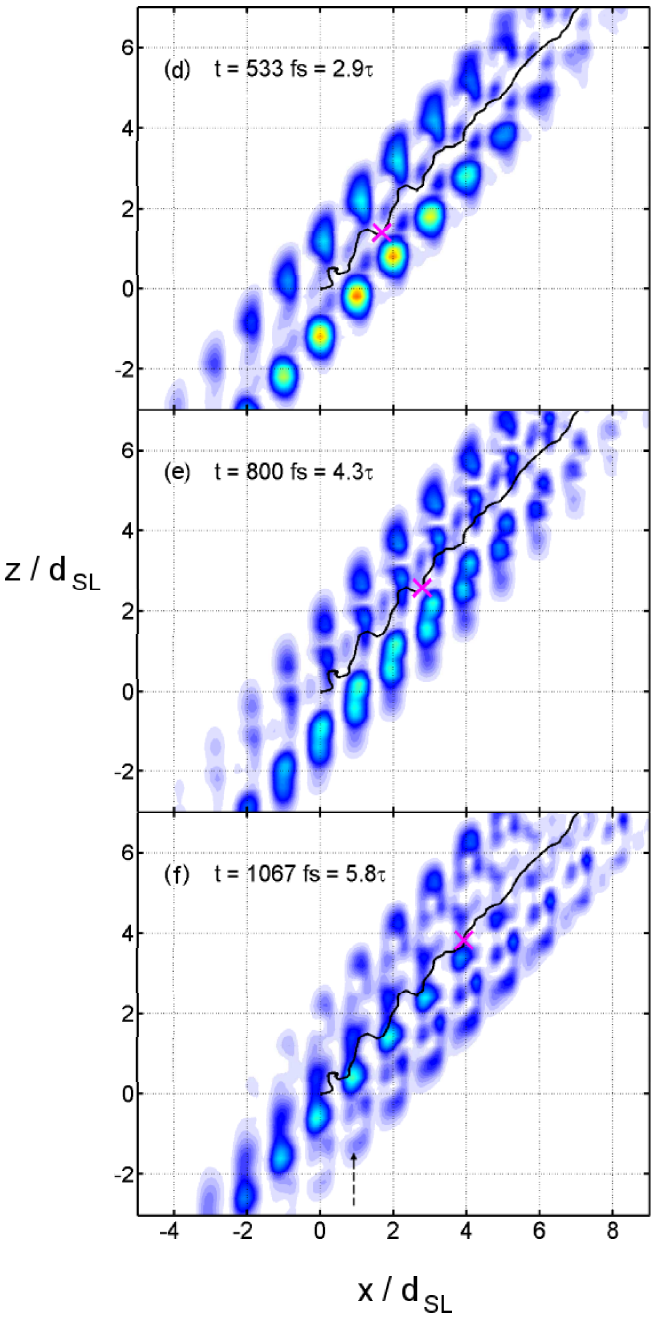

Figure 4.26: Continued.

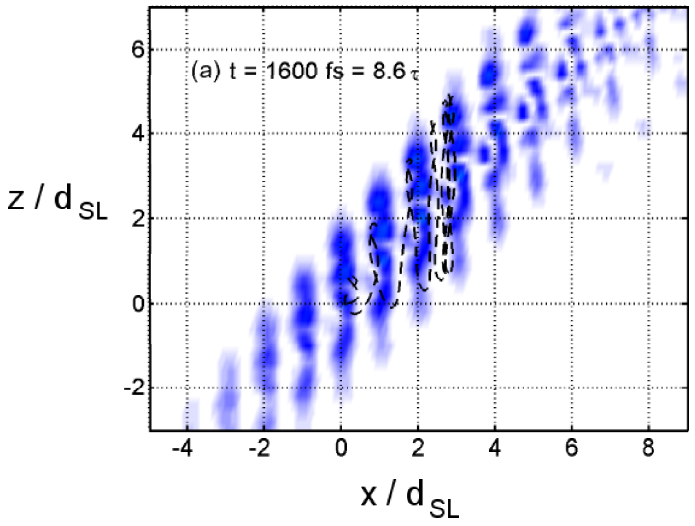

(a)

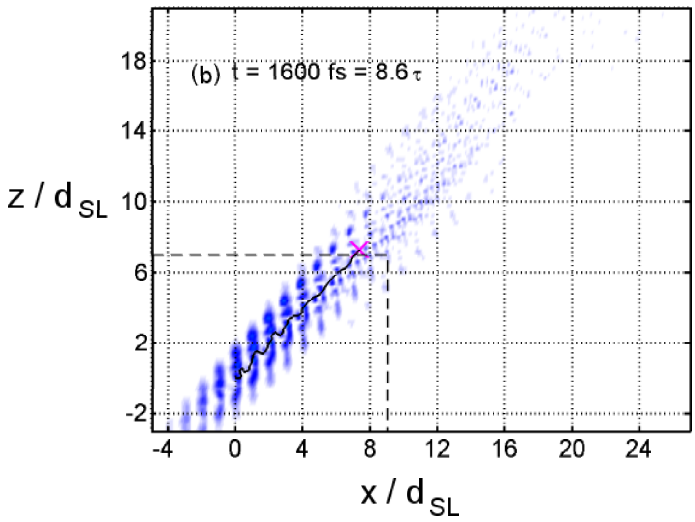

(b)

Figure 4.27: Snapshots of the time-evolution of the electron probability distribution in sample NU2299, for $r = 2$, $B = 14$ T and $\theta = 45°$, at time $t = 1600$ fs. (a) The semiclassical path is overlaid. (b) The x and z axes extend 3 times further than the axes in figure 4.26, which are indicated by the dashed box. The mean quantum mechanical path is overlaid, and the magenta cross marks the expectation value of the electron position at this time.

4.3.3 Wigner functions of the system

As discussed in section 3.3.1, the quantum mechanical analogue of a Poincaré section is the Wigner function. For the system in question in this chapter, the Wigner function is given by

$$W(x,z,p_x,p_z) = \frac{1}{h^2}\int_{-\infty}^{\infty}\int_{-\infty}^{\infty}\Psi^*\left(x+\frac{\lambda_x}{2},z+\frac{\lambda_z}{2}\right)\Psi\left(x-\frac{\lambda_x}{2},z-\frac{\lambda_z}{2}\right) \times e^{-ip_x\lambda_x/\hbar}e^{-ip_z\lambda_z/\hbar}d\lambda_x d\lambda_z. \quad (4.50)$$

Since the Wigner functions are intended to correspond to Poincaré sections in (q_y, p_z), to calculate them we begin by specifying values for $q_y(t)$ and $p_z(t)$ which define a unique point in the phase space plot at some given time t. The other variables of the system can then be determined and the Wigner function at this unique point calculated. We now specify how these variables are determined.

Firstly, $p_x(t)$ is calculated using the following equation (determined earlier and restated here for convenience):

$$p_x(t) = p_x(0) + eFt - (p_z(t) - p_z(0))\tan\theta \quad (4.51)$$

where all terms are known except $p_x(t)$. Secondly, $x(t)$ can be found by rearranging the semiclassical Hamiltonian to give:

$$x(t) = \frac{1}{eF}\left(E(p_x) + \left(\frac{q_y^2(t)+p_z^2(t)}{2m^*}\right) - H\right) \quad (4.52)$$

where the value of H is determined by calculating the expectation value of the total energy of the wavefunction at $t=0$, $\langle E\rangle$:

$$\langle E\rangle = \int_{-\infty}^{\infty}\int_{-\infty}^{\infty}\Psi^* H\Psi dx dz. \quad (4.53)$$

Finally, $z(t)$ is given by

$$z(t) = \frac{1}{\cos\theta}\left(-\frac{q_y(t)}{eB} + x(t)\sin\theta\right), \quad (4.54)$$

which is again a simple rearrangement of equation (4.6).

Generating a Wigner distribution in this way leads to a snapshot of the probability distribution in phase space at time t. If such Wigner functions are gen-

erated at times separated by $2\pi/\omega_{||}$ (in the same way that points were added to the Poincaré sections by sampling at regularly spaced times) the set of Wigner functions (or their time average) should reveal some semblance of the web in the quantum mechanical phase space. In the following figures, we plot the normalised modulus, $|W|$, since the sign of the function in this case is irrelevant [6].

Figure 4.28 shows the quantum mechanical phase space of NU2299 when $r = 1$, $B = 14$ T and $\theta = 30°$, with the corresponding semiclassical Poincaré section overlaid. The corresponding real space evolution of the wavefunction was previously shown in figure 4.24. Figure 4.28(a) is the initial distribution of the wavefunction in momentum space, and figures 4.28(b), (c) and (d) are sampled at times $t = 2\pi/\omega_{||}$, $4\pi/\omega_{||}$ and $6\pi/\omega_{||}$ respectively. The parameters are the same as for figure 4.24 but the timescales are necessarily different. It is clear from figure 4.28(a) that the bulk of the wavefunction initially occupies stable regions of the phase space, and this is reflected in the later figures, which show that the Wigner function of the system spreads out in phase space but remains bounded by the first ring of the stochastic web. Note that the Wigner function does indeed appear to travel along the vertical filament (figure 4.28(b)), as predicted when $r = 1$ in the previous section, before looping around a cell of the web towards the "return" section of the filament (figures 4.28(c) and (d)).

Similarly, figures 4.29 and 4.30 show the same system but for tilt angles of $\theta = 45°$ and $\theta = 60°$ respectively. The corresponding real space wavefunctions are not presented since, due to the vast parameter space considered in this chapter, we are limited to a selection of the most interesting results. Again, the Wigner function remains bounded by the first ring of the web. Also notice how in figure 4.30, since the majority of the initial wavefunction occupies the chaotic sea in phase space, the Wigner function tends to avoid the stable islands within that sea.

Figures 4.31 and 4.32 relate to simulations where the initial wavefunction was defined such that the initial Wigner functions were located away from the radial filaments of the stochastic web. This was done with the hope of observing the Wigner function traversing the ring and then diffusing along a radial filament of the web. The $r = 1$ resonance of NU2299 at $B = 14$ T, $\theta = 30°$ was chosen for this test since the phase space is less complex than for higher order resonances or tilt angles. The approximate position and extent of the initial Wigner functions are shown by a magenta ring in figures 4.31(a) and 4.32(a). Figures 4.31(a), (b), (c) and (d) were sampled at times $t = 4\pi/\omega_{||}$, $6\pi/\omega_{||}$, $8\pi/\omega_{||}$ and $18\pi/\omega_{||}$. In

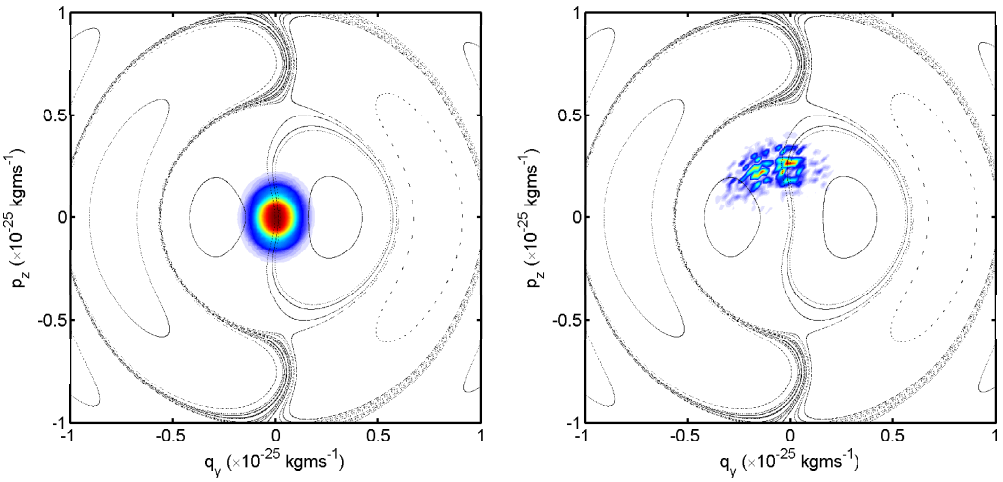

(a) $t = 0$ fs (b) $t = 2\pi/\omega_{||} = 198$ fs

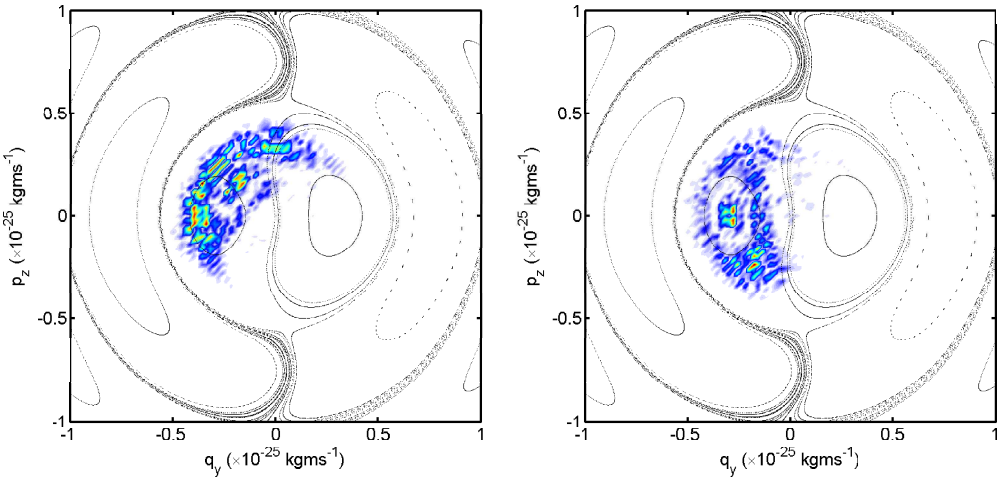

(c) $t = 4\pi/\omega_{||} = 395$ fs (d) $t = 6\pi/\omega_{||} = 593$ fs

Figure 4.28: Surface plots of the modulus of the Wigner function, calculated at stroboscopic times during the evolution of the electron wavefunction in sample NU2299 for $r = 1$, $B = 14$ T and $\theta = 30°$. Corresponding semiclassical stroboscopic Poincaré sections are overlaid.

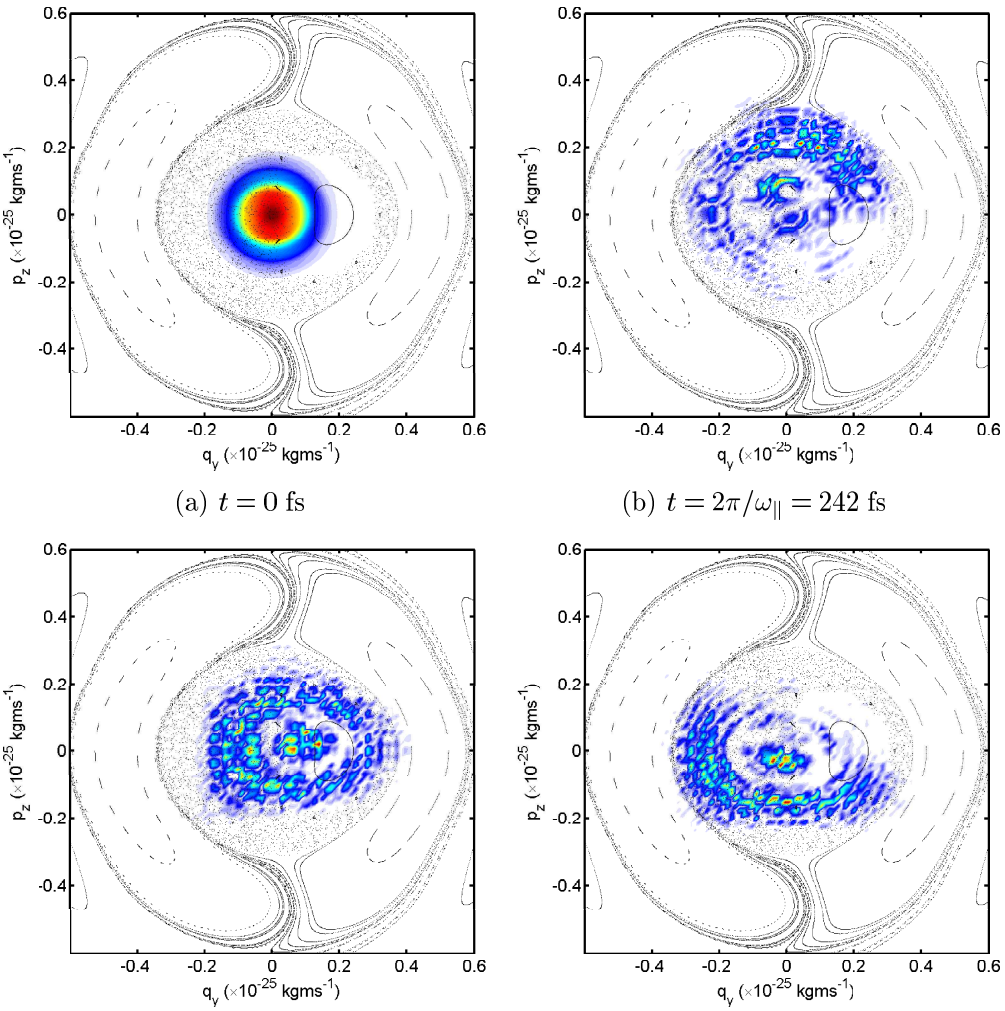

(a) $t = 0$ fs (b) $t = 2\pi/\omega_{||} = 242$ fs

(c) $t = 4\pi/\omega_{||} = 484$ fs (d) $t = 6\pi/\omega_{||} = 726$ fs

Figure 4.29: Surface plots of the modulus of the Wigner function, calculated at stroboscopic times during the evolution of the electron wavefunction in sample NU2299 for $r = 1$, $B = 14$ T and $\theta = 45°$. Corresponding semiclassical stroboscopic Poincaré sections are overlaid.

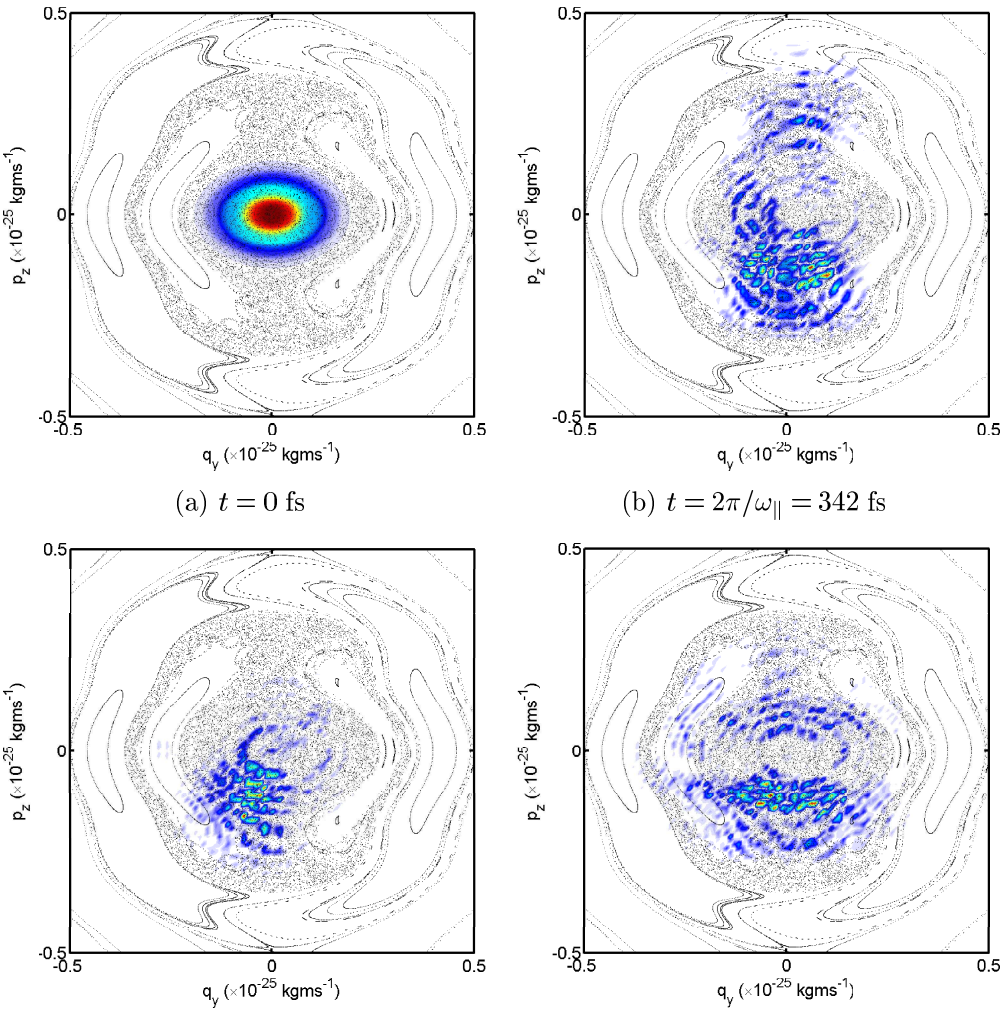

(a) $t = 0$ fs (b) $t = 2\pi/\omega_{||} = 342$ fs

(c) $t = 4\pi/\omega_{||} = 685$ fs (d) $t = 6\pi/\omega_{||} = 1027$ fs

Figure 4.30: Surface plots of the modulus of the Wigner function, calculated at stroboscopic times during the evolution of the electron wavefunction in sample NU2299 for $r = 1$, $B = 14$ T and $\theta = 60°$. Corresponding semiclassical stroboscopic Poincaré sections are overlaid.

this case, a large fraction of the Wigner function can be seen to diffuse outwards along the almost vertical radial web filament in 4.31(a) and (b), leaving behind any fractions that initially occupied areas of the stable central phase space within the first ring in 4.31(c). These fractions remain bounded indefinitely, as shown in 4.31(d).

Figures 4.32(a)-(f) were sampled at times $t = 2\pi/\omega_{||}$, $6\pi/\omega_{||}$, $8\pi/\omega_{||}$, $t = 10\pi/\omega_{||}$, $16\pi/\omega_{||}$ and $20\pi/\omega_{||}$. In this case, the Wigner function can be seen spreading around the first ring of the web in 4.32(a), and up the web filament in 4.32(b). However, rather than continue diffusing along the filament as in figure 4.31, the Wigner function is observed to continue orbiting both the first and second rings of the stochastic web, looping around the D-shaped cells of the web, as indicated by the "hotspots" of light blue and red. Although there are fractions of the Wigner function that occupy stable orbits (shown by the darker blue areas that are localised within the cells of the web), it is clear in 4.32(c), (e) and (f) that there are regions of high density localised around the rings of the semiclassical Poincaré section.

It was originally intended to calculate time-averaged Wigner functions. However, Gardiner [46] and Korsch [47] recommend that a minimum of approximately 100 periods be sampled in order to generate a time-averaged Wigner function. This presents difficulties for the superlattice systems for two reasons. Firstly, due to the discontinuities in the superlattice potential, it would take months of computing time to model the system with sufficient accuracy. Only ten stroboscopic periods were calculated for each set of results presented in this section, and since the period is given by

$$\frac{2\pi}{\omega_{||}} = \frac{2\pi m^*}{eB\cos\theta} \tag{4.55}$$

this equates to periods of 198 fs, 242 fs and 342 fs for figures 4.28 to 4.30 respectively. Given that the trajectories presented previously took place over times of just 1600 fs, it is clear that predicting the evolution of the wavefunctions needed for just 10 stroboscopic Wigner functions is a substantial challenge, whilst calculation of 100 periods is simply not feasible with currently available computing speeds. Indeed, only Wigner functions of sample NU2299 are presented here for that reason: the times required to model the more complicated superlattice potential of the NU2293 sample are unfeasibly long.

Furthermore, and more crucially, the very nature of the phase space we wish to investigate, namely the stochastic web, is unbounded. Thus, it is implicit

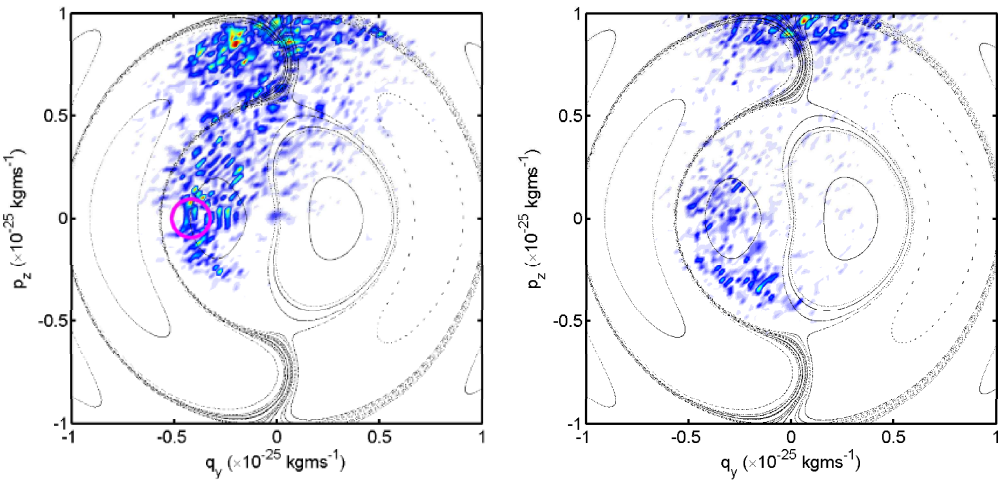

(a) $t = 4\pi/\omega_{||} = 395$ fs (b) $t = 6\pi/\omega_{||} = 593$ fs

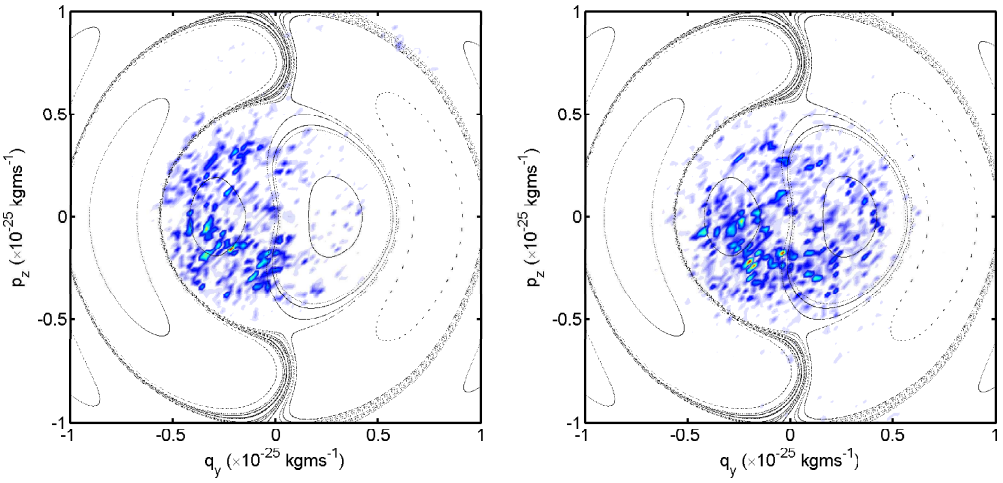

(c) $t = 8\pi/\omega_{||} = 791$ fs (d) $t = 18\pi/\omega_{||} = 1779$ fs

Figure 4.31: Surface plots of the modulus of the Wigner function, calculated at stroboscopic times during the evolution of the electron wavefunction in sample NU2299 for $r = 1$, $B = 14$ T and $\theta = 30°$. Corresponding semiclassical stroboscopic Poincaré sections are overlaid. The initial Wigner function of the system was localised within the area bounded by the magenta curve in (a), close to the first ring of the semiclassical Poincaré section, and away from the web filaments.

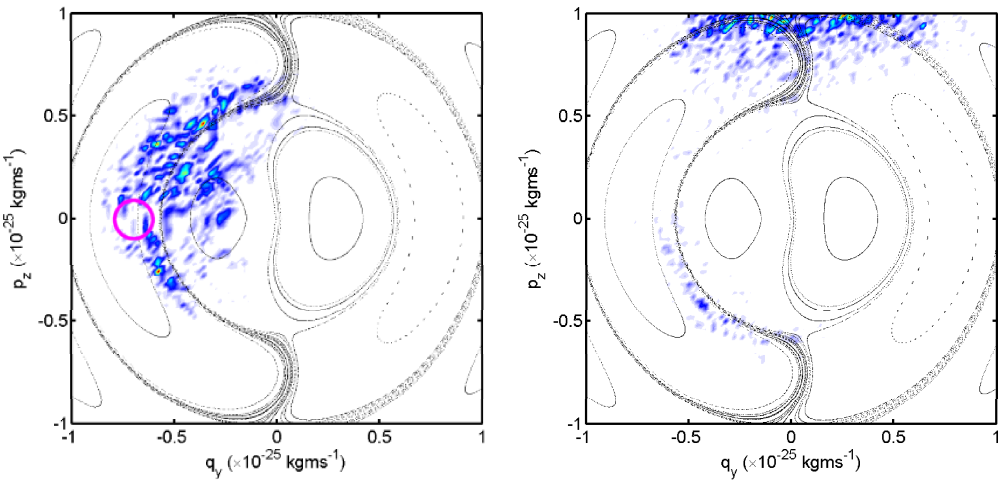

(a) $t = 2\pi/\omega_{||} = 395$ fs (b) $t = 6\pi/\omega_{||} = 593$ fs

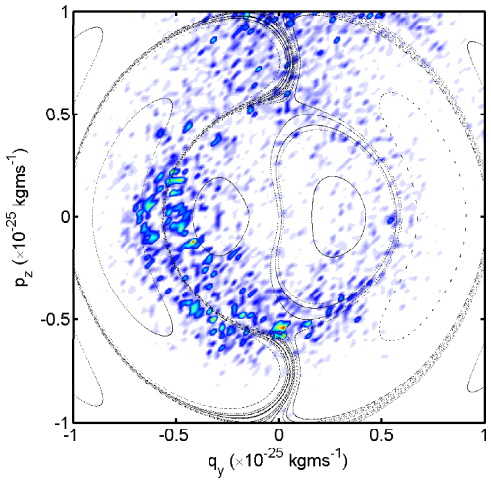

(c) $t = 8\pi/\omega_{||} = 791$ fs

Figure 4.32: Surface plots of the modulus of the Wigner function, calculated at stroboscopic times during the evolution of the electron wavefunction in sample NU2299 for $r = 1$, $B = 14$ T and $\theta = 30°$. Corresponding semiclassical stroboscopic Poincaré sections are overlaid. The initial Wigner function of the system was localised within the area bounded by the magenta curve in (a), close to the first ring of the semiclassical Poincaré section, and away from the web filaments.

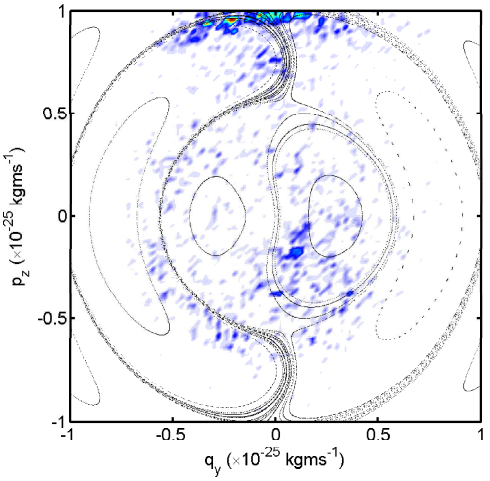

(d) $t = 10\pi/\omega_{||} = 981$ fs

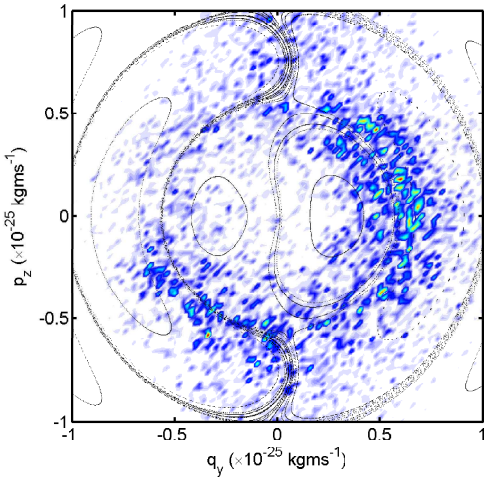

(e) $t = 16\pi/\omega_{||} = 1582$ fs

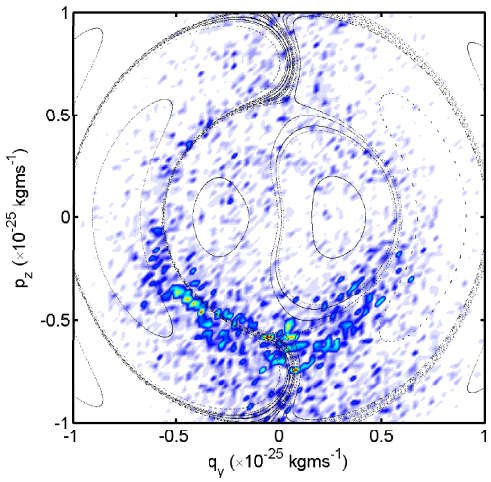

(f) $t = 20\pi/\omega_{||} = 1977$ fs

Figure 4.32: Continued.

that the longer the time simulated, the further the electron would be expected to diffuse along the web in that time, whereas an effective averaging technique relies upon the motion being periodic and repetitive. In particular, because Wigner functions are so time-consuming to calculate numerically, only a limited region of phase space may be examined, and by late times the electron has diffused beyond this region. Also, the nature of quantum mechanics means that it is impossible to define some initial wavepacket that lies either only on the web or entirely within the bounded cells - Heisenberg's uncertainty principle forbids such explicit knowledge of a system.

We have, however, shown that the evolution of the Wigner function in phase space corresponds closely to the motion of the quantum mechanical wavepacket calculated for when $\theta = 30°$, $B = 14$ T and $r = 1$ for NU2299. Note that only the $r = 1$ regime has been considered, where interminiband tunnelling is negligible, so that the single miniband Hamiltonian and Poincaré sections apply. We have also demonstrated that these new and interesting features of the Wigner function agree well with the Poincaré sections predicted at various tilt angles in the semiclassical case.

4.3.4 Quantum calculations of the drift velocity

In the quantum regime, the drift velocity of the electron is calculated by differentiating $\langle x \rangle$ with respect to time to determine $\langle v_x \rangle$, and then using

$$v_d = \int_0^\infty \langle v_x(t) \rangle P(t)\, dt. \tag{4.56}$$

where $P(t)\, dt$ is the probability that an electron is scattered in time dt. If the Esaki-Tsu model is applied, $P(t)$ is given by

$$P(t) = \frac{1}{\tau} e^{-t/\tau}, \tag{4.57}$$

where the scattering times for each sample were determined in section 4.2.3. Figure 4.33 shows the drift velocity field curves for sample NU2293, calculated from the quantum mechanical model of the electron motion for $B = 8$ T (a), 11 T (b) and 14 T (c) respectively. A cascade of plots for angles $\theta = 0 - 75°$ is shown for each magnetic field strength. The positions of resonances due to stochastic web formation in phase space are highlighted. Visual comparison of these plots

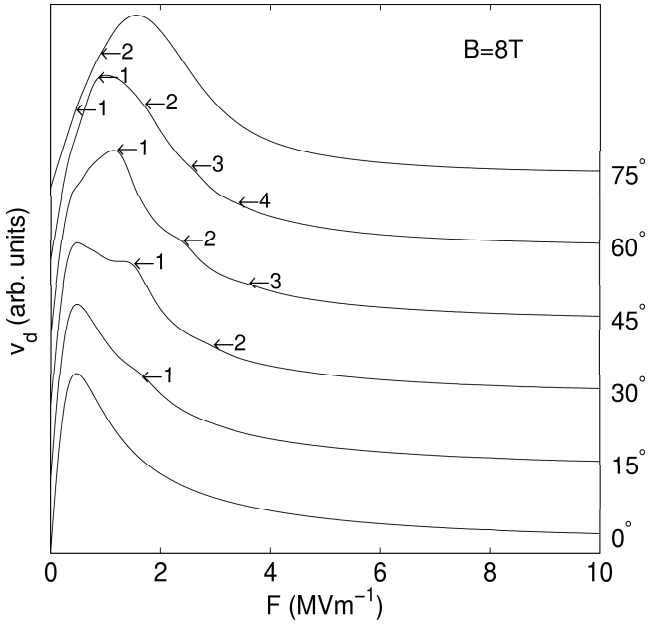

Figure 4.33: (a) Cascade plot of the drift velocity versus electric field relationship, numerically calculated using a quantum mechanical model, for sample NU2293 when $\theta = 0°$-$75°$ and $B = 8$ T. Similar plots are shown for (b) $B = 11$ T and (c) $B = 14$ T. The locations of a number of predicted resonance peaks are highlighted with arrows and corresponding r values.

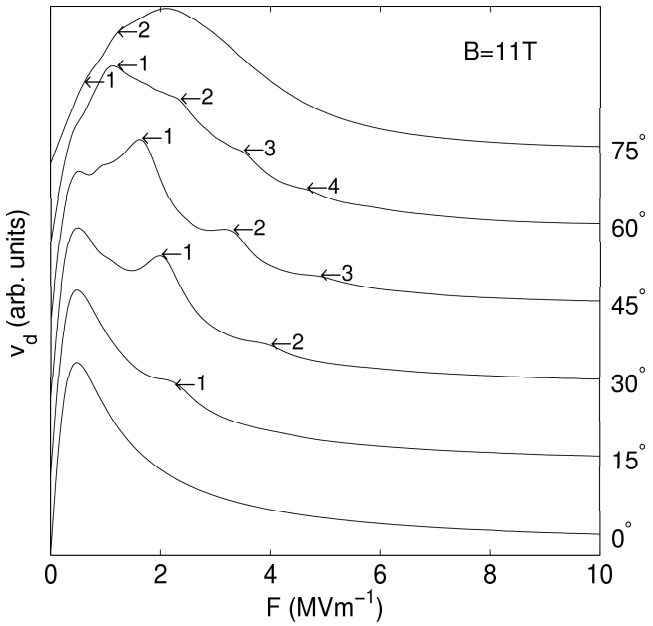

Figure 4.33: (b) Sample NU2293 when $B = 11$ T.

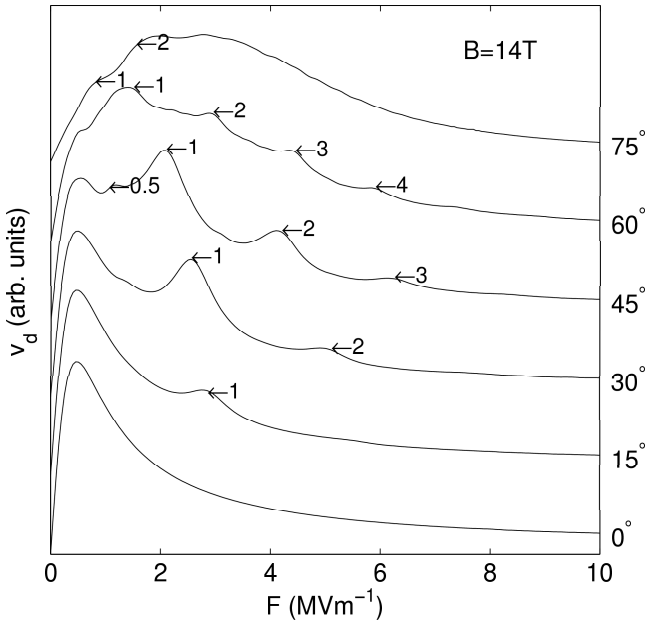

Figure 4.33: (c) Sample NU2293 when $B = 14$ T.

with the semiclassical curves presented earlier (figure 4.12) shows good general agreement.

Higher order resonances tend to appear more prominently in calculations of the quantum mechanical drift velocity compared with the semiclassical model (the quantum mechanical and semiclassical drift velocity curves will be compared in more detail later in this section). This may be because the exact initial conditions defined for a semiclassical electron may not coincide precisely with a web filament, so the resonance would not be observed strongly. However, a range of initial conditions are implicit in the quantum mechanical model, some of which may lie on a more favourable point for traversal of the filaments in phase space and observation of a resonance in the electron trajectory.

Figure 4.34 shows similar cascade plots of drift velocity versus electric field for sample NU2299. Once more, good agreement with the semiclassical model (figure 4.13) is seen at low values of electric field, and resonant peaks are clearly apparent. However, for electric fields $\gtrsim 2$ MVm^{-1}, a number of additional peaks can be seen in the quantum calculations that do not correspond with the semiclassical curves. These peaks are particularly pronounced at $\theta = 0°$, when no resonant peaks occur in a semiclassical picture, which produces the Esaki-Tsu $v_d(F)$ curve discussed previously. These additional peaks arise due to tunnelling, and will be now be explained in further detail.

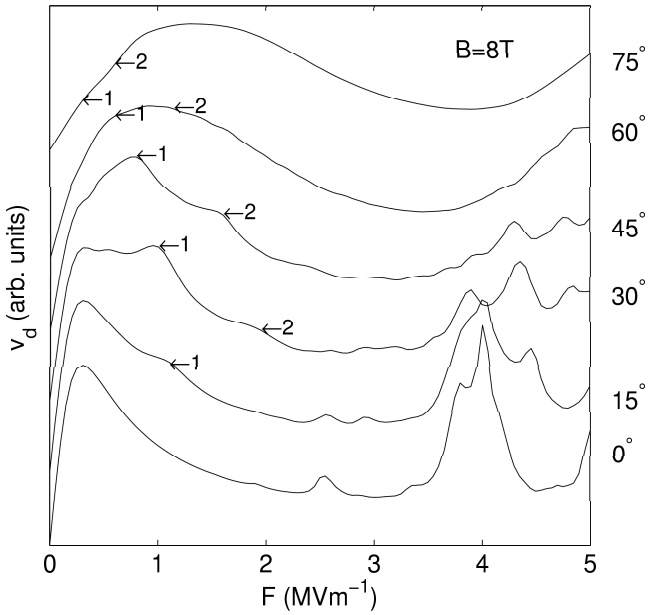

Figure 4.34: (a) Cascade plot of the drift velocity versus electric field relationship, numerically calculated using a quantum mechanical model, for sample NU2299 when $\theta = 0°$-$75°$ and $B = 8$ T. Similar plots are shown for (b) $B = 11$ T and (c) $B = 14$ T. The locations of a number of predicted resonance peaks are highlighted with arrows and corresponding r values.

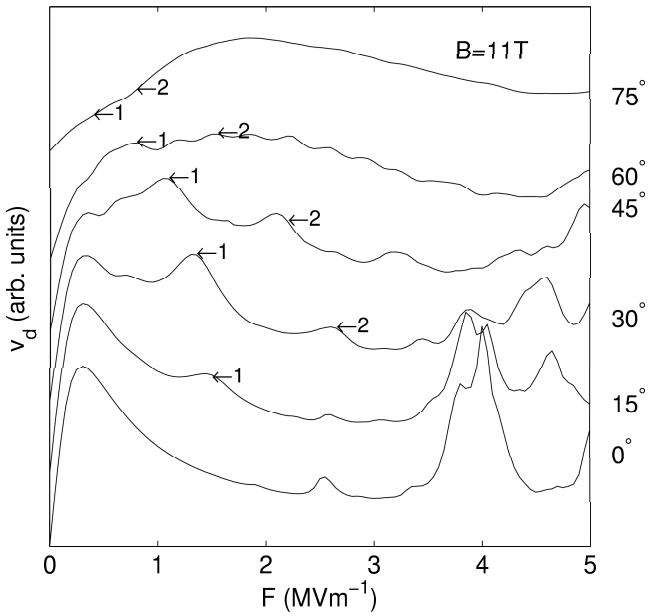

Figure 4.34: (b) Sample NU2299 when $B = 11$ T.

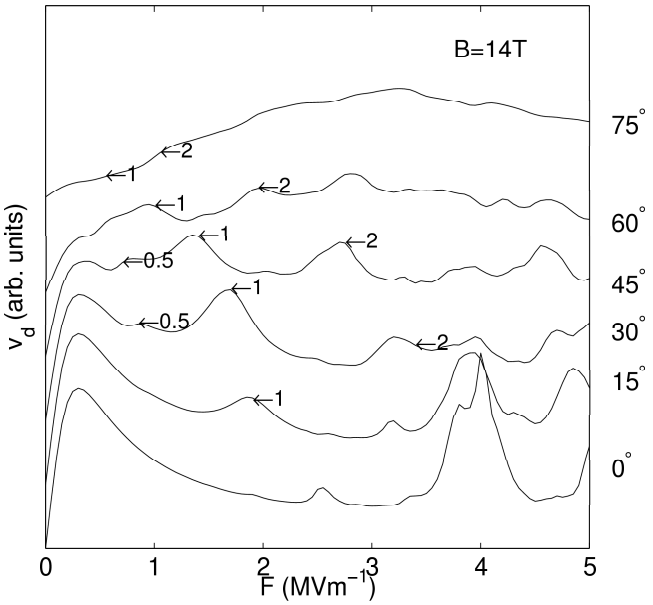

Figure 4.34: (c) Sample NU2299 when $B = 14$ T.

Discussion of the peaks due to tunnelling

When considering a biased superlattice, we imagine the superlattice potential to be tilted by the applied electric field, as illustrated in figure 4.35(a). For high values of electric field, the angle by which the superlattice potential is tilted becomes so great that the miniband transport picture breaks down. In this case we represent the superlattice potential as a series of quantum wells, whose energy levels coincide roughly with the energies of the former minibands. As the bias field increases and the superlattice potential is tilted further, a low energy level (level A, say) in the qth well might line with a level of higher energy (level B) in another well, the $(q+n)$th well say. Similarly, this would result in alignment of the same levels in wells $(q+1)$ and $(q+n+1)$, and so on. Alignment of the energy levels in this way would lead to some finite possibility of tunnelling between the two. The probability of such an event occurring would depend on the separation of the two wells, i.e. the distance nd_{SL}.

If the bias was further increased, eventually level A in well q would line up with level B in well $(q+n-1)$, with a separation of $(n-1)d_{SL}$ between the two levels, thus increasing the probability of tunnelling from level A to level B. This tilting process could be continued until levels A and B in wells q and $q+1$ were aligned (figure 4.35(b)), with the greatest probability of tunnelling between them. A diagram illustrating this idea schematically is shown in figures 4.35(a) and (b).

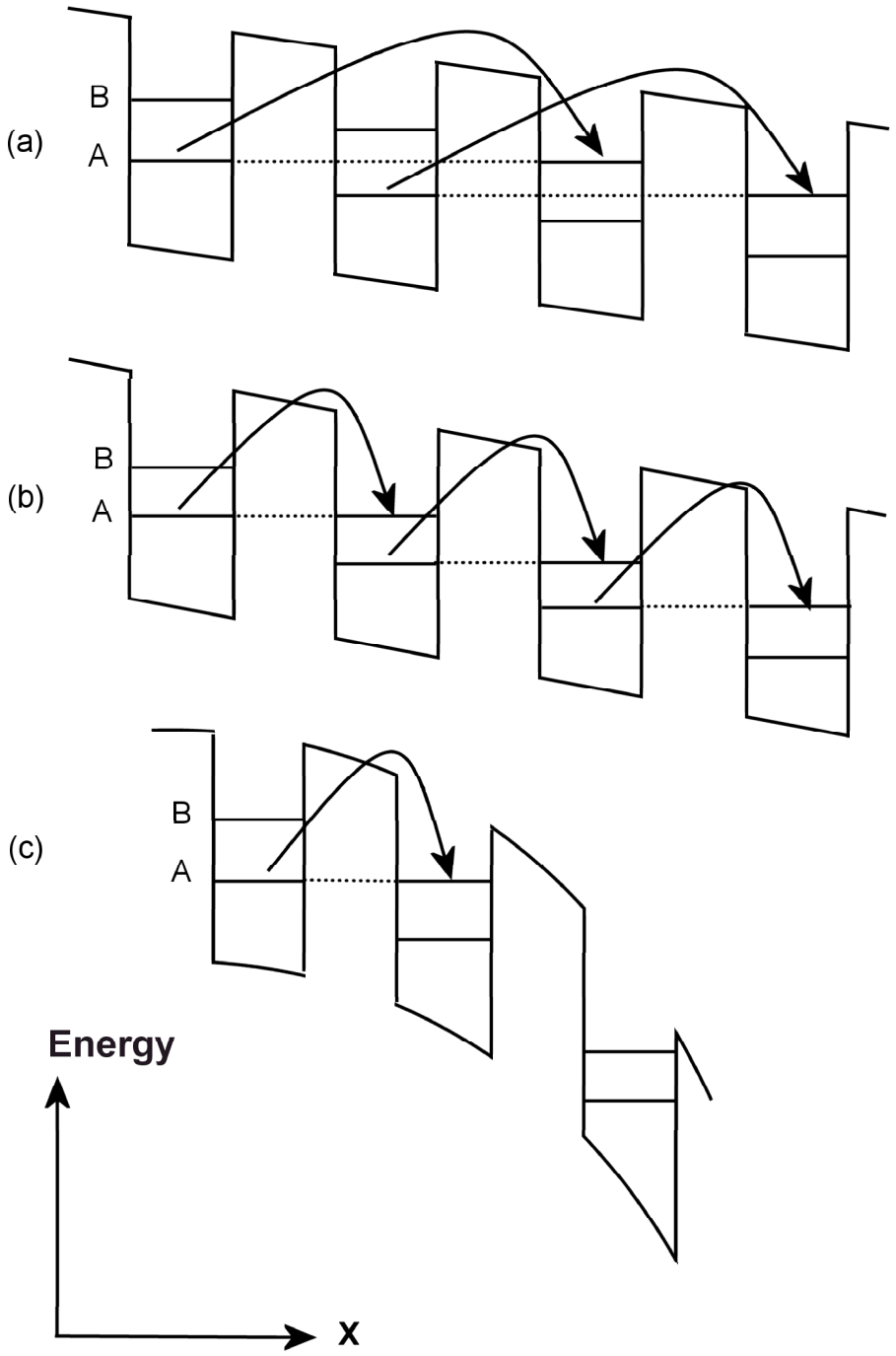

Figure 4.35: Effect of an applied electric field on the superlattice potential. (a) Applied electric field leads to the possibility of tunnelling between levels A and B in many *non-adjacent* wells ($n = 2$). (b) Increasing the strength of the applied field leads to possibilities of tunnelling between levels A and B in many *adjacent* wells ($n = 1$) in the superlattice potential. (c) In experiment, the applied electric field is non-linear at high field strengths, therefore the possibility of tunnelling between many wells simultaneously is eliminated.

Tunnelling from levels 1 to 2		Tunnelling from levels 1 to 3	
n	$F_n^{A,B}$ (MVm^{-1})	n	$F_n^{A,B}$ (MVm^{-1})
1	$F_1^{1,2} = 7.72$	3	$F_3^{1,3} = 6.80$
2	$F_2^{1,2} = 3.86$	4	$F_4^{1,3} = 5.10$
3	$F_3^{1,2} = 2.57$	5	$F_5^{1,3} = 4.08$
4	$F_4^{1,2} = 1.93$	6	$F_6^{1,3} = 3.40$

Table 4.4: Electric field strengths at which tunnelling between energy levels in wells separated by nd_{SL} is predicted.

A detailed description of such models of tunnelling in superlattice structures may be found in [63, 64].

In this description, whenever any two levels become aligned in a pair of wells, due to the linear nature of the electric field potential, the same two levels become aligned in many pairs of wells, leading to a theoretical possibility of many tunnelling events taking place simultaneously. However, in real experiments at high electric field strengths, the field becomes non-linear due to charge build-up effects. Thus, whilst levels may become aligned, it is usually only one pair of levels that line up (as shown in figure 4.35(c)) rather than a whole cascade of levels.

However, if the electric field is spatially uniform, the condition for levels A and B, in wells separated by a distance nd_{SL}, to be aligned is that the electric field satisfies:

$$F_n^{A,B} = \frac{E_B - E_A}{ned_{SL}} \tag{4.58}$$

where E_A and E_B are the energies of levels A and B. Table 4.4 lists field strengths satisfying equation (4.58) for tunnelling between the first and second levels and the first and third levels in sample NU2299. For each of these conditions, a peak is observed in the drift velocity field curve at $\theta = 0°$, as shown by the arrows in figure 4.36. The blue arrows highlight peaks where tunnelling between levels one and two takes place, and the red arrows correspond to tunnelling between levels one and three.

Peaks due to tunnelling are not present in quantum mechanical calculations for sample NU2293 due to the substantially larger minbandgaps (approximately three times larger than in NU2299) in the miniband structure of this superlattice

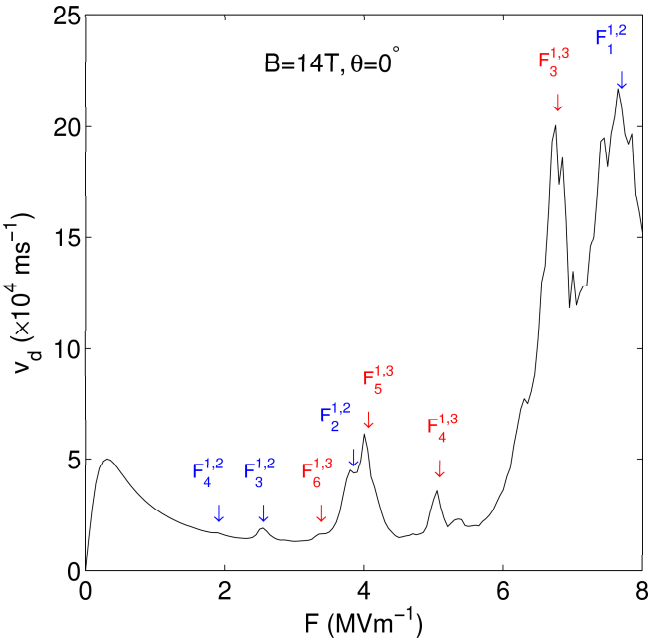

Figure 4.36: Drift velocity field curve for sample $NU2299$ when $B = 14$ T and $\theta = 0°$. Blue arrows indicate the fields at which table 4.4 predicts tunnelling between the first and second energy levels in quantum wells separated by a distance nd_{SL}, whilst red arrows predict tunnelling between levels one and three.

sample. The amplitude of the peaks seen in NU2299 is so great because of the tendency for levels in many wells to align simultaneously when F is uniform. Thus, when tunnelling events occur, they occur repeatedly creating an avalanche of probability density sweeping across the superlattice barriers in the next energy level. As the separation between aligned levels decreases (i.e. n decreases, and F increases) the probability of tunnelling events taking place increases as predicted, and the peaks increase in amplitude with increasing F. The only exception to this is the $n = 5$ tunnelling peak at $F \approx 4\,\mathrm{MVm}^{-1}$ (between levels one and three), whose amplitude is reinforced due to the overlap with the $n = 2$ peak relating to levels one and two. Note that the higher field strength associated with decreasing n also increases the probability of tunnelling by effectively pushing the electrons harder through the superlattice potential.

Rearranging equation (4.58) shows that the frequency with which the tunnelling peaks occur is inversely proportional to the electric field strength:

$$n = \frac{E_B - E_A}{eFd_{SL}}. \tag{4.59}$$

Therefore, peaks due to tunnelling between two given levels are periodic in $1/F$.

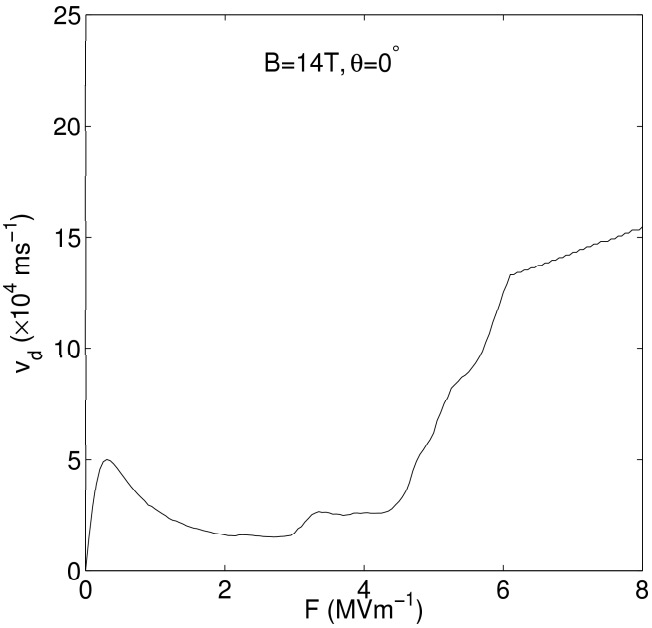

Figure 4.37: Smoothed drift velocity field curve for sample $NU2299$ when $B = 14$ T and $\theta = 0°$. Smoothing has been performed over the period in $1/F$ of first-to-second level tunnelling.

Hence, a plot of drift velocity as a function of $1/F$ can be smoothed over a range equal to the periodicity of the peaks in order to suppress these inter-level transition peaks, as occurs in a real device due to the strong spatial variation of F. Figure 4.37 shows the drift velocity field curve after smoothing over the period of the first to second level peaks in $1/F$, and figure 4.38 has been smoothed again over the period of the first to third level peaks. The smoothing process yields a plot much more like the smoothly rising background that is observed in experimental current-voltage measurements.

It is worth noting that the small minibandgaps seen in sample NU2299 are in fact desirable in experiments. The fact that they lead to increased tunnelling is thought to reduce the level of charge build up in the structure, increasing the amplitude of the resonant peaks due to stochastic web formation and thereby making them easier to identify than in NU2293.

Comparison of quantum mechanical and semiclassical drift velocity field curves

Figure 4.39 shows quantum mechanical drift velocity field curves (red) on the same axes as the corresponding semiclassical calculations (black) for sample

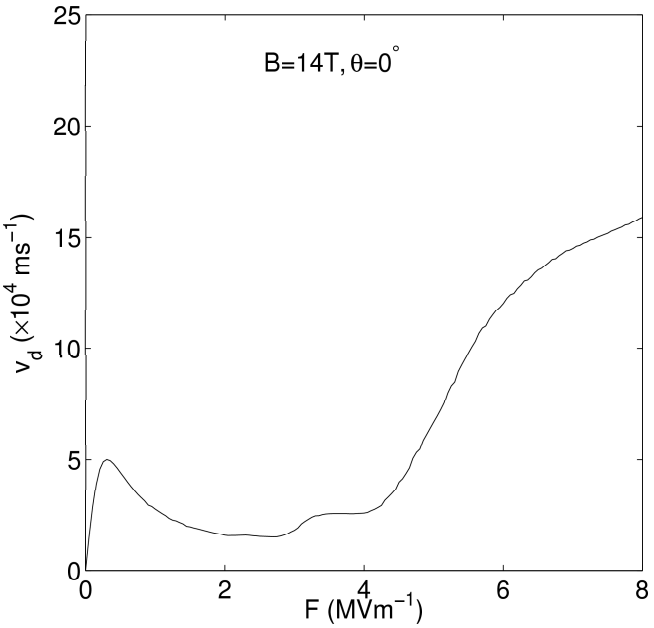

Figure 4.38: Smoothed drift velocity field curve for sample $NU2299$ when $B = 14$ T and $\theta = 0°$. Smoothing has been performed firstly over the period in $1/F$ of first-to-second level tunnelling, and secondly over the period in $1/F$ of first-to-third level tunnelling.

NU2299. Figure 4.39(a) also shows the Esaki-Tsu curve calculated using 10 terms of the miniband dispersion relation (blue circles). For each plot, $B = 14$ T and for (a) $\theta = 0°$, (b) $\theta = 15°$, (c) $\theta = 30°$ and (d) $\theta = 45°$. When $\theta = 0°$ the agreement between quantum, semiclassical and Esaki-Tsu models is ideal at low fields $\lesssim 2$ MVm^{-1} (the anomalous peaks in the quantum mechanical curve observed at higher F values originate from inter-level tunnelling, as explained previously). When $\theta = 15°$, agreement between the semiclassical and quantum curves is still good. However, as the tilt angle continues to increase, the calculated values of drift velocity in the quantum mechanical model begin to fall well below the semiclassical results.

The same trend is observed in figure 4.40 which compares the quantum mechanical drift velocity calculations (red) for sample NU2293 at $B = 11$ T to the semiclassical results (black), for (a) $\theta = 0°$, (b) $\theta = 15°$, (c) $\theta = 30°$ and (d) $\theta = 45°$. Again, as the tilt angle is increased, the height discrepancy between the two sets of results grows larger.

This increasing discrepancy at higher θ values is due to the influence of the

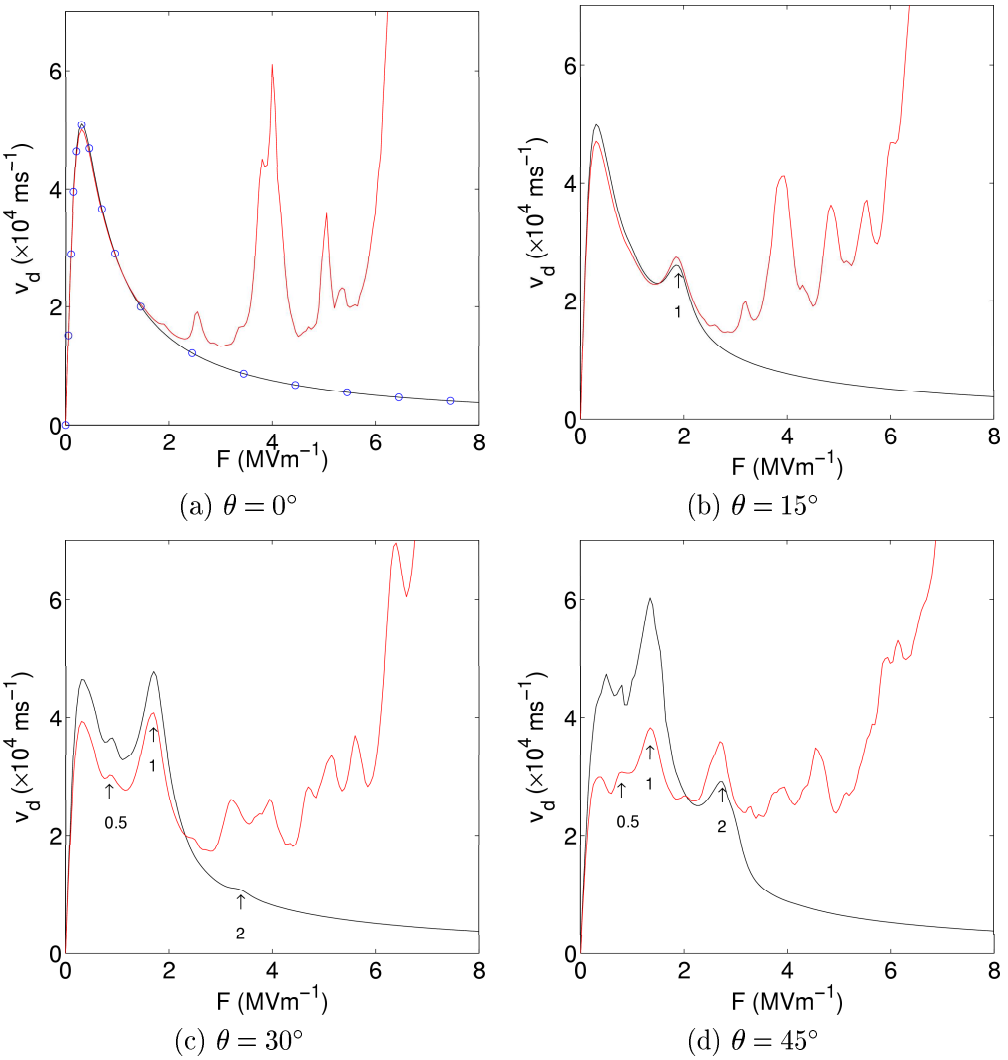

(a) $\theta = 0°$ (b) $\theta = 15°$

(c) $\theta = 30°$ (d) $\theta = 45°$

Figure 4.39: Comparison of drift velocity field curves, calculated both semiclassically (black) and quantum mechanically (red) for sample NU2299 when $B = 14$ T for various tilt angles. In (a) the theoretical Esaki-Tsu curve (calculated using 10 terms of the Fourier expansion of the first miniband dispersion relation) is represented by blue circles.

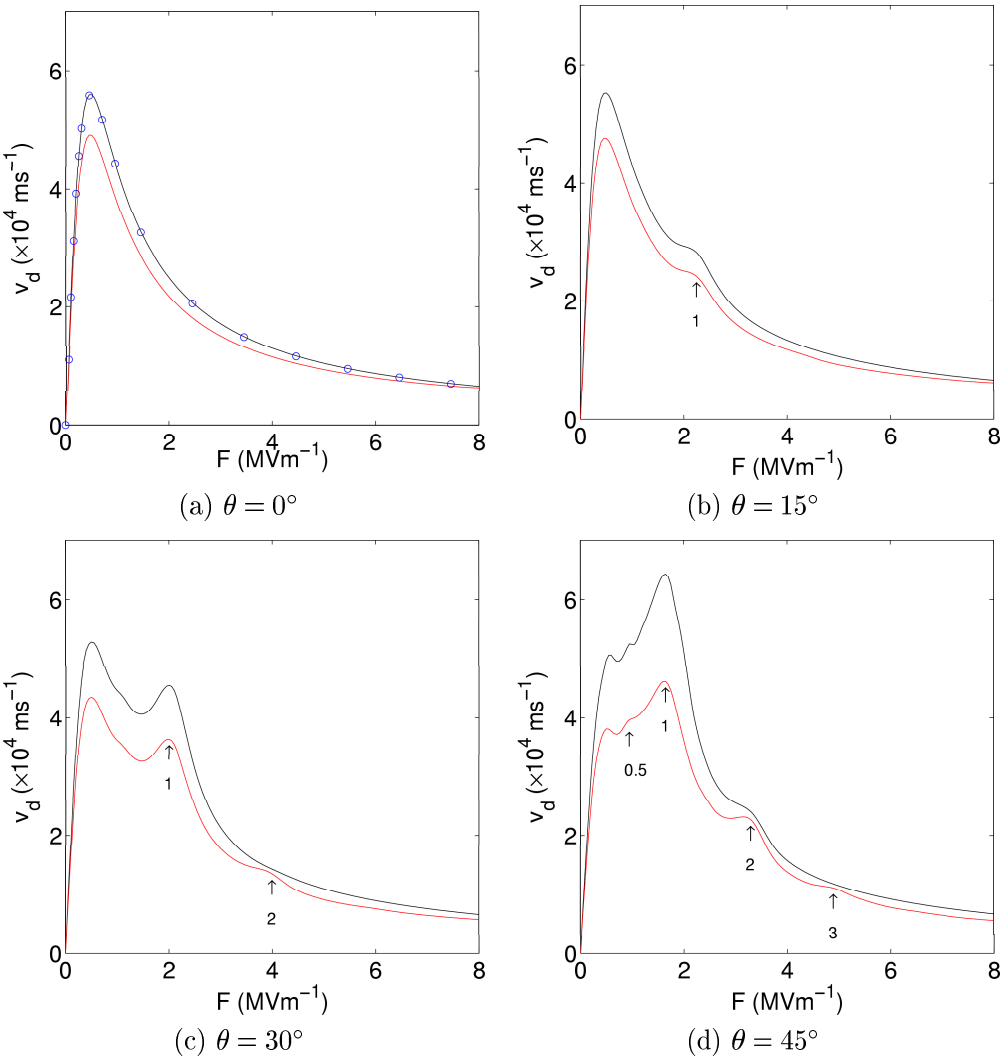

(a) $\theta = 0°$ (b) $\theta = 15°$

(c) $\theta = 30°$ (d) $\theta = 45°$

Figure 4.40: Comparison of drift velocity field curves, calculated both semiclassically (black) and quantum mechanically (red) for sample NU2293 when $B = 11$ T for various tilt angles. In (a) the theoretical Esaki-Tsu curve (calculated using 10 terms of the Fourier expansion of the first miniband dispersion relation) is represented by blue circles.

magnetic field. The magnetic potential is of the form

$$V_B(x,z) = \frac{1}{2}m^*\omega_c^2\left(x\sin\theta - (z-z_0)\cos\theta\right)^2, \tag{4.60}$$

i.e. parabolic, therefore when the wavepacket is displaced within this potential, the mean restoring force is always greater than the restoring force at the mean position of the wavepacket. For example, when displaced in the positive x direction, the wavepacket moves up the parabolic potential. The trailing edge of the wavepacket is subjected to a lower magnetic potential, and the leading edge to a higher potential. However due to the asymmetry of the curvature of the magnetic potential at such a point, the net result is that the average force acting on the electron to push it back along the negative x direction in the quantum mechanical case is larger than the force which acts upon a semiclassical electron located at the mean position of the wavepacket. This is true whether the wavepacket is displaced in either the positive or negative x direction: $\partial V/\partial x$ is always larger at the extremeties of the motion due to the magnetic field. This extra force reduces the Bloch amplitude in the x direction, increasing the localisation of the electron and hence decreasing the calculated drift velocity. Note that this localising effect is also present in the z direction, where the cyclotron radius is decreased. This effect is confirmed by comparison of the quantum mechanical position expectation values (red) and semiclassical (black) trajectories in figure 4.41. Trajectories calculated for sample NU2293 with $r = 1$ and $B = 11$ T are shown in (a) and (b), for $\theta = 15°$ and $\theta = 30°$ respectively, and for sample NU2299 with $r = 1$ and $B = 14$ T in (c) and (d) for $\theta = 15°$ and $\theta = 30°$. The reduction in the spatial extent of the quantum mechanical trajectory is particularly apparent for $\theta = 30°$ (figures 4.41(b) and (d)). Note that the reversal of the lag in figure 4.41(c), such that the quantum mechanical trajectory *leads* the semiclassical one for $r = 1$ and $\theta = 15°$ in NU2299, will be addressed shortly.

Since the drift velocity is calculated only in the x direction, the reduction in the amplitude of oscillation in the x direction is the important factor here. At $\theta = 0°$, the magnetic field has no effect on this x motion, but the greater the tilt angle, the steeper the barrier that is presented in the x direction, and the greater the difference in the restoring forces at the leading and trailing edges. Therefore as θ is increased, the localising effect is reinforced. This analysis is further justified by considering the changes in the drift velocity field curves that occur as B is varied (for a given tilt angle). Figure 4.42 shows drift velocity field

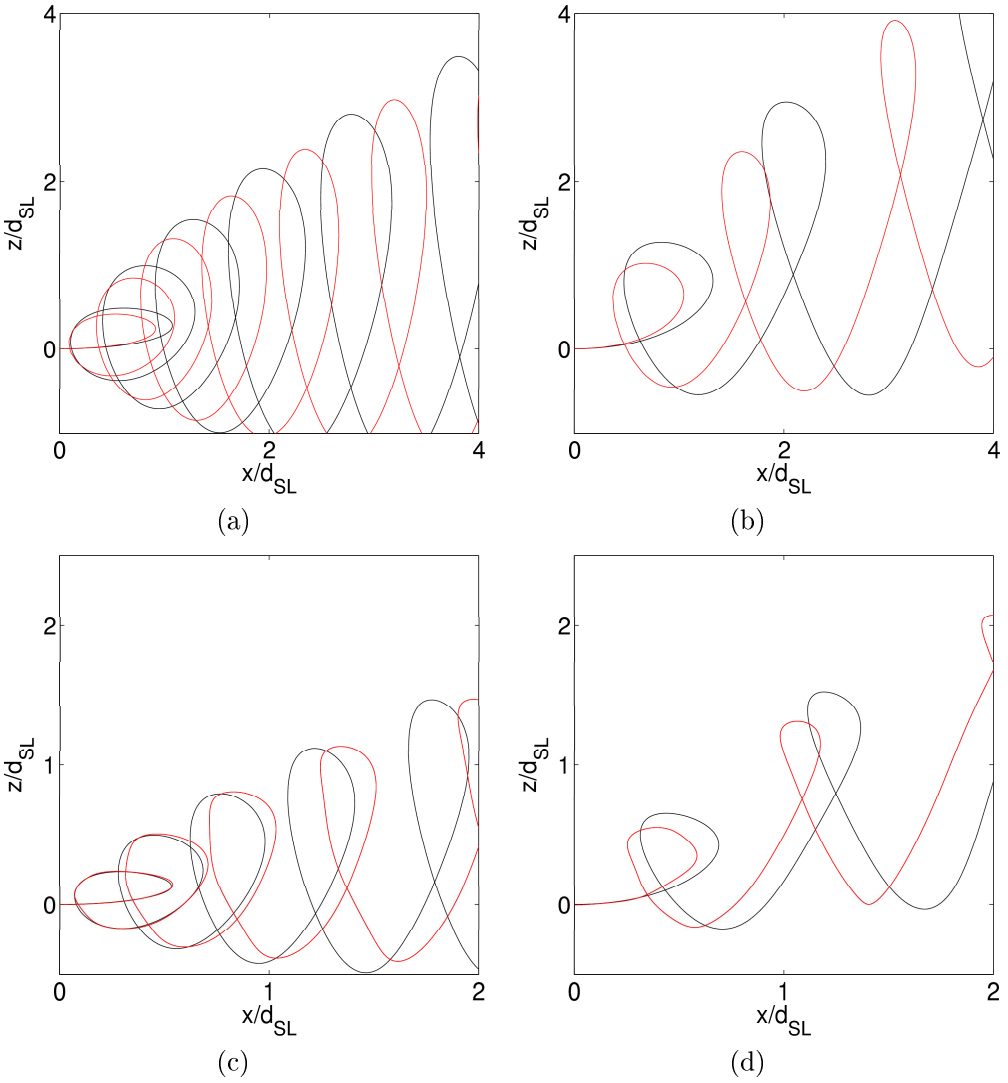

Figure 4.41: Comparison of semiclassical (black) and quantum mechanical (red) electron trajectories. Sample NU2293 is shown for $r = 1$ and $B = 11$ T when (a) $\theta = 15°$ and (b) $\theta = 30°$. Sample NU2299 is shown for $r = 1$ and $B = 14$ T when (c) $\theta = 15°$ and (d) $\theta = 30°$.

curves for both quantum mechanical (red) and semiclassical (black) models for NU2299 with $\theta = 45°$ and (a) $B = 8$ T, (b) $B = 11$ T and (c) $B = 14$ T. Figure 4.43 shows the same plots for sample NU2293. The average difference between the semiclassical and quantum mechanical curves was calculated over fields of 0-1.5 MVm^{-1} and is quoted on each plot. The increase in the discrepancy between the two curves as the strength of the magnetic field is increased confirms that the magnetically-enhanced restoring force is the cause of the deviation. It is also apparent that the rate at which the discrepancy increases with B is greater in NU2299 than in NU2293 (figures 4.42 and 4.43). This is because the spread of the initial state in real space is much greater for NU2299 than for NU2293 (figures 4.16 and 4.17), and hence the differential forces acting across the wavepacket are larger for a given magnetic field strength.

Note that only values of $F = 0 - 1.5$ MVm^{-1} were considered in the above analysis since the tunnelling effects in sample NU2299 start to affect the drift velocity at fields of around $F = 2$ MVm^{-1}. Indeed, not only do the curves cross over at around this point in figure 4.42, but the discrepancies seen in sample NU2293 also become less at these fields (figure 4.43). This is because at high F the electric force acting on the electron becomes much larger than the additional magnetic force experienced at the leading edge of the wavepacket.

The crossover of the semiclassical and quantum mechanical drift velocity curves for NU2299 in figure 4.42 due to inter-well tunnelling is the reason why the quantum mechanical trajectory (red) at $\theta = 15°$ (figure 4.41(c)) extends further than the semiclassical case (black). We see from figure 4.42(a) that the tunnelling effects begin to increase the calculated drift velocity at almost precisely the same field strengths as the $r = 1$ resonance occurs for $\theta = 15°$ (4.42(b)). Thus, a small amount of the wavepacket is tunnelling into higher minibands under these conditions, thereby increasing the effective Bloch amplitude of the wavepacket, leading to a higher drift velocity. Whilst this is also true when $\theta = 30°$, the localising effect of the magnetic force is substantially stronger due to the increase in θ, and therefore the quantum mechanical trajectory lags behind the semiclassical in this case.

We will now return to consider why the quantum mechanical drift velocity is always smaller than the semiclassical value at $\theta = 0°$ in NU2293 (figure 4.40(a)). This difference can be explained by considering the spread of the electron wavepacket in k-space. Figure 4.44 illustrates a typical cosinusoidal dispersion relation and shows the spread Δk of a Gaussian wavepacket described by

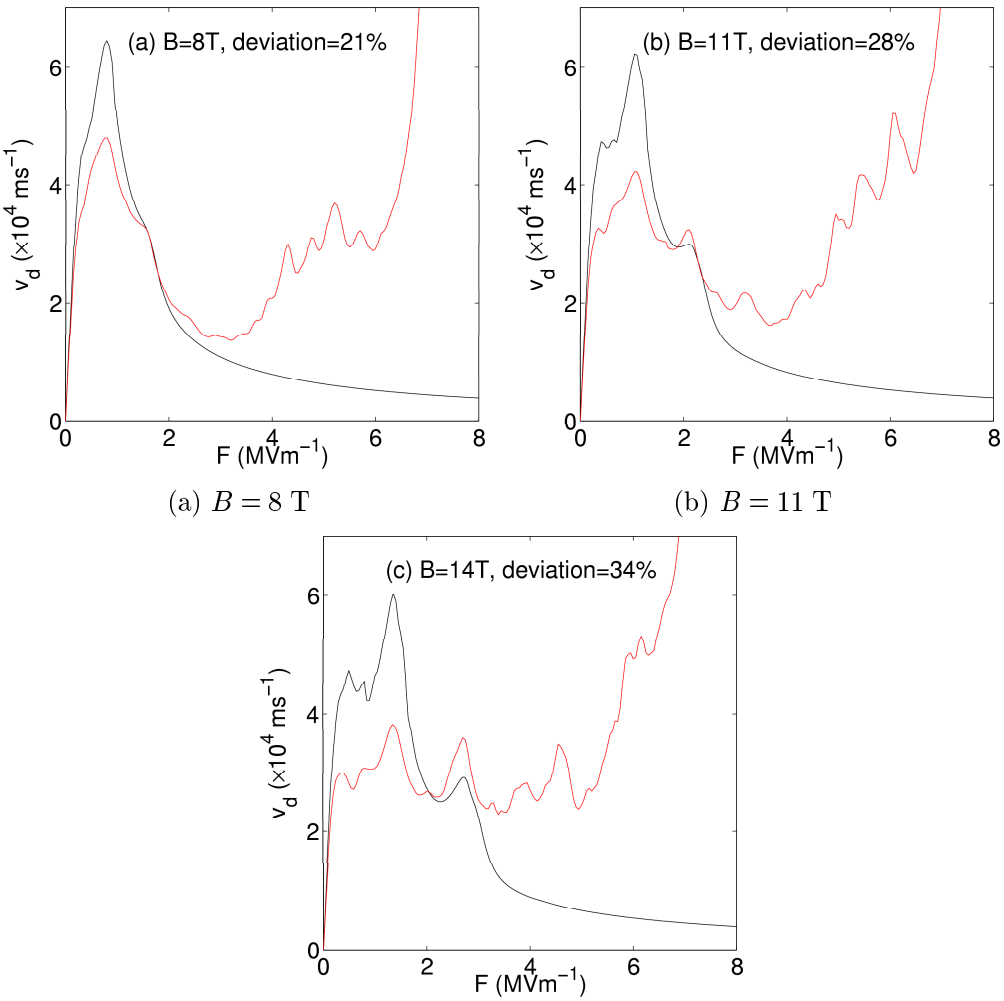

(a) $B = 8$ T (b) $B = 11$ T

(c) $B = 14$ T

Figure 4.42: Comparison of drift velocity field curves, calculated both semiclassically (black) and quantum mechanically (red) for sample NU2299 when (a) $B = 8$ T, (b) $B = 11$ T and (c) $B = 14$ T for $\theta = 45°$. Average percentage errors between the two curves are calculated over a field range of $F = 0 - 1.5$ MVm^{-1}.

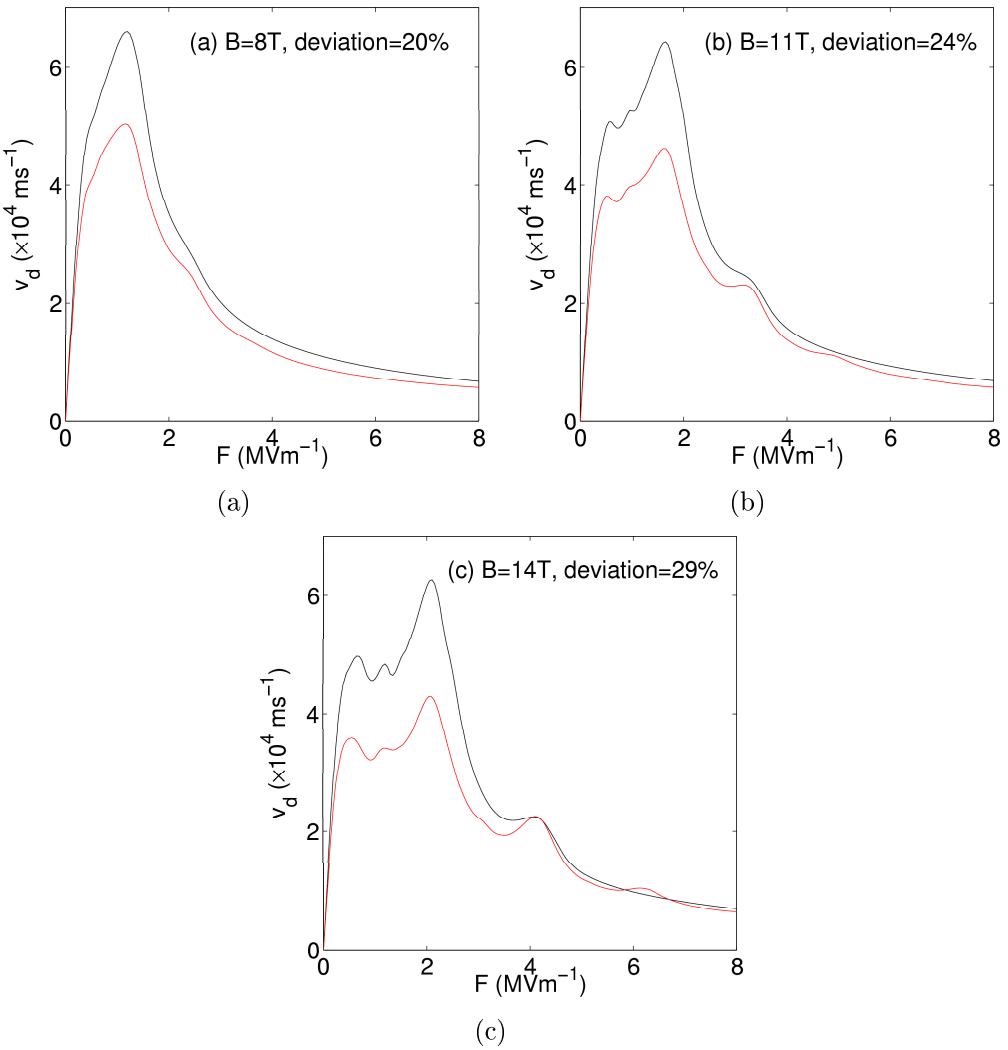

Figure 4.43: Comparison of drift velocity field curves, calculated both semiclassically (black) and quantum mechanically (red) for sample NU2293 when (a) $B = 8$ T, (b) $B = 11$ T and (c) $B = 14$ T for $\theta = 45°$. Average percentage errors between the two curves are calculated over a field range of $F = 0 - 1.5$ MVm^{-1}.

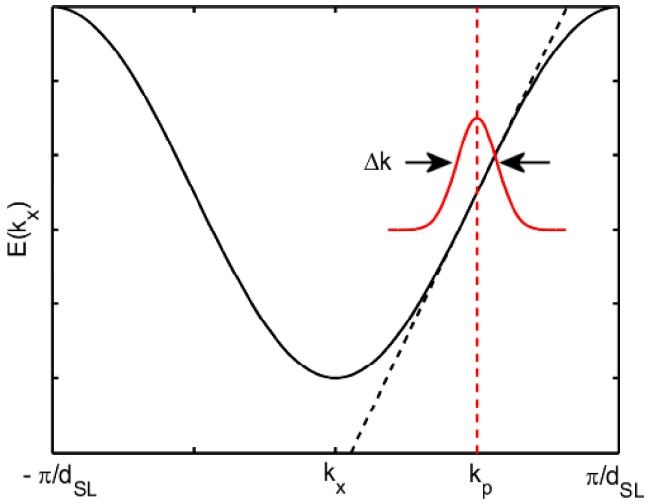

Figure 4.44: Typical cosinusoidal dispersion relation (black curve), with the black dashed line highlighting the maximum gradient located at k_p. Shown in red is an example of a wavepacket with significant spread Δk in k-space, centred at k_p.

the function

$$f(k-k_p) \propto \exp\left(\frac{-(k-k_p)^2}{\Delta k^2}\right), \tag{4.61}$$

where k_p is the k value for which the semiclassical electron velocity

$$\mathbf{v} = \frac{1}{\hbar}\frac{\partial E}{\partial \mathbf{k}} \tag{4.62}$$

is maximal. In the quantum mechanical case however, when the mean position of the wavepacket is at $k = k_p$, the average velocity $\bar{v}$ is given by

$$\bar{v} = \int_k f^2\left(k-k_p\right) v\left(k\right) dk, \tag{4.63}$$

where we take into account the fact that each point in the wavepacket is located at a different point along the dispersion relation leading to a range of velocities across the wavepacket. We can expand the term $v(k)$ in equation (4.63) as a Taylor series about k_p:

$$v\left(k\right) = v\left(k_p\right) + \left(k-k_p\right)\left.\frac{\partial v}{\partial k}\right|_{k_p} + \frac{\left(k-k_p\right)^2}{2}\left.\frac{\partial^2 v}{\partial k^2}\right|_{k_p} + \ldots \tag{4.64}$$

Substituting this into equation (4.63) gives

$$\begin{aligned}\bar{v} = \quad & v\left(k_p\right)\int_k f^2\left(k-k_p\right)dk \\ & + \left.\frac{\partial v}{\partial k}\right|_{k_p}\int_k \left(k-k_p\right) f^2\left(k-k_p\right)dk \\ & + \left.\frac{\partial^2 v}{\partial k^2}\right|_{k_p}\int_k \frac{\left(k-k_p\right)^2}{2} f^2\left(k-k_p\right)dk, \end{aligned} \tag{4.65}$$

neglecting higher order terms in the expansion of $v(k)$. Since the wavefunction probability density is normalised to unity, the integral of $f^2\left(k-k_p\right)$ over all of k-space must also be unity. We also know that $\partial v/\partial k$ evaluated at k_p, the point of maximum velocity, must be zero. Thus we have

$$\bar{v} = v\left(k_p\right) + C\left.\frac{\partial^2 v}{\partial k^2}\right|_{k_p}, \tag{4.66}$$

where

$$C = \int_k \frac{\left(k-k_p\right)^2}{2} f^2\left(k-k_p\right)dk. \tag{4.67}$$

Due to the fact that k_p represents a maximum in the velocity, we can say that

$$\left.\frac{\partial^2 v}{\partial k^2}\right|_{k_p} < 0. \tag{4.68}$$

Furthermore, it is clear that $C > 0$, and so we can write

$$\bar{v} = v\left(k_p\right) - C' \tag{4.69}$$

where C' is positive. Hence we expect that for a wavepacket with significant spread in k-space, the maximum mean velocity calculated quantum mechanically will be less than the maximum velocity in the semiclassical case, $v(k_p)$. This explains why, even when $\theta = 0^\circ$ and the magnetic field has no effect, the quantum mechanical drift velocity curve lies below the semiclassical one (figure 4.40(a)). The initial wavefunction chosen in sample NU2293 is such that the probability density is spread over only $\sim 6d_{SL}$ (figure 4.16), leading to a wavepacket which is fairly broad in k-space, and so the effect described above is significant. However, the initial probability density in NU2299 is spread over $\sim 12d_{SL}$ (figure

4.17) leading to a narrow wavepacket in k-space, and hence we observe a much smaller discrepancy in the quantum mechanical and semiclassical drift velocities calculated for NU2299 at $\theta = 0°$ (figure 4.39(a)).

Dual scattering time model

The reader should note that the quantum mechanical model presented thus far does not take into account the possibility of LO-phonon scattering of the electron. This phenomenon can only occur if the electron has sufficient energy to generate an LO-phonon. In GaAs, the critical kinetic energy above which LO-phonon creation is possible, E_{crit}, is ~ 36 meV. In regimes where LO-phonon scattering becomes possible, the scattering time used in calculations of the drift velocity should be much shorter, and $P(t)$ is no longer given by equation (4.57). A new scattering probability must be recalculated each time the expectation value of the kinetic energy, $\langle E_k \rangle$,

$$\langle E_k \rangle = -\int_{-\infty}^{\infty}\int_{-\infty}^{\infty} \Psi^* \left[\frac{\hbar^2}{2m^*}\left(\frac{\partial^2}{\partial x^2}+\frac{\partial^2}{\partial z^2}\right)\right]\Psi dx dz \tag{4.70}$$

crosses the 36 meV threshold. Figure 4.45 illustrates this, depicting how, as the electron's kinetic energy varies, it may pass through the threshold several times. Below E_{crit} the scattering time $\tau = 176$ fs applies (see section 4.2.3). However, above E_{crit} the characteristic scattering time τ_{LO} applies, which is a newly calculated scattering time that takes into account τ_i^{LO}, the scattering time characterising LO phonon emission from electrons.

Firstly, we define a new inelastic scattering time τ_i^{NEW} as

$$\frac{1}{\tau_i^{NEW}} = \frac{1}{\tau_i} + \frac{1}{\tau_i^{LO}}. \tag{4.71}$$

The new scattering time for use when $\langle E_k \rangle > E_{crit}$ is now given by

$$\tau_{LO} = \left(\frac{\tau_e}{\tau_e + \tau_i^{NEW}}\right)^{\frac{1}{2}} \tau_i^{NEW}. \tag{4.72}$$

In sample NU2299 $\tau_i^{LO} = 0.1$ ps, $\tau_i^{NEW} = 93$ fs and $\tau_{LO} = 44$ fs. The new expression for $P(t)$ is derived as follows.

Consider a time interval $t \rightarrow t + dt$. During this interval, the number of

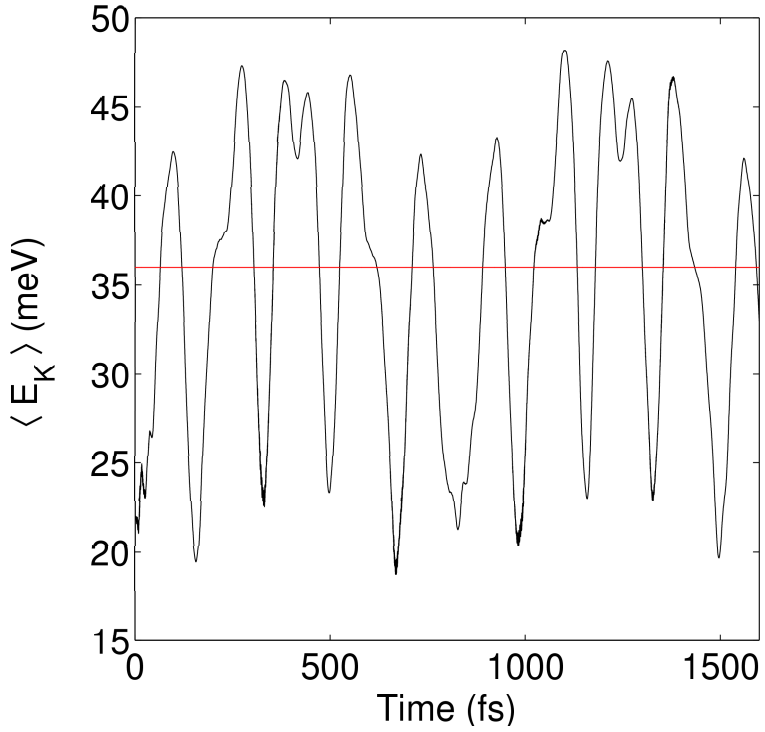

Figure 4.45: Example of how the expectation value of the electron kinetic energy varies as a function of time during the evolution of a quantum mechanical wavepacket. The kinetic energy of the electron is plotted in black, whilst the red line at 36 meV is the critical energy above which LO-phonon scattering is possible (provided $\theta \neq 0°$).

electrons that scatter is given by dN, and we can write

$$\frac{dN}{N} = -\frac{dt}{\tau_n}, \tag{4.73}$$

where N is the total number of unscattered electrons at time t and τ_n is the scattering time applicable in the interval $t_n \to t_{n+1}$, either τ or τ_{LO}. Initially at $t_0 = 0$, there are N_0 electrons unscattered. After some time t_1, when the number of unscattered electrons is given by N_1, the kinetic energy of the electrons exceeds E_{crit} and the decay rate is greatly increased since the scattering time has decreased from $\tau_0 = \tau$ to $\tau_1 = \tau_{LO}$. Conversely, at $t = t_2$ when the kinetic energy has fallen past E_{crit}, the rate at which N is decaying is now governed by $\tau_2 = \tau$ and the decline becomes less steep.

So supposing that t is between times t_n and t_{n+1}, then

$$\int_{N(t_n)}^{N(t)} \frac{dN}{N} = -\int_{t_n}^{t} \frac{dt}{\tau_n}, \tag{4.74}$$

integrating which results in

$$N(t) = N(t_n)e^{-\frac{(t-t_n)}{\tau_n}}. \tag{4.75}$$

Thus the number of unscattered electrons at any time t depends on the value of N the last time the E_{crit} threshold was crossed, for example:

$$N_1 = N_0 e^{-\frac{(t_1-t_0)}{\tau}} = N_0 e^{-\frac{t_1}{\tau}} \tag{4.76a}$$

$$N_2 = N_1 e^{-\frac{(t_2-t_1)}{\tau_{LO}}} \tag{4.76b}$$

$$N_3 = N_2 e^{-\frac{(t_3-t_2)}{\tau}} \tag{4.76c}$$

and so on. Clearly these equations can be combined in the following form:

$$N_3 = N_1 e^{-\frac{(t_2-t_1)}{\tau_{LO}}} e^{-\frac{(t_3-t_2)}{\tau}} \tag{4.77a}$$

$$= N_0 e^{-\frac{t_1}{\tau}} e^{-\frac{(t_2-t_1)}{\tau_{LO}}} e^{-\frac{(t_3-t_2)}{\tau}}. \tag{4.77b}$$

Generalising this result, we have:

$$N(t_n) = N_0 \prod_{k=1}^{n} e^{-\frac{(t_k-t_{k-1})}{\tau_k}} \tag{4.78}$$

where $t_0 = 0$ and $\tau_k = \tau$ or τ_{LO} and is the scattering time between time t_{k+1} and t_k. Combining equation (4.75) with equation (4.78) gives

$$N(t) = N_0 e^{-\frac{(t-t_n)}{\tau_n}} \prod_{k=1}^{n} e^{-\frac{(t_k - t_{k-1})}{\tau_k}}. \tag{4.79}$$

Note that if $\tau_{LO} = \tau$, equation (4.79) becomes

$$N(t) = N_0 e^{-\frac{t}{\tau}} \tag{4.80}$$

and we recover the previous model for exponential decay at a constant rate.

The probability that an electron scatters between time t and $t + dt$ is

$$P(t)dt = \frac{|dN|}{N_0}. \tag{4.81}$$

Therefore by first differentiating equation (4.79) with respect to time for $\frac{dN}{dt}$

$$\frac{dN}{dt} = -\frac{N_0}{\tau_n} e^{-\frac{t-t_n}{\tau_n}} \prod_{k=1}^{n} e^{-\frac{(t_k - t_{k-1})}{\tau_k}} \tag{4.82}$$

which can be rearranged for $\frac{|dN|}{N_0}$ such that we have

$$P(t)dt = \frac{|dN|}{N_0} = \frac{dt}{\tau_n} e^{-\frac{t-t_n}{\tau_n}} \prod_{k=1}^{n} e^{-\frac{(t_k - t_{k-1})}{\tau_k}}. \tag{4.83}$$

Again, it is worth noting that the Esaki-Tsu scattering probability given in equation (4.57) is recovered if a constant scattering rate is considered. Also note that $\langle E_k \rangle > E_{crit}$ is not possible when $\theta = 0°$ since $\Delta^1_{SL} < 36$ meV and there is no way energy can be transferred between the z and x directions.

Figure 4.46 shows a cascade of drift velocity field curves calculated using the dual scattering time model for sample NU2299 with $B = 14$ T. It is clear that the peaks are very weak and the curves are generally rough, in contradiction with experiment, therefore this model does not appear to accurately reflect the dynamics of the system and does not improve the quantum mechanical calculations.

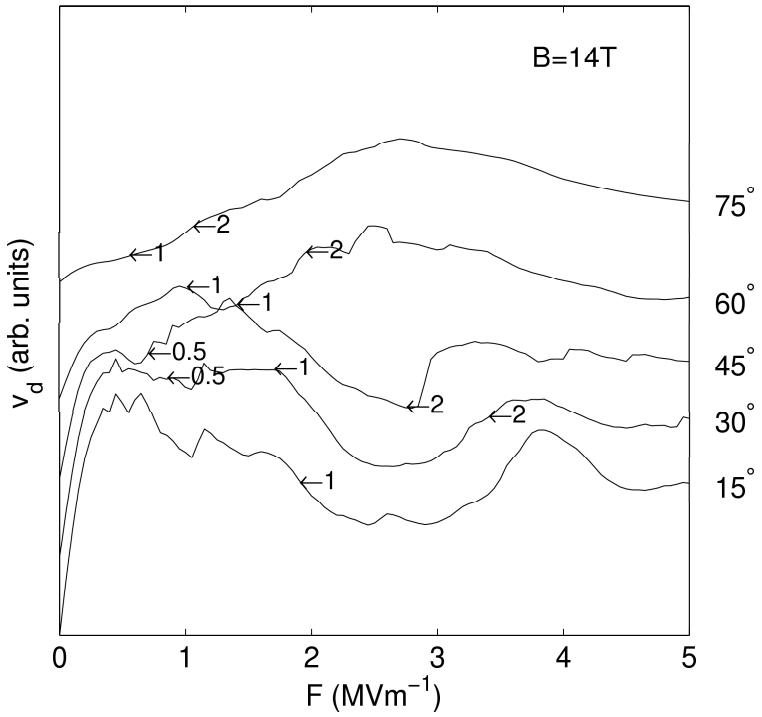

Figure 4.46: Cascade plot of the drift velocity field relationship, numerically calculated using a dual scattering time quantum mechanical model, for sample NU2299 when $B = 14$ T and $\theta = 15°$-$75°$. The locations of a number of predicted resonance peaks are highlighted for reference.

4.4 Comparison of theory with experiment

Experiments performed on superlattice samples generate current voltage ($I-V$) characteristics rather than drift velocity field curves, so it is useful to consider the form of the $I-V$ characteristics resulting from the quantum mechanical drift velocity calculations presented in previous sections. The corresponding $I-V$ curve is determined by modelling the superlattice as N layers of width Δx and considering the local volume density of electrons in each layer, along with the local electric field. The current continuity equation may then be solved in each layer. The details of this calculation are beyond the scope of this thesis. However, the $I-V$ characteristics (provided by D. Hardwick, University of Nottingham) for sample NU2293 are presented alongside experimental results (provided by D. Fowler, University of Nottingham). Also presented are plots of the differential conductance,

$$G = \frac{dI}{dV} \tag{4.84}$$

which allow resonances to be seen more clearly than in plots of $I-V$. Experimental and theoretical $I-V$ and $G-V$ curves are shown for magnetic field strengths of $B = 8$, 11 and 14 T in figures 4.47 to 4.52. Results are for angles $\theta = 0-75^\circ$ at 15° intervals, as considered previously. Peaks in the theoretical curves (figures 4.48, 4.50 and 4.52) due to the $r = 1$ resonance can be observed in both the $I-V$ and $G-V$ plots for all magnetic field strengths and tilt angles greater than zero. The arrow in each $G-V$ plot guides the reader to the location of the $r = 1$ resonance. Good agreement is seen between theoretical and experimental results under all applied field conditions. A comparison of experimental and theoretical $I-V$ and $G-V$ curves for NU2299 is not included, since work to smooth the corresponding drift velocity curves to give better agreement with experiment is still ongoing.

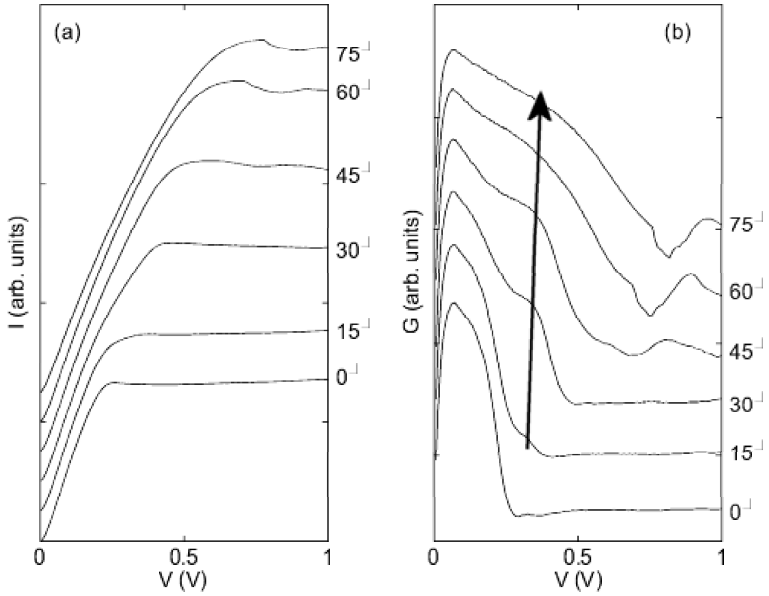

Figure 4.47: Experimentally measured plots of $I-V$ and $G-V$ data for NU2293 when $B = 8$ T and θ varies between 0°-90° in steps of 5°. The arrow highlights the $r = 1$ resonance. Reproduced with permission of D. Fowler.

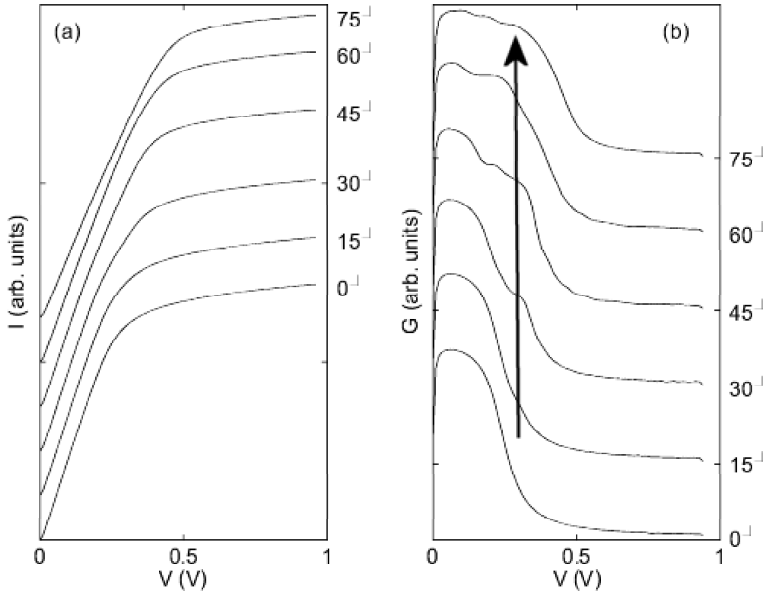

Figure 4.48: Numerically calculated plots of $I-V$ and $G-V$ data for NU2293 when $B = 8$ T and θ varies between 0°-75° in steps of 15°. The arrow highlights the $r = 1$ resonance. Curves were calculated by D. Hardwick with data generated by the quantum mechanical model.

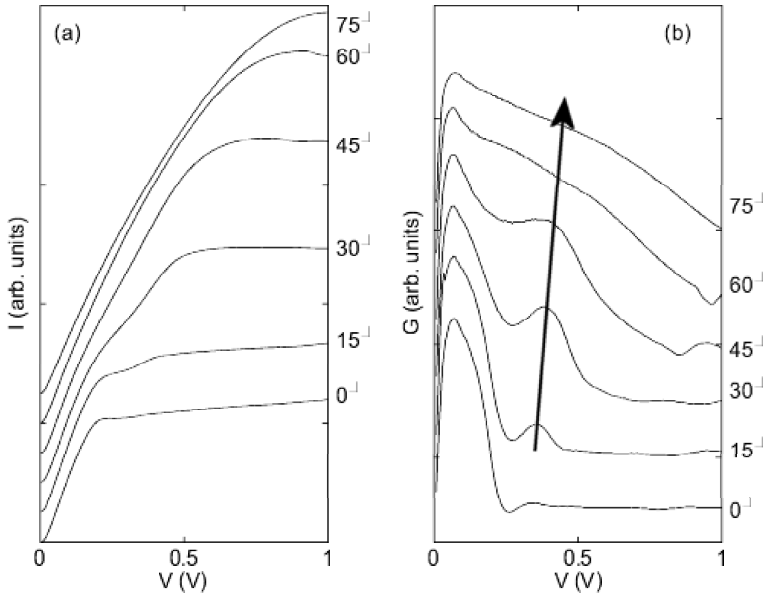

Figure 4.49: Experimentally measured plots of $I-V$ and $G-V$ data for NU2293 when $B = 11$ T and θ varies between 0°-90° in steps of 5°. The arrow highlights the $r = 1$ resonance. Reproduced with permission of D. Fowler.

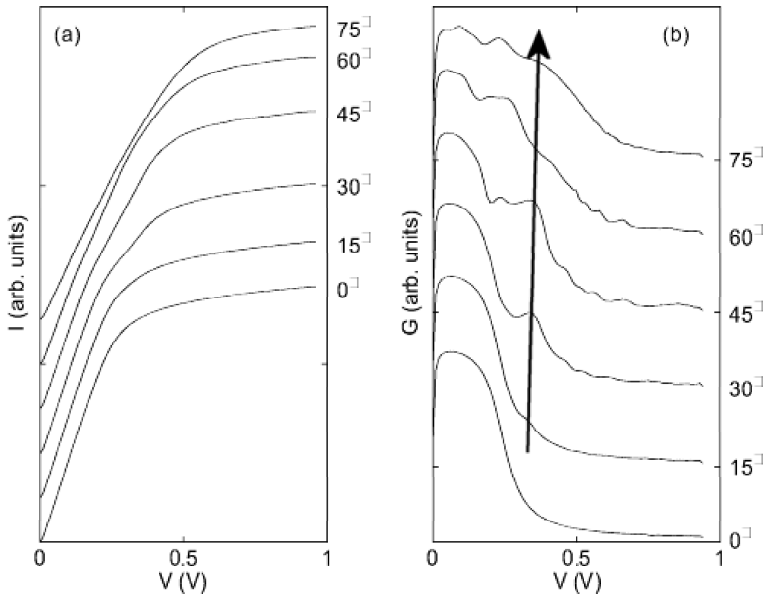

Figure 4.50: Numerically calculated plots of $I-V$ and $G-V$ data for NU2293 when $B = 11$ T and θ varies between 0°-75° in steps of 15°. The arrow highlights the $r = 1$ resonance. Curves were calculated by D. Hardwick with data generated by the quantum mechanical model.

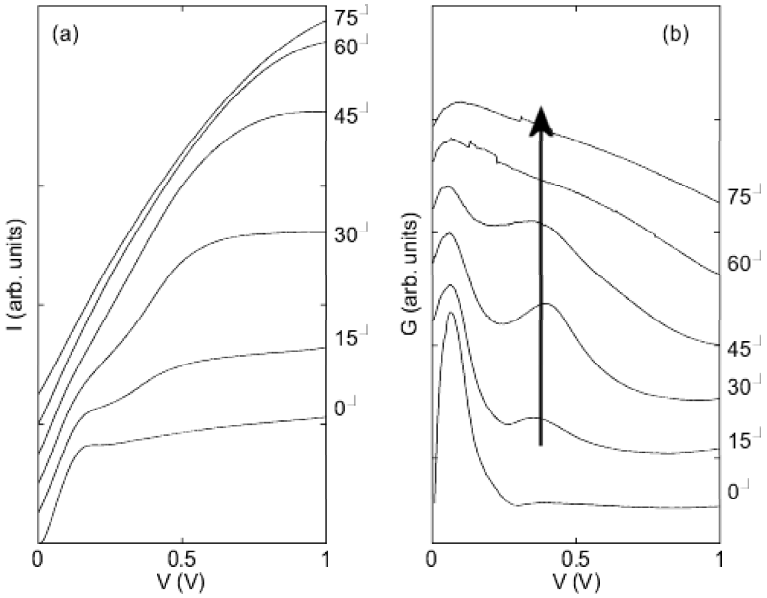

Figure 4.51: Experimentally measured plots of $I-V$ and $G-V$ data for NU2293 when $B = 14$ T and θ varies between 0°-90° in steps of 5°. The arrow highlights the $r = 1$ resonance. Reproduced with permission of D. Fowler.

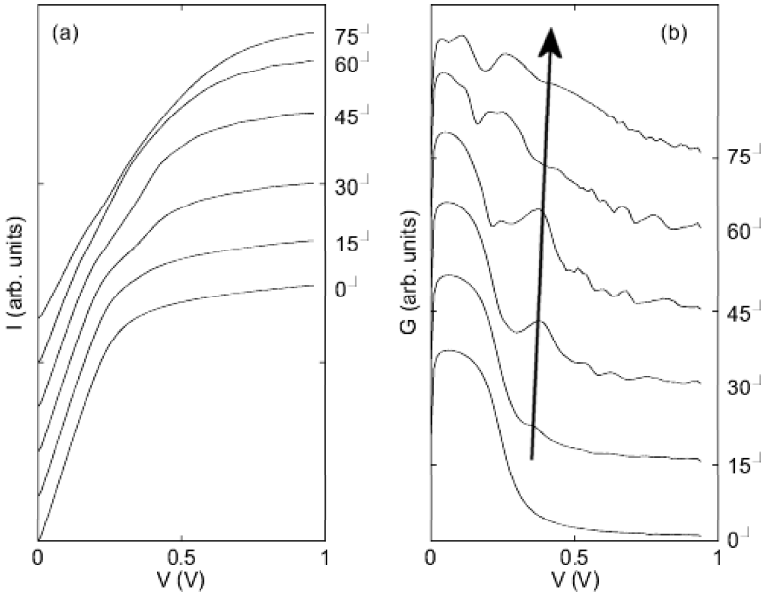

Figure 4.52: Numerically calculated plots of $I-V$ and $G-V$ data for NU2293 when $B = 14$ T and θ varies between 0°-75° in steps of 15°. The arrow highlights the $r = 1$ resonance. Curves were calculated by D. Hardwick with data generated by the quantum mechanical model.

Chapter 5

Dynamics of an ultracold sodium atom in an optical lattice and a tilted magnetic gutter

5.1 Introduction

In chapter 4, non-KAM chaos was considered in the context of an electron in a superlattice subjected to applied electric and magnetic fields. In this chapter, we realise similar chaotic dynamics using an optical lattice rather than a superlattice. Specifically, we study a magnetically confined atom as it falls through an optical lattice under the influence of gravity.

The advantages of this system over the previous one are manifold. Optical lattices are well suited to experimental studies of the correspondence between classical and quantum mechanics and are therefore ideal for exploring quantum chaos [12, 65]. Firstly, they are free of defects and impurities, and secondly, since no lattice vibrations are present either, there is almost no scattering in the system. In addition, the lattice can be switched off at will - not only does this offer an extra degree of control over the experimental system, it allows direct measurement of the atomic momenta. Also, because the optical lattice period is much greater than the typical superlattice period, the resultant motion takes place over much longer timescales and hence the dynamics may be observed and measured with greater ease. This is further enhanced by the consideration of atomic rather than electronic dynamics: due to their greater size and mass, atoms move far more slowly than electrons (on a timescale of milliseconds compared to picoseconds).

Neither do single atoms suffer from effects such as charge build up that come into play in experimental studies of superlattice band transport.

The following research considers a neutral sodium (^{23}Na) atom in a one-dimensional optical lattice, where the x axis lies along the optical lattice. The atom is initially trapped in a two-dimensional harmonic magnetic potential which can be tilted with respect to the lattice (in the x-z plane), as shown in figure 5.1(a). Again, we define co-ordinates x_t, z_t where x_t is along the axis of the gutter and z_t is perpendicular to the gutter axis such that

$$x_t = x\cos\theta + z\sin\theta \tag{5.1}$$

$$z_t = -x\sin\theta + z\cos\theta \tag{5.2}$$

where θ is the angle through which the gutter is tilted relative to the x-axis. The trapping frequencies are ω_x, ω_z in the x_t and z_t directions respectively. Once the atom is in the ground state of the magnetic trap, which may be achieved using laser and evaporative cooling, the trap is switched off along one direction by setting ω_x to zero (resulting in a two-dimensional gutter shaped potential - see figure 5.1(b)) and we simultaneously accelerate the atom through the lattice by allowing it to fall under the influence of gravity, with the x-axis vertical as in experimental studies of quantum transport in optical lattices [66].

We expect to observe non-KAM chaos when nonlinear resonances of the system are excited. The atom will perform Bloch oscillations in the x direction with frequency ω_B - this motion is induced by the atom falling through the periodic potential. When the characteristic frequency which defines the shape of the harmonic gutter is on resonance with the frequency of the Bloch oscillations, we expect to see stochastic webs form in phase space. The condition for resonance is given by

$$r = \frac{\omega_B}{\omega_{||}} \tag{5.3}$$

where in this case $\omega_{||} = \omega_z\cos\theta$, $\omega_B = m_a g d_{OL}/\hbar$ and r is again an integer labelling the order of the resonance. In the expression for ω_B, $g = 9.81$ ms^{-2} is the acceleration due to gravity and $m_a = 3.82 \times 10^{-26}$ kg is the mass of the sodium atom, whilst $d_{OL} = \lambda/2 = 294.5$ nm is the period of the optical lattice where λ is the wavelength of the laser beam.

Employing an optical lattice rather than a superlattice allows more control over the lattice parameters. Since we can specify the period and depth of the

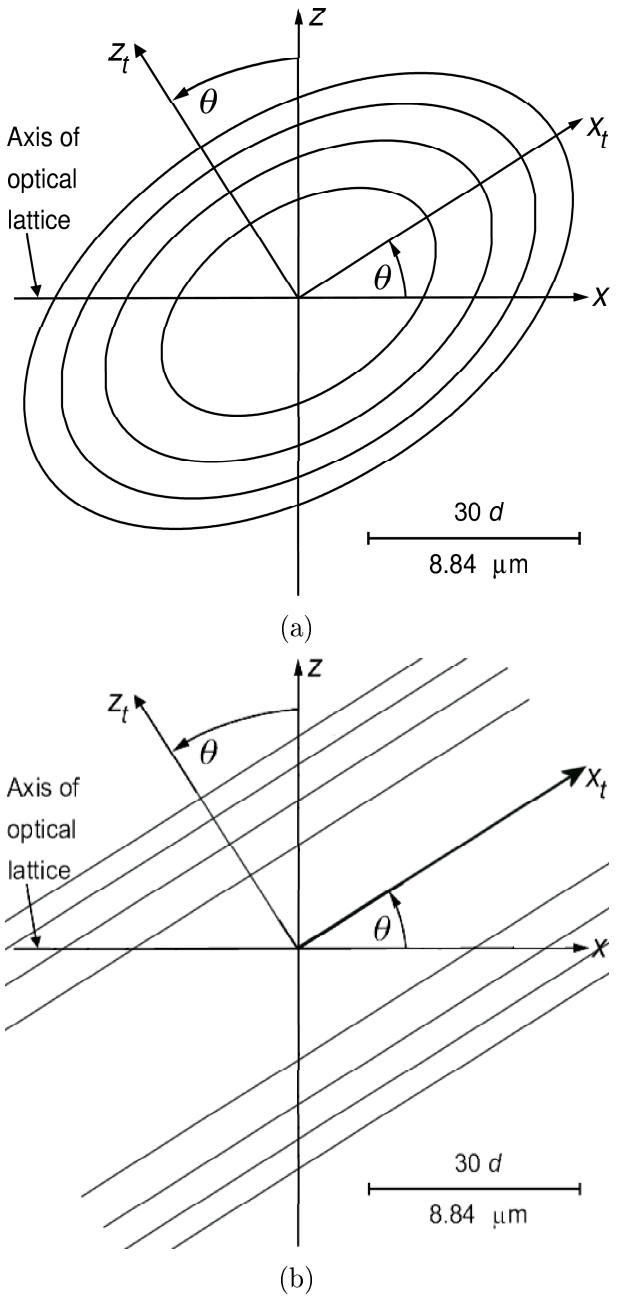

Figure 5.1: Schematic diagram showing the orientation of the potential energy fields. The optical lattice is along the x axis, as is the pull of gravity. The ellipses in (a) show the contours of potential energy in the $x-z$ plane for a sodium atom confined by a harmonic trap. The axes of the trap are in the x_t and z_t directions. The x_t axis of the trap makes an angle θ with the axis of the optical lattice. The case when the confining potential in the x_t direction has been switched off is shown in (b). The equipotentials now represent a gutter potential parallel to the x_t direction and inclined at an angle θ to the x direction.

lattice, we can tailor the band structure. However it is important to ensure that the laser frequencies are detuned from atomic resonances. The parameters defining the optical lattice potential in this study are taken from experiment [67]. Figure 5.2(a) shows the form of the optical lattice potential, $V_{OL}(x)$. The decision to study a sodium atom was made because the trapping frequencies required for resonance (as determined by equation (5.3)) are experimentally accessible, and sodium has been manipulated in similar potentials in experiments [67, 68]. In addition, the necessary trapping frequencies are low enough that the effect of the gutter potential upon the band structure is negligible.

Both the semiclassical and the quantum mechanical regimes of the system will be explored via numerical simulations of the atom dynamics. The gutter frequency ω_z will be varied in order to satisfy different resonance conditions and semiclassical and quantum trajectories studied for evidence of increased delocalisation of the atom when the resonance condition is satisfied. We will also look for the appearance of stochastic webs in the semiclassical phase space.

5.2 The semiclassical mechanics of the system

As in chapter 4, the semiclassical equations of motion governing the system are taken from the general derivation in section 3.2.5, where it was shown that motion in the y direction is separable. Knowing that motion in the y direction is simple harmonic, we shall consider only motion in the x-z plane for the remainder of the chapter. The two-dimensional semiclassical Hamiltonian for an atom in a band subjected to externally varying fields is

$$H_0 = E(p_x) + \frac{p_z^2}{2m_a} + V_{ext}(x, z) \tag{5.4}$$

where $E(p_x)$ is the dispersion relation of the optical lattice and V_{ext} is the potential due to the applied fields. The dispersion relation of the first band is represented by a Fourier series:

$$E(p_x) = \frac{\Delta_{OL}}{2}\left(a_0 - \sum_{n=1}^{\infty} a_n \cos\left(n\frac{p_x d_{OL}}{\hbar}\right)\right) \tag{5.5}$$

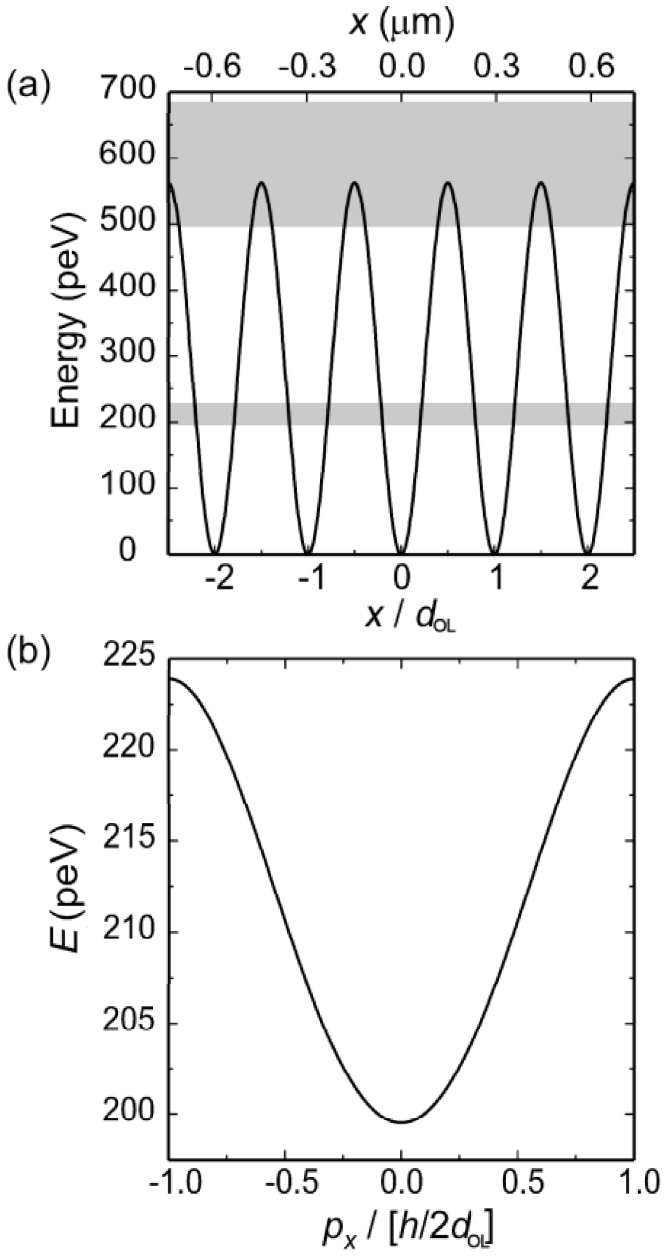

Figure 5.2: (a) Plot showing the potential energy profile of the optical lattice. The corresponding energy band structure (first and second bands only) is highlighted by the shaded areas. (b) Dispersion relation of the first energy band where $p_x = \hbar k_x$.

where the coefficients a_n are determined in Appendix A. Figure 5.2(b) shows the form of $E(p_x)$. Initially the atom is held in a potential

$$V_{ext}(x,z) = V_{trap}(x,z) = \frac{1}{2}m_a\left(\omega_x^2 x_t^2 + \omega_z^2 z_t^2\right). \tag{5.6}$$

The trapping frequency in the z_t direction is defined by the resonance condition, and varies according to the order of resonance one wishes to excite. Substituting for ω_B and $\omega_{\|}$ in equation (5.3) and rearranging for ω_z gives

$$\omega_z = \frac{m_a g d_{OL}}{\hbar r \cos\theta}. \tag{5.7}$$

The trapping frequency in the x_t direction is chosen to be 50 rad s^{-1}, however this frequency only plays a part in the initial trapping of the atom. To examine the non-KAM dynamics of the system, ω_x is set to zero and the atom is allowed to fall through the lattice. The external potential is then given by

$$V_{ext}(x,z) = \frac{1}{2}m_a\omega_z^2 z_t^2 - m_a g x. \tag{5.8}$$

As demonstrated in section 3.2.5, a system of this nature may be reduced to a single second-order differential equation in p_z by determining Hamilton's equations of motion for the system and combining them. It can be shown that this single governing equation has the form of a driven simple harmonic oscillator:

$$\ddot{p}_z + \omega_{\|}^2 p_z = A\sum_{n=1}^{\infty} n a_n \sin\left(n\left(Kp_z - \omega_B t - \phi\right)\right) \tag{5.9}$$

where for this system

$$A = \frac{-m_a\omega_z^2 d_{OL}\Delta_{OL}\sin\theta\cos\theta}{2\hbar} \tag{5.10}$$

$$K = \frac{d_{OL}\tan\theta}{\hbar} \tag{5.11}$$

$$\phi = \frac{d_{OL}}{\hbar}\left(p_x(0) + p_z(0)\tan\theta\right). \tag{5.12}$$

As before, to determine the atom dynamics, one must first solve equation (5.9)

for p_z, and subsequently solve the following equations (derived in section 3.2.5):

$$p_x(t) = p_x(0) + m_a g t - (p_z(t) - p_z(0)) \tan\theta \tag{5.13a}$$

$$\dot{x} = \frac{\partial E(p_x)}{\partial x} \tag{5.13b}$$

$$\dot{z} = \frac{p_z}{m_a} \tag{5.13c}$$

for p_x, x and z respectively. As in chapter 4, this system of equations is solved using the Runge-Kutta method detailed in Appendix B. The initial state of the atom was specified as $x(0) = z(0) = p_x(0) = p_z(0) = t(0) = 0$. Resonances of $r = 1, 2, 3$ were studied, and also an off resonance value of $r = (1+\sqrt{5})/4 \approx 0.809$. For each value of r, tilt angles of 0°, 15°, 30°, 45°, 60° and 75° were explored, with ω_z determined in each case from equation (5.7).

5.2.1 Semiclassical atom trajectories

Figure 5.3 shows the comparison between semiclassical atomic trajectories for on and off resonance conditions of the system. In this case, $\theta = 45°$, and the black trajectory represents the $r = 1$ resonance (with $\omega_z = 2\pi \times 236$ rad s^{-1}). The red trajectory is non-resonant, with $r = (1 + \sqrt{5})/4$ and consequently $\omega_z = 2\pi \times 291$ rad s^{-1}. The increase in delocalisation upon resonance is self-evident, with the trajectory extending approximately three times further along the axis of the optical lattice than in the off resonance case.

Figure 5.4 shows $r = 1$ resonant trajectories for angles (a) 15°, (b) 30°, (c) 45°, (d) 60° and (e) 75°. The corresponding gutter frequencies are $\omega_z = 2\pi \times 172$, $2\pi \times 192$, $2\pi \times 236$, $2\pi \times 333$ and $2\pi \times 643$ rad s^{-1} respectively. For angles 15°, 30° and 45° the motion is similar, with the paths displaying the familiar characteristic looping pattern observed in the superlattice system studied in chapter 4. As θ is increased towards 45°, the loops become less pronounced and the delocalisation increases to a maximum, as predicted in section 3.2.5. As θ is further increased to 60°, the trajectory becomes less orderly and the level of delocalisation begins to decrease (although remaining significant). For $\theta = 75°$, the trajectory becomes increasingly chaotic whilst extending a great distance in the z direction, signalling the approach to $\theta = 90°$ whereupon the motion is expected to become unbounded in the z direction as derived for the analogous superlattice system previously.

Figure 5.5 shows resonant trajectories for (a) $r = 2$ and (b) $r = 3$ for $\theta = 15°$. The gutter frequencies are $\omega_z = 2\pi \times 86$ and $2\pi \times 57$ rad s^{-1} respectively. Figure

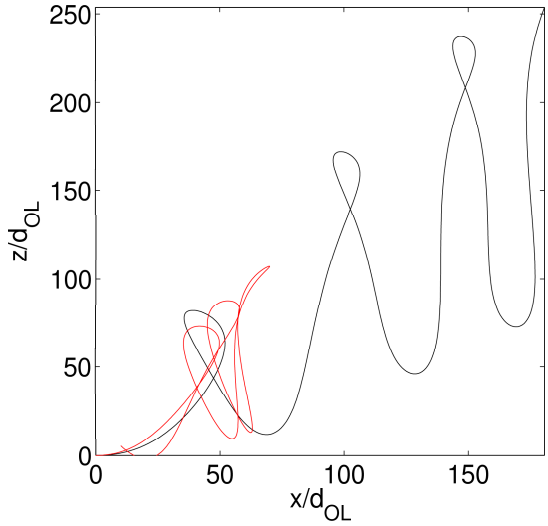

Figure 5.3: Comparison of on (black) and off (red) resonance semiclassical sodium atom trajectories. The gutter potential is tilted at an angle $\theta = 45°$, while $r = 1$ in the on resonance case and $r = (1 + \sqrt{5})/4$ in the off resonance case. The trapping frequencies are given by $\omega_z = 2\pi \times 236$ rad s^{-1} and $\omega_z = 2\pi \times 291$ rad s^{-1} respectively.

5.6 shows (a) $r = 2$ ($\omega_z = 2\pi \times 118$) and (b) $r = 3$ ($\omega_z = 2\pi \times 79$) trajectories for $\theta = 45°$. The extent of all of these trajectories is significantly less than the $r = 1$ case for the same tilt angles. Figure 5.7 shows (a) $r = 2$ ($\omega_z = 2\pi \times 322$) and (b) $r = 3$ ($\omega_z = 2\pi \times 214$) trajectories for $\theta = 75°$. Whilst the $r = 3$ trajectory shows a reduction in scale from the corresponding $r = 1$ resonance (figure 5.4(e)), the $r = 2$ trajectory appears to be little different.

These changes in the extent of the atomic paths as r varies can be explained in the following way. In chapter 4, when modelling the electron motion semiclassically, the force driving the electron through the lattice potential was varied in order to examine a variety of resonances for a given magnetic field strength. It was shown that increasing the magnitude of B improved the clarity of resonant peaks in the drift velocity field relationship, because an increase in B leads to an increase in the cyclotron frequency and hence the electron is able to complete more cyclotron orbits before scattering.

In this system, the gutter potential (characterised by ω_z) is analogous to B. The atomic resonance is varied by altering ω_z, whilst the force that drives the atom through the optical lattice, mg, is constant. Our definition of the resonance condition in equation (5.7) states that ω_z is inversely proportional to r, thus to excite higher order resonances the steepness of the gutter potential must be

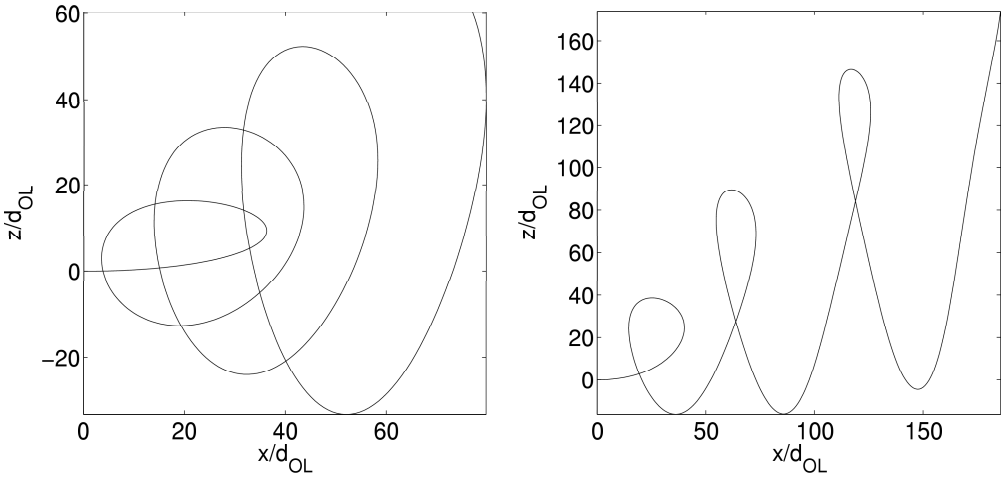

(a) $\theta = 15°$, $\omega_z = 2\pi \times 172$ rad s^{-1}

(b) $\theta = 30°$, $\omega_z = 2\pi \times 192$ rad s^{-1}

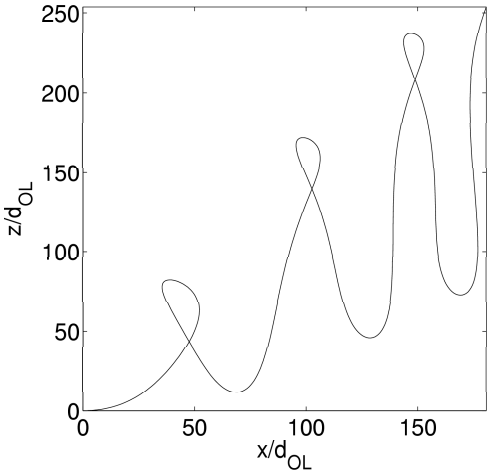

(c) $\theta = 45°$, $\omega_z = 2\pi \times 236$ rad s^{-1}

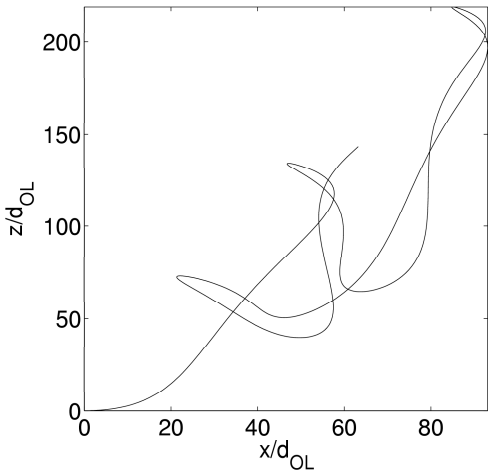

(d) $\theta = 60°$, $\omega_z = 2\pi \times 333$ rad s^{-1}

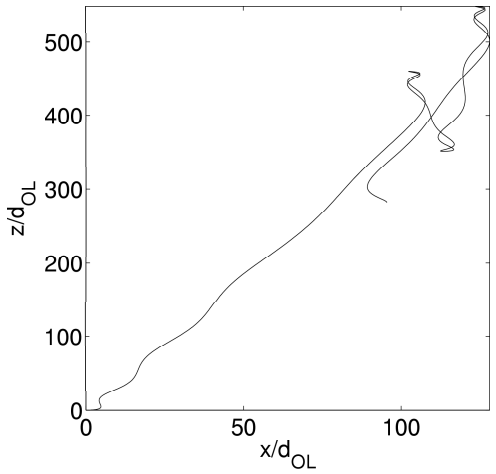

(e) $\theta = 75°$, $\omega_z = 2\pi \times 643$ rad s^{-1}

Figure 5.4: Selection of on resonance ($r = 1$) semiclassical sodium atom trajectories. The atom is initially at rest.

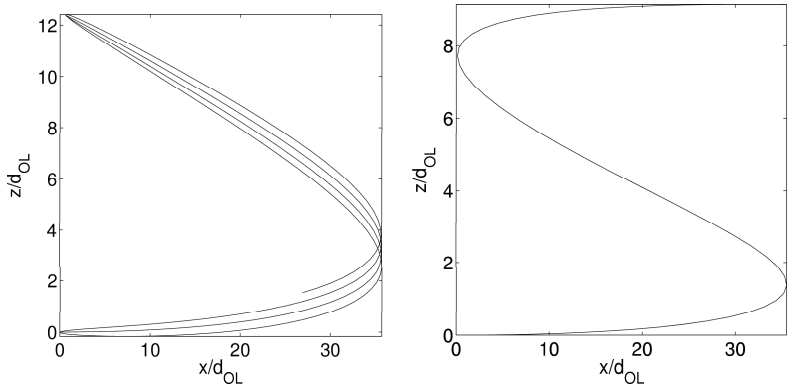

(a) $r = 2$, $\omega_z = 2\pi \times 86$ rad s^{-1} (b) $r = 3$, $\omega_z = 2\pi \times 57$ rad s^{-1}

Figure 5.5: Resonant semiclassical sodium atom trajectories for $\theta = 15°$. The atom is initially at rest.

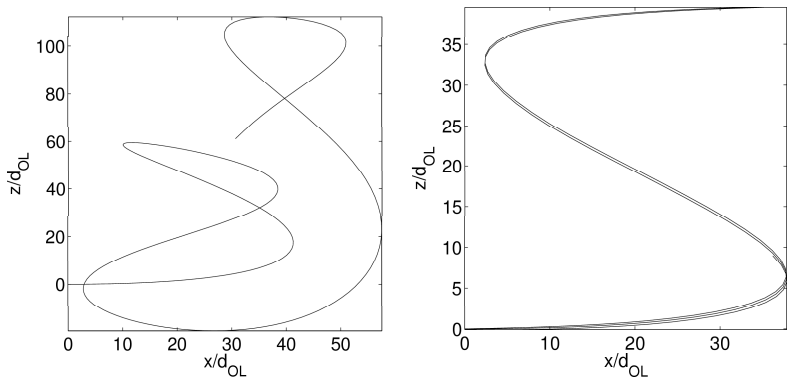

(a) $r = 2$, $\omega_z = 2\pi \times 118$ rad s^{-1} (b) $r = 3$, $\omega_z = 2\pi \times 79$ rad s^{-1}

Figure 5.6: Resonant semiclassical sodium atom trajectories for $\theta = 45°$. The atom is initially at rest.

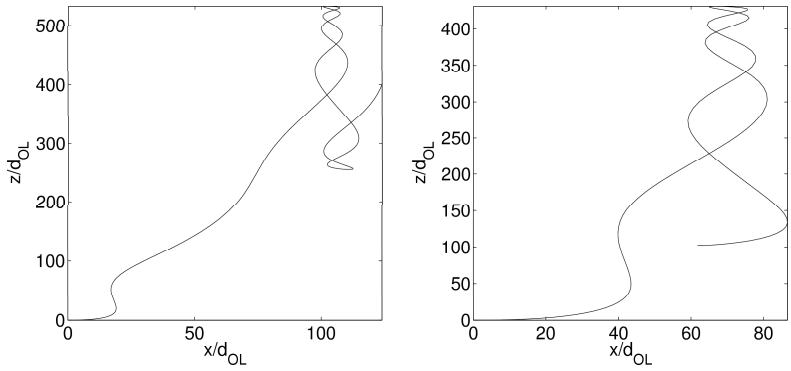

(a) $r = 2$, $\omega_z = 2\pi \times 322$ rad s^{-1} (b) $r = 3$, $\omega_z = 2\pi \times 214$ rad s^{-1}

Figure 5.7: Resonant semiclassical sodium atom trajectories for $\theta = 75°$. The atom is initially at rest.

Ring	$\theta = 15°$	$\theta = 30°$	$\theta = 45°$	$\theta = 60°$
1	0.51	0.24	0.14	0.08
2	0.94	0.44	0.25	0.15
3	1.36	0.63	0.36	0.21

Table 5.1: Predicted radii of the first three rings of the $r = 1$ stochastic web in phase space, for a selection of angles. Radii are quoted in units of 10^{-25} kg ms^{-1}.

reduced - equivalent to decreasing B in the superlattice system. Since ω_B is unchanged, the atom completes more Bloch oscillations per oscillation along z and therefore tends to localise on the scale of the Bloch orbit. To observe chaos, strong coupling of similar ω_B and $\omega_{||}$ frequencies is required, whereas here $\omega_B > \omega_{||}$. At higher r values, the Bloch-like motion is better defined and less strongly perturbed by the coupling between the x and z directions. Furthermore, consideration of equation (5.9) shows that the amplitude of the plane waves perturbing the system is proportional to ω_z, thus we would expect a reduction in ω_z to excite resonances less strongly and so decrease the distance travelled by the atom.

For high tilt angles, there is strong coupling between the x and z directions even for larger values of r, and so chaos is established. Consequently, the orbits when $\theta = 75°$ (figures 5.7(a) and (b)) exhibit a higher degree of delocalisation. It seems likely that this factor will manifest itself by the formation of a chaotic sea in the centre of the phase space at high tilt angles, as was seen in the case of the electron in the superlattice. We confirm this by considering Poincaré sections of the system in the next section.

5.2.2 Stroboscopic Poincaré sections

The prediction of stochastic webs in phase space in section 3.2.5 is applicable to this system. The atomic motion predicted via the Runge-Kutte method is once more sampled at times separated by $\Delta t = \frac{2\pi}{\omega_{||}}$ to generate stroboscopic Poincaré sections of the (P_z, p_z) phase space, where $P_z = \dot{p}_z/\omega_{||}$. The radii of the web rings predicted for the $r = 1$ resonance for $\theta = 15° - 60°$ are listed in table 5.1.

Figure 5.8 shows stroboscopic Poincaré sections for the $r = 1$ resonance for the angles included in table 5.1. As expected, stochastic webs do indeed form in the phase space, with $2r$ filaments and rotational symmetry of π. The positions of

the rings show good agreement with the analytical theory, and periodic orbits are clearly bounded by the cells of the web structure. As the tilt angle becomes large, a chaotic sea forms in the centre of the phase space and the filaments become distorted, as does the shape of the periodic orbits.

Figure 5.9 shows similar Poincaré sections for (a) $r = 2$ and (b) $r = 3$ resonances, when $\theta = 15°$. Once more, $2r$ filaments divide the phase space into a web structure, bounding regions of periodic orbits, and the rotational symmetry is π/r. In figure 5.10, stroboscopic Poincaré sections for (a) $r = 2$ and (b) $r = 3$ resonances, when $\theta = 60°$ are shown. Whilst the general features of the web structure are retained, the filaments are again highly distorted now that the tilt angle is large, and the central chaotic sea remains significant, confirming our earlier predictions in connection with the extent of the atomic trajectories for resonances $r > 1$ at large tilt angles.

5.3 The quantum mechanics of the system

In the quantum mechanical regime, the potential felt by the atom due to the optical lattice is included explicitly in the model. The potential energy of the sodium atom in the optical lattice is described by

$$V_{OL} = V_0 \sin^2\left(\frac{\pi x}{d_{OL}}\right) \tag{5.14}$$

where V_0, the amplitude of the lattice potential, is 562.52 peV (refer back to figure 5.2(a) for a diagram of the optical lattice potential). Given V_{OL}, we can write the two-dimensional quantum mechanical Hamiltonian of a sodium atom in this system as

$$H = -\frac{\hbar^2}{2m_a}\left(\frac{\partial^2}{\partial x^2} + \frac{\partial^2}{\partial z^2}\right) + V_{OL}(x) + V_{ext}(x, z), \tag{5.15}$$

where $V_{ext}(x.z)$ is specified by equations (5.6) and (5.8) in section 5.2. To determine the evolution of the wavefunction of the atom, $\Psi(x, z)$, the time-dependent Schrödinger equation:

$$i\hbar\frac{\partial\Psi(x, z)}{\partial t} = H\Psi(x, z), \tag{5.16}$$

must once more be discretised and solved numerically via the Crank-Nicolson method [60] (refer to Appendix C for further details of this technique).

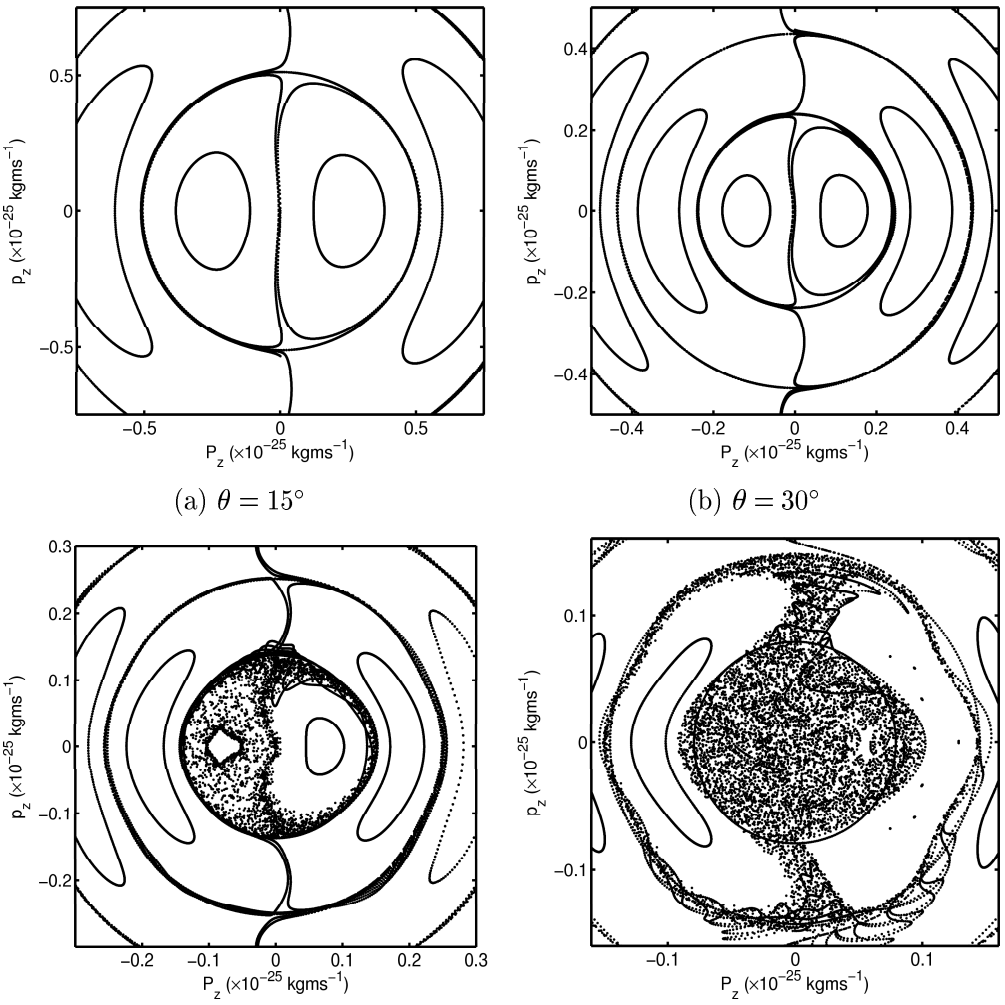

(a) $\theta = 15°$ (b) $\theta = 30°$

(c) $\theta = 45°$ (d) $\theta = 60°$

Figure 5.8: Stroboscopic Poincaré sections of the (P_z, p_z) phase space of the sodium atom when the system fulfills the $r = 1$ resonance condition. (a) $\omega_z = 2\pi \times 172$ rad s^{-1} (b) $\omega_z = 2\pi \times 192$ rad s^{-1} (c) $\omega_z = 2\pi \times 236$ rad s^{-1} (d) $\omega_z = 2\pi \times 333$ rad s^{-1}

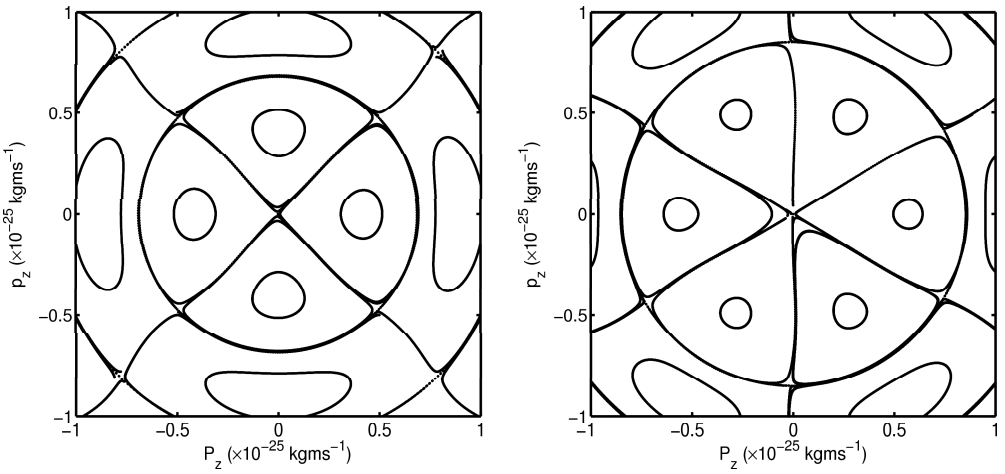

(a) $r = 2$ (b) $r = 3$

Figure 5.9: Stroboscopic Poincaré sections of the (P_z, p_z) phase space of the sodium atom when the system fulfills the (a) $r = 2$ and (b) $r = 3$ resonance conditions for $\theta = 15°$. (a) $\omega_z = 2\pi \times 86$ rad s^{-1} (b) $\omega_z = 2\pi \times 57$ rad s^{-1}

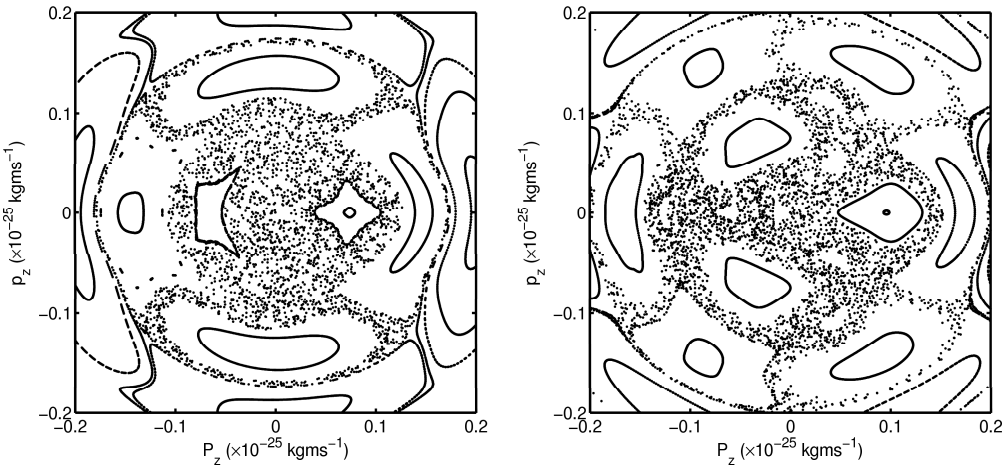

(a) $r = 2$ (b) $r = 3$

Figure 5.10: Stroboscopic Poincaré sections of the (P_z, p_z) phase space of the sodium atom when the system fulfills the (a) $r = 2$ and (b) $r = 3$ resonance conditions for $\theta = 60°$. (a) $\omega_z = 2\pi \times 167$ rad s^{-1} (b) $\omega_z = 2\pi \times 111$ rad s^{-1}

Simulations of the quantum dynamics were produced for the same parameters ω_z, θ as were considered semiclassically in section 5.2. Section 5.3.1 describes how the initial wavefunction was generated such that it represented a stationary atom in the ground state of the system centred at $x = z = 0$ before the trap was switched off in the x_t direction. The wavefunction was then allowed to evolve whilst falling through the lattice under the influence of gravity.

5.3.1 Determining the ground state

It was important to ensure that the de Broglie wavelength of the atom should be of the order of several optical lattice periods to ensure that quantum mechanical band dynamics would be observed, and not simply dynamics analogous to the motion of a single classical particle in a single well. All simulations begin with the wavefunction of the atom in the ground state of the system when subjected to the combined potential due to the optical lattice and the harmonic trap. An *imaginary time algorithm* was used to determine the ground state numerically [69]. This technique is identical in form to the method of determining the real time evolution via the Crank-Nicolson method [60] - however we instead consider the evolution of some arbitrary initial wavefunction in *imaginary* time rather than *real* time. This causes the wavefunction to converge upon the ground state of the system [12]. Adapting the Crank-Nicolson method to run in imaginary time is a trivial matter of substituting $-i\Delta_t$ in place of each Δ_t which appears in the finite difference approximations described in Appendix C.

The success of this method is easily understood. Consider making some initial guess at the ground state wavefunction of the system, Ψ_{guess}. This guess may be written as a linear combination of the eigenfunctions Ψ_n of the atomic wavefunction in the external potential:

$$\Psi_{guess} = \sum_n c_n \Psi_n e^{-\frac{iE_n t}{\hbar}} \tag{5.17}$$

where E_n is the energy of the nth eigenstate, and c_n is a measure of the weight given by the nth eigenstate to Ψ_{guess}. If imaginary time is now considered, a substitution of $t \to it$ must be made, and equation (5.17) becomes

$$\Psi_{guess} = \sum_n c_n \Psi_n e^{-\frac{E_n t}{\hbar}}. \tag{5.18}$$

It is clear that as the simulation progresses in imaginary time, increasing t will cause each of the terms in the summation in equation (5.18) to decay exponentially. Since the ground state has the lowest energy - that is, $E_0 < E_{n>0}$ - the contribution of this state will decay more slowly than that due to all other eigenfunctions. Thus eventually after some sufficiently long time, only the ground state will remain. Therefore, as long as a reasonable initial guess is provided, the imaginary time simulation will converge to the ground state of the system.

It is essential to note, however, that since the ground state is also decaying with time, it is necessary to renormalise the wavefunction to unity after every iteration of the Crank-Nicolson method, according to

$$R \int_z \int_y \int_x |\Psi|^2 \, dxdydz = 1 \tag{5.19}$$

where R is the normalisation constant. Since only two dimensions are considered here, namely x and z, the wavefunction is independent of y and so integration with respect to y produces a constant, L_y. This is known as the characteristic spread of the atomic wavefunction in the y-direction [12]. Hence equation (5.19) simplifies to

$$R \int_z \int_x |\Psi|^2 \, dxdz = RI_{x,z} = \frac{1}{L_y}. \tag{5.20}$$

For the purposes of normalisation it is reasonable to set L_y equal to L_z, the spread in the z-direction, which is given by

$$L_z = L_y = 2\sqrt{\int_{x,z} \Psi^* z^2 \Psi dxdz}. \tag{5.21}$$

Hence the normalisation constant is

$$R = \frac{1}{I_{x,z} L_y} \tag{5.22}$$

and the renormalised wavefunction Ψ_R is given by $\Psi_R = \sqrt{R}\Psi$. Obviously, the initial wavefunction will be different for each combination of system parameters r, θ and ω_z studied. However, an example of the form of the ground state probability density is shown in figure 5.11, for conditions $r = 1$, $\theta = 15°$ and $\omega_z = 2\pi \times 172$ rad s^{-1}. Recall also that the additional trapping frequency, ω_x, employed in determining the initial wavefuntion is $\omega_x = 2\pi \times 50$ rad s^{-1}.

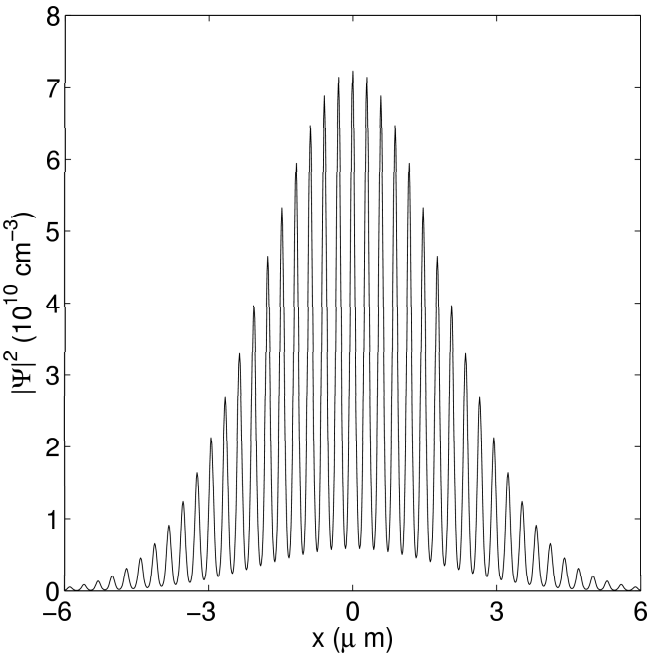

Figure 5.11: Illustration of the probability density function of the ground state of the sodium atom. A cross section of the probability density taken along $z = 0$ is shown, for the case when $r = 1$, $\theta = 15°$ and $\omega_z = 2\pi \times 172$ rad s^{-1}.

5.3.2 Quantum mechanical atom trajectories

The quantum mechanical trajectories are determined by calculating the expectation values, $\langle x \rangle$ and $\langle z \rangle$, of the wavefunction at discrete times, as was done in chapter 4 for the electron wavefunction (see equations (4.47a) and (4.47b)).

Figure 5.12 shows quantum mechanical trajectories (red) plotted alongside semiclassical paths (black) for $r = 1$ and (a) $\theta = 0°$, (b) $\theta = 15°$, (c) $\theta = 30°$, (d) $\theta = 45°$, (e) $\theta = 60°$ and (f) $\theta = 75°$. The red curve in figure 5.12(a) plots $\langle x \rangle$ versus t since there is no motion in the z direction, whereas for $\theta \neq 0°$ (figures 5.12(b)-(f)), $\langle z \rangle$ versus $\langle x \rangle$ is plotted in the red curve.

It is clear that when $\theta = 0°$, there is perfect agreement between the quantum mechanical and semiclassical models. Bloch oscillations are observed in both models, with equal amplitudes and periods, and with no significant deviation between the two paths for the entire duration of the simulation. This fits with our previous observation that for an initial wavefunction which is highly diffuse in real space, it is narrow in k-space and hence the mean quantum mechanical motion should agree well with the semiclassical case at $\theta = 0°$. However, as θ is increased and the gutter potential begins to influence the motion, the agreement between the two sets of trajectories becomes increasingly poor. There is satisfac-

tory correspondence between quantum mechanics and semiclassics when $\theta = 15°$ (figure 5.12(b)), and also at short times when $\theta \geq 30°$ (figures 5.12(c) to (f)). However, at long times when $\theta \geq 45°$ (figures 5.12(d) to (f)) the paths deviate from one another considerably.

Figure 5.13 shows quantum mechanical (red) and semiclassical (black) paths for $r = (1 + \sqrt{5})/4$ when (a) $\theta = 15°$ and (b) $\theta = 45°$. These show the same characteristics described in the previous comparisons - satisfactory agreement for small angles, with the deviation becoming significant as the tilt angle is increased. The fact that similar observations are made for both on and off resonance conditions implies that the deviation does not arise solely as a result of the resonance, so it is necessary to consider the behaviour of the atom wavefunction in order to gain more insight in to the nature of the discrepancies.

5.3.3 Time evolution of the atom wavefunction

We begin by considering the form of the atom wavefunction when agreement between quantum mechanical and semiclassical models is good. Figure 5.14 shows snapshots of the probability density function for the atom at times 0 ms and 30 ms. There is no observable difference between the two plots.

Figure 5.15 shows snapshots of the probability density at different times when $r = (1+\sqrt{5})/4$ and $\theta = 15°$. The quantum mechanical mean trajectory is overlaid. Note that the time duration of the trajectory shown here is greater than was shown in figure 5.13(a). The decision was made to show a shorter trajectory in the earlier figure in order to provide the reader with a less confusing visual comparison between the two trajectories in figure 5.13(a). It is clear from figure 5.15 that there is little difference between the probability distribution at times (a) 0 ms and (c) 30 ms, except that it is perhaps a little more diffuse at the later time. In figure 5.15(b), the probability density has the appearance of being slightly stretched out in the x direction as it makes a sharp change in direction.

Figure 5.16 shows the probability density when $r = 1$ and $\theta = 15°$ with the quantum mechanical trajectory overlaid. In this case, whilst the general shape and structure of the probability density function remains the same throughout, the final form is noticeably more diffuse than the initial state. However, the wavefunction clearly remains intact as it follows the mean path.

Figure 5.17 shows the changing probability density for $r = 1$ when $\theta = 45°$. In this case however, both the mean quantum mechanical trajectory (solid line)

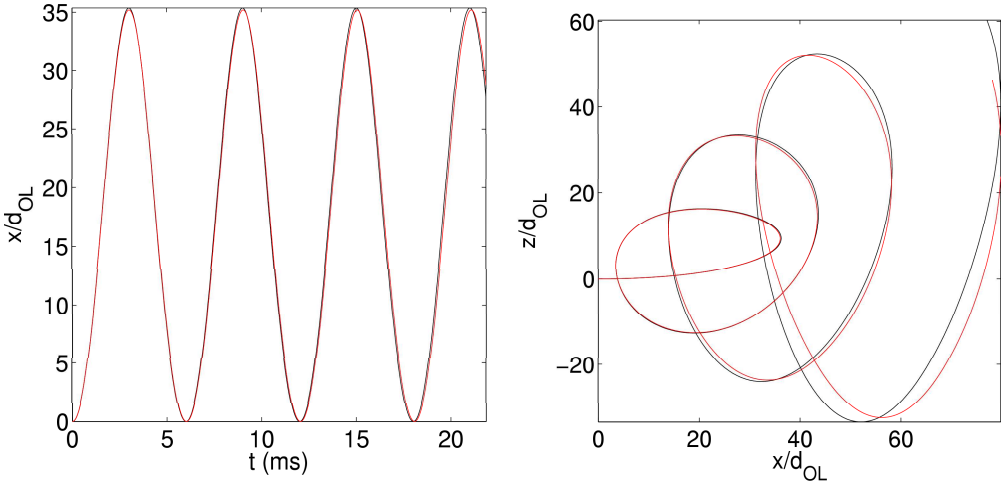

(a) $\theta = 0°$ (b) $\theta = 15°$

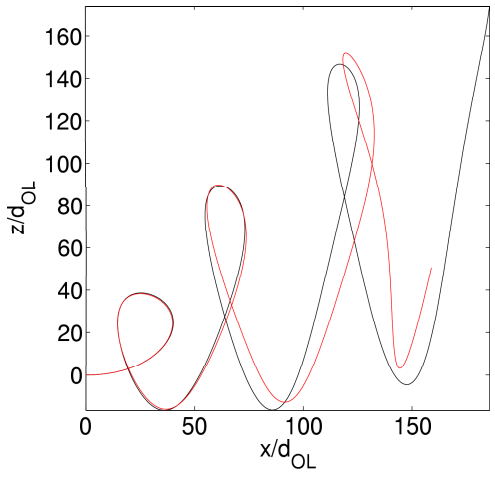

(c) $\theta = 30°$

Figure 5.12: Comparison between resonant $r = 1$ semiclassical (black) and mean quantum mechanical (red) atomic trajectories for tilt angles between $\theta = 0°$-$\theta = 75°$ in steps of $\theta = 15°$. (a) $\omega_z = 2\pi \times 167$ rad s^{-1} (b) $\omega_z = 2\pi \times 172$ rad s^{-1} (c) $\omega_z = 2\pi \times 192$ rad s^{-1}

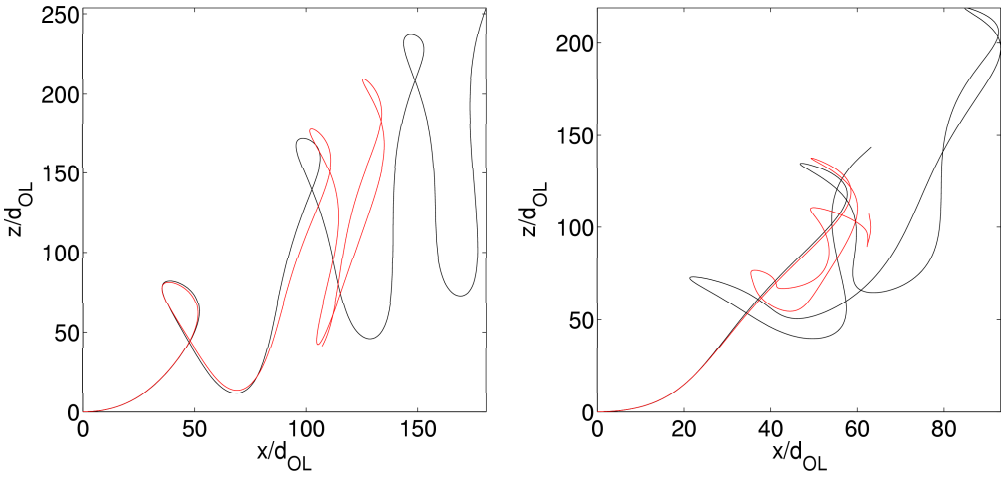

(d) $\theta = 45°$ (e) $\theta = 60°$

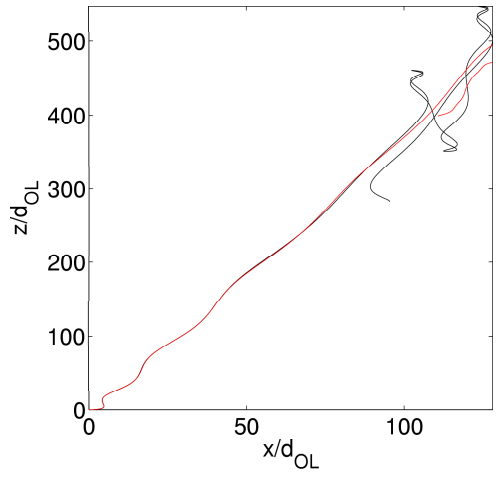

(f) $\theta = 75°$

Figure 5.12: Continued: (d) $\omega_z = 2\pi \times 236$ rad s^{-1} (e) $\omega_z = 2\pi \times 333$ rad s^{-1} (f) $\omega_z = 2\pi \times 643$ rad s^{-1}

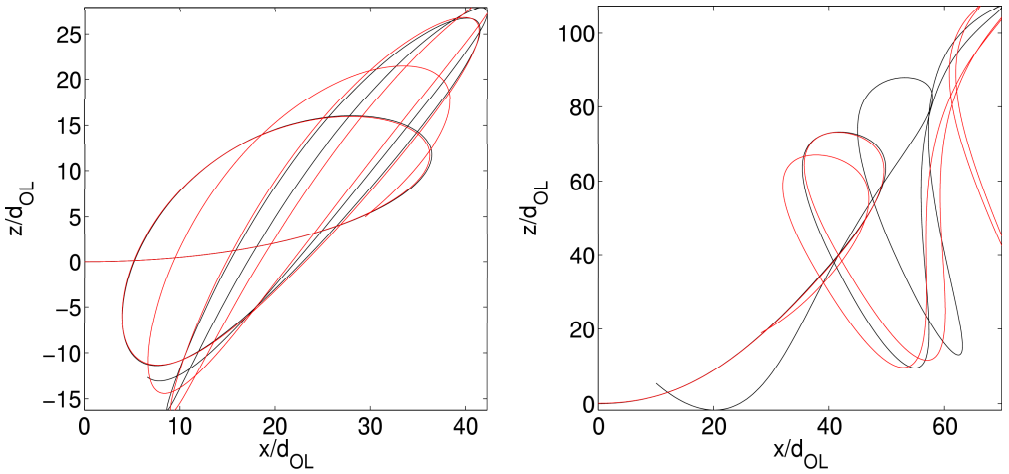

(a) $\theta = 15°$ (b) $\theta = 45°$

Figure 5.13: Comparison between non-resonant $r = (1 + \sqrt{5})/4$ semiclassical (black) and mean quantum mechanical (red) atomic trajectories for different tilt angles. (a) $\omega_z = 2\pi \times 213$ rad s^{-1} (b) $\omega_z = 2\pi \times 291$ rad s^{-1}

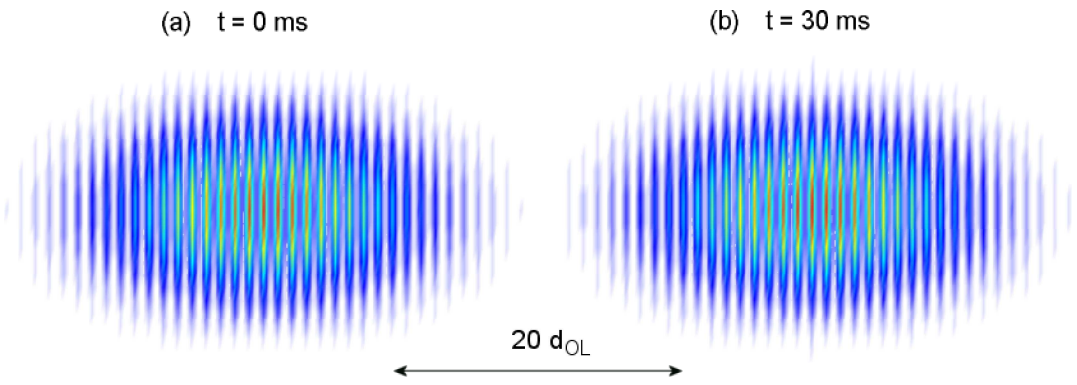

Figure 5.14: Surface plot of the sodium atom probability density function at times $t = 0$ ms and $t = 30$ ms, for $\theta = 0°$ and $\omega_z = 2\pi \times 167$ rad s^{-1}.

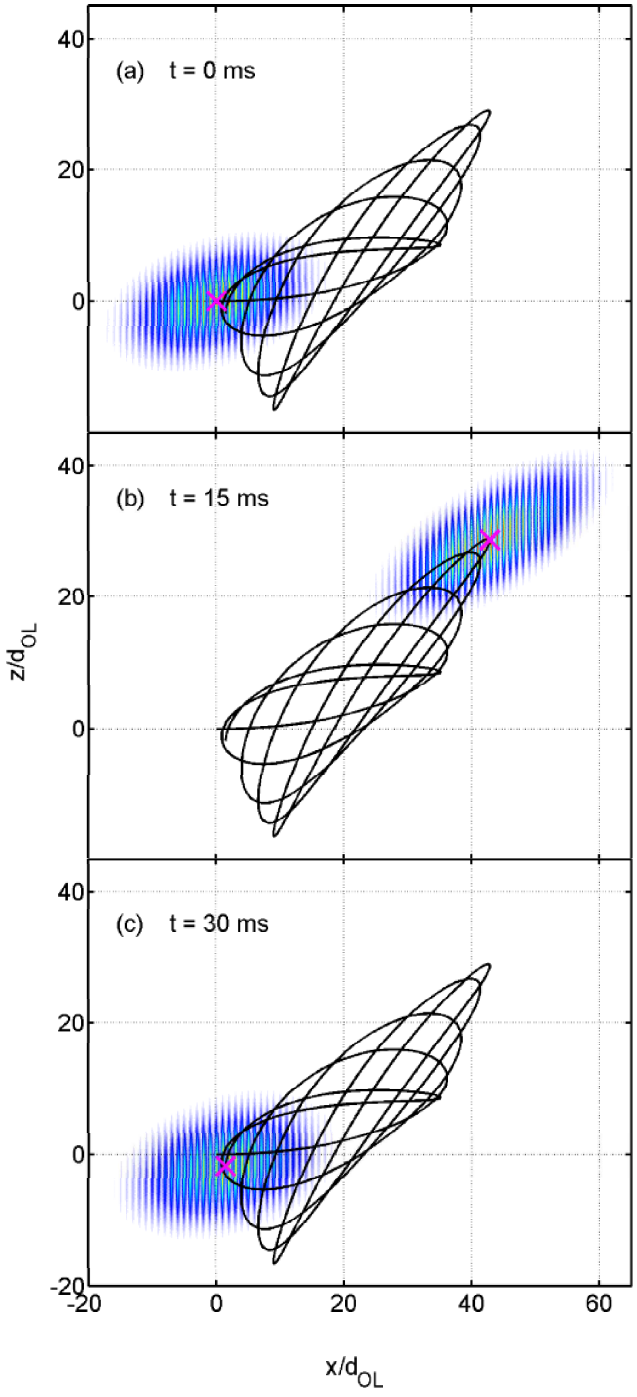

Figure 5.15: Snapshots of the time-evolution of the atomic probability distribution, for $r = (1+\sqrt{5})/4$, $\theta = 15°$ and $\omega_z = 2\pi \times 213$ rad s^{-1}. Surface plots of the probability distribution at times (a) $t = 0$ ms, (b) $t = 15$ ms and (c) $t = 30$ ms are shown. The mean trajectory is overlaid in black, whilst the magenta cross marks the point on the trajectory corresponding to the current frame.

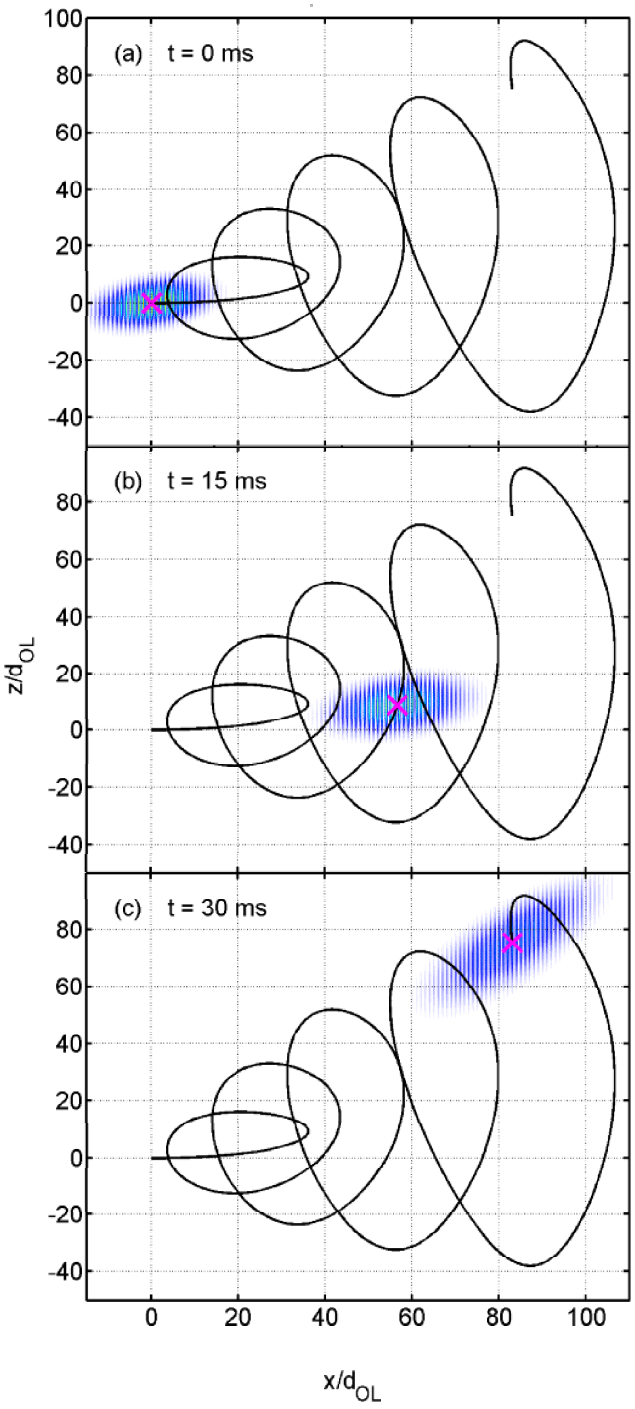

Figure 5.16: Snapshots of the time-evolution of the atomic probability distribution, for $r = 1$, $\theta = 15°$ and $\omega_z = 2\pi \times 172$ rad s^{-1}. Surface plots of the probability distribution at times (a) $t = 0$ ms, (b) $t = 15$ ms and (c) $t = 30$ ms are shown. The mean trajectory is overlaid in black, whilst the magenta cross marks the point on the trajectory corresponding to the current frame.

and the corresponding semiclassical trajectory (dotted line) are overlaid upon the motion. In figures 5.17(a) and (b), the agreement between the two trajectories is good and the probability density function shows little sign of change. However in figure 5.17(c), after the first turning point, the probability density is clearly much more diffuse. By figure 5.17(d) the mean position of the wavefunction has separated from the semiclassical path, and the probability density becomes yet more diffuse upon executing another loop in figure 5.17(e). In figures 5.17(f), (g) and (h), whilst some part of the wavefunction appears to lie on the semiclassical path, a large fraction has been reflected back along the direction of the gutter potential whilst still executing oscillations in the z direction.

Figure 5.18 depicts the variations in probability density for $r = 1$ when $\theta = 60°$. Once more, whilst 5.18(a) and (b) show good agreement between the quantum mechanical (solid) and semiclassical (dotted) paths, 5.18(c) marks a sudden elongation in the probability density function at the first sharp turning point, after which part of the wavefunction appears to follow the semiclassical trajectory in some sense in figures 5.18(d), (e) and (f). The majority, however, appears to be deflected backwards to oscillate along the length of the gutter potential.

Clearly, the significant changes that occur in the wavepacket as θ is increased show that it is not behaving as a single point particle, hence the deviation of the quantum mechanical paths from the semiclassical case shown in section 5.3.2 is to be expected. Changes in the internal structure affect the centre-of-mass motion, which then deviates from the single particle case. This is because forces are acting to change the wavepacket, which alters the energy associated with its internal structure, as well as its centre-of-mass motion. It is proposed that the origin of these deforming forces is the gutter potential, just as the magnetic field potential was responsible for the difference between quantum mechanical and semiclassical electron trajectories in the previous chapter.

When $\theta > 0°$, the gutter presents a potential energy barrier to the atom. This potential increases nonlinearly in both the x and z directions, thus the force which it exerts upon the atom increases nonlinearly with distance travelled. As the tilt angle of the gutter is increased, it rises increasingly steeply in the x direction. Furthermore, to satisfy the resonance condition, ω_z must increase as θ increases, making the curvature of the gutter potential even greater at high tilt angles. Thus, if a wavefunction is diffuse in real space, the force exerted by the gutter (which is responsible for xz coupling) varies significantly across the atomic wavepacket.

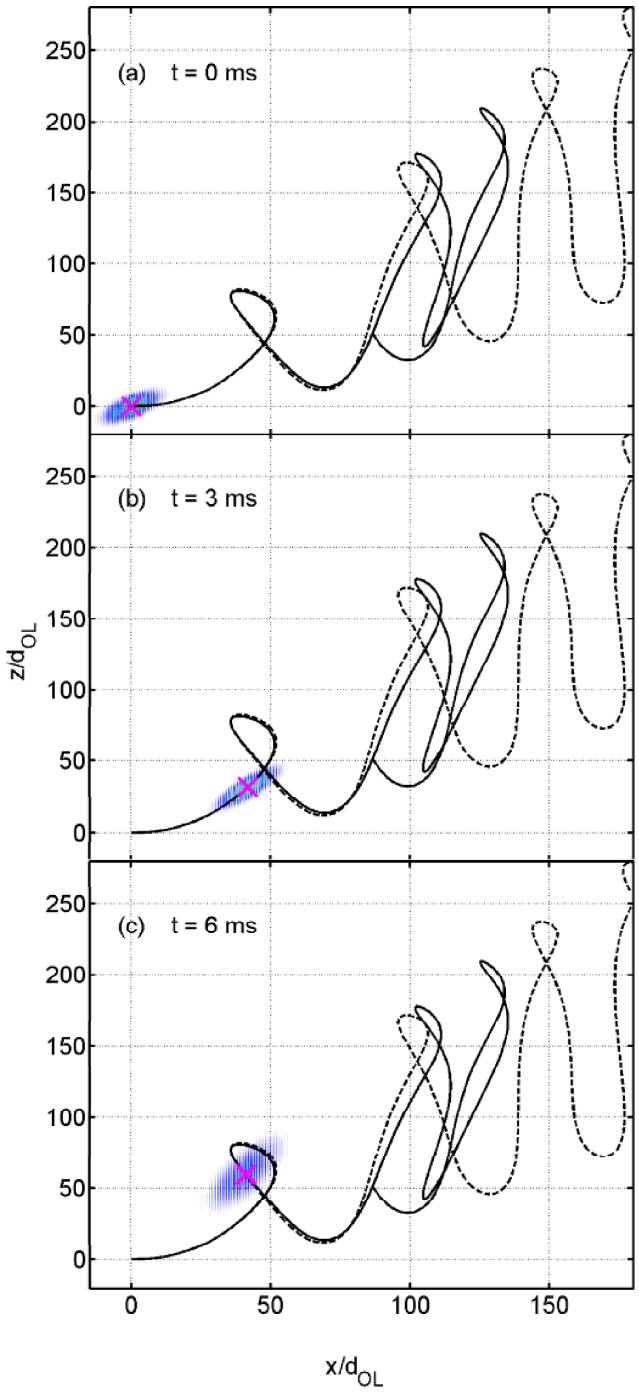

Figure 5.17: Snapshots of the time-evolution of the atomic probability distribution, for $r = 1$, $\theta = 45°$ and $\omega_z = 2\pi \times 236$ rad s^{-1}. Surface plots of the probability distribution at times (a) $t = 0$ ms, (b) $t = 3$ ms, (c) $t = 6$ ms, (d) $t = 9$ ms, (e) $t = 12$ ms, (f) $t = 15$ ms, (g) $t = 18$ ms and (h) $t = 21$ ms are shown. The mean trajectory is overlaid in black, whilst the magenta cross marks the point on the trajectory corresponding to the current frame.

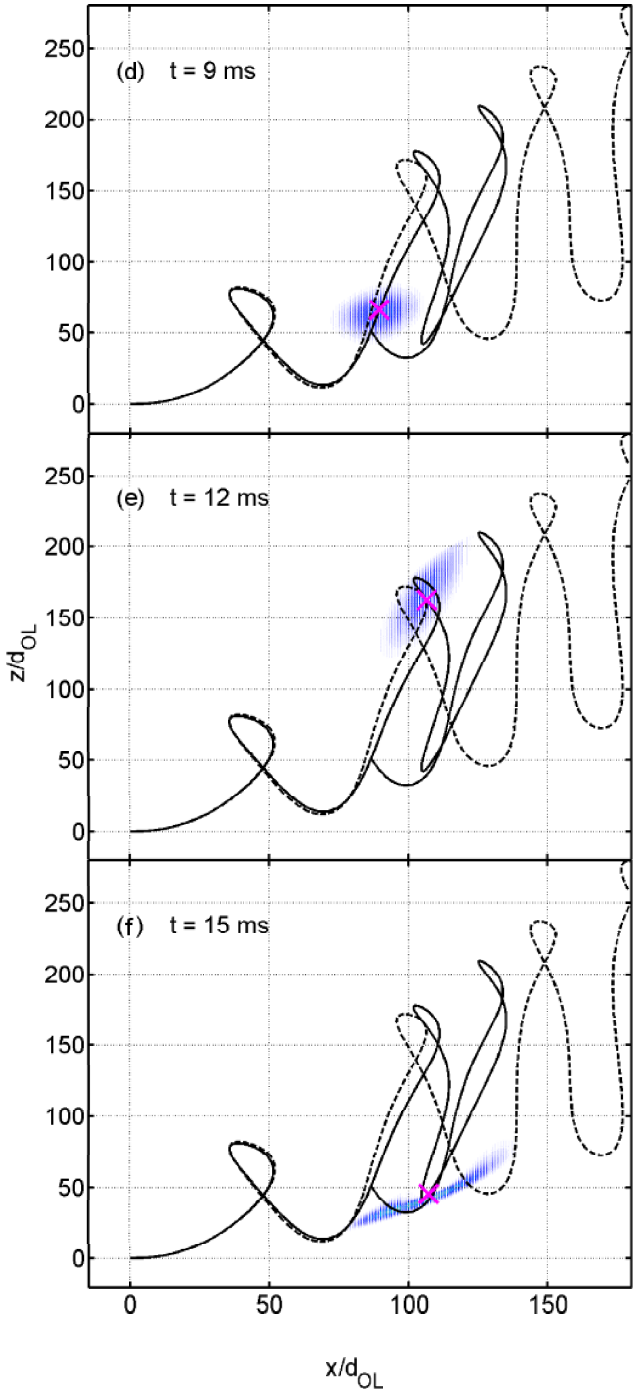

Figure 5.17: Continued.

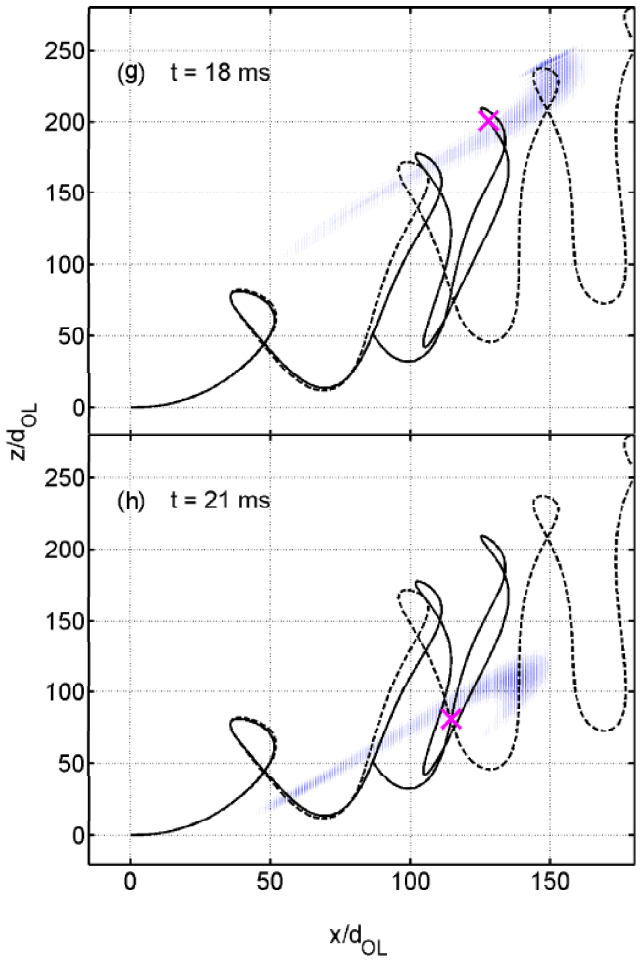

Figure 5.17: Continued.

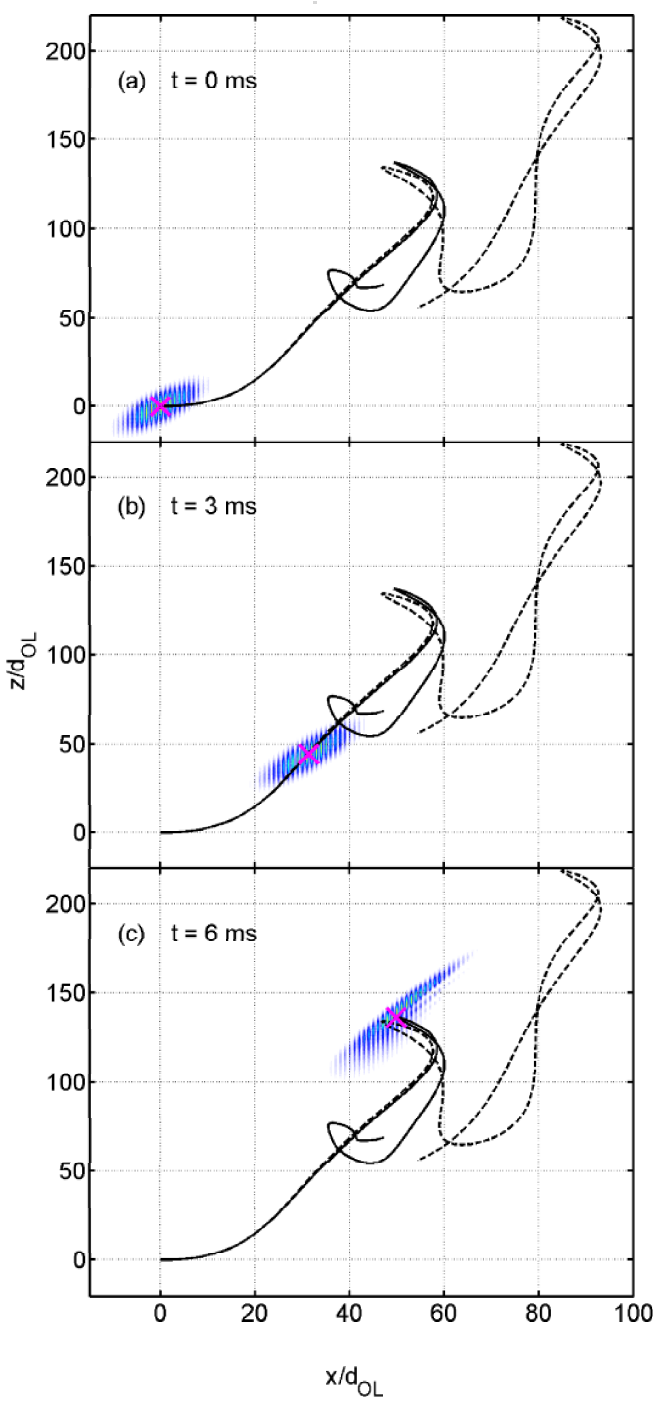

Figure 5.18: Snapshots of the time-evolution of the atomic probability distribution, for $r = 1$, $\theta = 60°$ and $\omega_z = 2\pi \times 333$ rad s^{-1}. Surface plots of the probability distribution at times (a) $t = 0$ ms, (b) $t = 3$ ms, (c) $t = 6$ ms, (d) $t = 9$ ms, (e) $t = 12$ ms and (f) $t = 15$ ms are shown. The mean trajectory is overlaid in black, whilst the magenta cross marks the point on the trajectory corresponding to the current frame.

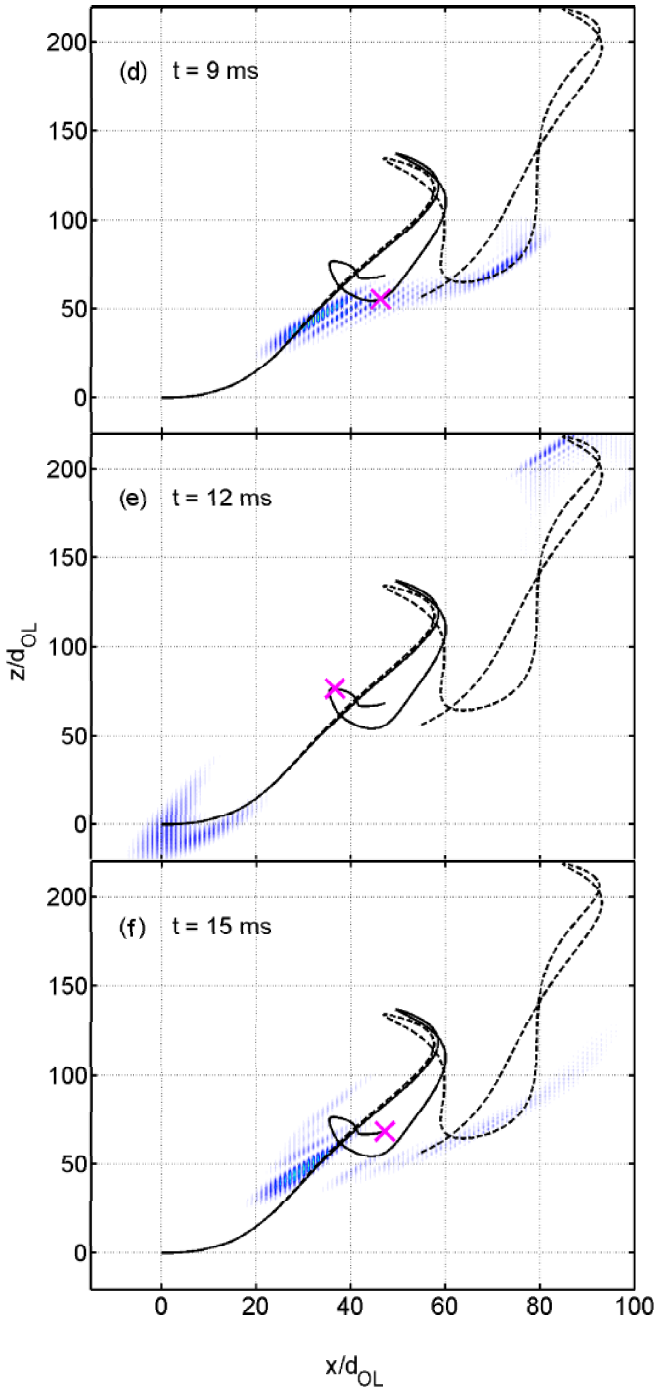

Figure 5.18: Continued.

Hence the wavepacket responds to an average force that is not equal to the local force at the point of highest probability density (due to the spatial nonlinearity of the gutter potential). For correspondence with semiclassical dynamics the assumption that force varies slowly over the wavepacket must be valid, and this is clearly not the case here. At turning points in the trajectory, the leading edge of the wavepacket experiences very high differential forces due to the gutter potential. These forces strongly distort the wavepacket, triggering the deviation of the quantum mechanical and semiclassical paths, as is particularly apparent in figures 5.17 and 5.18. Note that the atomic wavepacket (figure 5.11) is very much more diffuse than was the case for the electron previously studied (figure 4.17). This difference in extent arose as a result of the different approaches taken to selecting the initial wavefunction (discussed in sections 4.3.1 and 5.3.1). As a result, the differential forces acting across the wavepacket due to the changing gutter potential are very much larger in the atomic case, which explains the fact that even at high tilt angles the quantum mechanical electron analysis still tended to show a reasonable level of consistency with the semiclassical model.

It also helps to consider the relative magnitudes of the gravitational and confining potential energies for various angles. Firstly, note that the change in gravitational potential energy per lattice period is always the same, regardless of atomic position or tilt angle:

$$-m_a g d_{OL} \sim 0.5 \text{ peV}. \tag{5.23}$$

The effect of this is to try and push the atom through the optical lattice, moving it in the direction of the gutter. However, calculating the change in gutter potential energy (due to movement between points b and a separated by a distance d_{OL} in the direction of the lattice):

$$\frac{1}{2} m_a \omega_z^2 (z_t^2(b) - z_t^2(a)), \tag{5.24}$$

we find that equation (5.24) yields approximately 1.2 peV, 1.8 peV and 2.2 peV for $\theta = 30°$, $45°$ and $60°$ respectively in the region where each trajectory begins to deviate significantly. So when we begin to observe large separations in the two paths, the effect of the gutter potential is approximately four times greater than that of the force pushing the atom through the system. Combined with this factor is the issue of the barriers presented by the optical lattice. As the gutter

is tilted, even though the applied gravitational force remains in the x direction, the overall direction of motion is along the direction of the gutter. Therefore the effective thickness of the barriers presented by the optical lattice potential along the direction of motion increases as θ increases. Furthermore, when the atom travels a long way up the banks of the gutter, the high potential energy (~ 100 peV when the atom deviates for $\theta = 30°$) will begin to strongly perturb or even break the band structure in that region.

The net effect is that when an atom moving along a narrow tilted gutter potential undergoes a rapid change in direction, there is some quantum mechanical probability that the atom will be reflected back along the gutter. When the gutter is tilted at a large angle, the intial wavefunction is more diffuse since it can spread a greater distance along the gutter, leading to a reduction in the amplitude of the cross-sectional probability density in the x direction. In addition, the atom tends to have higher velocities when θ is large and so the wavefunction is required to respond more quickly to sudden changes. Under these conditions there appears to be an increased chance that a substantial part of the wavefunction is reflected. Hence a large fraction is dominated by the influence of the gutter potential, whilst a small part continues to spread along the semiclassical path. Since the mean trajectory is an average of both of these effects, it separates from the semiclassical path at the point when the wavefunction distorts.

Chapter 6

Bose-Einstein condensates in an optical lattice and a tilted magnetic gutter

6.1 Introduction

In the previous chapter, non-KAM chaotic dynamics of a single ultracold sodium atom were investigated. Here, we consider a related system involving a Bose-Einstein condensate (BEC): a dilute cloud typically containing many thousands of ultracold atoms, of which approximately 99% are in the gound state of the system following cooling to nanokelvin temperatures. When there are no changes in the internal structure of a condensate, its quantum mechanical motion mimics the semiclassical dynamics of the single atom case. However, if the internal structure of the BEC changes, the quantum behaviour deviates from this semiclassical path. Hence such deviations provide a useful test to see whether changes in the internal structure of a condensate are significant. Previous studies have applied this idea to the case of a condensate performing Bloch oscillations in the lowest band of an optical lattice [70]. It was found that when manipulating the condensate's phase and density via Bloch oscillations, solitons and vortices were produced, which led to breakdown of the Bloch oscillations. Here, we will consider the motion of a condensate in a non-KAM chaotic regime and compare this to the results obtained in chapter 5 in order to study whether the onset of chaos creates topological excitations in the BEC, which change the internal structure of the atom cloud.

When analysing the dynamics of a BEC, we must take into account the leading role that the interatomic interactions play in the energetics of the system. The strength of the interactions is characterised by the s-wave scattering length, a (see section 2.4). It is possible, by applying a magnetic field, to tune the magnitude and sign of the effective atom-atom interaction via Feshbach resonances [7]. Near a Feshbach resonance, the scattering length is given by

$$a = \tilde{a}\left(1 - \frac{\Delta_{FB}}{B - B_0}\right) \tag{6.1}$$

where $\tilde{a}$ is the scattering length away from the resonance and Δ_{FB} parametrises the width of the resonance at $B = B_0$. Predictions of the Feshbach resonances in sodium were made in 1995 [71], and these were observed experimentally in a sodium condensate in 1998 [72]. By comparing the case of a non-interacting atom firstly to a BEC in a weakly interacting regime, and then secondly to the strongly interacting regime, the theorist can more easily identify the role played by interactions in the system. We will consider the non-KAM chaotic quantum dynamics for different strengths of the interaction parameter.

We shall model a ^{23}Na condensate comprising $N_A = 10^4$ atoms which is prepared in a one-dimensional optical lattice and a harmonic trapping potential. Experimentally, this type of trap has been created using lasers rather than magnetically [7] - a necessary factor since an optical trapping potential is not affected by the application of magnetic fields to excite Feshbach resonances [72]. One can therefore apply an additional magnetic field to vary a by means of the Feshbach resonance. Other than this, the system is identical to that specified in chapter 5. Once the condensate has settled into the ground state of the system, the trap is again switched off in the x_t direction to create a gutter potential. Numerical simulations of the wavefunction in two dimensions are then performed with the interatomic interactions set initially to a low strength interaction and later, to the full strength of interactions between sodium atoms in a dilute cloud. The gutter frequency ω_z is adjusted to produce both on and off resonance conditions for various tilt angles, and once more the quantum mechanical trajectories of the wavefunctions are calculated as the atom falls through the optical lattice, for comparison to single-atom semiclassical results.

Although one- and two-dimensional systems may at first seem to have no relevance to real systems, Choi reminds us that it is reasonable to model BEC dynamics in the direction of the standing wave in a 1D approximation provid-

ing the proposed experimental processes along this direction have much shorter temporal periods than any effects which may occur in the perpendicular directions [73]. The reader should also note that work on condensates is often done using nearly two dimensional systems, such as a cigar-shaped or pancake-shaped BEC, in which the third dimension is very small compared with the other two due to very high trap frequencies. Hence, theoretical two dimensional studies are frequently of interest, whilst also being much faster to calculate than the three-dimensional case.

6.2 The quantum mechanics of the system

The quantum mechanical Hamiltonian of the system is as in previous chapters:

$$H = -\frac{\hbar^2}{2m_a}\left(\frac{\partial^2}{\partial x^2} + \frac{\partial^2}{\partial z^2}\right) + V_{ext}(x,z) + V_{OL}(x) \tag{6.2}$$

where the optical lattice is again defined as in the experiment by Wilkinson [67], such that

$$V_{OL}(x) = V_0 \sin^2\left(\frac{\pi x}{d_{OL}}\right), \tag{6.3}$$

and where V_{ext} is as previously specified by equations (5.6) and (5.8) in section 5.2 for the trapping and the dynamical stages of the calculations respectively. However, when modelling a BEC the Schrödinger equation is no longer sufficient - the Gross-Pitaevskii equation (see section 2.4.2) must be employed to incorporate the effects of the interatomic forces. The effective interaction between two particles at low energies is given by

$$U_0 = \frac{4\pi\hbar^2 a}{m_a}, \tag{6.4}$$

where for an alkali atom a is typically of order one hundred times the Bohr radius, $a_0 \approx 0.0529$ nm. Treating the system using a mean-field approximation results in a nonlinear Schrödinger equation

$$i\hbar\frac{\partial\Psi}{\partial t} = H\Psi + U_0|\Psi|^2\Psi \tag{6.5}$$

where the Hamiltonian has been defined in equation (6.2).

The Gross-Pitaevskii equation assumes firstly that the temperature of the

condensate is absolute zero (which is a good approximation for condensates well below the transition temperature, T_c). For the parameters studied here, T_c will be in the range [7]

$$T_c \approx 4.5 \left(\frac{\bar{\omega}}{100\pi}\right) \left(\frac{N_A}{8}\right)^{\frac{1}{3}} \sim 100 \text{ - } 250 \text{ nK}, \tag{6.6}$$

where the expression for T_c is approximated from the rigorous derivation of T_c in [7], and where $\bar{\omega}$ is the geometric mean of the trapping frequencies:

$$\bar{\omega} = (\omega_x \omega_y \omega_z)^{\frac{1}{3}} . \tag{6.7}$$

The second assumption is that the mean inter-particle spacing is much greater than a. For the condensates considered here, the densities are of order 10^{14} cm^{-3} and so the mean inter-particle spacing is $\sim$200 nm. Therefore, since the typical value of a is $\sim 100a_0 \sim 5$ nm, use of the Gross-Pitaevskii equation is clearly justified. This equation is solved numerically via the Crank-Nicolson method [60], which is described as applied to the Gross-Pitaevskii equation in Appendix C.

It is particularly important to be sure that the condensate wavefunction is in the ground state of the system before attempting to predict its time-dependent evolution, since an initially excited wavefunction may well lead to confusion when trying to ascertain the effect of chaos on the system. An imaginary time algorithm is again employed to determine the ground state of the system numerically [69], as described for the single atom case in section 5.3.1. However, in the case of the condensate, the wavefunction is renormalised to the total number of atoms. Simulations are performed with a taken to be either 0.45 nm or 4.5 nm (the latter being the typical interaction parameter for ^{23}Na [7]), with the aim of clarifying the role of interactions in the system.

Figures 6.1 and 6.2 show examples of the initial condensate density. In figure 6.1, $\theta = 15°$ and $a = 0.45$ nm, and in figure 6.2 $\theta = 60°$ and $a = 4.5$ nm. A cross section of the density in the x direction (for $z = 0$) is plotted in (a), whilst (b) is a surface plot of the density. Both surface plots use the same scale to allow direct appreciation of the effects of varying θ and a.

When θ is small, the area occupied by the initial state is small and the peak density is high (see figure 6.1(b)). Increasing θ increases the size of the BEC because the wavefunction is able to spread out further along the gutter (figure 6.2(b)). This also causes a decrease in the peak condensate density. When a

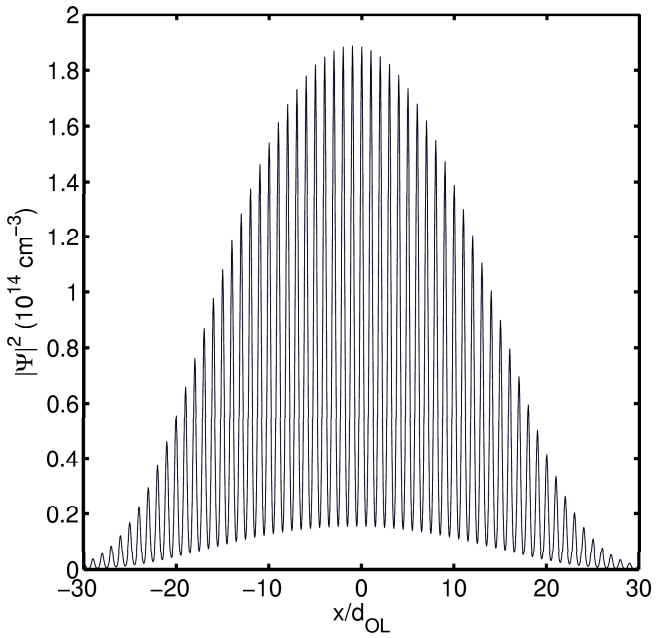

(a)

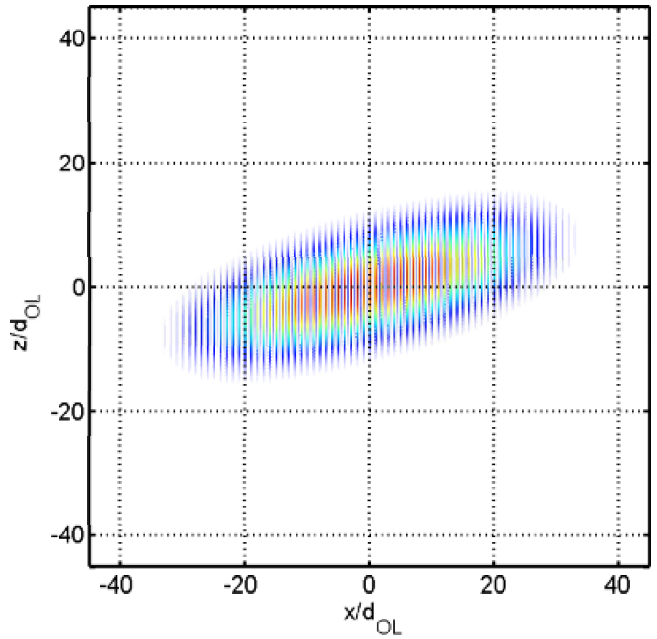

(b)

Figure 6.1: Ground state of the condensate for the case when $\theta = 15°$ and the interaction parameter $a = 0.45$ nm. (a) Cross section of the density along $z = 0$. (b) Surface plot of the condensate density.

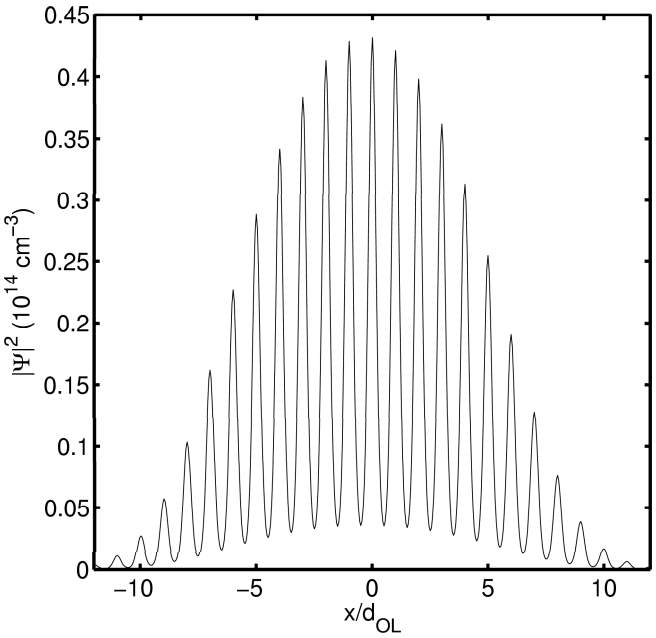

(a)

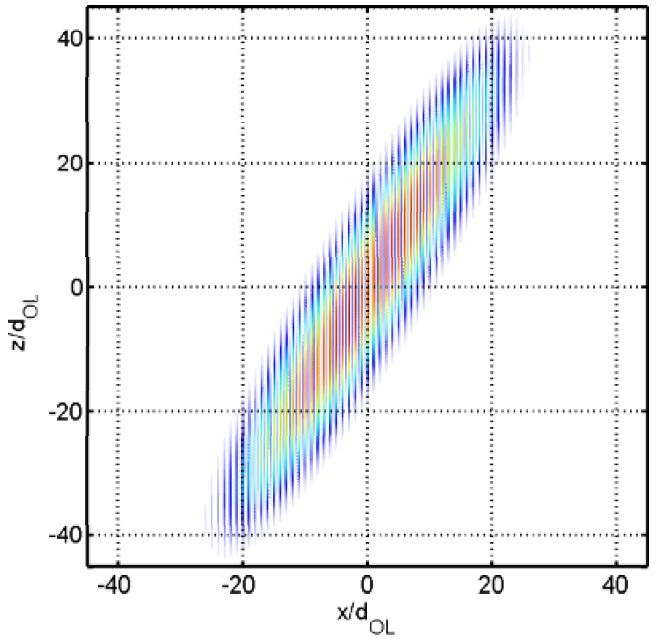

(b)

Figure 6.2: Ground state of the condensate for the case when $\theta = 60°$ and the interaction parameter $a = 4.5$ nm. (a) Cross section of the density along $z = 0$. (b) Surface plot of the condensate density.

is small there is less repulsive force between the atoms of the condensate, thus smaller atom clouds of higher densities are possible. When a is large, the increased repulsion causes the atoms to spread out further, tending to increase the size of the atom cloud and lower the peak density.

6.3 Quantum mechanical trajectories

The trajectory of the wavepacket is determined in each instance by calculating $\langle x \rangle$ and $\langle z \rangle$ as a function of time as in previous chapters (see equations (4.47a) and (4.47b)). Plots of $< x >$ versus $< z >$ can then be compared to the results obtained in the semiclassical analysis of a single sodium atom in section 5.2. Taking into account the results obtained in chapter 5 for the single atom wavefunction, it seemed prudent to focus particularly on the case when $\theta = 15°$ since the quantum and semiclassical paths give better agreement at small θ.

6.3.1 Results for $a = 0.45$ nm

Figure 6.3(a) shows the mean path of the weakly interacting condensate (red) when $\theta = 0°$. Superimposed on the plot is the semiclassical single atom trajectory (black). Only motion in the x direction as a function of time is presented, since the z direction is of little interest when $\theta = 0°$. The condensate performs damped Bloch oscillations of the same frequency and initial amplitude as in the semiclassical model. This is as expected from the work of Scott [70], who numerically modelled damped Bloch oscillations in trapped Bose-Einstein condensates using an optical lattice potential.

Figure 6.3(b) shows the condensate and semiclassical single atom trajectories for $r = (1 + \sqrt{5})/4$, $\theta = 15°$ and $\omega_z = 2\pi \times 213$ rad s^{-1}. As in figure 6.3(a), the form of the trajectories shows good agreement, although the scale of the condensate path becomes gradually smaller than the semiclassical curve. The same is true of figure 6.3(c), where $r = 1$, $\theta = 15°$ and $\omega_z = 2\pi \times 172$ rad s^{-1}.

6.3.2 Results for $a = 4.5$ nm

In figure 6.3(d), $r = 1$, $\theta = 15°$ and $\omega_z = 2\pi \times 172$ rad s^{-1} (just as for figure 6.3(c)). But, the increased interaction strength causes the semiclassical and quantum mechanical paths to deviate much sooner and by a much greater amount than was

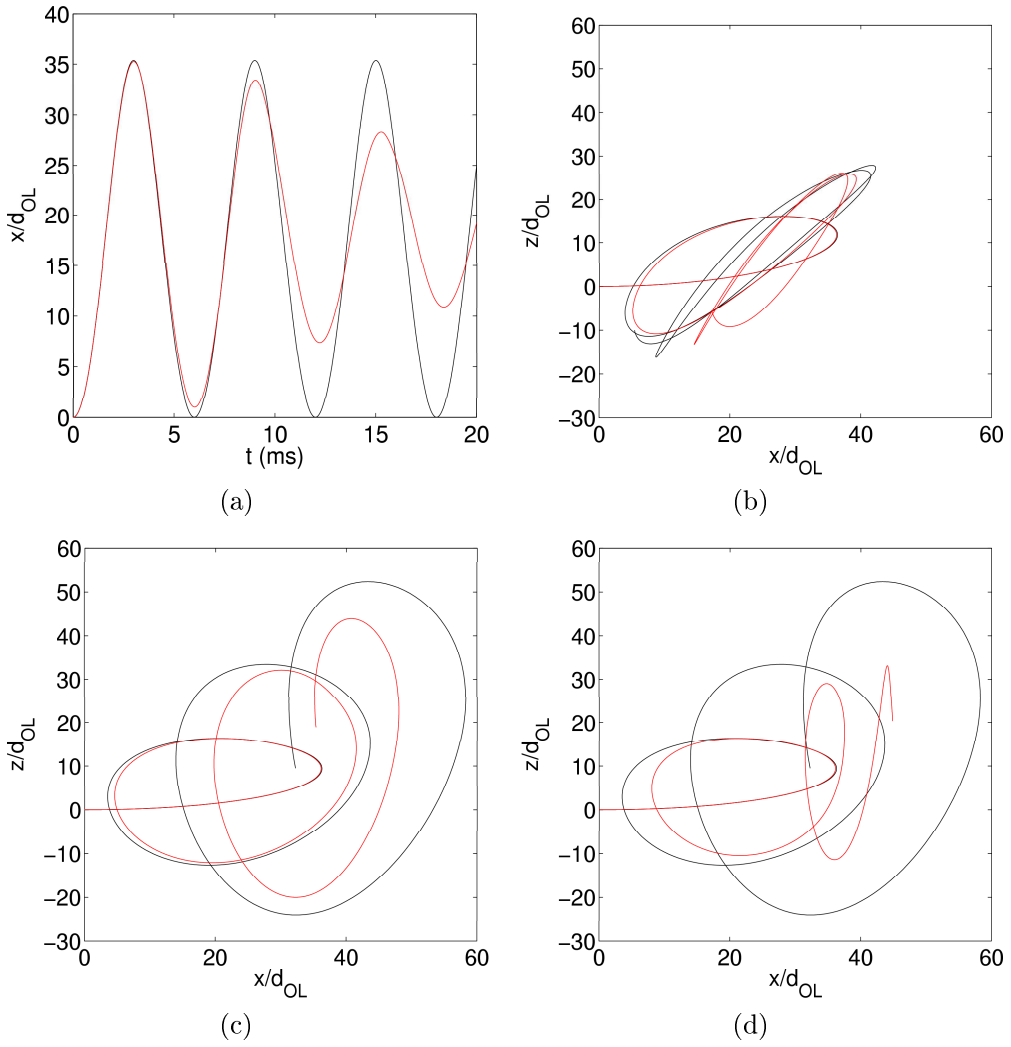

Figure 6.3: Comparison of semiclassical (black) single atom trajectories with mean quantum mechanical trajectories (red) calculated from the time evolution of the condensate wavefunction. (a) $a = 0.45$ nm, $\theta = 0°$, $\omega_z = 2\pi \times 167$ rad s^{-1} (b) $r = (1 + \sqrt{5})/4$, $a = 0.45$ nm, $\theta = 15°$, $\omega_z = 2\pi \times 213$ rad s^{-1} (c) $r = 1$, $a = 0.45$ nm, $\theta = 15°$, $\omega_z = 2\pi \times 172$ rad s^{-1} (d) $r = 1$, $a = 4.5$ nm, $\theta = 15°$, $\omega_z = 2\pi \times 172$ rad s^{-1}

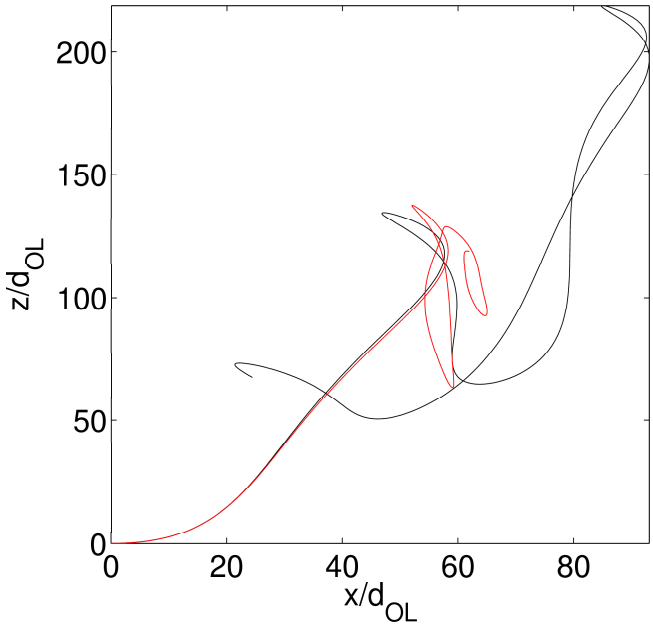

Figure 6.4: Comparison of semiclassical (black) single atom trajectory with mean quantum mechanical trajectory (red) calculated from the time evolution of the condensate wavefunction, for the case when $r = 1$, $a = 4.5$ nm, $\theta = 60°$, $\omega_z = 2\pi \times 333$ rad s^{-1}.

the case in figure 6.3(c). The mean motion of the strongly interacting condensate initially resembles the semiclassical model, however it quickly deviates from this.

Figure 6.4 shows a comparison of quantum and semiclassical trajectories for the case when $r = 1$, $\theta = 60°$ and $\omega_z = 2\pi \times 333$ rad s^{-1}. Under these circumstances, the paths are coincident at short times until the first turning point is reached. But thereafter, the correspondence is rapidly lost. Indeed, the mean position of the condensate appears to become localised in a fairly small region compared with the highly extended single-atom paths that occur when $\theta = 60°$.

6.4 Consideration of the condensate wavefunction

This section explores the nature of the condensate wavefunction as it evolves along the mean trajectories presented in the previous section. Snapshots of the density are shown at various times for a selection of system parameters, overlaid with plots of the quantum mechanical mean position and (in some cases) the corresponding semiclassical path.

6.4.1 Results for $a = 0.45$ nm

In figures 6.5 and 6.6, $\theta = 15°$. The system is off resonance in figure 6.5 ($r = (1 + \sqrt{5})/4$, $\omega_z = 2\pi \times 213$ rad s^{-1}), and on resonance in figure 6.6 ($r = 1$, $\omega_z = 2\pi \times 172$ rad s^{-1}). In both cases the evolution of the condensate density displays similar properties. At $t = 3$ ms (figure 6.5(b) and figure 6.6(b)) the initial structure of the BEC remains intact. However, from $t = 6$ ms to $t = 9$ ms (figures 6.5(c)-(d) and 6.6(c)-(d)) the shape begins to change, indicating that the leading section of the condensate may break away. By $t = 12$ ms (figures 6.5(e) and 6.6(e)), the structure has clearly undergone substantial fragmentation, yet despite becoming increasingly dispersed as time proceeds (figures 6.5(f)-(h) and 6.6(f)-(h)), the mean position of the condensate continues to follow a damped version of the semiclassical path. Note that the semiclassical path has been omitted in figure 6.5 to avoid confusion due to the complex nature of the trajectory. However, the reader may refer back to figure 6.3(b) to view the semiclassical path.

In figure 6.7, the phase of the condensate wavefunction, defined as

$$\phi = \tan^{-1} \frac{Im\{\Psi\}}{Re\{\Psi\}}, \ 0 \leq \phi < 2\pi, \tag{6.8}$$

is considered at $t = 3$ ms for $r = 1$ (corresponding to the probability density shown in figure 6.6(b)). Figure 6.7(a) is a surface plot of the phase (neglecting points where the density is less than 2% of the maximum). White represents a phase of 0, whilst black is 2π. A cross section of the phase taken along the dashed line is shown in (b). The form of the condensate density along this line is also included in (c) for reference.

Scott [70] found that for a condensate performing simple Bloch oscillations, a standing wave is formed at the point of Bragg reflection, where the minima in the modulated probability density fall to zero at the maxima in $V_{OL}(x)$ and, across each zero, the phase changes abruptly by π. He showed that such standing waves were able to generate stationary solitons, depending upon the condensate density and the Bloch period. In figure 6.7(b), a number of discontinuities close to π can be seen in the phase (only one of these actually has magnitude π). Figure 6.7(c) also shows that the corresponding density minima have fallen sharply in comparison to the modulation observed in the initial state in figure 6.1, and are close to zero.

The reason we do not see a perfect standing wave as Scott did is because of

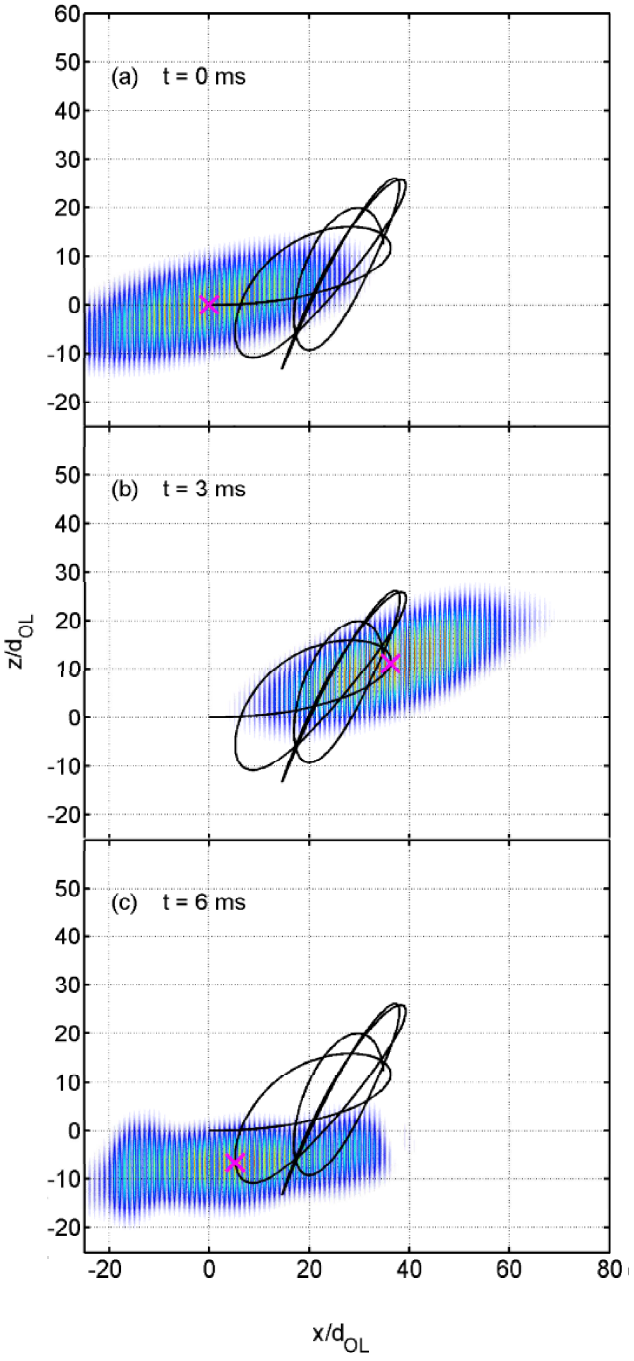

Figure 6.5: Snapshots of the time-evolution of the condensate density, for $r = (1+\sqrt{5})/4$, $a = 0.45$ nm, $\theta = 15°$ and $\omega_z = 2\pi \times 213$ rad s^{-1}. Surface plots of the probability distribution at times (a) $t = 0$ ms, (b) $t = 3$ ms, (c) $t = 6$ ms, (d) $t = 9$ ms, (e) $t = 12$ ms, (f) $t = 15$ ms, (g) $t = 18$ ms and (h) $t = 21$ ms are shown. The mean quantum mechanical trajectory is overlaid in black, whilst the magenta cross marks the point on the trajectory corresponding to the current frame.

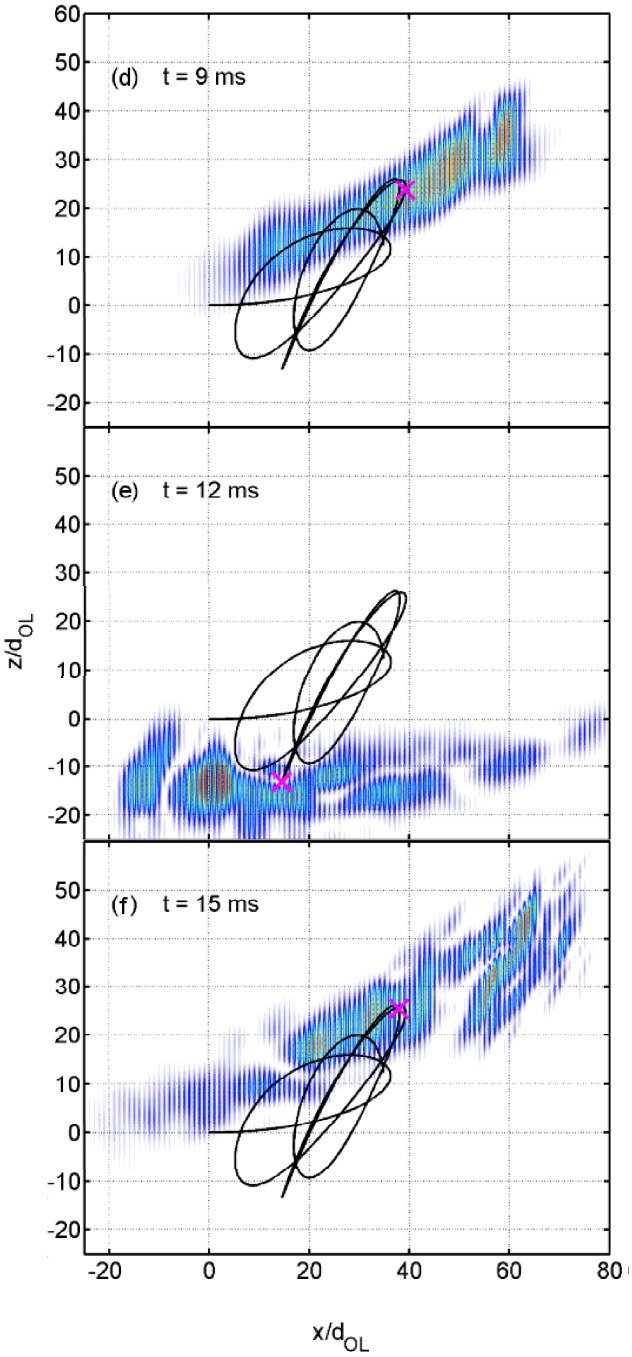

Figure 6.5: Continued.

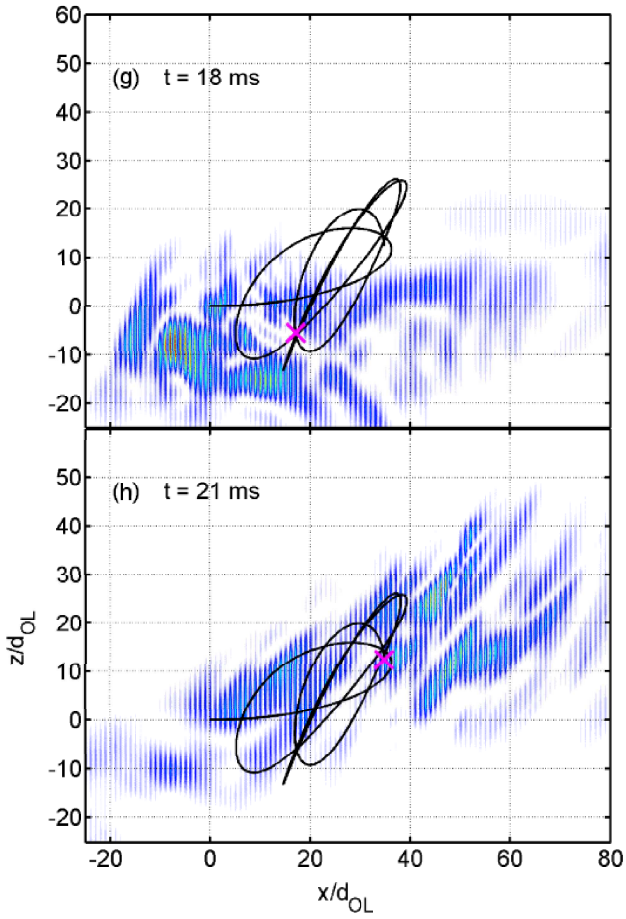

Figure 6.5: Continued.

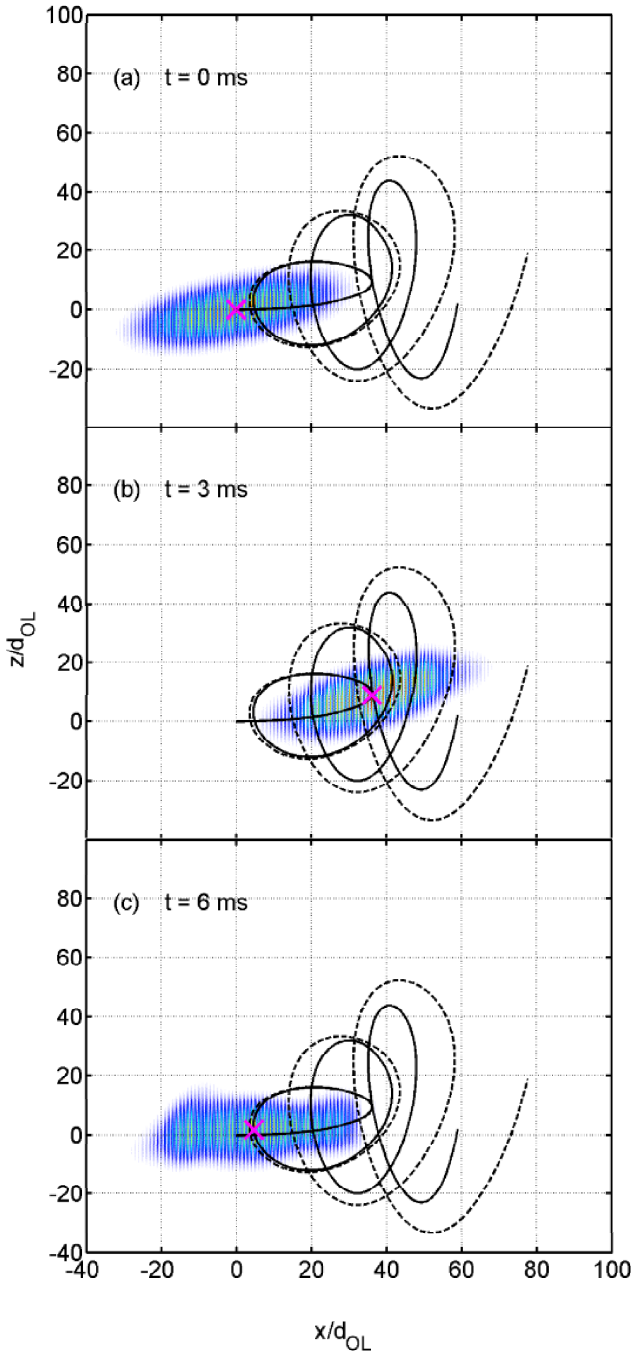

Figure 6.6: Snapshots of the time-evolution of the condensate density, for $r = 1$, $a = 0.45$ nm, $\theta = 15°$ and $\omega_z = 2\pi \times 172$ rad s^{-1}. Surface plots of the probability distribution at times (a) $t = 0$ ms, (b) $t = 3$ ms, (c) $t = 6$ ms, (d) $t = 9$ ms, (e) $t = 12$ ms, (f) $t = 15$ ms, (g) $t = 18$ ms and (h) $t = 21$ ms are shown. Both the mean quantum mechanical trajectory (solid line) and semiclassical single atom trajectory (dotted line) are overlaid, whilst the magenta cross marks the point on the quantum mechanical trajectory corresponding to the current frame.

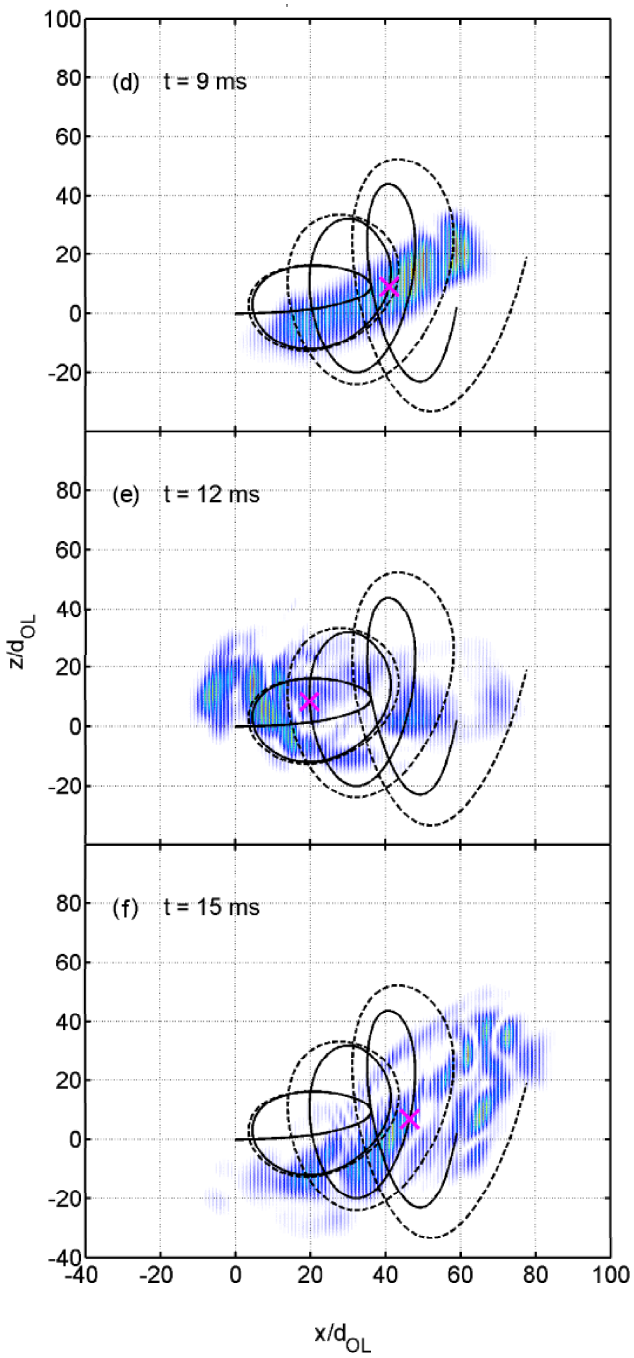

Figure 6.6: Continued.

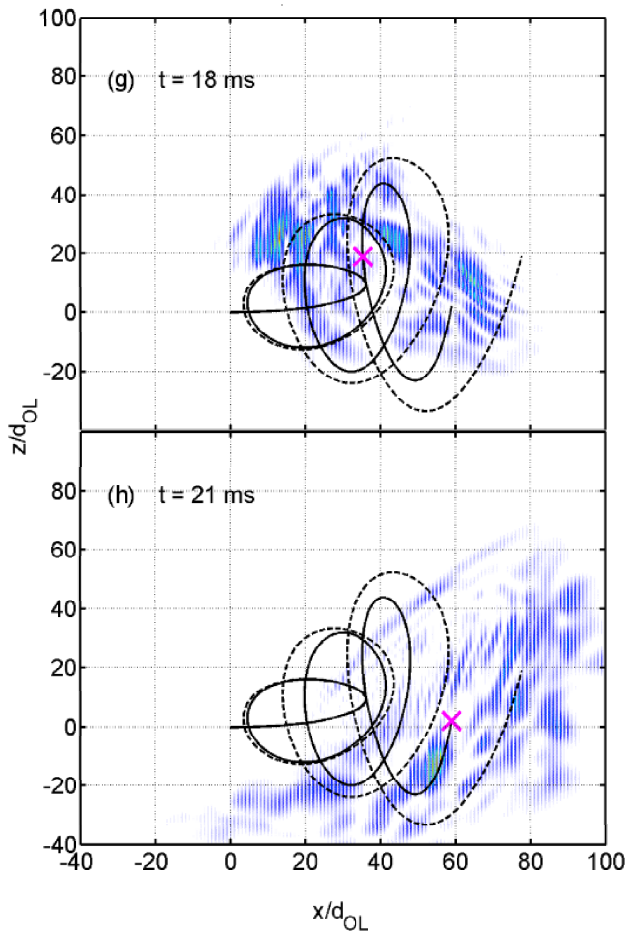

Figure 6.6: Continued.

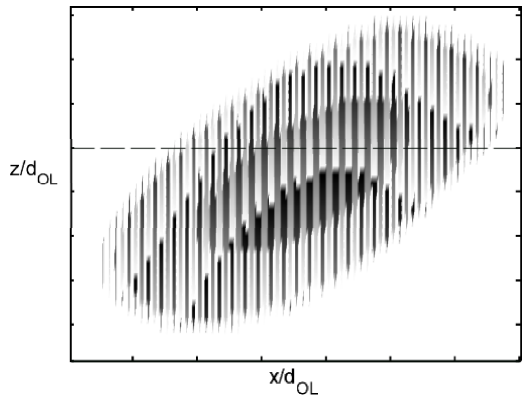

(a)

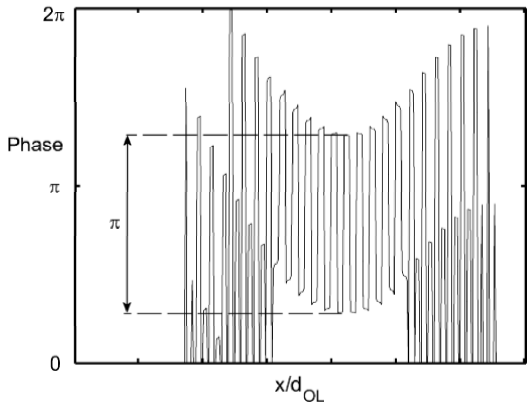

(b)

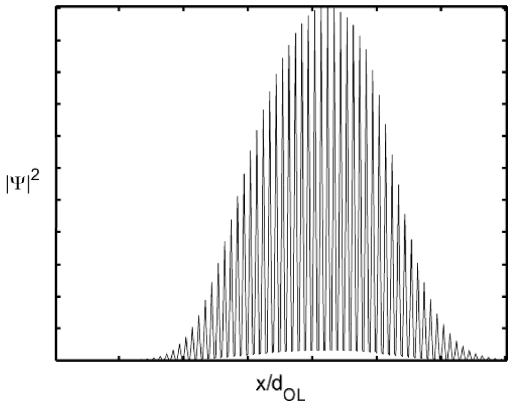

(c)

Figure 6.7: The phase of the condensate wavefunction (modulo 2π) at $t = 3$ ms for $r = 1$, $a = 0.45$ nm, $\theta = 15°$ and $\omega_z = 2\pi \times 172$ rad s^{-1}. (a) Surface plot of the phase. Black corresponds to a phase of 2π, white to zero phase. Phase is only shown for points where the probability density is at least 2% of the maximum value. (b) Cross section of the phase, taken along the dashed line in (a). (c) Cross section of the probability density function along the dashed line in (a).

the asymmetry of motion in this case. Scott's condensate underwent motion in the x direction only, in a symmetrical trap, whilst the condensate here is moving in a circular fashion through the x-z plane in an asymmetric potential. This prevents the appearance of a perfect interference pattern at the turning point. The fact that the wavepacket is not entirely stationary at the turning points here is the reason that the chain of discontinuities observed in the phase (figure 6.7(b)) do not have magnitude of exactly π. In experiments, laser illumination has been used to produce π phase shifts which subsequently evolved into dark solitons [30, 74, 75]. Thus it is reasonable to propose that the chain of phase changes $\sim \pi$ seen here also generate unstable solitons, that are responsible for the fragmentation of the condensate at times $t \gtrsim 12$ ms shown in figures 6.6(g) and (h).

However, the condensate motion begins to deviate from the semiclassical single atom path at significantly earlier times than this. Recall the discussion of the reduction in the mean quantum mechanical atomic velocity in the previous chapter, where the spread in real space of the wavepacket combined with the nonlinear curvature of the gutter potential led to large differential forces acting across the wavepacket. The same effect applies in this case, but since the interatomic interactions cause the wavepacket to spread out further in real space, greater deviations of the quantum mechanical trajectory from the semiclassical are seen at shorter times. This effect is reinforced, since the variation in force across the wavepacket leads to a variation in $\dot{k}$ across the wavepacket. Hence, the spread of the wavepacket in k-space will change, and any increase in the spread results in a decrease in the mean velocity, as shown previously.

6.4.2 Results for $a = 4.5$ nm

Figure 6.8 illustrates the density in the strongly interacting case when $r = 1$, $\theta = 15^\circ$ and $\omega_z = 2\pi \times 172$ rad s^{-1}. The mean path of the condensate (solid line) and semiclassical single atom trajectory (dashed line) are overlaid once more. In figure 6.8(a)-(c) the density remains uniform and there is little change to the condensate structure. However in 6.8(d)-(f), we see the condensate begin to deform shortly after the first significant change in direction. Soliton and vortex formation follows almost immediately, with regions of zero density appearing and deforming the shape of the condensate (e.g. the vortex marked by the arrow in figure 6.8(e)). This change in internal structure causes the quantum mechanical

path to deviate from the semiclassical one (figure 6.8(d)-(f)). Large numbers of similar patches of zero density subsequently appear (figure 6.8(g)-(i)), causing the condensate to explode, with the fragments continuing to oscillate along the gutter potential, and the correspondence between quantum mechanical and semiclassical paths is lost.

The reader should note that the time elapsing between frames is shorter than in previous figures since the breakdown of the condensate occurs more quickly due to the stronger interatomic interactions when $a = 4.5$ nm. Also, frames at later times are omitted entirely as there are no notable developments in the probability density function subsequent to the explosion of the condensate.

In figure 6.9, $r = 1$, $\theta = 60^\circ$ and $\omega_z = 2\pi \times 333$ rad s^{-1}. In this case, the condensate explodes even more rapidly (by $t = 9$ ms in figure 6.9(g)) and catastrophically than was the case when $\theta = 15^\circ$. It is clear that for $t \geq 9$ ms (figure 6.9(g) and (h)), the fragments of the wavefunction are simply diffusing along the gutter potential in both directions, with the result that the mean position remains approximately stationary in the x direction, whilst oscillating in the gutter in the z direction.

In the strongly interacting condensate, the spread of the wavepacket in real space is even larger. Thus, the differential forces acting due to the gutter potential are greater still (particularly at large tilt angles), and lead to enormous deformation of the wavepacket at much shorter times than in the weakly interacting case. It has been shown that strong spatial disruption of an atom cloud results in a huge spread in k-space due to the fact that atoms are moving in all directions [70]. Consequently $(k - k_p)^2$ increases substantially, reducing the mean velocity - a fact which is intuitive if we consider the fact that under such conditions the atoms are moving less coherently. Furthermore, explosive expansion of the atom cloud contributes an extra force acting along the direction of the lattice, which reduces the Bloch amplitude. These factors combine to produce the very low amplitudes of oscillation in the x direction observed at long times in the strongly interacting case.

Previous studies have focused on the effect that the initial density of the condensate has on the rate of soliton production [12]. High peak densities reduce the healing length ξ of the condensate, and so the expected width of solitons, $w \approx 2\xi$ decreases. As the soliton width approaches the spatial period of the optical lattice, soliton production becomes easier since the density nodes imprinted at Bragg reflection already closely resemble a chain of dark solitons. However,

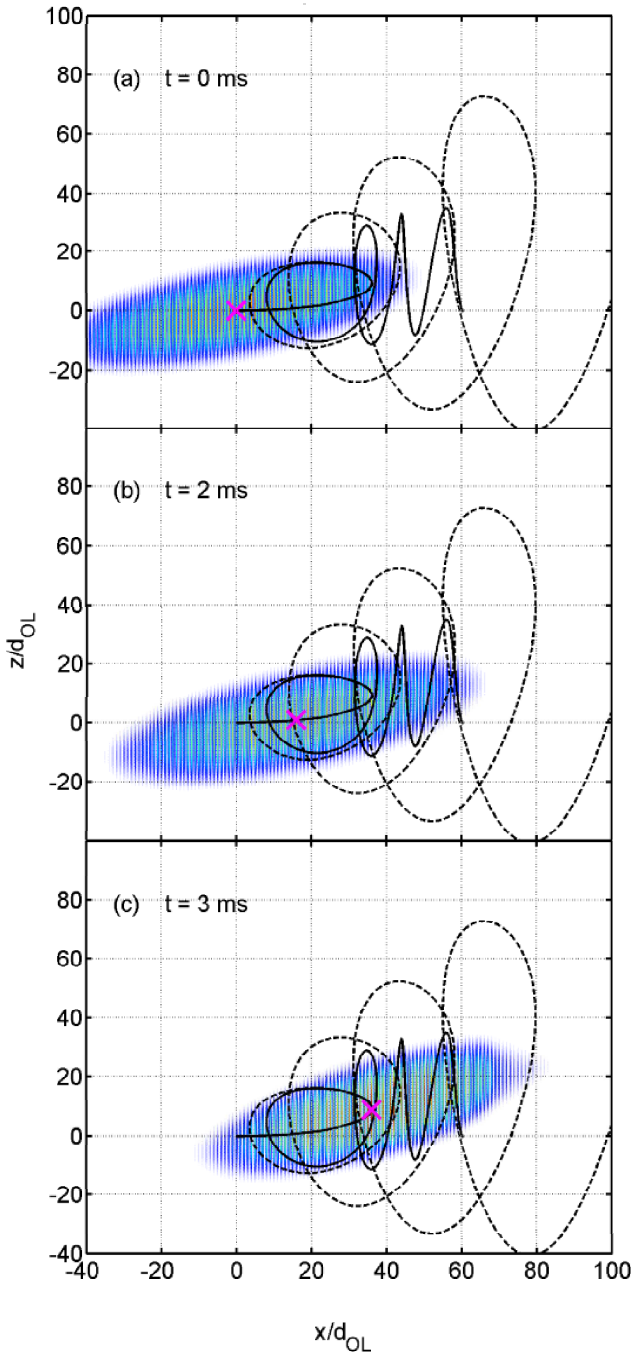

Figure 6.8: Snapshots of the time-evolution of the condensate density, for $r = 1$, $a = 4.5$ nm, $\theta = 15°$ and $\omega_z = 2\pi \times 172$ rad s^{-1}. Surface plots of the probability distribution at times (a) $t = 0$ ms, (b) $t = 2$ ms, (c) $t = 3$ ms, (d) $t = 5$ ms, (e) $t = 6$ ms, (f) $t = 8$ ms, (g) $t = 9$ ms, (h) $t = 11$ ms and (i) $t = 12$ ms are shown. Both the mean quantum mechanical trajectory (solid line) and semiclassical single atom trajectory (dotted line) are overlaid, whilst the magenta cross marks the point on the quantum mechanical trajectory corresponding to the current frame. The arrow in (e) marks the location of a vortex.

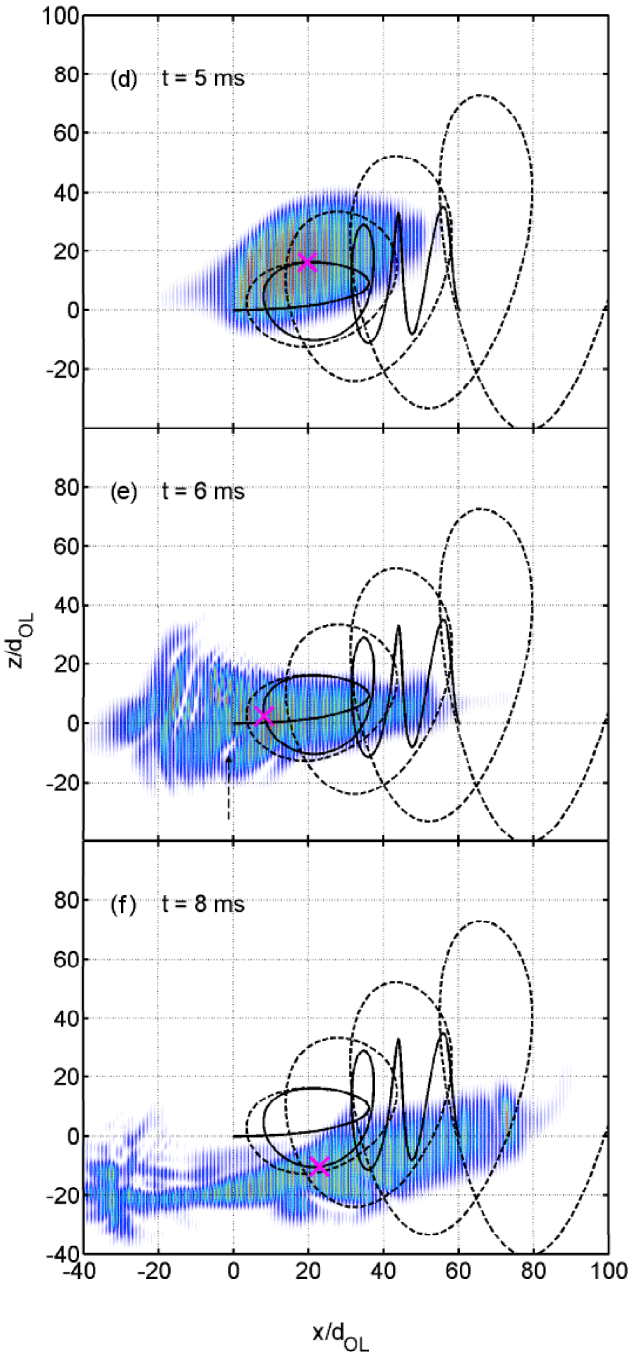

Figure 6.8: Continued.

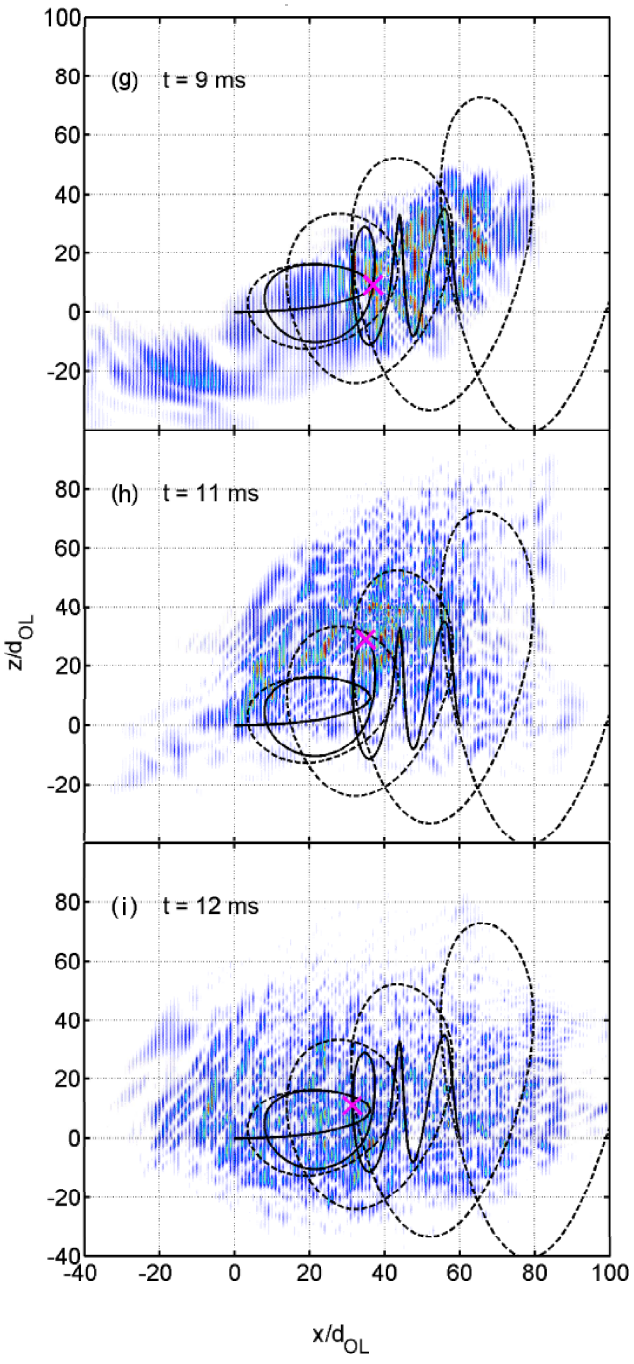

Figure 6.8: Continued.

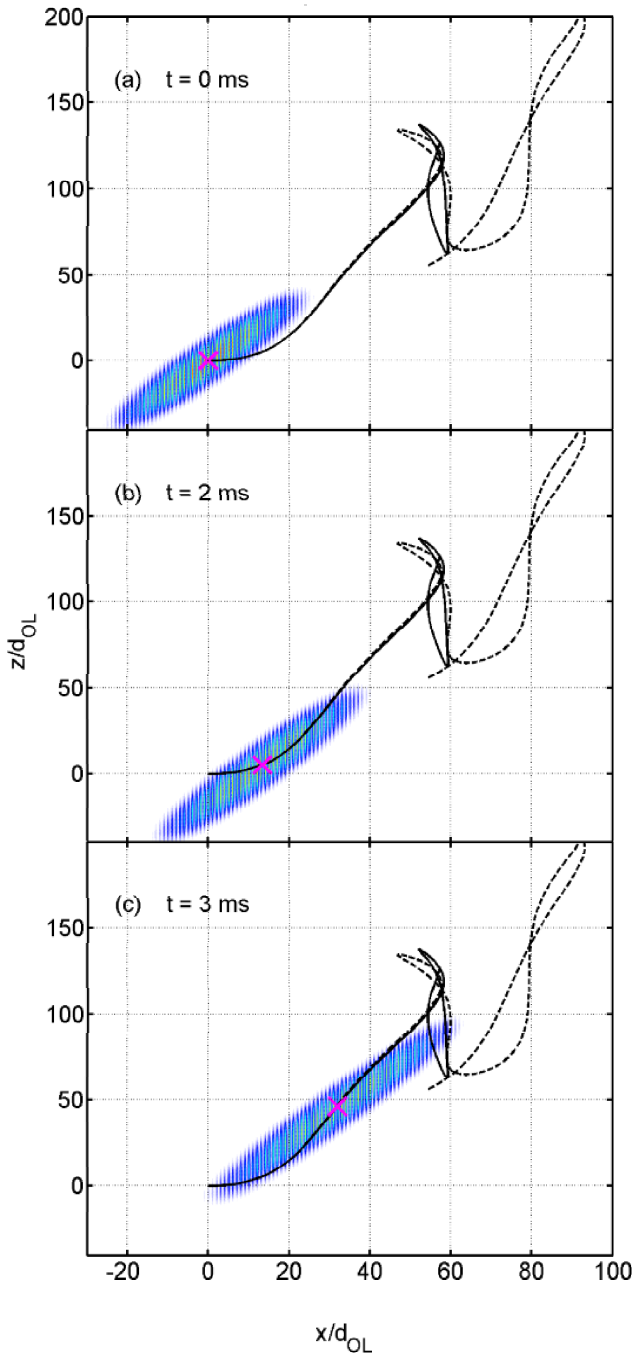

Figure 6.9: Snapshots of the time-evolution of the condensate density, for $r = 1$, $a = 4.5$ nm, $\theta = 60°$ and $\omega_z = 2\pi \times 333$ rad s^{-1}. Surface plots of the probability distribution at times (a) $t = 0$ ms, (b) $t = 2$ ms, (c) $t = 3$ ms, (d) $t = 5$ ms, (e) $t = 6$ ms, (f) $t = 8$ ms, (g) $t = 9$ ms and (h) $t = 11$ ms are shown. Both the mean quantum mechanical trajectory (solid line) and semiclassical single atom trajectory (dotted line) are overlaid, whilst the magenta cross marks the point on the quantum mechanical trajectory corresponding to the current frame.

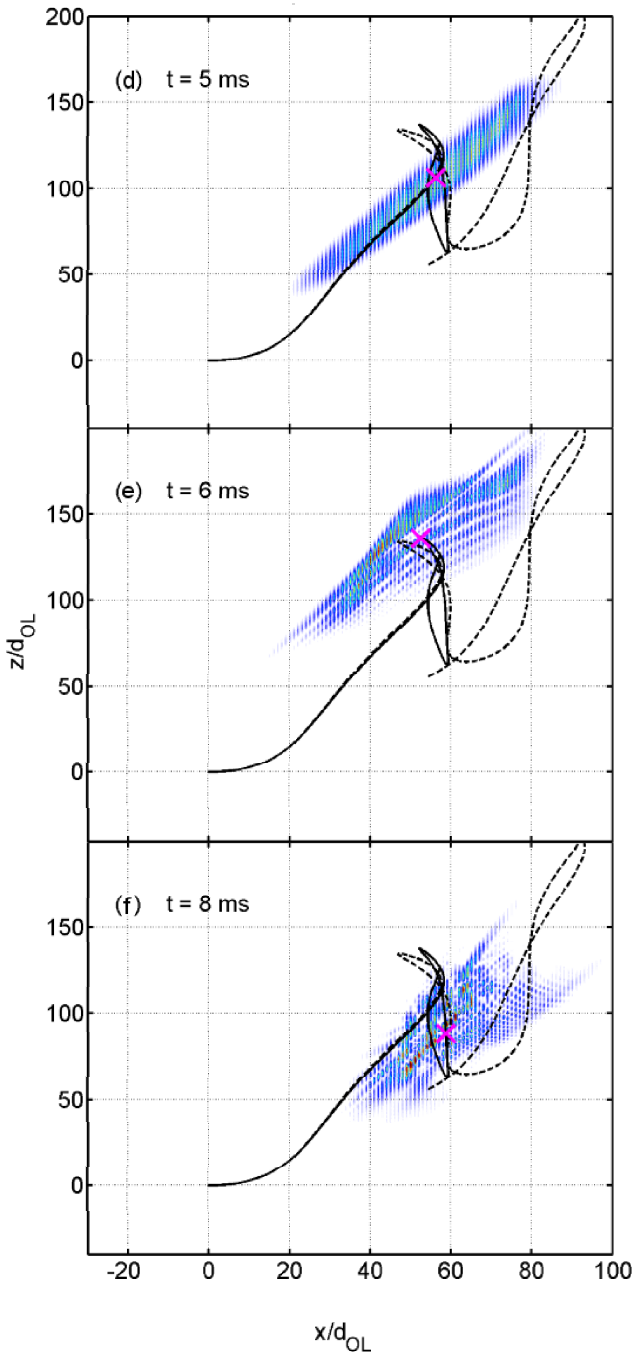

Figure 6.9: Continued.

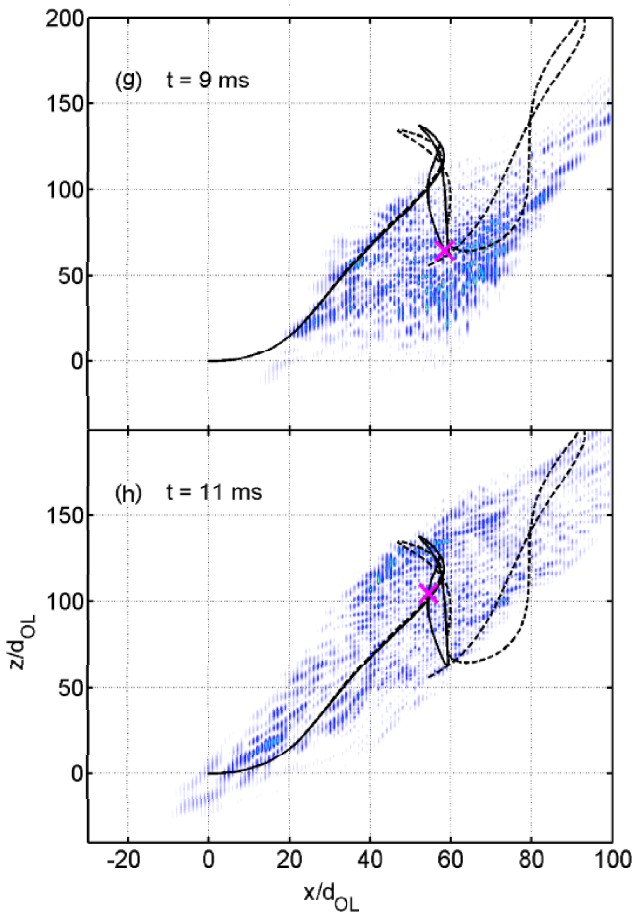

Figure 6.9: Continued.

recalling that the healing length is defined by

$$\xi = \frac{1}{\sqrt{8\pi n a}}, \tag{6.9}$$

we see that varying the strength of the effective interaction parameter also affects soliton formation. And indeed, whilst increasing both the tilt angle and the interaction parameter had the effect of reducing n by a factor of 4 in figures 6.1(a) and 6.2(a), the interaction parameter has itself increased by a factor of 10. This has the result that the healing length is approximately halved, to $\sim 2d_{OL}$ in figures 6.9 to 6.9 when the condensate explodes catastrophically. Thus we conclude that in order to further investigate this dynamic regime in Bose-Einstein condensates, it is recommended that the Feshbach resonance be employed in order to reduce the effective strength of the interatomic interactions and hence reduce the rate of soliton production.

Chapter 7

Conclusion

7.1 Summary and overview

This thesis has probed dynamics arising from periodic potentials. The results have illustrated that both superlattices and optical lattices are viable systems for the study of non-KAM chaos. In a non-KAM system chaos switches on abruptly throughout the entire phase space when the temporal frequency of a perturbation reaches certain critical values. Chaos switches on globally rather than locally making the system attractive as a switching mechanism [39]. The high degree of control possible over the properties of optical lattices renders them particularly attractive as a tool for studying this rare type of chaos.

Chapter 4 studied non-KAM chaos in biased superlattices subjected to a tilted magnetic field. The electron dynamics in such systems were described both semiclassically and quantum mechanically, and the results of such models were related by an analysis of the motion in real and phase space. Non-KAM chaos was observed when the Bloch and cyclotron frequencies were commensurate, leading to the formation of stochastic webs in phase space. Electronic transport properties were also calculated, and good agreement between theoretical and experimental I-V curves was demonstrated. It is notable that the stochastic web-induced current resonances observed in the superlattices are two orders of magnitude stronger than those originating from quantum chaos in previous semiconductor devices and, for the first time, even present at room temperature. The strength of the applied magnetic field was shown to influence the correspondence between semiclassical and quantum mechanical theories of transport. In addition, the design of the superlattice structure was also shown to have an important effect on

the transport properties, altering the likelihood of interminiband tunnelling.

Chapter 5 examined the possibility of creating non-KAM chaos in an alternative system: that of a single sodium atom confined in a tilted gutter potential and falling through an optical lattice. However, allowing the atom to fall under the influence of gravity greatly limited the number of resonances which could be observed. Under conditions where the gutter was tilted by a small angle with respect to the optical lattice, correspondence between semiclassical and quantum mechanical theory was good. However, large tilt angles require tightly confining gutter potentials in order to satisfy the resonance condition. These narrow gutters reduce the level of correspondence between the semiclassical and full quantum mechanical models, and we observed fragmentation of the atomic wavefunction.

Chapter 6 extended the work on the single sodium atom to consider the case of a Bose-Einstein condensate containing 10^4 sodium atoms. Knowing that the Feshbach resonance has been used to vary the effective interaction parameter in experiments on sodium condensates [72], the interaction parameter was adjusted to produce both weakly and strongly interacting condensates. We found that the mean trajectories of weakly interacting condensates resembles single-atom trajectories at small tilt angles despite fragmentation of the condensate wavefunction. Strongly interacting condensates became highly fragmented and their paths deviated rapidly and significantly from single-atom behaviour, even at small tilt angles.

7.2 Suggestions for further study

There are several avenues of investigation that remain unexplored at the conclusion of this thesis due to time constraints. One particular area of interest in chapter 4 is the quantum mechanical calculation of drift velocity field curves for superlattice sample NU2299. Smoothing of the peaks due to tunnelling was only carried out for the case when the tilt angle of the magnetic field was zero. However it would be useful to predict the electric fields at which tunnelling effects may be occurring at larger tilt angles and, following further smoothing, to produce I-V and G-V characteristics which may better approximate to real experimental results. Yet more realistic would be to model the charge build up in a superlattice sample and hence incorporate a more realistic non-linear electric field into the quantum mechanical model - this would hopefully minimize the unrealistic levels of tunnelling observed previously.

In the case of the single atom system, there is motivation for calculation of atomic drift velocity curves, as have been measured in recent experiments [76]. It may be possible to excite resonant stochastic web formation by accelerating the atom past the optical lattice by detuning the lasers, rather than allowing it to fall under gravity [11]. In this way, the acceleration of the atom could take a wide range of values. Firstly, this would enable calculation of an atomic drift velocity curve analogous to the drift velocity field relationships calculated for electrons in chapter 4. Secondly, it would also allow the use of low trapping frequencies which might avoid the breakdown of the wavefunction at high tilt angles.

In addition, it would be interesting to investigate the effect of including a weak confining potential in the x direction, as was applied when determining the ground state of the system. If this potential were allowed to remain in place, instead of being switched off at $t = 0$, it may prevent spreading of the atomic wavefunction, yet would also have some effect on the formation of stochastic webs. It is likely that some semblance of the web would still appear in the central region of phase space where the system is only weakly perturbed by the additional trapping potential. However, it is expected that the web would break down away from its centre as the perturbing effect of the trap becomes stronger and destroys the resonance. How strong could this extra confinement be made before the stochastic dynamics entirely break down?

In chapter 6 it would be useful to consider the effect of the confining potential in the x direction applied when calculating the ground state of the Bose-Einstein condensate. The choice of this potential may, by altering the initial peak density, influence the rate of soliton production in the condensate and hence affect the likelihood that the wavefunction explodes [12]. Investigating this factor would also enable us be more confident in proposing whether excitations in the condensate form as a result of the stochastic dynamics or simply result from the initial peak density. Again, utilising an accelerating lattice in place of gravity would allow the selection of more favourable conditions, namely, lower trapping frequencies in the z direction.

Appendix A

Derivation of the Fourier coefficients for the dispersion relation of the lowest energy band of a 1D periodic potential

The relation between energy E and wavevector k_x for a miniband with inversion symmetry about the centre of the Brillouin zone ($k_x = 0$) may be written

$$E(k_x) = \frac{\Delta}{2}\left(a_0 - \sum_{n=1}^{\infty} a_n \cos\left(n k_x d_{SL}\right)\right) \tag{A.1}$$

where the coefficients a_n are determined as follows.

Firstly, multiply equation (A.1) by a factor

$$\cos\left(n' k_x d_{SL}\right) \tag{A.2}$$

where n' is a positive integer. Secondly, integrate the result over the first Brillouin zone:

$$\begin{aligned} &\int_{-\pi/d_{SL}}^{+\pi/d_{SL}} E(k_x)\cos\left(n' k_x d_{SL}\right) dk_x \\ &= \frac{\Delta}{2}\int_{-\pi/d_{SL}}^{+\pi/d_{SL}} \left(a_0 - \sum_{n=1}^{\infty} a_n \cos\left(n k_x d_{SL}\right)\right)\cos\left(n' k_x d_{SL}\right) dk_x. \end{aligned} \tag{A.3}$$

Consider the right hand side of this equation for two separate cases: when $n' = 0$

and when $n' > 0$. In the first case, $n' = 0$, the right hand side of equation (A.3) is

$$\frac{\Delta\pi}{d_{SL}} a_0. \tag{A.4}$$

In the case when $n' > 0$, the right hand side terms in equation (A.3) vanish unless $n' = n$, so we have

$$-\frac{\Delta}{2} a_{n'} \int_{-\pi/d_{SL}}^{+\pi/d_{SL}} \cos^2\left(n' k_x d_{SL}\right) dk_x. \tag{A.5}$$

Since

$$\cos^2\left(n' k_x d_{SL}\right) = \frac{1}{2}\left(1 + \cos\left(2n' k_x d_{SL}\right)\right), \tag{A.6}$$

we see that the right hand side of equation (A.3) is now given by

$$-\frac{\Delta\pi}{2d_{SL}} a_{n'}. \tag{A.7}$$

Therefore, if we ignore the prime, we can write the nth coefficient of $E(k_x)$ as

$$a_n = \alpha \frac{d_{SL}}{\Delta\pi} \int_{-\pi/d_{SL}}^{+\pi/d_{SL}} E(k_x) \cos\left(n k_x d_{SL}\right) dk_x. \qquad \alpha = \begin{cases} +1 & \text{if } n = 0 \\ -2 & \text{if } n > 0 \end{cases} \tag{A.8}$$

Appendix B

The $4^{\text{th}}/5^{\text{th}}$ order adaptive Runge-Kutta method

The fourth order Runge-Kutta method is a fast, simple and highly accurate numerical technique. There follows a description of its implementation to solve a second-order ordinary differential equation of the form

$$\ddot{\mathbf{x}} + a(\mathbf{x}, t)\mathbf{x} = b(\mathbf{x}, t) \tag{B.1}$$

where $\mathbf{x}$ is some vector of simultaneous variables and $a(\mathbf{x}, t)$ and $b(\mathbf{x}, t)$ are arbitrary functions. An adaptive step size is also employed in order to increase the accuracy of the final result to fifth order. For a more detailed description of this procedure refer to [60].

We begin by rewriting equation (B.1) as a coupled set of first-order differential equations:

$$\dot{\mathbf{x}}_1 = \mathbf{x}_2 \tag{B.2}$$

$$\dot{\mathbf{x}_2} = f(\mathbf{x}_1, t) \tag{B.3}$$

where $f(\mathbf{x}_1, t) = b(\mathbf{x}_1, t) - a(\mathbf{x}_1, t)\,\mathbf{x}_1$. A single element x of the vector $\mathbf{x_1}$ will be considered here for clarity: the same method should be applied to each of the simultaneous variables represented by the vector. So we now seek a solution to

$$\frac{dx}{dt} = f(x, t) \tag{B.4}$$

where some explicit form of $f(x, t)$ is known, along with some initial condition

(x_0, t_0). This information will be used to determine subsequent values x_n of x at discrete times t_n, where $n = 1, 2, 3, \ldots$

The Taylor expansion of $x(t)$ about (x_n, t_n) is used to write down an expression for x_{n+1} at some time $t_{n+1} = t_n + \Delta_t$ in terms of x_n:

$$x_{n+1} = x_n + \Delta_t \left.\frac{dx}{dt}\right|_{x_n,t_n} + \frac{1}{2}\Delta_t^2 \left.\frac{d^2x}{dt^2}\right|_{x_n,t_n} + \ldots \,, \tag{B.5}$$

where Δ_t is the discrete time step. This can be used to write x_{n+1} correct to fourth order in Δ_t, in the form [60]

$$x_{n+1} = x_n + \frac{1}{6}\left(k_1 + 2k_2 + 2k_3 + k_4\right) + O(\Delta_t^5) \,, \tag{B.6}$$

where

$$\begin{aligned} k_1 &= \Delta_t f(x_n, t_n) \\ k_2 &= \Delta_t f(x_n + k_1/2, t_n + \Delta_t/2) \\ k_3 &= \Delta_t f(x_n + k_2/2, t_n + \Delta_t/2) \\ k_4 &= \Delta_t f(x_n + k_3, t_n + \Delta_t) \,, \end{aligned}$$

and $O(\Delta_t^5)$ represents the terms of higher than fourth order which have been neglected. This method is based upon the idea of taking trial points across the time interval to improve the accuracy of the final result.

An adaptive step size approach is used to increase both the speed and accuracy of the simulation. This involves calculating two estimates of x_{n+1}: the first estimate, x_s, is calculated using a single time step Δ_t over the interval $t_n \to t_n + \Delta_t$, and the second, x_d employs a time step $\Delta_t/2$ to take two steps over the interval, that is $t_n \to t_n + \Delta_t/2 \to t_n + \Delta_t$. The accuracy of the final result is improved as follows.

If $x(t+\Delta_t)$ is the exact solution of x at time $t+\Delta_t$, then the two fourth order approximations x_s and x_d may be used to write:

$$x(t + \Delta_t) = x_s + \Delta_t^5 \alpha + O(\Delta_t^6) \tag{B.7}$$

$$x(t + \Delta_t) = x_d + 2\left(\frac{\Delta_t}{2}\right)^5 \alpha + O(\Delta_t^6) \tag{B.8}$$

where $\alpha \sim \frac{1}{5!} d^5x/dt^5$. Subtracting equation (B.7) from equation (B.8) we can write

$$x_d - x_s = \frac{15}{16}\Delta_t^5 \alpha = \gamma \tag{B.9}$$

where γ is the truncation error to sixth order. Thus an improved estimate that makes use of equation (B.9) may be written:

$$x_{n+1} = x_d + \frac{\gamma}{15} + O(\Delta_t^6), \tag{B.10}$$

where the accuracy is now to fifth order.

The reader might imagine that effectively tripling the number of calculations required per time step would increase the computational time so much that the gain in accuracy is outweighed. However, knowledge of the truncation error for a given choice of time step may be used to refine the interval size in the next iteration. If a maximum limit, γ_n, is specified for the truncation, then the time step Δ_n necessary to limit the error to γ_n must satisfy

$$\frac{\Delta_n}{\Delta_t} = \left| \frac{\gamma_n}{\gamma} \right|^{\frac{1}{5}} , \tag{B.11}$$

since the truncation is proportional to Δ_t^5. For nonlinear systems, where x may take large values yet vary rapidly on a small scale, it is appropriate to base the choice of γ_n upon the local error such that

$$\gamma_n = \Gamma \Delta_t f(x,t) \tag{B.12}$$

where $\Gamma \sim 1 \times 10^{-3}$ is a tolerance [6]. The step size may then be adjusted so that the largest of the errors relating to the simultaneous variables lies within the tolerance limit - although it is essential to place a lower limit on the value of Δ_t so that it cannot tend to zero. Varying the step size in this way enables the theorist to devote more computational time to rapidly varying sections of a trajectory, whilst spending less time on linear regions. Tests of the simple fourth order method versus the adaptive fifth order version (upon a similar system) showed that the adaptive code is approximately twenty times faster for the same overall accuracy [6].

Appendix C

The Crank-Nicolson Method

Chapters 4, 5 and 6 all make use of the Crank-Nicolson method [60] to predict numerical solutions of quantum dynamics. While chapters 4 and 5 solve only the Schrödinger equation, chapter 6 solves the Gross-Pitaevskii equation which is an extension of the Schrödinger equation that applies to interacting particles (see section 2.4.2). The method described here is applied to the Gross-Pitaevskii equation, since it is then a simple matter to set the strength of inter-particle interactions to zero in order to determine solutions for the Schrödinger equation.

Due to the nonlinear form of the Gross-Pitaevskii equation, only the simplest cases may be solved analytically. Consequently, numerical techniques must usually be employed. If all the potential energy terms are combined together, the time-dependent Gross-Pitaevskii equation for a 3D system is

$$i\hbar\frac{\partial\Psi\left(\mathbf{r},t\right)}{\partial t}=-\frac{\hbar^{2}}{2m}\nabla^{2}\Psi\left(\mathbf{r},t\right)+V\left(\mathbf{r},t\right)\Psi\left(\mathbf{r},t\right) \tag{C.1}$$

where

$$V\left(\mathbf{r},t\right)=V_{ext}\left(\mathbf{r}\right)+U_{0}\left|\Psi\left(\mathbf{r},t\right)\right|^{2}. \tag{C.2}$$

where $V_{ext}\left(\mathbf{r}\right)$ describes the externally applied potential and U_0 is a real constant. For the BEC considered in chapter 6, U_0 is a function of the s-wave scattering length and therefore characterises the strength of the mean field due to interactions. In chapter 6, equation (C.1) was integrated using *finite difference methods* in two dimensions. This technique superimposes an equally spaced spatial grid of points upon the system and approximates the wavefunction derivatives according to the grid, so that the wavefunction may be estimated at each of these discrete spatial points at finite time steps.

The first stage in the method is to rewrite equation (C.1) in terms of the x and z coordinates only (since it was shown in section 3.2.5 that the motion in the y direction is separable and trivial):

$$i\hbar\frac{\partial\Psi}{\partial t} = -\frac{\hbar^2}{2m}\left\{\frac{\partial^2\Psi}{\partial x^2} + \frac{\partial^2\Psi}{\partial z^2}\right\} + V(x,z)\,\Psi. \tag{C.3}$$

The finite difference approximation for the first order temporal derivative at the nth time step is written as

$$\frac{\partial\Psi}{\partial t} \approx \frac{\Psi_{j,l}^{n+1} - \Psi_{j,l}^{n}}{\Delta_t}, \tag{C.4}$$

where Δ_t is the time interval, and the integers j and l specify the coordinates of a particular point on the grid. For the second order spatial derivatives, one must first consider approximate Taylor expansions (omitting the superscript that specifies the time step):

$$\Psi_{j+1,l} \approx \Psi_{j,l} + \Delta_x\frac{\partial\Psi}{\partial x}\bigg|_{j,l} + \frac{\Delta_x^2}{2}\frac{\partial^2\Psi}{\partial x^2}\bigg|_{j,l} \tag{C.5}$$

$$\Psi_{j-1,l} \approx \Psi_{j,l} - \Delta_x\frac{\partial\Psi}{\partial x}\bigg|_{j,l} + \frac{\Delta_x^2}{2}\frac{\partial^2\Psi}{\partial x^2}\bigg|_{j,l} \tag{C.6}$$

where Δ_x is the grid spacing in the x direction. Summing equations (C.5) and (C.6) results in

$$\frac{\partial^2\Psi}{\partial x^2}\bigg|_{j,l} \approx \frac{\Psi_{j+1,l} - 2\Psi_{j,l} + \Psi_{j-1,l}}{\Delta_x^2}, \tag{C.7}$$

and similarly, we can also write

$$\frac{\partial^2\Psi}{\partial z^2}\bigg|_{j,l} \approx \frac{\Psi_{j,l+1} - 2\Psi_{j,l} + \Psi_{j,l-1}}{\Delta_z^2} \tag{C.8}$$

where Δ_z is the spacing in the z direction. Substituting equations (C.4), (C.7)

and (C.8) into equation (C.3) gives

$$\begin{aligned}\frac{\Psi_{j,l}^{n+1}-\Psi_{j,l}^{n}}{\Delta_t} &= \frac{i\hbar}{2m}\left(\frac{\Psi_{j+1,l}^{n}-2\Psi_{j,l}^{n}+\Psi_{j-1,l}^{n}}{\Delta_x^2}\right)\\ &+\frac{i\hbar}{2m}\left(\frac{\Psi_{j,l+1}^{n}-2\Psi_{j,l}^{n}+\Psi_{j,l-1}^{n}}{\Delta_z^2}\right)\\ &-\frac{i}{\hbar}V_{j,l}^{n}\Psi_{j,l}^{n}. \end{aligned} \tag{C.9}$$

This is known as an *explicit scheme*, since there is only one unknown quantity, $\Psi_{j,l}^{n+1}$, for which the equation is easily solvable. However there is an equally valid *implicit scheme* in which the right hand side of equation (C.9) is evaluated at time t^{n+1} rather than t^n as previously:

$$\begin{aligned}\frac{\Psi_{j,l}^{n+1}-\Psi_{j,l}^{n}}{\Delta_t} &= \frac{i\hbar}{2m}\left(\frac{\Psi_{j+1,l}^{n+1}-2\Psi_{j,l}^{n+1}+\Psi_{j-1,l}^{n+1}}{\Delta_x^2}\right)\\ &+\frac{i\hbar}{2m}\left(\frac{\Psi_{j,l+1}^{n+1}-2\Psi_{j,l}^{n+1}+\Psi_{j,l-1}^{n+1}}{\Delta_z^2}\right)\\ &-\frac{i}{\hbar}V_{j,l}^{n+1}\Psi_{j,l}^{n+1}. \end{aligned} \tag{C.10}$$

In this case, there are many unknowns and therefore the equations are coupled and are difficult to solve. The Crank-Nicolson method takes advantage of both the accuracy of the explicit scheme and the stability of the implicit scheme [60] by averaging equations (C.9) and (C.10) to give an expression for the temporal derivative which is centred at time $t^{n+1/2}$:

$$\begin{aligned}\frac{\Psi_{j,l}^{n+1}-\Psi_{j,l}^{n}}{\Delta_t} &= \frac{1}{2}\times\\ &\left[\frac{i\hbar}{2m\Delta_x^2}\left\{\left(\Psi_{j+1,l}^{n+1}-2\Psi_{j,l}^{n+1}+\Psi_{j-1,l}^{n+1}\right)+\left(\Psi_{j+1,l}^{n}-2\Psi_{j,l}^{n}+\Psi_{j-1,l}^{n}\right)\right\}\right.\\ &+\frac{i\hbar}{2m\Delta_z^2}\left\{\left(\Psi_{j,l+1}^{n+1}-2\Psi_{j,l}^{n+1}+\Psi_{j,l-1}^{n+1}\right)+\left(\Psi_{j,l+1}^{n}-2\Psi_{j,l}^{n}+\Psi_{j,l-1}^{n}\right)\right\}\\ &\left.-\frac{i}{\hbar}\left\{V_{j,l}^{n+1}\Psi_{j,l}^{n+1}+V_{j,l}^{n}\Psi_{j,l}^{n}\right\}\right]. \end{aligned} \tag{C.11}$$

In principal, equation (C.11) could be rearranged so that terms in Ψ^n and Ψ^{n+1} are on opposite sides, and the equation solved directly by matrix methods. However, the vast amounts of computer time and memory that such an operation would require prevent this. Instead a technique known as the *operator splitting*

method is exploited [60].

The operator splitting method, or *alternating direction implicit (ADI) method* as it is sometimes known, splits each time step into two shorter steps of time $\Delta_t/2$ and treats a different spatial dimension implicitly in each step. That is, during the first step, $\Psi_{j,l}^{n+1/2}$ is evaluated, with terms in x calculated at time $t^{n+1/2}$ and terms in z at t^n. The second step then evaluates $\Psi_{j,l}^{n+1}$, calculating x-dependent terms at $t^{n+1/2}$ and z-dependent terms at t^{n+1}. Thus, in our two-step process we must first solve:

$$\begin{aligned}\Psi_{j,l}^{n+1/2} = \Psi_{j,l}^{n} + \frac{\Delta_t}{2i\hbar}\times \\ \left\{\frac{-\hbar^2}{2m\Delta_{xz}^2}\left(\Psi_{j+1,l}^{n+1/2} - 2\Psi_{j,l}^{n+1/2} + \Psi_{j-1,l}^{n+1/2}\right)\right. \\ \frac{-\hbar^2}{2m\Delta_{xz}^2}\left(\Psi_{j,l+1}^{n} - 2\Psi_{j,l}^{n} + \Psi_{j,l-1}^{n}\right) \\ \frac{V_{ext}}{2}\left(\Psi_{j,l}^{n+1/2} + \Psi_{j,l}^{n}\right) \\ \left.\frac{U_0}{2}\left(\left|\Psi_{j,l}^{n+1/2}\right|^2 \Psi_{j,l}^{n+1/2} + \left|\Psi_{j,l}^{n}\right|^2 \Psi_{j,l}^{n}\right)\right\}\end{aligned} \tag{C.12}$$

followed by:

$$\begin{aligned}\Psi_{j,l}^{n+1/2} = \Psi_{j,l}^{n} + \frac{\Delta_t}{2i\hbar}\times \\ \left\{\frac{-\hbar^2}{2m\Delta_{xz}^2}\left(\Psi_{j+1,l}^{n+1/2} - 2\Psi_{j,l}^{n+1/2} + \Psi_{j-1,l}^{n+1/2}\right)\right. \\ \frac{-\hbar^2}{2m\Delta_{xz}^2}\left(\Psi_{j,l+1}^{n+1} - 2\Psi_{j,l}^{n+1} + \Psi_{j,l-1}^{n+1}\right) \\ \frac{V_{ext}}{2}\left(\Psi_{j,l}^{n+1} + \Psi_{j,l}^{n+1/2}\right) \\ \left.\frac{U_0}{2}\left(\left|\Psi_{j,l}^{n+1}\right|^2 \Psi_{j,l}^{n+1} + \left|\Psi_{j,l}^{n+1/2}\right|^2 \Psi_{j,l}^{n+1/2}\right)\right\}\end{aligned} \tag{C.13}$$

where $\Delta_{xz} = \Delta_x = \Delta_z$. Although the sum of equations (C.12) and (C.13) is not exactly equal to equation (C.11), it is a very close approximation to it.

Both equation (C.12) and equation (C.13) may be written as matrix problems whose coefficient matrices relate only to terms in either Ψ^n, $\Psi^{n+1/2}$ or Ψ^{n+1}:

$$\mathbf{A}\Psi^{n+1/2} = \mathbf{B}\Psi^{n} \tag{C.14}$$

$$\mathbf{A}\Psi^{n+1} = \mathbf{B}\Psi^{n+1/2} \tag{C.15}$$

$\mathbf{A}$, $\mathbf{B}$, $\mathbf{A}'$ and $\mathbf{B}'$ are tridiagonal matrices and Ψ is written as a column matrix. Having tridiagonal matrix equations is a major advantage as it enormously reduces the amount of computing resources required to solve the problem. Each part of the problem may be further divided into simple triangular matrix problems, which are trivial to solve. Consider the equation

$$\mathbf{M}\Psi = \mathbf{C} \tag{C.16}$$

where $\mathbf{M}$ is tridiagonal and Ψ and $\mathbf{C}$ are column matrices. By performing *LU decomposition* [60] on $\mathbf{M}$ we obtain

$$\mathbf{M}\Psi = (\mathbf{L} \times \mathbf{U})\,\Psi = \mathbf{L} \times (\mathbf{U} \times \Psi) = \mathbf{C} \tag{C.17}$$

where $\mathbf{M}$ has been replaced by the product of a lower triangular matrix $\mathbf{L}$ and an upper triangular matrix $\mathbf{U}$. Thus, defining $\mathbf{Y} = \mathbf{U} \times \Psi$, we may solve

$$\mathbf{L} \times \mathbf{Y} = \mathbf{C} \tag{C.18}$$

for $\mathbf{Y}$, and subsequently,

$$\mathbf{Y} = \mathbf{U} \times \Psi \tag{C.19}$$

for Ψ, by a technique known as *forward and backward substitution* [60]. Note however that in order to evaluate $\mathbf{A}$ and $\mathbf{A}'$, the nonlinearity means that knowledge of $\Psi^{n+1/2}$ or Ψ^{n+1} respectively is needed, i.e. the very quantity which we wish to determine. To overcome this, a two-step iteration process is employed at each stage, where we obtain an initial estimate, $\widetilde{\Psi}$, of the new wavefunction, making use of its current value to approximate the nonlinear potential. The estimate is then improved by repeating the calculation using the initial estimate in the nonlinearity. This is summarised as follows:

$$\mathbf{A}\left(\Psi^{n}\right)\widetilde{\Psi}^{n+1/2} = \mathbf{B}\left(\Psi^{n}\right)\Psi^{n} = \mathbf{C} \tag{C.20}$$

$$\mathbf{A}\left(\widetilde{\Psi}^{n+1/2}\right)\Psi^{n+1/2} = \mathbf{B}\left(\Psi^{n}\right)\Psi^{n} = \mathbf{C} \tag{C.21}$$

$$\mathbf{A}'\left(\Psi^{n+1/2}\right)\widetilde{\Psi}^{n+1} = \mathbf{B}'\left(\Psi^{n+1/2}\right)\Psi^{n+1/2} = \mathbf{D} \tag{C.22}$$

$$\mathbf{A}'\left(\widetilde{\Psi}^{n+1}\right)\Psi^{n+1} = \mathbf{B}'\left(\Psi^{n+1/2}\right)\Psi^{n+1/2} = \mathbf{D}. \tag{C.23}$$

Appendix D

Choice of colourscale for two-dimensional surface plots

The majority of surface plots presented in this thesis are coloured according to the scale illustrated in figure D.1. The only exception to this is in the case of the Wigner functions plotted in section 4.3.3 - the scale applied in these plots varies very slightly from that in other figures, as will be explained shortly.

When plotting surfaces of probability density, the maximum density D_{max} of the function at time $t = 0$ is set to unity on the colourbar. However, during the time evolution of the wavefunction, it is possible for peaks of higher density to occur, therefore the colourscale applied must take this into account if there is to be meaningful comparison of each frame in a sequence. Preliminary studies indicated that a colourscale maximum of $1.2D_{max}$ is more than adequate to take account of such variations.

When plotting the Wigner functions, it was found that the peak of the localised Wigner plot at $t = 0$ always displayed the highest value W_{max}. Later Wigner functions, being more diffuse in phase space, were consistently lower valued than W_{max} at all points. In addition, since computing constraints only allow

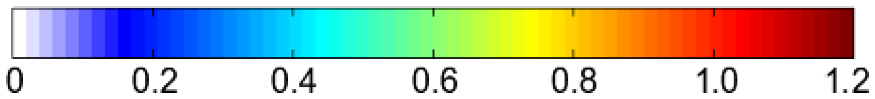

Figure D.1: Colourscale applied to all surface plots presented in this thesis, with the exception of the Wigner functions plotted in chapter 4. The numerical values indicate density as a proportion of D_{max}, the maximum of the probability function at time $t = 0$.

consideration of a small region of phase space, portions of the Wigner function may lie outside the area of study in later frames. Therefore, it is the distribution of the Wigner function rather than its actual value that is relevant, as we cannot truly compare the evolution of the function frame by frame. Due to these limitations, each Wigner function is coloured independently. The same colour variation as in figure D.1 is applied, however the maximum of the colourscale is always scaled to the maximum of the Wigner function in a given plot.

References

[1] L. Esaki and R. Tsu. Superlattice and negative differential conductivity in semiconductors. *IBM J. Res. Dev.*, 14(1):61, 1970.

[2] J.R. Hook and H.E. Hall. *Solid State Physics.* John Wiley and sons, 1996.

[3] N.W. Ashcroft and N.D. Mermin. *Solid State Physics.* W.B. Saunders Company, International edition, 1976.

[4] A. Patanè, D. Sherwood, L. Eaves, T.M. Fromhold, M. Henini, P.C. Main, and G. Hill. Tailoring the electronic properties of GaAs/AlAs superlattices by InAs layer insertions. *Appl. Phys. Lett.*, 81(4):661–663, 2002.

[5] A.A. Krokhin, T.M. Fromhold, A.E. Belyaev, H.M. Murphy, L. Eaves, D. Sherwood, P.C. Main, and M. Henini. Suppression of electron injection into a finite superlattice in an applied magnetic field. *Phys. Rev. B*, 63:195323, 2001.

[6] D. Sherwood. *Effect of Stochastic webs on electron transport in semiconductor superlattices.* PhD thesis, University of Nottingham, 2003.

[7] C.J. Pethick and H.Smith. *Bose-Einstein Condensation in dilute gases.* Cambridge University Press, 2002.

[8] K. Drese and M. Holthaus. Ultracold atoms in modulated standing light waves. *Chemical Physics*, 201:201–219, 1997.

[9] H.J. Metcalf and P. van der Straten. *Laser cooling and trapping.* Springer-Verlag, 1999.

[10] M. Ben Dahan, E. Peik, J. Reichel, Y. Castin, and C. Salomon. Bloch oscillations of atoms in an optical potential. *Phys. Rev. Lett.*, 76(24):4508–4511, 1996.

[11] O. Morsch, J.H. Müller, M. Cristiani, D. Campini, and E. Arimondo. Bloch oscillations and mean-field effects of Bose-Einstein condensates in 1D optical lattices. *Phys. Rev. Lett.*, 87(14):140402, 2001.

[12] R.G. Scott. *Cold atoms in optical lattices.* PhD thesis, University of Nottingham, 2003.

[13] G.K. Woodgate. *Elementary atomic structure.* Oxford University Press, 2nd edition, 1980.

[14] W. Wing. On neutral particle trapping in quasistatic electromagnetic fields. *Prog. Quantum Electron.*, 8:181, 1984.

[15] V.V. Vladimirskii. A magnetic mirror for neutral particles. *Sov. Phys. JETP*, 12:740, 1961.

[16] J. Schmiedmayer. Guiding and trapping a neutral atom on a wire. *Appl. Phys. A*, 52:R13, July 1995.

[17] M.H. Anderson, J.R. Ensher, M.R. Matthews, C.E. Wieman, and E.A. Cornell. Observation of Bose-Einstein condensation in a dilute atomic vapor. *Science*, 269(198), 1995.

[18] Y. Gott, M. Ioffe, and V. Tel'kovskii. Some new results on confinement in magnetic traps. *Nucl. Fusion Suppl*, 3:10445, 1962.

[19] D. Pritchard. Cooling neutral atoms in a magnetic trap for precision spectroscopy. *Phys. Rev. Lett.*, 51:1336–1339, 1983.

[20] C.J. Foot. Laser cooling and trapping of atoms. *Contemporary Physics*, 32(6):369–381, 1991.

[21] J. Dalibard and C. Cohen-Tannoudji. Laser cooling below the Doppler limit by polarization gradients: simple theoretical models. *J. Opt. Soc. Am. B*, 6:2023, 1989.

[22] C.E. Wieman. The Richtmyer memorial lecture: Bose-Einstein condensation in an ultracold gas. *Am. J. Phys.*, 64(7):847–855, 1996.

[23] W. Ketterle. Experimental studies of Bose-Einstein condensation. *Physics Today*, pages 30–35, December 1999.

[24] Y. Castin, R. Dun, and A. Sinatra. Bose condensates make quantum leaps and bounds. *Physics World*, pages 37–42, August 1999.

[25] Keith Burnett, Mark Edwards, and Charles W. Clark. The theory of Bose-Einstein condensation of dilute gases. *Physics Today*, pages 37–42, December 1999.

[26] Kristian Helmerson, David Hutchinson, Keith Burnett, and William D Phillips. Atom lasers. *Physics World*, pages 31–35, August 1999.

[27] R. Bowley and Mariana Sánchez. *Introductory Statistical Mechanics.* Oxford Science Publications, 2nd edition, 1999.

[28] Charles Kittel. *Introduction to Solid State Physics.* John Wiley and Sons, Inc., 7th edition, 1996.

[29] C.C. Bradley, C.A. Sackett, and R.G. Hulet. Bose-Einstein condensation of lithium. *Phys. Rev. Lett.*, 78(6):985–989, 1997.

[30] S. Burger, L.D. Carr, P. Öhberg, K. Sendgstock, and A. Sanpera. Generation and interaction of solitons in Bose-Einstein condensates. *Phys. Rev. A*, 65:043611, 2002.

[31] B.P. Anderson, P.C. Haljan, C.A. Regal, D.L. Feder, L.A. collins, C.W. Clark, and E.A. Cornell. Watching dark solitons decay into vortex rings in a Bose-Einstein condensate. *Phys. Rev. Lett.*, 86(14):2926–2929, 2001.

[32] T. Tsuzuki. Nonlinear waves in the Pitaevskii-Gross equation. *Low Temp. Phys.*, 4(4):441–457, 1971.

[33] R.C. Hilborn. *Chaos and Nonlinear Dynamics.* Oxford University Press, 2nd edition, 2000.

[34] J. Gleick. *Chaos.* Minerva, 1997.

[35] G.M. Zaslavsky et al. *Weak Chaos and Quasi-Regular Patterns.* Cambridge University Press, 1991.

[36] P.B. Wilkinson. *Quantum chaos in resonant tunnelling diodes.* PhD thesis, University of Nottingham, 1997.

[37] R.S. MacKay and J.D. Meiss, editors. *Hamiltonian Dynamical Systems.* Adam Hilger, 1987.

[38] G.M. Zaslavsky et al. *Chaos in Dynamic Systems.* Harwood Academic Publishers, 1987.

[39] T.M. Fromhold et al. Chaotic electron diffusion through stochastic webs enhances current flow in superlattices. *Nature*, 428(6984):726–730, 2004.

[40] M.L. Boas. *Mathematical Methods in the Physical Sciences.* John Wiley and sons, 2nd edition, 1983.

[41] H.-J. Stöckmann. *Quantum chaos: an introduction.* Cambridge University Press, 1999.

[42] E. Wigner. On the quantum correction for thermodynamic equilibrium. *Physical Review*, 40:749–759, 1932.

[43] M. C. Gutzwiller. *Chaos in Classical and Quantum Mechanics.* Springer-Verlag, 1990.

[44] P.A. Dando and T.S. Monteiro. Quantum surfaces of section for the diamagnetic hydrogen atom: Husimi functions versus Wigner functions. *Journal of Physics B*, 27:2681, 1994.

[45] J. Hutchinson and R. Wyatt. Quantum surfaces of section for the diamagnetic hydrogen atom: Husimi functions versus Wigner functions. *Chemical Physics Letters*, 72:378, 1980.

[46] S.A. Gardiner, D. Jaksch, R. Dum, J.I. Cirac, and P. Zoller. Nonlinear matter wave dynamics with a chaotic potential. *Phys. Rev. A*, 62(2):023612, 2000.

[47] H.J. Korsch and H. Wiescher. Quantum chaos. In K.H. Hoffmann and M. Schreiber, editors, *Computational Physics: Selected Methods, Simple Exercises, Serious Applications*, pages 225–244. Springer, 1996.

[48] J.P. Bird et al. Lead-orientation-dependent wavefunction scarring in open quantum dots. *Phys. Rev. Lett.*, 82:4691, 1999.

[49] T.M. Fromhold et al. Magnetotunneling spectroscopy of a quantum well in the regime of classical chaos. *Phys. Rev. Lett.*, 72:2608, 1994.

[50] T.M. Fromhold et al. Manifestations of classical chaos in the energy-level spectrum of a quantum-well. *Phys. Rev. Lett.*, 75(6):1142, 1995.

[51] K.J. Luo et al. Explosive bifurcation to chaos in weakly coupled semiconductor superlattices. *Phys. Rev. Lett.*, 81:1290, 1998.

[52] J. Kastrup et al. Multistability of the current-voltage characteristics in doped GaAs-AlAs superlattices. *Appl. Phys. Lett.*, 75:1808, 1994.

[53] K.N. Alekseev, G.P. Berman, D.K. Campbell, E.H. Cannon, and M.C. Cargo. Dissipative chaos in semiconductor superlattices. *Phys. Rev. B*, 54:10625, 1996.

[54] B. Hu et al. Quantum chaos of a kicked particle in an infinite potential well. *Phys. Rev. Lett.*, 82:4224, 1999.

[55] S.A. Gardiner, J.I. Cirac, and P. Zoller. Quantum chaos in an ion trap: The delta-kicked harmonic oscillator. *Phys. Rev. Lett.*, 79(24):4790–4793, 1997.

[56] P.-K Chia, L. Schmitz, and R.W. Conn. Stochastic ion behaviour in subharmonic and superharmonic electrostatic waves. *Phys. Plasmas*, 3:1545, 1996.

[57] D.I. Kamenev and G.P. Berman. *Quantum Chaos: A Harmonic Oscillator in a Monochromatic Wave.* Rinton Press, 2000.

[58] C. Rauch et al. Transition between coherent and incoherent electron transport in GaAs/GaAlAs superlattices. *Phys. Rev. Lett.*, 81(16):3495, 1998.

[59] S. Adachi. *GaAs and Related Materials.* World Scientific Singapore, 1994.

[60] William H. Press, Saul A. Teukolsky, William T. Vetterling, and Brian P. Flannery. *Numerical Recipes, the art of scientific computing.* Cambridge University Press, 2nd edition, 2002.

[61] Anatoly A. Ignatov and K.F. Renk. Easki-Tsu superlattice oscillator: Josephson-like dynamics of carriers. *Phys. Rev. Lett.*, 70(13):1996–1999, 1993.

[62] T. Hartmann, F. Keck, H.J. Korsch, and S. Mossmann. Dynamics of Bloch oscillations. *New J. Phys.*, 6:2, 2004.

[63] A. Wacker. Semiconductor superlattices: a model system for nonlinear transport. *Phys. Rep.*, 357(1):1–111, 2002.

[64] John H. Davies. *The physics of low-dimensional semiconductors - an introduction.* Cambridge University Press, 1998.

[65] R.G. Scott, S. Bujkiewicz, T.M. Fromhold, P.B. Wilkinson, and F.W. Sheard. Effects of chaotic energy-band transport on the quantized states of ultracold sodium atoms in an optical lattice with a tilted harmonic trap. *Phys. Rev. A*, 66:023407, 2002.

[66] B.P. Anderson and M.A. Kasevich. Macroscopic quantum interference from atomic tunnel arrays. *Science*, 282:1686–1689, November 1998.

[67] S. Wilkinson, C. Bharucha, K. Madison, Q. Niu, and M. Raizen. Observation of atomic Wannier-Stark ladders in an accelerating optical potential. *Phys. Rev. Lett.*, 76:4512, 1996.

[68] K.B. Davis, M.-O. Mewes, M.R. Andrews, N.J. van Druten, D.S. Durfee, D.M. Kurn, and W. Ketterle. Bose-Einstein condensation in a gas of Sodium atoms. *Phys. Rev. Lett.*, 75(22):3969–3973, 1995.

[69] M.L. Chiofalo, S. Succi, and M.P. Tosi. Ground state of a trapped interacting Bose-Einstein condensates by an explicit imaginary time algorithm. *Phys. Rev. E.*, 62(5):7438–7443, 2000.

[70] R.G. Scott, A.M. Martin, T.M. Fromhold, S. Bujkiewicz, F.W. Sheard, and M. Leadbeater. Creation of solitons and vortices by bragg reflection of Bose-Einstein condensates in an optical lattice. *Phys. Rev. Lett.*, 90(11):110404, 2003.

[71] A.J. Moerdijk, B.J. Verhaar, and A. Axelsson. Resonances in ultracold collisions of ^{6}Li, ^{7}Li, ^{23}Na. *Phys. Rev. A*, 51:4852–4861, 1995.

[72] S. Inouye, M.R. Andrews, J. Stenger, H.-J. Miesner, D.M. Stamper-Kurn, and W. Ketterle. Observation of Feshbach resonances in a Bose-Einstein condensate. *Nature*, 392:151–154, March 1998.

[73] Dae-Il Choi and Quian Niu. Bose-Einstein condensates in an optical lattice. *Phys. Rev. Lett.*, 82(10):2022–2025, 1999.

[74] S. Burger, K. Bongs, S. Dettmers, W. Ertmer, K. Sengstock, A. Sanpera, G. Shlyapinikov, and M. Lewenstein. Dark solitons in Bose-Einstein condensates. *Phys. Rev. Lett.*, 83:5198, 1999.

[75] J. Denschlag, J. Simsarian, D. Feder, C.W. Clark, L. Collins, J. Cubizolles, L. Deng, E. Hagley, K. Helmerson, and W. Reinhardt. Generating solitons by phase engineering of a Bose-Einstein condensate. *Science*, 287:97, 2000.

[76] A.V. Ponomarev, J. Madronero, A.R. Kolovsky, and A. Buchleitner. Atomic current across an optical lattice. *Accepted for publication in Phys. Rev. Lett.*, 2005.

Publications

Effect of inter-miniband tunneling on current resonances due to the formation of stochastic conduction networks in superlattices, D.P.A. Hardwick, S.L. Naylor, S. Bujkiewicz, T.M. Fromhold, D. Fowler, A. Patanè, L. Eaves, A.A. Krokhin, P.B. Wilkinson, M. Henini and F.W. Sheard, Proc. 12th International Conference on Modulated Semiconductor Structures, Santa Fe, USA, July 2005. Accepted for publication in Physica E in 2006.

Manifestations of non-KAM chaos in the quantised states and wavepacket dynamics of electrons in superlattices, D.P.A. Hardwick, S.L. Naylor, T.M. Fromhold, D. Fowler, A. Patanè, L. Eaves, A.A. Krokhin and M. Henini, in preparation for Phys. Rev. B.

Effect of inter-miniband tunneling on single-electron chaos and charge domain formation in superlattices, D.P.A. Hardwick, S.L. Naylor, T.M. Fromhold, D. Fowler, A. Patanè, L. Eaves, A.A. Krokhin and M. Henini, in preparation for Phys. Rev. B.

Manifestations of quantum chaos in the dynamics of single cold atoms and Bose-Einstein condensates in optical lattices, S.L. Naylor and T.M. Fromhold, in preparation for Phys. Rev. A.

Presentations

Stochastic Dynamics for Ultracold Atoms in Optical Lattices (Poster presentation) Annual Meeting of the Institute of Physics Theory of Condensed Matter Group, University of Warwick, UK, December 2004.

Stochastic Dynamics for Ultracold Atoms in Optical Lattices (Poster presentation) École Prédoctorale de Physique des Houches: Laser Cooling and Applications, L'École de Physique des Houches, Les Houches, France, September 2004.

Observation of strong current resonances due to the formation of stochastic conduction networks in superlattices, D.P.A. Hardwick, S.L. Naylor, D. Fowler, T.M. Fromhold, A. Patanè, L. Eaves and M. Henini, Institute of Physics Condensed Matter and Materials Physics, Exeter, UK, April 2006.